UNIVERSITY OF IOANNINA
SCHOOL OF SCIENCES
DEPARTMENT OF MATHEMATICS
APPLIED AND COMPUTATIONAL
MATHEMATICS

Konstantina Kyriakoudi

Biofluid Mechanics Using Numerical and Approximate Analytical Methods

---

Doctoral Thesis

Mathematician

Ioannina, 2026

ΠΑΝΕΠΙΣΤΗΜΙΟ ΙΩΑΝΝΙΝΩΝ
ΣΧΟΛΗ ΘΕΤΙΚΩΝ ΕΠΙΣΤΗΜΩΝ
ΤΜΗΜΑ ΜΑΘΗΜΑΤΙΚΩΝ
ΤΟΜΕΑΣ ΕΦΑΡΜΟΣΜΕΩΝ ΚΑΙ
ΥΠΟΛΟΓΙΣΤΙΚΩΝ ΜΑΘΗΜΑΤΙΚΩΝ

Κωνσταντίνα Κυριακούδη

Μελετη Προβληματων της Ρευστομηχανικης με Εμφαση στα Βιορευστα με την Βοηθεια Αριθμητικων και Προσεγγιστικων Αναλυτικων Μεθοδων

ΔΙΔΑΚΤΟΡΙΚΗ ΔΙΑΤΡΙΒΗ

ΜΑΘΗΜΑΤΙΚΟΣ

Ιωάννινα, 2026

Αφιερώνεται στην οικογένειά μου

Dedicated to my family

Η παρούσα Διδακτορική Διατριβή εκπονήθηκε στο πλαίσιο των σπουδών για την απόκτηση Διδακτορικού Διπλώματος που απονέμει το Τμήμα Μαθηματικών του Πανεπιστημίου Ιωαννίνων.

Εγκρίθηκε την 11/06/2026 από την συμβουλευτική επιτροπή:

Συμβουλευτική Επιτροπή

Ονοματεπώνυμο	**Βαθμίδα**
Μιχάλης Ξένος	Καθηγητής
Danny Bluestein	Διακεκριμένος Καθηγητής του SUNY
Ευγενία Πετροπούλου	Αναπληρώτρια Καθηγήτρια

Εγκρίθηκε την 11/06/2026 από την εξεταστική επιτροπή:

Εξεταστική Επιτροπή

Ονοματεπώνυμο	**Βαθμίδα**
Θεόδωρος Χωρίκης	Καθηγητής
Φωτεινή Καρακατσάνη	Επίκουρη Καθηγήτρια
Ευάγγελος Χατζηγεωργίου	Καθηγητής
Γεώργιος Κανελλοπουλος	Επίκουρος Καθηγητής

ΥΠΕΥΘΥΝΗ ΔΗΛΩΣΗ

“Δηλώνω υπεύθυνα ότι η παρούσα διατριβή εκπονήθηκε κάτω από τους διεθνείς ηθικούς και ακαδημαϊκούς κανόνες δεοντολογίας και προστασίας της πνευματικής ιδιοκτησίας. Σύμφωνα με τους κανόνες αυτούς, δεν έχω προβεί σε ιδιοποίηση ξένου επιστημονικού έργου και έχω πλήρως αναφέρει τις πηγές που χρησιμοποίησα στην εργασία αυτή.”

Κωνσταντίνα Κυριακούδη

The present Doctoral Thesis was carried out in the context of the studies for the obtaining Doctoral Degree, awarded by the Mathematics Department of University of Ioannina.

Accepted by the three members of the advisory committee on 11/06/2026:

Advisory Committee

Full Name	**Rank**
Michalis Xenos	Professor
Danny Bluestein	SUNY Distinguished Professor
Eugenia Petropoulou	Associate Professor

Approved by the seven members of the examination committeeon 11/06/2026:

Evaluation Committee

Full Name	**Rank**
Theodoros Horikis	Professor
Fotini Karakatsani	Assistant Professor
Evangelos Hadjigeorgiou	Professor
Georgios Kanellopoulos	Assistant Professor

Statutory Declaration

"I hereby declare that the present thesis was carried out in accordance with the international ethical and academic standards of conduct and the protection of intellectual property. In compliance with these standards, I have not appropriated the scientific work of others and I have fully acknowledged all the sources used in this work"

Konstantina Kyriakoudi

Ευχαριστιες

Η παρούσα διατριβή εκπονήθηκε στο Τμήμα Μαθηματικών του Πανεπιστημίου Ιωαννίνων. Με την ολοκλήρωση της θα ήθελα να εκφράσω την ειλικρινή μου ευγνωμοσύνη σε όλους όσοι συνέβαλαν με οποιονδήποτε τρόπο στην πραγματοποίηση αυτής της ερευνητικής προσπάθειας.

Πρώτα από όλα, θα ήθελα να ευχαριστήσω τον επιβλέποντά μου, Καθηγητή Μιχαήλ Ξένο, για την ανεκτίμητη καθοδήγηση, τις συμβουλές, τον χρόνο και την αδιάκοπη ενθάρρυνσή του. Γνωρίζοντάς με από τον πρώτο χρόνο των προπτυχιακών μου σπουδών, υπήρξε συνεχής πηγή στήριξης και έμπνευσης, και η καθοδήγησή του υπήρξε καθοριστική τόσο σε ακαδημαϊκό όσο και σε προσωπικό επίπεδο.

Θα ήθελα επίσης να εκφράσω την εκτίμησή μου στα άλλα δύο μέλη της επιτροπής αξιολόγησης, τον Καθηγητή Danny Bluestein και την Αναπληρώτρια Καθηγήτρια Ευγενία Πετροπούλου, για τα πολύτιμα σχόλια τους, τις προτάσεις και τον χρόνο που αφιέρωσαν στη βελτίωση αυτής της εργασίας. Ευχαριστίες εκτείνονται επίσης στα υπόλοιπα μέλη της εξεταστικής επιτροπής για τον χρόνο, τα πολύτιμα σχόλια και τις προτάσεις τους που συνέβαλαν στη βελτίωση της διατριβής.

Είμαι βαθιά ευγνώμων σε όλους τους Καθηγητές του Τμήματος Μαθηματικών, παρόντες και παρελθόντες, για τις γνώσεις, την καθοδήγηση και την έμπνευση που μου έχουν προσφέρει καθ' όλη τη διάρκεια των προπτυχιακών και μεταπτυχιακών μου σπουδών, καθώς και για την εξαιρετική συνεργασία που είχαμε όλα αυτά τα χρόνια.

Επιπλέον, θα ήθελα να ευχαριστήσω την κα. Αναστασία Αίθρα Σαμαρά Πιτσέλη και τον κο. Γεώργιο Βελισσάρη για τη διαρκή παρουσία και την αμέριστη στήριξή τους καθ' όλη τη διάρκεια του διδακτορικού μου. Η προθυμία τους να βοηθήσουν, να ακούσουν και να με υποστηρίξουν με κάθε δυνατό τρόπο υπήρξε ανεκτίμητη κάνοντας τις προκλήσεις αυτού του ταξιδιού πιο διαχειρίσιμες. Είμαι επίσης ευγνώμων στους Δρ. Ελένη Ήλκου, Δρ. Σπυρίδων Τζίμα, Δρ. Γεώργιο Βαρδάκα, κο. Γρηγόριο Παπιγκιώτη, κο. Βασίλειο Βαχτσεβάνο, κο. Σπυρίδων Ζαφείρη και την κα. Σοφία Κατσίβελου. Η αλληλεπίδραση μαζί τους, οι συζητήσεις μας για ακαδημαικά και μη θέματα, καθώς και η ενθάρρυνση και η κατανόηση που μου προσέφεραν, κατέστησαν

την καθημερινότητα πιο ευχάριστη και ουσιαστική.

Τέλος, η βαθύτερη ευγνωμοσύνη μου ανήκει στους γονείς μου, για την αμετάβλητη αγάπη, ενθάρρυνση και πίστη τους σε μένα, που υπήρξαν η βάση όλων των επιτευγμάτων μου. Η στήριξή τους καθ' όλη τη διάρκεια των ακαδημαϊκών και προσωπικών μου προσπαθειών υπήρξε ανιδιοτελής, και τους οφείλω περισσότερα από όσα μπορούν να εκφράσουν οι λέξεις.

Ιωάννινα 2026,
Κωνσταντίνα Κυριακούδη

Χρηματοδότηση

Η παρούσα έρευνα χρηματοδοτήθηκε από τους παρακάτω πόρους:

- Ανταποδοτική Υποτροφία στο πλαίσιο του προγράμματος “ΔΙΩΝΗ: Υπολογιστική Υποδομή Επεξεργασίας και Ανάλυσης Μεγάλου Όγκου Δεδομένων” (MIS 5047222), το οποίο συγχρηματοδοτείται από την Ευρωπαϊκή Ένωση και την Ελλάδα μέσω του Επιχειρησιακού Προγράμματος “Ανταγωνιστικότητα, Επιχειρηματικότητα, Καινοτομία”, ΕΣΠΑ 2014–2020.

- Ανταποδοτική Υποτροφία στο πλαίσιο της δράσης “Υποστήριξη των εκπαιδευτικών δραστηριοτήτων του Πανεπιστημίου Ιωαννίνων κατά το ακαδημαϊκό έτος 2021–2022 με την ενσωμάτωση ενισχυτικής διδασκαλίας επιπρόσθετα των κύριων διαλέξεων” (MIS 5161679), η οποία συγχρηματοδοτείται από την Ευρωπαϊκή Ένωση και την Ελλάδα μέσω του Επιχειρησιακού Προγράμματος “Ανάπτυξη Ανθρώπινου Δυναμικού, Εκπαίδευση και Διά Βίου Μάθηση”, ΕΣΠΑ 2014–2020.

- Ανταποδοτική Υποτροφία στο πλαίσιο του προγράμματος “Safe Aorta: Σύστημα Υποστήριξης Κλινικών Αποφάσεων για τη Νόσο των Ανευρυσμάτων

Κοιλιακής Αορτής βασισμένο σε μοντέλα Τεχνητής Νοημοσύνης" (TAEDR-0535983), το οποίο εντάχθηκε στη δράση "Εμβληματικές δράσεις σε διαθεματικές επιστημονικές περιοχές με ειδικό ενδιαφέρον για τη σύνδεση με τον παραγωγικό ιστό" στο πλαίσιο της χρηματοδότησης "Ελλάδα 2.0 – Εθνικό Σχέδιο Ανάκαμψης και Ανθεκτικότητας".

Acknowledgements

This dissertation was completed at the Department of Mathematics of the University of Ioannina. With its completion, I would like to express my sincere gratitude to all those whose support and contribution were decisive throughout this journey.

First and foremost, I am profoundly grateful to my supervisor, Michael Xenos, for his invaluable guidance, advice, time, and continuous encouragement. Having known me since the first year of my undergraduate studies, he has been a constant source of support and inspiration, and his guidance has been decisive both academically and personally.

I would also like to express my appreciation to the other two members of the evaluation committee Prof. Danny Bluestein and Prof. Eugenia Petropoulou, for their insightful comments, constructive suggestions, and the time they devoted to improving this work. Many thanks are also extended to the rest of the examining committee for their time, valuable comments, and suggestions that helped improve this dissertation.

I am deeply grateful to all the Professors of the Department of Mathematics, both past and present, for the knowledge, guidance and inspiration they have provided me throughout my undergraduate and postgraduate studies, as well as for the excellent collaboration we have shared over the years.

Furthermore, I would like to thank Ms. Anastasia Aithra Samara Pitseli and Mr. George Velissaris for their constant presence and unwavering support throughout my PhD journey. Their willingness to help, listen, and support me in every possible way has been invaluable, making the challenges of this journey more manageable. I am also grateful to Dr. Eleni Ilkou, Dr. Spyridon Tzimas, Dr. Georgios Vardakas, Mr. Grigorios Papigkiotis, Mr. Vasileios Vachtsevanos, Mr. Spyridon Zafeiris, and Ms. Sofia Katsivelou. Our interactions, our discussions on both academic and non-academic matters, as well as the encouragement and understanding they offered, made my daily life more enjoyable and meaningful.

Finally, my deepest gratitude goes to my parents, whose unwavering love, encour-

agement and faith in me have been the foundation of all my achievements. Their support throughout my academic and personal endeavors has been unconditional, and I owe them more than words can express.

Ioannina 2026,
Konstantina Kyriakoudi

Funding

The present research was funded by the following sources:

- Compensatory Scholarship under the programme “DIONI: Computational Infrastructure for Processing and Analysis of Large-Scale Data” (MIS 5047222), co-financed by the European Union and Greece through the Operational Programme “Competitiveness, Entrepreneurship and Innovation”, NSRF 2014–2020.

- Compensatory Scholarship under the action “Support of the educational activities of the University of Ioannina during the academic year 2021–2022 through the integration of supplementary teaching in addition to the main lectures” (MIS 5161679), co-financed by the European Union and Greece through the Operational Programme “Human Resources Development, Education and Lifelong Learning”, NSRF 2014–2020.

- Compensatory Scholarship under the programme “Safe Aorta: Clinical Decision Support System for Abdominal Aortic Aneurysm Disease Based on Artificial Intelligence Models” (TAEDR-0535983), which was implemented within

the action “Flagship actions in interdisciplinary scientific areas with particular interest in linking research with the productive sector”, under the funding scheme “Greece 2.0 – National Recovery and Resilience Plan”.

Περιληψη

Η παρούσα διπλωματική εργασία επικεντρώνεται σε αριθμητικές και προσεγγιστικές αναλυτικές μεθόδους που χρησιμοποιούνται σε προβλήματα μηχανικής βιορευστών. Αρχικά, παρουσιάζεται το μαθηματικό υπόβαθρο μέσω της μελέτης της Μεθόδου Πεπερασμένων Στοιχείων (FEM), της Μεθόδου Πεπερασμένων Όγκων (FVM) και των διαδικασιών διακριτοποίησής τους. Επιπλέον, οι μη γραμμικές εξισώσεις της ροής των ρευστών αντιμετωπίζονται χρησιμοποιώντας προσεγγιστικές αναλυτικές τεχνικές, και συγκεκριμένα με τη Θεωρία Διαταραχών και τη Μέθοδο Ομοτοπικής Ανάλυσης (HAM).

Με αυτό το μαθηματικό υπόβαθρο, η διατριβή παρουσιάζει υπολογιστικά μοντέλα για τη διερεύνηση της αιμοδυναμικής του καρδιαγγειακού συστήματος. Αρχικά, διατυπώνεται μια δισδιάστατη μικτή θεώρηση Euler-Lagrange, η οποία ενσωματώνει τη Μαγνητοϋδροδυναμική (MHD), για τη μελέτη παλμικής ροής. Η προσέγγιση αυτή επεκτείνεται σε έναν ισχυρό τρισδιάστατο επιλύτη αλληλεπίδρασης Ρευστού-Στερεού (FSI), συγκρίνοντας την αιμοδυναμική σε παλλόμενα και άκαμπτα τοιχώματα. Οι επιλύτες αυτοί εφαρμόζονται σε παθολογικές αρτηριακές καταστάσεις, αξιοποιώντας ένα μοντέλο πολλαπλών κλιμάκων και στατιστική ανάλυση, προκειμένου να συνδεθεί η ανευρυσματική γεωμετρία με κρίσιμες αιμοδυναμικές παραμέτρους, όπως οι διατμητικές τάσεις του τοιχώματος και οι δείκτες ταλαντούμενης ροής. Τέλος, η έρευνα επεκτείνεται στη μηχανική στερεών, εστιάζοντας ειδικότερα στη μαθηματική μοντελοποίηση των προσθετικών αντικατάστασης αορτικής βαλβίδας. Εν κατακλείδι, η μελέτη αυτή αναδεικνύει τη σημασία των προηγμένων υπολογιστικών προσεγγίσεων και των τεχνικών αλληλεπίδρασης ρευστού-στερεού στην κατανόηση των πολύπλοκων φυσικών φαινομένων που διέπουν το καρδιαγγειακό σύστημα.

Λέξεις–Κλειδιά: Υπολογιστική Ρευστομηχανική, Αλληλεπίδραση Ρευστού–Στερεού, Μικτή Θεώρηση Euler–Lagrange, Σύστημα Γενικευμένων Καμπυλόγραμμων Συντεταγμένων, Εξισώσεις Navier–Stokes, Παλμική Ροή, Μέθοδος Πεπερασμένων Στοιχείων, Μέθοδος Πεπερασμένων Όγκων, Μέθοδος Ομοτοπικής Ανάλυσης, Μαγνητοϋδροδυναμική, Βιοϊατρικές Εφαρμογές, Μοντελοποίηση Ροής Αίματος, Καρδιαγγειακές Ροές, Ανεύρυσμα Κοιλιακής Αορτής

Abstract

The present thesis focuses on numerical and approximate analytical methods used in biofluid mechanics problems. A strong mathematical basis is established by thoroughly studying the Finite Element Method (FEM), the Finite Volume Method (FVM), and the discretization procedures. Furthermore, the highly nonlinear governing equations of fluid flow are treated using approximate analytical techniques, particularly Perturbation Theory and the Homotopy Analysis Method (HAM).

With this mathematical foundation, the thesis presents computational models to investigate cardiovascular hemodynamics. First, a two-dimensional mixed Euler–Lagrange approach incorporating Magnetohydrodynamics (MHD) is formulated to study pulsatile flow. This approach is advanced into a robust three-dimensional Fluid–Structure Interaction (FSI) solver, comparing the hemodynamics on deformable and rigid walls. These solvers are applied to pathological arterial conditions utilizing a multiscale model and statistical analysis to link aneurysmal geometry with critical hemodynamic parameters such as wall shear stress and oscillatory flow indices. Finally, the research extends to the mathematical modelling of structural mechanics and especially the modeling of aortic valve replacements. Ultimately, this study examines the importance of advanced computational approaches in understanding the complicated physical phenomena governing the cardiovascular system combining fluid-structure interaction techniques.

Keywords: Computational Fluid Dynamics, Fluid–Structure Interaction, Mixed Euler–Lagrange Formulation, Generalized Curvilinear Coordinate System, Navier–Stokes Equations, Pulsatile Flow, Finite Element Method, Finite Volume Method, Homotopy Analysis Method, Magnetohydrodynamics, Biomedical Applications, Blood Flow Modeling, Cardiovascular Flows, Abdominal Aortic Aneurysm

Contents

CHAPTER 1

INTRODUCTION

1.1 Introduction

Mathematical modelling of physical phenomena relies on systems of partial differential equations, usually non-linear and based on the fundamental theory and first principle laws that describe each problem. The analytical solution of such systems is often difficult or impossible. Consequently, the necessity to employ alternative computational tools arises. More specifically, numerical methods such as the Finite Element and Finite Volume methods are employed for approximating the solution. In other cases, analytical, semi-analytical and approximation methods such as perturbation methods and the homotopy analysis method, are preferred.

These solving approaches are employed in Fluid Mechanics problems. Fluid Mechanics is a particular branch of applied mathematics whose primary object of research is the static and dynamic behaviour of fluids. Fluid is characterised as any substance presenting a flow, i.e. refers to liquids and gases whose cohesion forces are weak, so that they each take the shape of the space they occupy or the medium through which they move.

In this thesis, the focus lies on fluid mechanics problems combined with the biomedical field. In particular, the study of blood flow in the cardiovascular system requires foundational knowledge of both mathematics and fluid dynamics. Mathematical modelling provides tools to describe the flow of fluids such as blood and its interaction with the vessels and the rest of the circulatory system. The governing equations derived from the fluid mechanics principles and fundamental laws, describe the relationship among velocity, pressure and external forces in the fluid. Furthermore, these equations can be modified to account for any complex phenomena such as the magnetic fields, arterial wall pulsations, non-Newtonian behaviour, and vessel wall elasticity.

Computational methods are essential for solving the governing equations in real-

istic geometries. The Navier-Stokes equations used in the present thesis represent a significant open problem; therefore, research primarily focuses on numerical approximations. This approach allows us to approximate the solution, providing insightful information on the flow patterns, pressure distributions, and the stresses on the arterial walls.

This chapter provides a historical overview of the relevant literature and outlines the medical context and challenges relevant to this thesis. Establishing this background ensures the reader can easily understand the mathematical concepts and formulations presented in the following chapters.

1.2 Mathematical Methods and Fluid Mechanics

As its name suggests, **fluid mechanics** is the branch of classical mechanics that studies the fluid flow behaviour. So, it is important first to understand what a fluid is

Definition 1.2.1. Fluid is a substance, liquid or gas, that deforms continuously (it flows) under the influence of stresses (mainly shear) or external forces.

In fluid mechanics, the most known equations for describing flow problems are the Navier-Stokes equations for incompressible flow which have existed since 1827. Fluids are usually classified according to their relationship between shear stresses and rate of deformation. Thus, there is a distinction of fluids to Newtonian and non-Newtonian fluids, each having specific role in the mathematical modelling of flow problems.

In **Newtonian** fluids the shear stress has a linear connection with the strain rate. Common examples include water, air, and many common liquids under standard conditions. In contrast, non Newtonian fluids have a more complex stress-strain relationship, that may be shear-thinning/thickening or viscoelastic [91, 93, 135].

The choice between these models forms the equations and the numerical scheme and simulations, accordingly. Both approaches offer distinct advantages depending on the application: the Newtonian model provides computational efficiency by simplifying the governing equations, whereas non-Newtonian models are utilised to capture detailed velocity and pressure dynamics. In the cardiovascular system, the model is chosen based on the scale of interest, flow regime and the condition under examination. It is common for larger arteries, such as the aorta, to assume Newtonian fluid behaviour while in smaller ones it would not be a good description approach.

Navier-Stokes equations describe how inertial, pressure and viscous forces, as well as any external forces, e.g magnetic field, affect the fluid motion:

$$\underbrace{\rho\frac{\partial \mathbf{u}}{\partial t}}_{\text{Local acceleration}} + \underbrace{\rho(\mathbf{u}\cdot\nabla)\mathbf{u}}_{\text{Convective acceleration}} = \underbrace{-\nabla p}_{\text{Pressure gradient}} + \underbrace{\mu\nabla^2\mathbf{u}}_{\text{Viscous diffusion}} + \underbrace{\mathbf{f}}_{\text{External forces}},$$

where each term represents:

- Local acceleration, $\rho\frac{\partial \mathbf{u}}{\partial t}$: Change of velocity at a fixed point in space over time.
- Convective acceleration, $\rho(\mathbf{u}\cdot\nabla)\mathbf{u}$: Change of velocity along the flow path due to fluid motion.
- Pressure gradient, $-\nabla p$: Drives the flow from high-pressure regions to low-pressure regions.
- Viscous diffusion, $\mu\nabla^2\mathbf{u}$: Internal stress forces acting on the fluid.
- External forces, $\mathbf{f}$: Body forces such as gravity or magnetic forces in MHD.

The non-linear convective term, $\rho(\mathbf{u}\cdot\nabla)\mathbf{u}$, is responsible for the complexity of the system, leading also to instabilities, vortices, and turbulence. Analytical solutions of the Navier-Stokes equations remain challenging making it one of the most significant open problems in mathematics. While global existence and uniqueness have been proven for cases such as the incompressible two-dimensional flow, the three-dimensional problem remains a Millennium Prize Problem [66]. Consequently, computational fluid dynamics (CFD) is utilised to provide numerical approximations for more complicated three-dimensional problems.

1.2.1 Analytical and Semi-Analytical Methods

Non-linear problems are generally difficult to solve analytically, particularly in the field of fluid mechanics. Analytical and semi-analytical approaches introduce approximations that make these problems tractable, overcoming the non-linearity that hinders an exact analytical solution, aiming to keep the nature of the physical problem.

Analytical techniques, such as perturbation methods, typically rely on the existence of small or large dimensionless physical parameters [18, 123, 142].

Perturbation theory is a widely used collection of analytical techniques for the approximate solution of differential equations. The main idea is based on the existence of a small (or large) physical parameter, ε, in the governing equations and obtaining a solution in a series form based on that same parameter [18, 123, 142]. While this method is effective with "weak" non-linear problems, most of the problems do not have the required small (or large) parameter or the convergence is restricted in a very small region. Due to these limitations, alternative approaches have been introduced to overcome the limitation of the physical parameter.

To address such limitations, Liao introduced the Homotopy Analysis Method (HAM) in 1992, in which the basic concept is in the homotopy approach, which describes the continuous deformation of an object/scheme into another [115]. More specifically, this method creates a homotopy that deforms the initial guess of the solution into the exact solution of the problem. Unlike perturbation techniques, mentioned previously, homotopy analysis method is independent of small physical parameters enabling it to be applied to non-linear problems. However, this semi-analytic method introduces a convergence control parameter, $\overline{h}$ acting as assisting tool to optimise the convergence of the solution [112, 114].

1.2.2 Numerical Methods

Numerical methods are commonly used to complement and advance the analytical and semi-analytical methods especially, those related to the physical domain and the boundary conditions. Methods such as the Finite Element and the Finite Volume have gained a lot of interest over the past years.

The finite element method (FEM) has gained substantial momentum in the last decades. It was initially introduced for solid mechanics problems that were difficult to address analytically. The expansion of the method to fluid mechanics introduced additional challenges, mainly due to the non–linearities and instabilities of the solution of these problems.

The basic principles of the FEM were developed by the Swiss mathematician Ritz in 1909, while Hrenikoff, 1941, introduced the framework method, in which a continuous plane elastic medium could be replaced by an equivalent discrete system of structural rods. In 1943 Courant solved the torsion problem by applying the Rayleigh–Ritz method over triangular subregions based on the principle of minimum potential energy [9, 183].

1.2.3 Computational Fluid Dynamics - Fluid Structure Interaction

Computational fluid dynamics (CFD) is a branch of fluid mechanics that utilises numerical analysis and algorithms to simulate and predict fluid flow [167]. The solution of a flow problem (velocity, pressure, temperature etc.) can be found on the nodes of each cell of the grid. Better approximations yield from fine grids, e.g grids with a larger number of cells. However, as the number increases, the computational cost is also increasing, as it is dependent on the grid size [195]. As another step further, to make the simulation more realistic, we have to take under consideration the interaction of fluid and solid surfaces as it is commonly found in nature. Fluid Structure Interaction (FSI) is the approach that enables us to describe the interaction between the fluid and the solid interface eg. blood and the arterial wall. Examples of CFD and FSI problems can be found in aerofoil design, wind turbines, flow in arteries and the design of mechanical heart valves.

In the present study, pulsating wall motion is introduced by modelling the vessel wall as a moving boundary. This approach enables the interaction effects between the fluid and the wall, keeping the numerical scheme relatively simple. Although this strategy does not account for the mechanics of the wall, it is a good step, providing useful insights into the FSI modelling.

The initial fluid equations are in an Eulerian form. However, in many applications where there is the interaction with the solid interface, or solid deformation, the need of a different formulation arises, such as the Lagrangian description of body motion. The most appropriate formulation for such applications that combine solid motion with deformable interfaces in combination with fluid motion (FSI approach) a mixed formulation is applied. Such formulation is called Euler-Lagrange or Eulerian-Lagrangian form. Specifically in the Lagrangian approach, the observer is moving through space with a known trajectory. In contrast, the Eulerian approach describes the motion from a fixed point. The observer can fully describe quantities as velocity and pressure at a specific location. In this case, the initial and final positions, as well as the path they follow, are not of interest.

The mixed Euler-Lagrange approach counts motion with both the description, offering better insight. Fluid is then modelled with the mixed (Euler-Lagrange) approach, whereas the motion of the boundary can be described with the Lagrange description.

1.3 Biomedical Applications

1.3.1 Blood and Blood Flow

Blood is a complex fluid that consists of cells, proteins, lipids, and plasma that transports oxygen and nutrients throughout the body while removing the waste. Plasma, which can be considered mostly as water, contains dissolved proteins, electrolytes, nutrients, and metabolic waste products. The primary function of blood is the transport of oxygen and nutrients and the discharge of metabolic by-products, thereby maintaining homeostasis.

The continuous rhythmic contraction of the heart generates a pulsatile pressure waveform that contributes to the circulation of blood. Pulsatility is the key factor for the haemodynamic environment as it helps blood to transfer through the arterial systems, distributing oxygenated blood and nutrients from the heart to peripheral organs and tissues.

1.3.2 Pathological Arteries

Pathological conditions related to the arterial system significantly modify the haemodynamics and the geometry of the vessels. The geometry of blood vessels and blood flow characteristics are strongly connected. Alterations in the vascular geometry can modify flow and flow patterns and, conversely, haemodynamic forces influence the vascular domain and contribute to disease progression. This interaction plays a crucial role in the development and evolution of arterial pathologies. In this thesis, the attention is focused on two major arterial pathologies, stenosis and aneurysm formation. Additionally, cardiovascular interventions such as heart valve replacement are considered, as they help with blood flow in narrow areas and offer modifications to flow patterns and wall stresses. This bidirectional connection is crucial for the development and progression of vascular diseases.

Stenotic Arteries

Arterial stenosis is a common cardiovascular disease where a narrowing of the lumen disturbs and impedes blood flow in a local region of the blood vessel. Stenotic blood vessels induce wall shear stresses, which progressively weaken the arterial wall and thus it is prone to aneurysm-creation [101, 185]. The arteries that are usually affected from stenosis are large-to-mid sized arteries, like the aorta.

This pathological condition can cause major health issues, such as thrombosis, sudden myocardial infarction and cerebral strokes, therefore it is critical for the medical community to be able to investigate this condition. Fluid mechanics and especially, haemodynamics, can substantially contribute to this effort by modelling the blood flow process in stenotic arteries and extract significant results, for instance by incorporating various degrees of occlusion in numerical simulations of a stenotic blood vessel and by studying the blood flow and pressure in pre-stenotic and post-stenotic areas.

Regarding the fundamental characteristics and the configuration of a stenosis, four are on the scope of interest:

- The location that it appears (in which segment of the arterial vessel).
- The extension it has (i.e. multiple occasions of stenosis in a vessel).
- The length of stenosis (with a threshold of characterization of Small/Big at 10mm length).
- The shape and the geometric features (see Figures 1.1, 1.2) of the diseased segment, including its diameter, the smoothness or lack-of smoothness in contours, tapering, branchings, post-stenotic dilation and more [185].

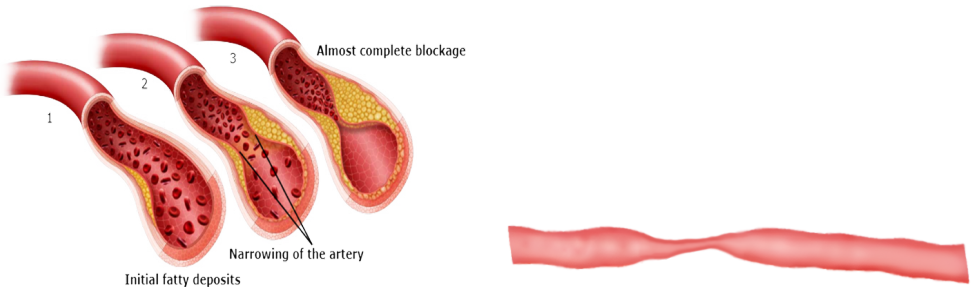

(a) Stenosis block (b) Stenosis

Figure 1.1. Stenosis geometries.

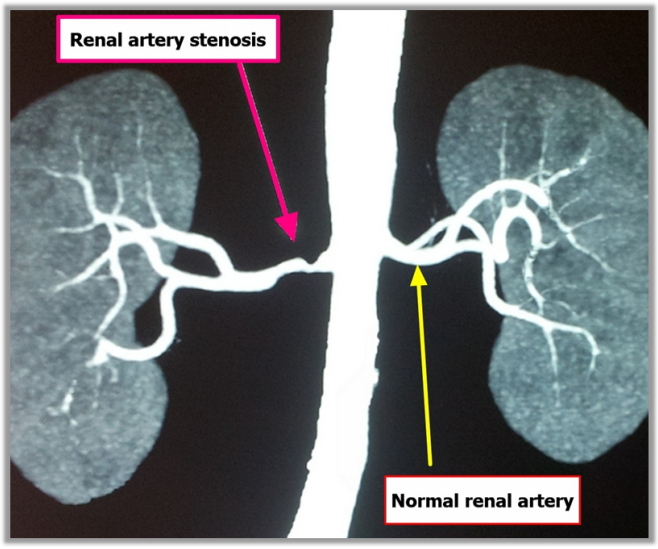

Figure 1.2. Real Case of Stenosis.

Aneurysmatic arteries

An aneurysm is a bulge in a blood vessel caused by a weakness in the wall of the vessel. The arterial wall can be weakened extensively by elevated blood pressure. There is a variety of arteries that can be affected by an aneurysm leading to pathological blood conditions. The most common locations for an aneurysm to be formed are the arteries supplying the brain and the heart, as well as the aorta. An aneurysm of the abdominal aorta is called an abdominal aortic aneurysm (AAA). Characteristic cases of AAA are shown in Figures 1.3, 1.4. An AAA does not usually threaten health, but there is a risk that a larger aneurysm could burst and rupture, which could be fatal in case of massive internal bleeding. Even smaller AAAs could rupture unexpectedly. Most unruptured aneurysms are asymptomatic and cannot be detected with the same ease. However, it could impede blood circulation to other tissues and organs. Suspicion of an unrupted aneurysm can be confirmed through diagnostic imaging, such as a Magnetic Resonance Imaging (MRI) or a Computed Tomography (CT) scan [53, 165].

Abdominal aortic aneurysm refers to the presence of an aneurysm in the lower part of the aorta and comprises the vast majority of aortic aneurysms, as the most common locations of aneurysm formation are the infrarenal abdominal aortic regions [125, 160]. The presence of an AAA can be detected either incidentally or after its rupture, while the enlargement of the AAA can be either observed as a stable increase of the diameter of the vessel or as a rapid enlargement in an unspecified period of

time.

The significance of AAA in a clinical context stems from the elevated mortality risk linked to the rupture of the aneurysm as the constant progression of the disease ultimately leading to a rupture, since approximately 50-75% of individuals experiencing a ruptured AAA do not survive [208]. With the aid of simulation software where Fluid-Structure Interaction (FSI) is implemented, it is possible to achieve a detailed CFD model featuring:

- parameters affecting the formation of AAAs,
- parameters affecting the weakening of the arterial wall,
- reconstructed aortic geometries and
- blood flow, pressure and wall-shear stresses,

and can help medical experts monitor the gradual progression of a healthy aorta to a diseased one and identifying a specific region of the arterial segment as a prone location to aneurysm formation, in an *a priori* fashion, which can be used as a medical predictive/prognostic tool.

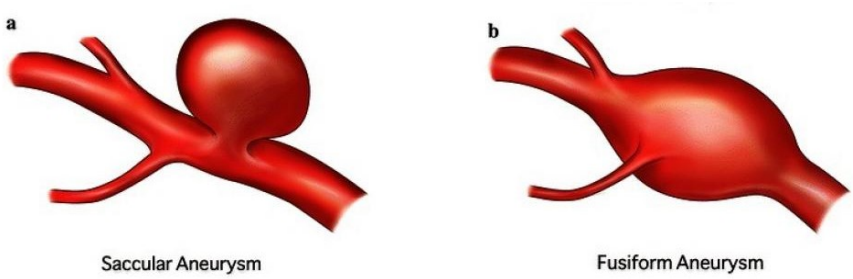

Figure 1.3. Cases of Abdominal Aortic Aneurysm

Heart Valves

The role of valves is to regulate unidirectional flow of the blood across the circulatory system. The aortic valve located between the left ventricle and the aorta is responsible for maintaining the forward flow during systole and preventing backflow during the diastole. Dysfunctions of the aortic valve, such as stenosis (narrowing) or regurgitation (leakage), alter the haemodynamics of the area significantly, leading to increased cardiac workload, disturbed flow patterns, and potential heart failure [120].

Figure 1.4. Real Case of Abdominal Aortic Aneurysm

In terms of fluid dynamics, heart valves introduce local gradients in velocity and pressure, as well, as flow separation areas and vortices near the leaflets. Additionally, the pulsatile flow generates forces and stresses on the leaflets and the vessel wall, which emphasizes the need for understanding the mechanisms of valve function [120].

Prosthetic heart valve replacements are the primary method to overcome the dysfunction in the aortic valve and can be either from natural, synthetic materials or titanium (older designs), with the second to offer better compatibility and extended durability. Transcatheter aortic valve replacement (TAVR) offers a minimally invasive process, in which the replacement is implanted in the correct position with the use of catheters [120].

The interaction between fluid and solid walls presents unique challenges in the computational modelling due to moving boundaries, complicated geometries and the interaction between the two surfaces [120]. Accurate models of valve dynamics are essential due to the insights that can provide improvements for patient specific treatments. Real and artificial heart valve models are presented in Figures 1.5 and 1.6.

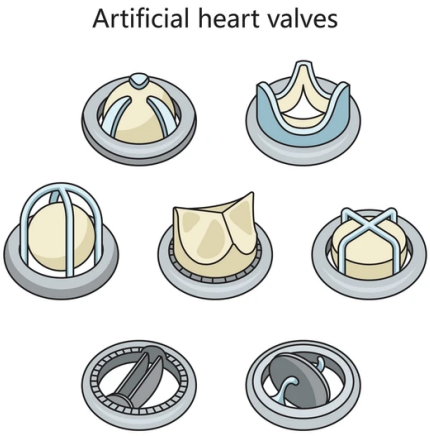

Figure 1.5. Types of heart valves

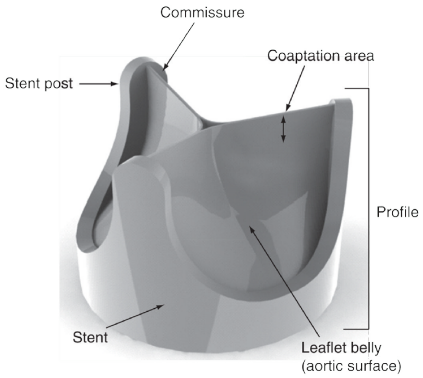

Figure 1.6. Real heart valves

1.4 Objectives & Outline of this Thesis

The main objective of the present thesis is the development and application of numerical approaches and solvers to simulate blood flow under pathological conditions. More specifically, the focus lies on the mixed Euler-Lagrange approach, for Fluid-Structure Interaction (FSI) problems such as blood flow and the motion of the arterial wall. The work focutilises more on aneurysmatic geometries, heart valve prosthetics and the inclusion of magnetic field with pulsating aortic walls. The implementation

contains the utilisation of numerical methods such as the finite element and finite volume methods, semi-analytic methods such as perturbation methods and the homotopy analysis method.

The remainder of the thesis is organized as follows:

- Chapter 2 introduces all the mathematical and computational tools required for this study, accompanied with some basic notions and configurations about the solving process.
- Chapter 3 presents recent results of the homotopy analysis method in a boundary-layer problem applied to the aortic wall.
- Chapter 4 presents a two dimensional methodology and solver of the Euler-Lagrange Navier-Stokes equations taking into consideration the pulsating nature of the wall and the effects of the magnetic field presence.
- Chapter 5 is an extension of the previous chapter presenting the three-dimensional version of the methodology and some results from patient based geometries.
- Chapter 6 provides a comprehensive haemodynamic and morphological analysis of abdominal aortic aneurysms, utilizing computational fluid dynamics across 74 patient-specific geometries to link geometric descriptors with key haemodynamic factors and rupture risk.
- Chapter 7 the materials used for the vessels and mainly for the development of aortic heart valve replacements, are studied, accompanied with some preliminary numerical results from our study.

CHAPTER 2

NUMERICAL METHODS

2.1 Introduction

In this chapter, the mathematical framework and solution methods used to solve the nonlinear partial differential equations (PDEs) arising in the fluid dynamics problems of this thesis are presented. To achieve a comprehensive understanding of these complex systems, we utilize a complementary set of tools: approximate analytical and semi-analytical techniques—which provide insight into the fundamental physics and serve as benchmarks—alongside robust numerical frameworks, which enable the simulation of realistic, complex geometries.

First, the focus lies on the fundamental numerical methods employed in the following chapters, specifically the Finite Element Method (FEM) and the Finite Volume Method (FVM). For the FEM, the basic theory is presented in one dimension with a simple example introducing the main concepts, after which the discussion is extended to two and three dimensions. Moreover, we introduce the h-, p-, and hp-versions of FEM, highlighting the method's flexibility in adjusting polynomial degrees and mesh refinement based on the problem's nature.

Regarding the FVM, the basic principles are similarly presented in a three-dimensional form. We then focus on the resulting nonlinear algebraic systems and the need for robust solvers, specifically Newton's method, trust-region approaches, and the Levenberg-Marquardt algorithm, which are essential to ensure convergence and stability in large-scale systems. Furthermore, we introduce development aspects of the computational grid, such as structured and unstructured grids and variable storage arrangements (collocated and staggered), highlighting the advantages and limitations of each selection for the simulations that follow.

Finally, the chapter explores the semi-analytical and approximation techniques utilized in this dissertation. In particular, the foundations of Perturbation Theory and the Homotopy Analysis Method (HAM) are presented, providing frameworks for con-

structing series solutions for cases where classical approaches may face convergence limitations. These methods are particularly useful for the boundary-layer flows and magnetohydrodynamic (MHD) extensions that appear in the subsequent chapters.

Overall, this chapter establishes the mathematical and computational background required for the development of the numerical and approximation methods used throughout the remainder of this dissertation [22, 107, 159].

2.2 Finite Element Method

This section outlines the foundational principles of the finite element method (FEM). Comprehensive theoretical details can be found in standard texts such as Brenner & Scott and Brezzi & Fortin [33, 34].

The physical phenomena investigated in this thesis are governed by partial differential equations (PDEs). Together with their respective boundary conditions, these equations constitute the *strong form* of the boundary value problem. Solving the strong form directly imposes strict continuity and differentiability requirements on the exact solution, which can be mathematically restrictive.

To overcome such limitations, the finite element method relies on the *weak* (or variational) formulation. By converting the differential equation into an integral form, this mathematical technique relaxes the "strong" continuity requirements. Consequently, the solution can be sought within broader functional spaces, specifically Sobolev spaces, where the differentiability requirements are less stringent. This relaxation is computationally advantageous, as it permits the use of lower-degree, piecewise polynomial basis functions for the numerical approximation.

The variational or weak form of a PDE seeks a solution u in an appropriate function space V such that

$$a(u, v) = (f, v), \quad \forall\, v \in V, \tag{2.1}$$

where $a(\cdot, \cdot)$ is a bilinear form and (f, v) is a linear functional. The discrete Galerkin approximation replaces V by a finite-dimensional subspace V_h, leading to a linear system that can be solved numerically. Existence and uniqueness of the solution to both problems are guaranteed by the Lax–Milgram theorem, provided the bilinear form is continuous and coercive on V [33, 34].

For incompressible flow problems the velocity–pressure formulation gives rise to a saddle-point system, whose discrete stability requires the finite-element spaces to satisfy the Ladyzhenskaya–Babuška–Brezzi (LBB) inf–sup condition [19, 184]. All

computations in this chapter use Taylor–Hood elements (P_k, P_{k-1}), $k \geq 2$, which are known to satisfy this condition.

2.2.1 FEM *h*-, *p*-, & *hp*-Versions

In complex fluid mechanics simulations, localized phenomena, such as high velocity gradients near boundaries or recirculation zones, require enhanced numerical resolution. Rather than performing a global, uniform subdivision of the multidimensional mesh (which drastically inflates computational cost), it is far more efficient to target specific regions using Adaptive Mesh Refinement (AMR) .

AMR generally falls into three main categories:

- *h-refinement*: The polynomial degree of the shape functions remains fixed, but the local element size h is reduced by subdividing specific elements in regions with high estimated errors.

- *p-refinement*: The mesh topology and element sizes remain completely fixed, but the polynomial degree p of the shape functions is locally elevated to increase precision.

- *r-refinement*: The total number of nodes and elements remains constant, but the nodal coordinates are repositioned, clustering them in areas that require optimization.

These strategies can also be coupled to maximize efficiency, most notably in *hp*-refinement [218, 219].

Regarding convergence, the expected rate is fundamentally dictated by the approximation properties of the chosen finite element space. In the standard *h*-version of FEM, convergence is algebraically bounded by the fixed degree of the polynomials; for instance, piecewise linear elements can yield at best $\mathcal{O}(h^2)$ convergence in the L^2-norm, assuming a sufficiently smooth solution. Conversely, the *p*- and *hp*-versions of the finite element method have the theoretical capability to bypass this algebraic limit, yielding exponential convergence rates for smooth problems [56, 179]. This makes them highly advantageous for efficiently resolving the complex flow patterns encountered in the subsequent chapters of this thesis.

2.2.2 Applications in Fluid Mechanics

This section is dedicated to applications. In the following problems, the main focus is on the effects of the increase in the degree of the polynomials. More specifically, to demonstrate how the mesh changes as the degree of the polynomial increases, adaptive mesh refinement is used. The following results were obtained using FEniCS.

The Poisson Equation

Assume the following problem

$$\begin{cases} -\Delta u = f, & \text{in } \Omega \\ u = u_D, & \text{on } \partial\Omega \end{cases} \tag{2.2}$$

where

$$u_D = \begin{cases} 1, & x = 0 \\ 0, & x = 1 \end{cases}$$

The domain Ω is defined as the unit square $[0, 1] \times [0, 1]$. Dirichlet boundary conditions are assumed on the left and right edges and introduce a source term f with a non-linear scalar field distribution in the interior. The weak form of the finite element method is:

$$\int_\Omega \nabla u \nabla v = \int_\Omega fv \tag{2.3}$$

$$a(u, v) = (f, v) \tag{2.4}$$

where the source function is defined as, $f(x, y) = 10e^{-\frac{(x-0.5)^2+(y-0.5)^2}{0.02}}$.

The domain is a unit square with 128 elements in the initial mesh, as shown in Figure 2.1.

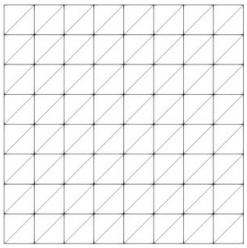

Figure 2.1. Initial Mesh with 128 Elements

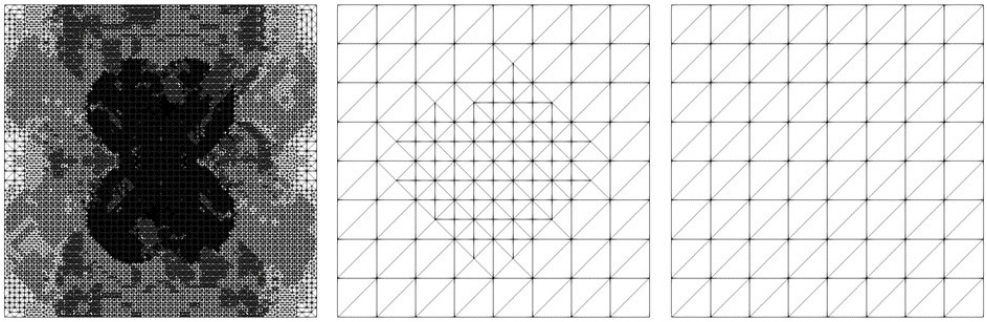

a) b) c)

Figure 2.2. Adaptive Meshes with a) 57110 b) 234 and c) 128 Elements

In each case, the initial mesh has 128 elements. It can be easily seen that as the order of the polynomials is increased, the adapted mesh needs fewer elements for the solution without sacrificing the scalar field results, as shown in Table 2.1. In Figure 2.2 *c)* the adapted mesh is the same as the initial, the only difference is the increase of the degree from 1 to 3. The exact number of elements in meshes is 57110 when there are first-order polynomials, 234 for second-order, and 128 for third-order polynomials.

Error	**Initial Mesh**	**Adapted Mesh**
$k = 1$	1.72055	1.71608
$k = 2$	1.71829	1.71634
$k = 3$	1.71824	1.71824

Table 2.1. Error in the L_2 norm for initial and adapted meshes.

The error in both the original case as well as in the adapted case decreases as the order increases. As depicted in Figure 2.3, the numerical solution of the Poisson equation exhibits a smooth, radial distribution with a distinct maximum peak concentrated at the center of the domain. This behaviour corresponds directly to the applied source term, with the values smoothly transitioning outward to satisfy the prescribed Dirichlet boundary conditions at the edges.

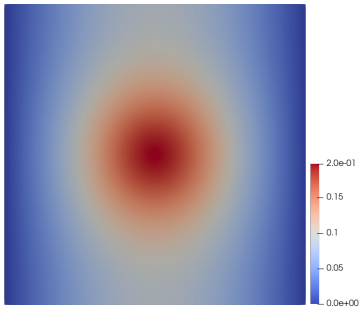

Figure 2.3. Numerical Solution of the Poisson Equation

The Stokes Equation

The following problem is the Stokes equations

$$\begin{cases} -\nu\Delta\mathbf{u} + \nabla p = \mathbf{f} \ \ in \ \ \Omega \\ \nabla \cdot \mathbf{u} = 0 \ \ in \ \ \Omega \\ \mathbf{u} = 0 \ \ on \ \ \partial\Omega. \end{cases} \tag{2.5}$$

where ν denotes the kinematic viscosity and $\Omega \subset \mathbb{R}^2$ is a bounded domain. The function $\mathbf{u}$ denotes the velocity and p the pressure. The corresponding weak form of the Stokes equation is

$$\nu(\nabla\mathbf{u}, \nabla\mathbf{v}) - (\nabla \cdot \mathbf{v}, p) = (f, v) \tag{2.6}$$

$$(\nabla \cdot \mathbf{u}, q) = 0 \tag{2.7}$$

In the cases studied below a mixed function space $W = V \times Q$ is utilised with Taylor-Hood Elements. Taylor-Hood is a mixed element containing the (P_k, P_{k-1}) pair of polynomials with $k \geq 2$.

Backward Facing Step A well-known test problem of the Stokes problem, for internal flows, is the Backward Facing Step. Due to the geometry, it creates a recirculation

zone near the wall of the step. The problem has the following formulation:

$$\begin{cases} -\nu\Delta\mathbf{u} + \nabla p = \mathbf{f} & \text{in } \Omega \\ \nabla\mathbf{u} \cdot \mathbf{n} + p\mathbf{n} = g & \text{on } \Gamma_N \\ \mathbf{u} = \mathbf{u}_D & \text{on } \Gamma_D \end{cases} \tag{2.8}$$

where Γ_D, Γ_N are the Dirichlet and Neumann boundary conditions, respectively. The weak form is:

$$\int_\Omega [\nu\nabla\mathbf{u} \cdot \nabla\mathbf{v} - (\nabla \cdot \mathbf{v})p + (\nabla \cdot \mathbf{u})q]\, d\Omega = \int_\Omega \mathbf{f} \cdot \mathbf{v}\, d\Omega + \int_{\Gamma_N} \mathbf{g} \cdot \mathbf{v}\, ds$$
$$a\left((\mathbf{u}, p), (\mathbf{v}, q)\right) = L(\mathbf{v}, q)$$

Figure 2.4 shows that the initial domain is discretised into 890 elements. When employing adaptive mesh refinement with the (P_2, P_1) finite element space, the mesh refines locally, particularly around the step corner where the flow abruptly changes, resulting in an adapted mesh of 1131 elements, Figure 2.5*a)*. However, as the polynomial order increases, the adapted mesh requires fewer elements to achieve the target accuracy. This reduction is clearly visible as the element count drops to 1093 and 909 elements, Figures 2.5*b)* and 2.5*c)*, respectively. The adapted mesh ultimately tends back toward the initial configuration when $k = 10$ and (P_{10}, P_9) polynomials are used.

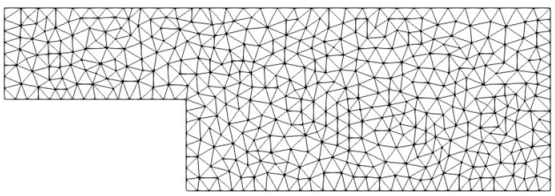

Figure 2.4. Initial Mesh with 890 Elements

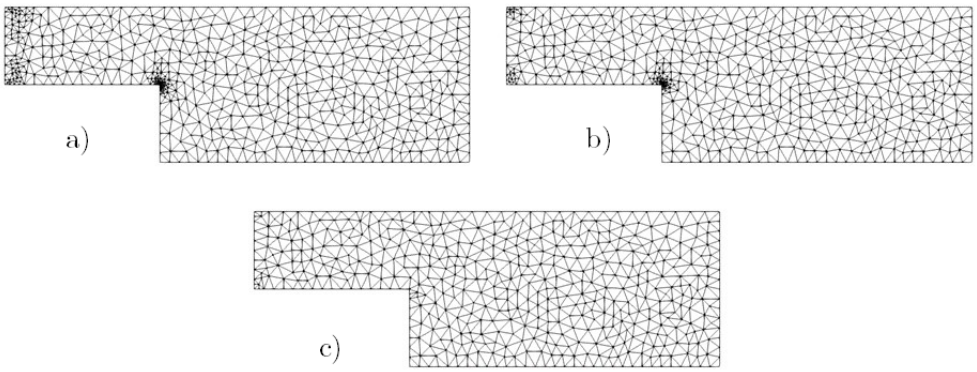

Figure 2.5. Adaptive Meshes with a) 1131, b) 1093 and c) 909 elements

Table 2.2 summarises the L_2 norm errors for both the initial and adapted meshes across various polynomial degrees. The overall error generally stabilises or decreases as the number of elements tends toward the initial count. Slight fluctuations in the error occur because, in certain cases, the adaptation algorithm faces mathematical difficulty in reducing the number of elements, resulting in the element count remaining constant or slightly increasing between polynomial degrees.

Error	**Initial Mesh**	**Adapted Mesh**
(P_2, P_1)	0.912279	0.911745
(P_3, P_2)	0.911585	0.911762
(P_4, P_3)	0.911806	0.911780
(P_5, P_4)	0.911766	0.911765
(P_6, P_5)	0.911816	0.911774
(P_7, P_6)	0.911788	0.911769
(P_8, P_7)	0.911805	0.911775
(P_9, P_8)	0.911787	0.911778
(P_{10}, P_9)	0.911796	0.911796

Table 2.2. Error in the L_2 norm for various polynomial degree combinations.

Finally, the computed velocity field is depicted in Figure 2.6. The numerical solution clearly captures the characteristic flow behaviour over the backward-facing step. As the fluid flows over the sudden expansion, the main flow separates from the corner,

leading to the formation of the distinct, lower-velocity recirculation zone immediately downstream of the step.

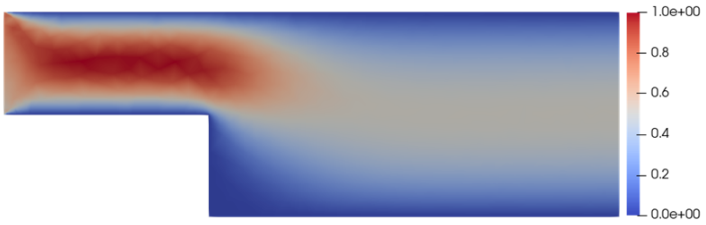

Figure 2.6. Numerical Solution of the Backward Step

Lid Driven Cavity The Lid Driven Cavity problem is another benchmark problem that is used in fluid mechanics. This problem is mainly studied due to the fact that it exhibits a variety of phenomena that occur in incompressible flows such as secondary flows, complex flow patterns, turbulence, etc. There is a square domain with three rigid walls with no-slip conditions and a moving lid. In this problem, velocity is set to be equal to 1.

$$\begin{cases} -\nu\Delta\mathbf{u} + (\mathbf{u}\cdot\nabla)\mathbf{u} + \nabla p = \mathbf{0} & \text{in } \Omega \\ \nabla\cdot\mathbf{u} = 0 & \text{in } \Omega \\ \mathbf{u} = (1,0) & \text{on the top wall (lid)} \\ \mathbf{u} = (0,0) & \text{on the remaining walls} \end{cases} \tag{2.9}$$

The initial coarse mesh consists of 128 elements, as in Figure 2.7. When adaptive mesh refinement is applied using low-order polynomials, the mesh refines heavily, especially near the top corners where the moving lid introduces flow singularities, resulting in an adapted mesh of 4669 elements, Figure 2.8*a)*. However, as the order of the polynomials is increased, the adapted mesh requires significantly fewer elements to achieve the target accuracy, dropping to 391 and 173 elements, Figures 2.8*b)* and 2.8*c)*, respectively. The final adapted mesh tends to closely resemble the starting configuration.

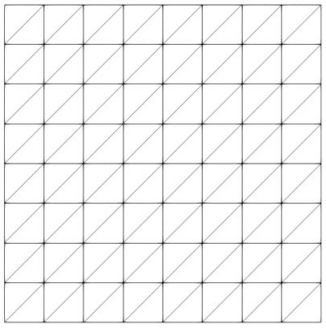

Figure 2.7. Initial Mesh with 128 Elements.

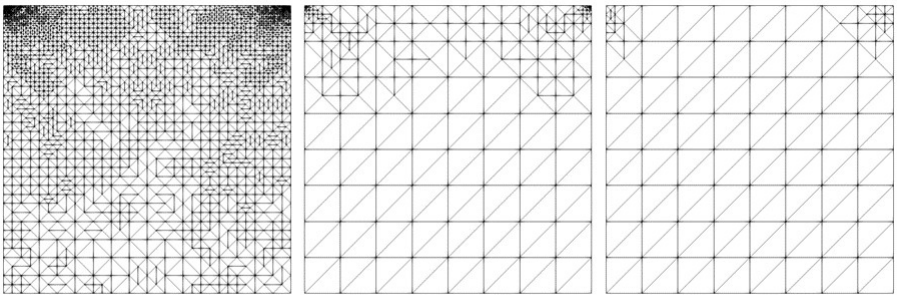

Figure 2.8. Adaptive Meshes with a) 4669, b) 391 and c) 173 Elements

Table 2.3 details the L_2 norm errors for both the initial and adapted meshes across various polynomial degree combinations. As in the previous cases, a general reduction or stabilisation of the error is observed as the degree of the polynomials increases. In some instances, the adaptation process encounters difficulty in further reducing the number of elements, which leads to minor fluctuations where the element count or error remains constant or slightly increases.

The computed velocity field is depicted in Figure 2.9. The numerical solution effectively captures the classic features of the lid-driven cavity flow, most notably the large primary recirculation vortex driven by the horizontal motion of the top boundary, alongside the characteristic velocity gradients developing near the edges of the domain.

Error	**Initial Mesh**	**Adapted Mesh**
(P_2, P_1)	0.75425947	0.75309220
(P_3, P_2)	0.75317886	0.75308080
(P_4, P_3)	0.75317088	0.75309430
(P_5, P_4)	0.75307177	0.75309132
(P_6, P_5)	0.75314475	0.75312226
(P_7, P_6)	0.75310587	0.75307011

Table 2.3. Error in the L_2 norm for various polynomial degree combinations.

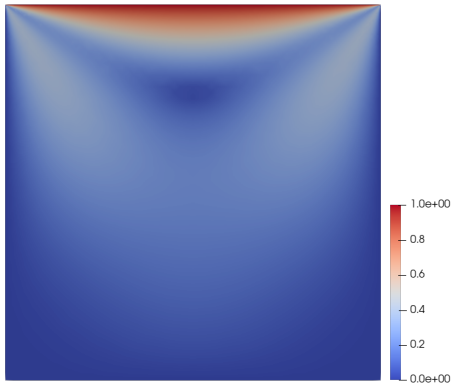

Figure 2.9. Numerical Solution of the lid driven cavity problem

2.3 Finite Volume Method

In Finite Volume Method (FVM) the partial differential equations transform to an algebraic system of equations over a finite volume. FVM is a well established numerical method based on integrals. The methodology of this approach includes the discretization of the domain into finite volumes, Figure 2.10. Then the equations are discretized using integration techniques.

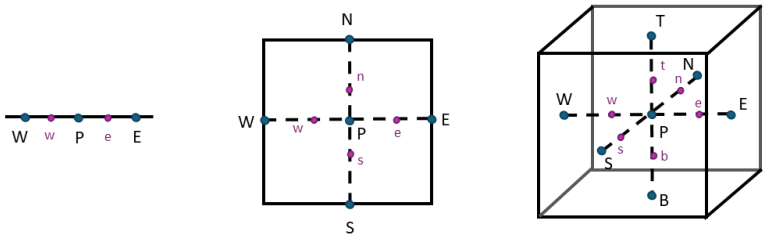

Figure 2.10. A finite volume in 1, 2 and 3 dimensions.

Consider the following equation describing the steady advection-diffusion,

$$div(\rho \mathbf{u}\phi) = div(\Gamma grad\phi) + S_\phi \tag{2.10}$$

Then by integrating over the control volume the equation is as follows:

$$\int_{CV} div(\rho \mathbf{u}\phi)dV = \int_{CV} div(\Gamma grad\phi)dV + \int_{CV} S_\phi dV$$
$$\int_{A} \mathbf{n} \cdot (\rho \mathbf{u}\phi)dA = \int_{A} \mathbf{n} \cdot (\Gamma grad\phi)dA + \int_{CV} S_\phi dV$$

Consider now the three-dimensional form of the previous equation.

$$\begin{aligned} &\frac{\partial}{\partial x}(\rho u\phi) + \frac{\partial}{\partial y}(\rho v\phi) + \frac{\partial}{\partial z}(\rho w\phi) \\ &\qquad = \frac{\partial}{\partial x}\left(\Gamma \frac{\partial \phi}{\partial x}\right) + \frac{\partial}{\partial y}\left(\Gamma \frac{\partial \phi}{\partial y}\right) + \frac{\partial}{\partial z}\left(\Gamma \frac{\partial \phi}{\partial z}\right) + S_\phi \end{aligned} \tag{2.11}$$

where Γ is the coefficient related to diffusion and S the source term.

The control volume in this case can be described as depicted in Figure 2.11,

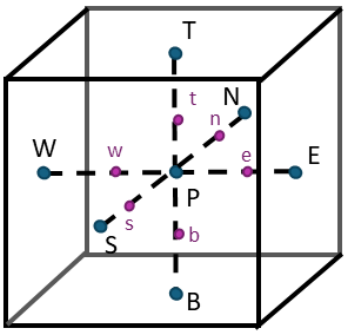

Figure 2.11. A finite volume in 3-dimensions showing the faces of the cell.

where P, W, E, N, S, T, B is the control volume and w, e, n, s, t, b are the faces of the cell. The integration over this control volume yields the following form.

$$\begin{aligned}&[\rho u A\phi]_w^e + [\rho v A\phi]_s^n + [\rho w A\phi]_b^t \\ &+ \left[\Gamma A\left(\frac{\partial\phi}{\partial x}\right)\right]_w^e + \left[\Gamma A\left(\frac{\partial\phi}{\partial y}\right)\right]_s^n + \left[\Gamma A\left(\frac{\partial\phi}{\partial z}\right)\right]_b^t + \bar{S}\Delta V = 0\end{aligned} \tag{2.12}$$

Thus, the discrete form is obtained as follows:

$$a_P\phi_P = a_W\phi_W + a_E\phi_E + a_S\phi_S + a_N\phi_N + a_B\phi_B + a_T\phi_T + S_P \tag{2.13}$$

where α_i are given as shown in Table 2.4,

Coefficient	**Expression**
α_W	$\rho u_w A_w - \dfrac{\Gamma_w A_w}{\Delta x_{WP}}$
α_E	$\rho u_e A_e - \dfrac{\Gamma_e A_e}{\Delta x_{PE}}$
α_S	$\rho v_s A_s - \dfrac{\Gamma_s A_s}{\Delta y_{SP}}$
α_N	$\rho v_n A_n - \dfrac{\Gamma_n A_n}{\Delta y_{PN}}$
α_B	$\rho w_b A_b - \dfrac{\Gamma_b A_b}{\Delta z_{BP}}$
α_T	$\rho w_t A_t - \dfrac{\Gamma_t A_t}{\Delta z_{PT}}$
α_P	$\alpha_W + \alpha_E + \alpha_S + \alpha_N + \alpha_B + \alpha_T - S_P$

Table 2.4. Discretized coefficients of the three-dimensional finite volume formulation.

and it can also be written as

$$\mathbf{A}\boldsymbol{\phi} = \mathbf{b} \tag{2.14}$$

where A, ϕ and b are the corresponding matrices shown below,

$$\boldsymbol{\phi} = \begin{bmatrix} \phi_1 \\ \phi_2 \\ \vdots \\ \phi_N \end{bmatrix}, \qquad \mathbf{b} = \begin{bmatrix} b_1 \\ b_2 \\ \vdots \\ b_N \end{bmatrix}. \tag{2.15}$$

and

$$\mathbf{A} = \begin{bmatrix} a_P & -a_E & 0 & \cdots & 0 \\ -a_W & a_P & -a_E & \cdots & 0 \\ 0 & -a_W & a_P & \cdots & 0 \\ \vdots & \vdots & \vdots & \ddots & -a_T \\ 0 & 0 & 0 & -a_B & a_P \end{bmatrix}. \tag{2.16}$$

where

$$A_{ii} = a_P, \qquad A_{ij} = -a_{xy}, \tag{2.17}$$

with $xy = W, E, S, N, B, T$. Notice that the coefficient matrix A is sparse.

2.3.1 Nonlinear Algebraic System

The discretization of the governing partial differential equations, using the finite volume method, transforms the continuous system into a nonlinear algebraic system of equations. Solving this system efficiently demands iterative methods. The classical Newton method has fast convergence using second order accuracy, but it can fail when the initial guess is far from the solution. Trust region methods overcome this problem by restricting the region of the initial guess, while the Levenberg-Marquardt combines Newton-Like methods with gradient descent approaches, providing better results.

Newton's Method

After the discretization of the system of PDEs using the FVM, a nonlinear algebraic system of equations is obtained. To solve this system the Newton's method is used. In the general form the problem can be described as,

$$\bar{f}(\bar{x}) = \bar{0}, \tag{2.18}$$

for n equations of n unknown variables with $\bar{f} = (f_1, ..., f_n)^T$, $\bar{x} = (x_1, ..., x_n)$. The methods suggest that there is $\bar{x}_{(0)}$ satisfying $\bar{f}(\bar{x}_{(0)}) \neq \bar{0}$. Then a $\Delta\bar{x}_{(0)}$ is required so $\bar{f}(\bar{x}_{(0)} + \Delta\bar{x}_{(0)}) = \bar{0}$. To obtain this expression, the function must be expanded using the Taylor series around $\bar{x}_{(0)}$ keeping first order terms,

$$\bar{f}(\bar{x}_{(0)} + \Delta\bar{x}_{(0)}) = \bar{f}(\bar{x}_{(0)}) + \bar{J_{(0)}}\Delta\bar{x}_{(0)}, \tag{2.19}$$

where J is the Jacobian matrix for n-dimensions.

We know that $\bar{f}(\bar{x}_{(0)} + \Delta\bar{x}_{(0)}) = \bar{0}$ so $\Delta\bar{x}_{(0)}$ must satisfy the equation,

$$\Delta\bar{x}_{(0)} \approx -\left(\bar{J_{(0)}}\right)^{-1} \bar{f}(\bar{x}_{(0)}), \tag{2.20}$$

or in general form,

$$\Delta\bar{x}_{(\nu)} \approx -\left(\bar{J_{(\nu)}}\right)^{-1} \bar{f}(\bar{x}_{(\nu)}), \tag{2.21}$$

where ν is the $\nu-$th iteration [45].

Now for the next step/iteration $\bar{x}_{(1)} = \bar{x}_{(0)} + \Delta\bar{x}_{(0)}$, the general form is,

$$\bar{x}_{(\nu+1)} = \bar{x}_{(\nu)} + \Delta\bar{x}_{(\nu)} = \bar{x}_{(\nu)} - \left(\bar{J}_{(\nu)}\right)^{-1} \bar{f}(\bar{x}_{(\nu)}). \tag{2.22}$$

The procedure continues until an $\bar{x}_{(\nu)}$ is found satisfying $||\bar{x}_{(\nu+1)} - \bar{x}_{(\nu)}|| \leq \varepsilon$, where ε is a specific tolerance. The procedure stops when the $\bar{x}_{(\nu)}$ is the solution of equation (2.22) and satisfies the tolerance criterion.

When the Jacobian is nonsingular and the initial guess is close to the solution, the convergence of Newton's method is quadratic, meaning that the error is squared at each step. However, convergence is not guaranteed for all cases, leading to a locally convergent method. This is due to the fact that the Jacobian can have the following property in any iteration.

Definition 2.3.1. A matrix A is singular if and only if : $\det(A) = 0$

Thus, when A is singular the inverse Jacobian cannot be defined. To address such issues, techniques such as trust region methods or the Levenberg-Marquardt method are employed, which modify the step of Newton's Method to guarantee convergence [38, 144].

Trust Region Method

Newton's method, although it converges rapidly to the solution, can fail when the initial guess is far from the solution, when the Jacobian is singular, or when the step is too large, omitting valid regions [144]. Thus, other approaches are required to overcome such limitations.

In trust region methods, a quadratic model of the function is constructed to generate steps. The steps are constrained in a region where the model function is considered

reliable. Let x_k denote the current iteration, then the function can be approximated using a Taylor expansion,

$$f(x_k + p) = f(x_k) + \bar{\nabla^T} f(x_k)p + \frac{1}{2}p^T \bar{\nabla^2} f(x_k + tp)p, \tag{2.23}$$

where $t \in (0, 1)$. This leads to a quadratic model $m_k(p)$ that involves the Hessian matrix,

$$m_k(p) = f(x_k) + \bar{\nabla^T} f(x_k)p + \frac{1}{2}p^T B_k p, \tag{2.24}$$

where B_k is a symmetric matrix. The step p is chosen to minimize the model function while remaining in the trusted region $\|p\| \leq \Delta_k$, where Δ_k is the radius of the region [147], i.e.

$$\min_p m_k(p) = \min_p \left(f(x_k) + \bar{\nabla^T} f(x_k)p + \frac{1}{2}p^T B_k p \right) \tag{2.25}$$

After computing the trial step, the effectiveness is evaluated using the reduction ratio, as defined below,

$$\rho_k = \frac{f(x_k) - f(x_k + p_k)}{m_k(0) - m_k(p_k)}, \tag{2.26}$$

which compares the actual reduction in the function to the reduction predicted by the model function. If the ratio gives a valid step, then the procedure continues by changing (increasing) the radius of the trust region. In any other case, the radius of the region is decreased until the step is successful. By this test, the method is ensured to be stable providing global convergence [144].

Levenberg-Marquardt algorithm

The Levenberg-Marquardt (LM) method is a stabilized algorithm based on the Newton's Method, designed for nonlinear least-squared problems [111, 128, 144]

Consider the following Nonlinear Least Squares Minimization problem The objective function f is defined as,

$$f(x) = \frac{1}{2}\sum_{j=1}^{m} r_j^2(x), \tag{2.27}$$

where $x = x(x_1, x_2, ...x_n)$ is a vector and each r_j is a residual. These can be gathered to $r(x)$ the residual vector and the problem can have the following form,

$$f(x) = \frac{1}{2} \|r(x)\|^2 . \tag{2.28}$$

Then the Gauss-Newton method approximates the Hessian of $f(x)$ by $J^T J$, where J is the Jacobian of $r(x)$. The step from the Gauss-Newton is obtained from,

$$J^T J \delta x = -J^T r. \tag{2.29}$$

However, sometimes this system may become singular or ill-conditioned, which can occur if the columns of J are nearly linearly dependent or residuals are independent of certain parameters. The Levenberg-Marquardt algorithm solves the following system in order to improve the robustness,

$$(J^T J + \lambda I)\delta x = -J^T r, \tag{2.30}$$

by introducing $\lambda \geq 0$ the damping parameter to regularize the system. Small values of λ lead to the Gauss-Newton method while large values lead to a gradient descent [137]. This dual form enables the method to be stable even when it is far from the solution, while having fast convergence.

The damping parameter is updated based on the trial step and how the objective function is reduced. When the step is correct then λ reduces to obtain faster convergence. When the step is not appropriate the value of λ increases [144].

This method can be seen as a trust region approach, where in each iteration the local quadratic model is minimized in a region where the model function approximates f. The size of the region is adjusted based on the difference of the prediction and the actual reduction in the objective function.

The Levenberg-Marquardt method is suitable for nonlinear PDEs and inverse problems where the presence of least squares occurs and the Jacobian is poorly conditioned. This is due to the combination of the Gauss-Newton Method (convergence) and the gradient descent (stability) [111, 128, 144].

2.3.2 Structured and Unstructured Meshes

In fluid flow simulations using numerical methods, the domain must be discretized in order to create the volumes (FV) or elements (FE). The selection of the topology

of the mesh affects the accuracy and computational cost of the solver. Two categories of computational meshes are commonly used: structured and unstructured meshes.

Structured Mesh

A structured grid is a mesh in which the connectivity of nodes follows a regular rectangular pattern. Each control volume is identified uniquely by three indices (i, j, k) in 3-dimensions or in Cartesian coordinates as $(x_{(i,j,k)}, y_{(i,j,k)}, z_{(i,j,k)})$. These volumes have a quadrilateral shape in 2D and a hexahedral shape in 3D. The existence of curved boundaries, leads to curvilinear structured grids [23, 67].

Structured grids offer an efficient way to access the neighbouring cells, which simplifies the evaluation of gradients, fluxes and the treatment of boundary conditions. Only the field variables need to be stored, thus reducing memory and computational cost. Additionally, the structure of the grids enables also parallelization as the domain can be easily divided.

Unstructured Mesh

In an unstructured grid the cells do not have a particular order. Neighbouring is identified through a connectivity list. Here the shape can be triangles or quadrilaterals for 2D, and tetrahedra, hexahedra, prisms, pyramids etc in 3D. In unstructured grids the use of mixed elements is very common as it can capture complex geometries and boundary layers [23, 67]. This implementation requires storing the connectivity list, leading to a more memory and cost consuming approach. However, such grids can accurately describe complicated geometries, curved boundaries etc while enabling adaptive mesh refinement.

2.3.3 Collocated vs Staggered Arrangements

In CFD, the choice of variable arrangement within a structured grid is crucial in terms of stability, accuracy, and computational efficiency of the numerical scheme. The main types of arrangements that are widely used with the finite volume method (FVM) are the staggered and the collocated grids , each offering its advantages and disadvantages.

In the staggered grid, all physical parameters of the flow are stored in different location within the control volume. The velocity components are stored at the cell faces, while pressure is stored at the cell center. This configuration prevents spurious

oscillations in pressure and ensures the coupling between pressure and velocity for incompressible flows [150, 195]. The staggered grid has been shown to perform better than the collocated in convective-dominated flows when applying the finite volume approach [67, 84].

In contrast, the collocated grid offers a simpler arrangement as all the variables are stored at the center of the cell. This approach simplifies the procedure; however, it is prone to the development of artificial pressure oscillations [131, 153]. The advantages and disadvantages of each arrangement are summarized in the Table 2.5:

Comparison between staggered and collocated grid arrangements in structured meshes

Aspect	Staggered Grid	Collocated Grid
Variable location	Pressure stored at cell centers; velocity components at cell faces.	All variables (pressure, velocity, scalars) stored at cell centers.
Pressure–velocity coupling	Naturally stable; avoids checkerboard pressure fields.	Requires interpolation schemes (e.g., Rhie–Chow) to prevent oscillations.
Implementation complexity	More complex indexing and data handling.	Simpler and more compact data structure.
Geometrical flexibility	Best suited for orthogonal grids.	Easily extended to non-orthogonal or curvilinear grids.
Memory requirement	Slightly higher due to velocity storage at faces.	Lower, as all variables share the same location.
Accuracy in pressure gradients	Excellent; direct evaluation between adjacent cells.	Depends on interpolation accuracy.
Recommended for	Incompressible or recirculating flows, strong pressure gradients.	3D simulations, complex geometries, and curvilinear coordinates.

Table 2.5. Comparison between staggered and collocated grid arrangements in structured meshes.

Several studies have conducted many experiments on staggered and collocated grids analyzing the performance of each arrangement. Peric et al. [153] compared both methods in two dimensional incompressible flows and found similar results, however the collocated grid offered simpler implementation and faster convergence. These grids were also tested with turbulence and multiphase cases, revealing that the staggered grid performs better when there are high pressure gradients or strong recirculations. The collocated grid, on the other hand, is more flexible for three dimensional configurations and complex geometries [131].

The fundamental difference between these two spatial arrangements is visually illustrated in Figure 2.12. In a collocated grid, Figure 2.12 left, all primary flow variables, such as pressure and velocity components, are evaluated and stored at the exact same computational nodes, typically the cell centers. In contrast, the staggered grid approach, Figure 2.12 right, evaluates scalar variables like pressure at the cell centers, while the velocity vectors are stored at the respective cell faces. This geometric offset in the staggered grid naturally couples the pressure and velocity fields, which helps prevent non-physical pressure oscillations without the need for additional mathematical interpolation schemes.

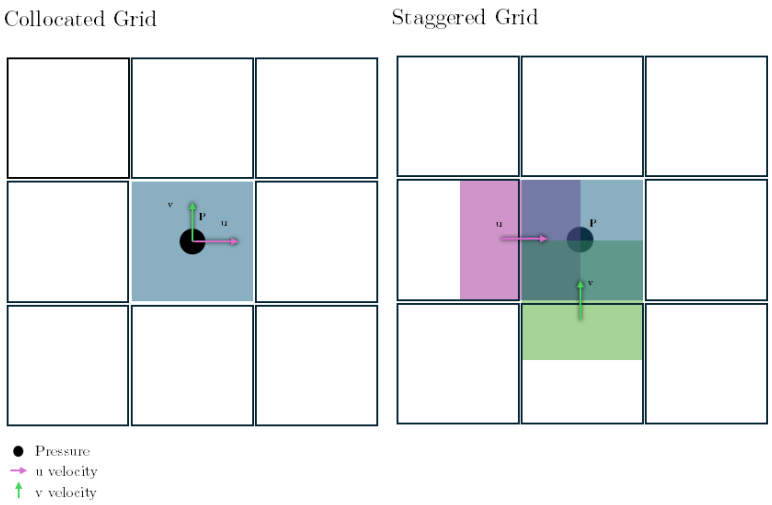

Figure 2.12. Schematics on how variables are stored in Collocated (left) and Staggered (right) grids.

2.4 Dimensionless Equations and Dimensionless Numbers

The mathematical description of physical phenomena is usually expressed by using a unit/metric system, where all quantities have dimensions. Although this representation is logical, it is not always convenient, especially when treated analytically, or numerically. Therefore, governing equations are often transformed to a dimensionless form, through scaling using characteristic values for the quantities used (e.g length (L), velocity (U), time (T) and pressure (P)). The dimensionless incompressible Navier–Stokes equations in vector form are,

$$\nabla \cdot \mathbf{u} = 0, \tag{2.31}$$

$$\frac{\partial \mathbf{u}}{\partial t} + \mathbf{u} \cdot \nabla \mathbf{u} = -\nabla p + \frac{1}{Re}\nabla^2 \mathbf{u} - M\mathbf{u}, \tag{2.32}$$

u represents the fluid velocity vector, p is the pressure, Re is the Reynolds number, and M is the magnetic parameter.

Reynolds Number

Reynolds number (Re) is a dimensionless quantity, that represents the ratio of inertial to viscous forces in a fluid flow and is widely used to characterize the flow regime.

$$Re = \frac{uL}{\nu} = \frac{\rho u L}{\mu} \tag{2.33}$$

where ρ is the density of the fluid, u the velocity, L a characteristic length (length of a tube), μ is the dynamic viscosity and ν the kinematic viscosity [14, 200].

At low Reynolds numbers, viscous forces dominate, resulting in smooth flow and in layers known as laminar flow. As Re increases, inertial forces become more prominent, promoting flows instabilities leading to turbulent flow, characterized by chaotic patterns and irregular flow.

Magnetic Number

If in the flow additional external forces occur, such as the influence of the magnetic field, then **Magnetic** number M can be introduced by

$$M = \frac{\sigma R B^2}{\rho u_0} \tag{2.34}$$

where R is the inlet length of the geometry under consideration, B is the magnetic field, and u_0 is a characteristic velocity of the flow [48, 52, 204]. M represents the ratio of electromagnetic to inertial forces, and it can reveal the intensity/influence of the magnetic field on the flow.

Womersley Number

The **Womersley** number, Wo, is a dimensionless number which expresses the pulsatile flow frequency in relation to viscous effects, and is defined by,

$$Wo = R\sqrt{\frac{\omega}{\nu}} \tag{2.35}$$

where R is the radius of the vessel, ω is the angular frequency, and ν is the kinematic viscosity of the fluid. The Womersley number is important, especially when scaling a problem [202, 203]. For $Wo \ll 1$, flow is quasi-steady and similar to Poiseuille flow, as the velocity has a parabolic profile. When the value is almost equal to 1 a transitional phase occurs between viscous-dominated and inertia-dominated pulsatile flow. Finally, when $Wo \gg 1$ flow is dominated by inertia forces and the velocity profile may be flattened. In the cardiovascular system the following values are commonly found for the Womersley number.

- Large Arteries: $Wo \gg 1$
- Medium Arteries: $Wo \sim 1 - 5$
- Small Arteries (Microcirculation, e.g arterioles, capillaries, venules): $Wo < 1$

As the diameter of the vessel decreases, viscous effects are more prominent and flow becomes quasi-steady. This alteration significantly affects cardiovascular scaling and haemodynamics [104, 152].

Courant–Friedrichs–Lewy Criterion

For time-dependent problems, the selection of the proper time step, Δt, cannot occur arbitrarily. The **CFL number** (Courant–Friedrichs–Lewy criterion) provides a stability criterion, ensuring that the time step is sufficiently small to capture the travelling information, e.g fluid motion.

In the case of Navier–Stokes equations, the CFL condition arises from the convective term, which represents the transport of fluid properties due to the velocity field. This term is associated with a characteristic velocity, often referred to as the local flow velocity.

The CFL number represents the ratio of the physical distance traveled by a fluid particle during one time step to the corresponding mesh size and it can be defined as,

$$C = \frac{u\Delta t}{\Delta x} \tag{2.36}$$

or in $n-$dimensions

$$C = \Delta t \left(\sum_{i=1}^{n} \frac{u_i}{\Delta x_i} \right) \tag{2.37}$$

where Δt is the time step, $\Delta x, \Delta x_i$ is the mesh size and u, u_i the velocity component.

If the time step exceeds the allowable limit, $C >$ Co, the numerical scheme may become unstable, leading to non-physical oscillations or even divergence of the solution. The selection of a smaller CFL number can improve stability and accuracy, at the expense of increased computational cost.

The characteristic velocity u_i depends on the specific problem under consideration and may vary throughout the computational domain. In practice, an estimate based on the maximum velocity, or an upper bound of the velocity field, is often used when evaluating the CFL condition.

In summary, the CFL criterion provides a practical guideline for selecting an appropriate time step in the numerical solution of the Navier–Stokes equations, ensuring stability and accuracy by accounting for both the flow velocity and the spatial discretization [47].

2.5 Analytic and Approximate Methods

Non-linear problems are generally difficult to solve, especially through analytical techniques. In this approach one can retain some features of the problem while approximating or forgetting other.

Traditional perturbation methods rely on the presence of small or large physical parameters [18, 123, 142]. The homotopy analysis method (HAM) is an analytic approach that can be effectively applied to strong non-linear problems [112, 114]. Unlike perturbation approaches, HAM is completely independent of any physical parameters, ensuring applicability in strongly non-linear problems. Furthermore, it offers convergence of the solution series, a key advantage when dealing with highly non-linear problems. Another important feature of HAM is the flexibility in selecting the auxiliary linear operator and base function, allowing great freedom in creating suitable solutions [116]. Finally, it has been shown that this approach includes as specific cases several analytical methods, highlighting its generality and versatility [114]. The method was first introduced in 1992 by Liao [115] and it's based on the homotopy,

found in many areas of mathematics, which describes a type of continuous variation or deformation, like a circle that deforms to an ellipse.

2.5.1 Perturbation Theory

In most problems of fluid mechanics finding the solution is really difficult, especially due to the non linear behaviour of the differential equations and the complicated boundary conditions. For this reason, approximation methods like perturbation techniques are employed in order to overcome such limitations.

Perturbation methods are based on the existence of a small physical parameter which can change the nature of the problem if it changes. Consider an ordinary differential equation of the form

$$F(t, y, y', y'', y''', ..., y^{(n)}) = 0, \quad t \in I, \tag{2.38}$$

where t is the independent variable, I is an interval and y the dependent variable. The term ε is a very small physical parameter, $\varepsilon \ll 1$. Then the following power series of ε

$$y(t) = y_0(t) + \varepsilon y_1(t) + \varepsilon^2 y_2(t) + ... = \sum_{i=0}^{\infty} y_i(t)\varepsilon^i, \tag{2.39}$$

describes the solution of the problem using perturbation methods.

Regular perturbation is based on the assumption that there is a solution of the problem given in a power series form as in (2.39), where $y_0, y_1, y_2, ...$ will be defined. The method is considered successful when the approximation is close to the true solution while $\varepsilon \to 0$ [18, 123, 142].

Convergence of the series

As previously discussed, the solution of perturbation methods is in a form of power series with a small parameter ε,

$$y(\varepsilon) = y_0 + \varepsilon y_1 + \varepsilon^2 y_2 + ... = \sum_{i=0}^{\infty} \varepsilon^i y_i, \tag{2.40}$$

Such a series can be convergent if the sequence of partial sums approaches the exact solution as the number of terms increases, for small values of the parameter ε. However, for nonlinear problems, the radius of convergence is restricted to a very small area of ε, and in many cases it may fail to converge [18, 123, 142].

Despite this, perturbation methods remain valuable. Even when the full series diverges the first few terms can provide accurate approximations to the true solution.

This behaviour is a characteristic of asymptotic expansions, where the series may not converge but the initial partial sums lead accurately to the solution.

Due to the above, convergence is not a primary requirement in perturbation theory. The focus lies on capturing the physical behaviour of the system. When the physical parameter is not small enough or the solution series deteriorates, other methods are employed, such as the homotopy analysis method [112].

2.5.2 Homotopy Analysis Method

When using HAM, instead of solving the original nonlinear ordinary differential equations (ODEs), a series of linear DEs is solved, and the solution of the nonlinear DE is expressed as a series of the solutions of these linear DEs. By applying HAM to the nonlinear ODE of n-th order,

$$A[y(t)] = 0, \tag{2.41}$$

with the following initial conditions

$$y(0) = a_0,\ y'(0) = a_1,\ ...y^{n-1}(0) = a_{n-1} \tag{2.42}$$

where $y(t)$ is the unknown function and $a_i,\ i = 0, 1, ..., n-1$ are known constants.

The initial approximation $y_0(t)$ of $y(t)$ is constructed with homotopy $\mathcal{H}$, so that

- $y_0(t)$ is a solution of the equation

$$\mathcal{H}[\Phi(t;q), q]|_{q=0} = 0,$$

- and $y(t)$ is a solution of

$$\mathcal{H}[\Phi(t;q), q]|_{q=1} = 0,$$

where $q \in [0, 1]$ is a parameter (embedding parameter).

Liao proposed the following homotopy [113],

$$\mathcal{H}[\Phi(t;q), q] = (1-q)\mathcal{L}[\Phi(t;q) - y_0(t)] - q\overline{h}H(t)\mathcal{A}[\Phi(t;q)], \tag{2.43}$$

where $\mathcal{L}$ is an auxiliary linear operator, and $\overline{h}, H(t)$ are nonzero auxiliary quantities, called convergence control parameter and auxiliary function, respectively. It is obvious that

$$\mathcal{H}[\Phi(t;q), q]|_{q=0} = 0 \Rightarrow \mathcal{L}[\Phi(t;q) - y_0(t)]|_{q=0} = 0 \Rightarrow \Phi(t;0) = y_0(t), \tag{2.44}$$

due to the linearity of $\mathcal{L}$ and

$$\mathcal{H}[\Phi(t;q),q]|_{q=1} = 0 \Rightarrow \mathcal{A}[\Phi(t;q)]|_{q=1} = 0. \tag{2.45}$$

Thus, as q varies from 0 to 1, then the solution $\Phi(t;q)$ of $\mathcal{H}[\Phi(t;q),q] = 0$, varies from $y_0(t)$ to $y(t)$.

$\Phi(t;q)$ depends on both t and q, so it can be expressed in the form of series,

$$\Phi(t;q) = y_0(t) + \sum_{k=1}^{\infty} y_k(t) q^k, \tag{2.46}$$

where $y_k(t) = \frac{1}{k!}\frac{\partial^k \Phi(t;q)}{\partial q^k}|q = 0$ satisfy the linear ODEs,

$$\mathcal{L}[y_k(t) - \chi_k y_{k-1}(t)] = \overline{h} H(t) \mathcal{R}_k[y_0(t), ..., y_{k-1}(t), t],\ k \geq 1, \tag{2.47}$$

called high-order deformation equations, where

$$\chi_k = \begin{cases} 0,\ k = 1 \\ 1,\ k = 2, 3, ... \end{cases} \tag{2.48}$$

and

$$\mathcal{R}_k[y_0(t), ..., y_{k-1}(t), t] = \frac{1}{(k-1)!}\frac{\partial^{k-1}\mathcal{A}(\Phi(t;q))}{\partial q^{k-1}}|q = 0, \tag{2.49}$$

the higher order terms. If all $y_k(t)$ can be found explicitly and if the RHS of equation (2.46) converges for $q = 1$ then the solution is given from the homotopy series,

$$y(t) = y_0(t) + \sum_{k=1}^{\infty} y_k(t), \tag{2.50}$$

In practice, K terms of the homotopy series are calculated in order to obtain an adequate approximation of $y(t)$. Then the approximate solution of K-order is,

$$y_{ap}(t) = y_0(t) + \sum_{k=1}^{K} y_k(t). \tag{2.51}$$

The initial approximation $y_0(t)$, the convergence parameter $\overline{h}$, the linear operator $\mathcal{L}$ and the auxiliary function $H(t)$ can be freely chosen in HAM. For this selection it is important to choose a set of base functions,

$$S_B = \{e_i(t),\ i = 0, 1, 2, ...\}.$$

This set is supposed to adequately describe the expected solution of Equations (2.41), (2.42). Then $y_0(t)$ should be chosen in a way that it a) can be expressed only in terms of S_B and b) should satisfy the initial conditions (2.42).

$$y(0) = a_0,\ y'(0) = a_1,\ ...y^{n-1}(0) = a_{n-1}.$$

The linear ODEs of Equation (2.47) are accompanied by the homogeneous initial conditions

$$y_k(0) = 0,\ y_k'(0) = 0,\ ...y_k^{n-1}(0) = 0\ k = 1, 2, ... \tag{2.52}$$

Then $\mathcal{L}$ and $H(t)$ are chosen so every $y_k(t),\ k = 1, 2, ..$ is expressed in a series form of $e_i(t)$,

$$y_k(t) = \sum_{i=0}^{\infty} c_{i,k} e_i(t),$$

where $c_{i,k},\ i = 0, 1, 2, ...$ are coefficients and $y(t)$ can also be expressed as,

$$y(t) = \sum_{i=0}^{\infty} c_i e_i(t),$$

where $c_i,\ i = 0, 1, 2, ...$ are coefficients. The workflow for this method can be summarized in the Figure 2.13,

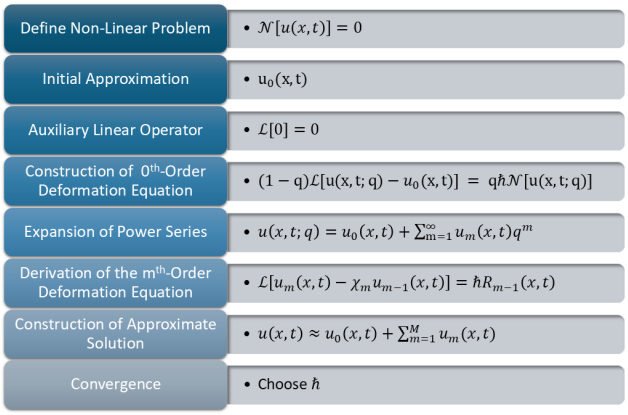

Figure 2.13. Homotopy Analysis Method steps/workflow.

Convergence

In the HAM, the convergence of the series solution depends on the selection of the convergence-control parameter $\hbar$. This ensures that the series describing the solution

is convergent. One way to determine $\overline{h}$ is through employing the $\overline{h}$-curves [112]. These curves are generated by quantities of $y_{ap}(t)$ evaluated at specific t values, where there is physical interest. For instance, the derivative of the approximate solution at a specific point, $y_{ap}^{n+1}(0)$, is often considered. If the series of $y(t)$ is convergent, this quantity remains constant over a range of $\overline{h}$ values. This means that the graph of $y_{ap}^{n+1}(0)$ over $\overline{h}$ will be a horizontal line, which is called the valid region of $\overline{h}$. If a value is chosen from this region, convergence is ensure in most cases. Another approach is to select $\overline{h}$ based on the "discrete squared residual" error, defined as,

$$E_k \approx \frac{1}{N+1} \sum_{j=0}^{N} \left[\mathcal{A}(y_{ap}(t_j))\right]^2, \tag{2.53}$$

where $t_j = j\Delta t$ and Δt is the discretization step of interval t using $N+1$ points. This method provides a good approximation of the total squared residual error, ensuring that the selected $\overline{h}$ leads to a convergent series for the solution [64, 114].

The following theorem is proved in [112]

Theorem 2.5.1. *Consider the series*

$$f(x,\eta) = f_0(x,\eta) + \sum_{m=1}^{\infty} f_m(x,\eta) \tag{2.54}$$

where $f_0(x,\eta)$ is the initial approximation of the solution and $f_k(x,\eta)$ satisfies equations (2.47),(2.52). If the series (2.54) converges, then it is a solution of the initial problem.

Conclusions

This chapter presented a thorough review of the numerical and analytical frameworks that form the basis of Computational Fluid Dynamics (CFD). The focus was divided between numerical methods using the finite element and finite volume and semi-analytical approximations based on perturbation theory and the homotopy analysis method.

- Numerical Methods: The basic theory of finite element and finite volume methods were introduced. For FEM, various applications were presented to show that the *p-version* offers better approximations due to high-order shape functions.
- Non-linear Solvers: The yielding algebraic systems, were solved using the Levenberg-Marquardt algorithm and trust region methods to ensure convergence in the presence of strong non-linearities.

- Approximation Techniques: The foundations of perturbation theory and homotopy analysis method were introduced, highlighting the difference on the dependence from physical parameters.

These approaches serve as strong foundation for the subsequent chapters, which will focus on applications of these frameworks to mathematically model pulsatile blood flow in vascular geometries.

CHAPTER 3

Analytic and Approximation Methods

3.1 Introduction

In many flow configurations involving viscous, incompressible fluids, the governing equations can be reduced to a simplified form that captures the development of the velocity near solid surfaces or within shear-dominated regions. This chapter focuses on reduced flow configurations and similarity equations using the Falkner-Scan transformation. The transformed equations are solved using two analytical approaches, the classical perturbation method and the homotopy analysis method.

First, a simple case is studied in which there is absence of the pressure gradient, leading to a Blasius like equation. The intensity of the magnetic field is then gradually increased to observe how the velocity is affected. In the second part, the pressure gradient is included and the flow depends on both the pressure gradient and the magnetic field.

The obtained results from the semi-analytical methods are compared with the numerical solution to assess the accuracy of the methods. The chapter begins with the governing equations and the Falkner-Skan transformation. The transformed equation is then solved analytically with the classical perturbation method and next with the homotopy analysis method. Finally, the results are presented and discussed for both cases studied.

3.2 The Problem and the Mathematical Formulation

In fluid mechanics, a boundary layer is a region close to a solid surface in which the viscous effects are significant and there are drastic shifts in the velocity, varying from zero at the surface to the free-stream velocity at a short distance. This concept was introduced by Prandtl (1904), for external flows [166].

In blood flow through vessels, although the flow is internal, a similar behaviour

can be observed. Close to the vessel wall, the viscous forces dominate the flow. In straight vessels with laminar flow, the velocity profile shows a boundary layer-like behaviour due to the conditions at the arterial wall. The region near the vessel wall is important to study as it reveals information about the alteration of the flow and wall shear stresses that can lead to many pathologies, e.g atherosclerosis.

The influence of an external magnetic field on blood flow has attracted increasing attention nowadays. Magnetic Resonance Imaging (MRI), is a widely used diagnostic technique that relies on magnetic field to obtain detailed images of the human body. Since blood is an electrically conducting fluid, the presence of a magnetic field can induce electromagnetic forces which interact with the flow and alter its direction. For this reason, the study of magnetohydrodynamics (MHD) and its influence on blood flow needs further investigation. Studies on magnetohydrodynamic effects in blood flow have considered a variety of configurations. MHD in porous media and rigid walls has been investigated to examine the interaction between the electromagnetic forces and the pulsatile flow [158, 1]. Additionally, pathological cases, such as irregular and multi-stenosed arteries, have been studied, highlighting the role of geometric complexity and unsteady effects [140].

3.2.1 Mathematical Modelling

Blood flow is modelled as a two-dimensional boundary layer flow over a wall, and a uniform magnetic field is applied normal to the flow direction, as shown in Figure 3.1.

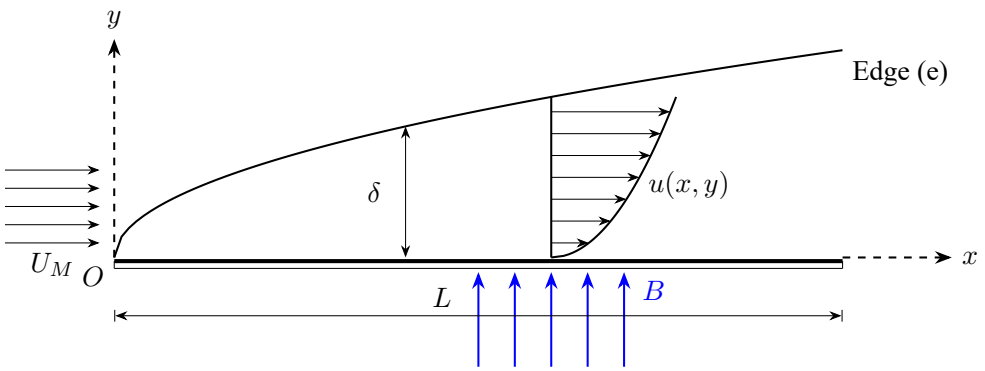

Figure 3.1. Flow configuration system.

The governing differential equations for a two-dimensional and incompressible

flow over a stretching wall are [210]:

continuity equation

$$\frac{\partial u}{\partial x} + \frac{\partial v}{\partial y} = 0, \tag{3.1}$$

x-momentum equation

$$u\frac{\partial u}{\partial x} + v\frac{\partial u}{\partial y} = -\frac{1}{\rho}\frac{dp}{dx} + \nu\frac{\partial^2 u}{\partial y^2} - \frac{\sigma u B^2}{\rho}, \tag{3.2}$$

with the following boundary conditions

$$y = 0 : u = v = 0,$$
$$y \to \delta : u = u_M,$$

where u, v are the velocity components, p the pressure, ρ the density, ν the kinematic viscosity, u_M the velocity at the edge of the boundary layer, δ the boundary layer thickness, and B is the magnitude of the magnetic field. The term $\sigma u B^2$ arises from the x-component of the Lorentz force $\overline{F}_{LOR} = \left(\overline{J} \times \overline{B}\right) = -\sigma u B^2$. The convection current is usually negligible and can therefore be omitted.

In this study a good assumption for adverse pressure gradient is a Howarth's flow assumption [166]. From Bernoulli's equation, pressure drop is linked with the flow at the edge of the boundary layer, thus:

$$-\frac{dp}{dx} = \rho u_M \frac{du_M}{dx} \tag{3.3}$$

and the $x-$ momentum equation transforms in the following,

x-momentum equation

$$u\frac{\partial u}{\partial x} + v\frac{\partial u}{\partial y} = u_M(x)\frac{du_M(x)}{dx} + \nu\frac{\partial^2 u}{\partial y^2} - \frac{\sigma u B^2}{\rho}, \tag{3.4}$$

where $u_M(x) = U\left(1 - \frac{x}{L}\right)$ is the maximum velocity. To simplify the problem before solving it, is necessary to make our equations and boundary conditions dimensionless [36]. This approach enables us to have a more generic and simplified form of the problem and also incorporates variables into only one new variable. For this purpose the Falkner - Skan transformation is employed by introducing the dimensionless function $f(\eta)$ where η is the dimensionless direction [61],

$$\psi = (\nu U x)^{1/2} f(x,\eta),$$
$$\eta = y\left(\frac{U}{\nu x}\right)^{1/2}.$$

where ψ is the stream function.

$$\frac{\partial u}{\partial x} = U' f'(\eta) + \frac{\eta}{2x}\left(U'x - U\right) f''(\eta)$$
$$\frac{\partial u}{\partial y} = U f''(\eta)\sqrt{\frac{U}{\nu x}}$$

In the rest of the text the notation $f', f^{(n)}$ correspond to a partial derivative with respect to η. The equations are transformed to their dimensionless equivalent forms by converting the terms using the new system of ψ, η variables.

continuity equation

$$\frac{\partial u}{\partial x} + \frac{\partial v}{\partial y} = \frac{\partial^2 \Psi}{\partial x \partial y} - \frac{\partial^2 \Psi}{\partial y \partial x} = 0 \tag{3.5}$$

x-momentum equation

$$\begin{aligned} LHS = u\frac{\partial u}{\partial x} + v\frac{\partial u}{\partial y} &= U f'(\eta)\left[U' f'(\eta) + \frac{\eta}{2x}\left(U'x - U\right) f''(\eta)\right] + \\ &+ \left[-\frac{1}{2}\frac{\nu(U + xU')}{\sqrt{\nu x U}} f(\eta) - \frac{1}{2}\frac{\sqrt{\nu x U}}{xU}\eta(xU' - U) f'(\eta)\right] U f''(\eta)\sqrt{\frac{U}{\nu x}}, \\ RHS = u_M(x)\frac{du_M(x)}{dx} + \nu\frac{\partial^2 u}{\partial y^2} - \frac{\sigma u B^2}{\rho} &= UU' + \nu\frac{U^2}{\nu x} f'''(\eta) - \frac{\sigma U B^2}{\rho} f'(\eta) \end{aligned} \tag{3.6}$$

The final form of $x-$ momentum equation (5.2) is:

$$\boxed{f^{(3)}(\eta) + \underbrace{\frac{1}{2U}(xU' + U)}_{a} f(\eta) f''(\eta) + \underbrace{x\frac{U'}{U}}_{b}\left[1 - (f'(\eta))^2\right] = \underbrace{-\frac{x}{U}\frac{\sigma B^2}{\rho}}_{M} f'(\eta)} \tag{3.7}$$

where a controls the strength of the nonlinearity, b is the pressure gradient parameter, and M is the magnetic parameter. Parameter b, characterizes the pressure gradient

along the surface, with $b = 0$ corresponding to no pressure gradient, $b < 0$ adverse pressure gradient and $b > 0$ favourable pressure gradient.

Equation (3.7) describes the two-dimensional flow of a viscous fluid over a surface as it is described by Blasius [166]. The terms $-\frac{x}{U}\sigma B^2 f'(\eta)$ arises due to the presence of the magnetic field. Accordingly, the boundary conditions are transformed as follows,

$$\eta = 0 : f(x,0) = f'(x,0) = 0,$$
$$\eta \longrightarrow \tilde{\delta} : f'(x,\eta) = 1.$$

where $\tilde{\delta}$ is the boundary layer thickness.

This transformation is commonly used in cases where similarity solutions are not valid, to simplify the solution process. Thus, all the equations are dependent on x, the Reynolds number, Re, is not involved and the function f has values in $[0, 1]$, [166].

3.2.2 Perturbation Methods

Initially, we seek to solve the problem with perturbation methods. To this, we define the perturbation parameter as:

$$\varepsilon = x\frac{U'}{U}. \tag{3.8}$$

The physical meaning of this parameter is that the free stream velocity is slowly varying. When $U = U_0$, $\varepsilon = 0$, which reduces to the classic Blasius problem. Assuming a slowly varying free stream such that $\varepsilon \ll 1$ equation (3.9) becomes,

$$\boxed{f^{(3)}(\eta) + \frac{1}{2}(\varepsilon+1)f(\eta)f''(\eta) + \varepsilon\left[1 - (f'(\eta))^2\right] = -\frac{\varepsilon}{U'}\frac{\sigma B^2}{\rho}f'(\eta)} \tag{3.9}$$

The boundary conditions for this problem are:

$$f(0) = 0, \quad f'(0) = 0, \quad f'(\eta \to \infty) = 1. \tag{3.10}$$

The solution of this problem will be in the series form,

$$f = \sum_{n=0}^{\infty} \varepsilon^n f_n. \tag{3.11}$$

where $f_0(\eta)$ is the zeroth-order (base) solution, and $f_n(\eta)$ for $n \geq 1$ are the higher-order corrections.

First, we analyze the case without a magnetic field, $B = 0$, when equation (3.9) takes the form,

$$f^{(3)}(\eta) + \frac{1}{2}(\varepsilon + 1) f(\eta) f''(\eta) + \varepsilon \left[1 - (f'(\eta))^2\right] = 0. \tag{3.12}$$

Substituting the series solution (3.11) into equation (3.12) and equating the coefficients of like powers of ε to zero yields the following sequence of boundary value problems:

$$\mathcal{O}(1): \quad f_0''' + \frac{1}{2} f_0 f_0'' = 0, \tag{3.13}$$

$$\mathcal{O}(\varepsilon): \quad f_1''' + \frac{1}{2} f_0 f_1'' + \frac{1}{2} f_0'' f_1 + \frac{1}{2} f_0 f_0'' - (f_0')^2 + 1 = 0, \tag{3.14}$$

$$\mathcal{O}(\varepsilon^2): \quad f_2''' + \frac{1}{2} f_0 f_2'' + \frac{1}{2} f_0'' f_2 + \frac{1}{2} f_1 f_1'' + \frac{1}{2} f_0 f_1'' + \frac{1}{2} f_1 f_0'' - 2 f_0' f_1' = 0. \tag{3.15}$$

The corresponding boundary conditions, derived by applying (3.11) to (3.10), are:

$$\mathcal{O}(1): \quad f_0(0) = 0, \quad f_0'(0) = 0, \quad f_0'(\infty) = 1, \tag{3.16}$$

$$\mathcal{O}(\varepsilon): \quad f_1(0) = 0, \quad f_1'(0) = 0, \quad f_1'(\infty) = 0, \tag{3.17}$$

$$\mathcal{O}(\varepsilon^2): \quad f_2(0) = 0, \quad f_2'(0) = 0, \quad f_2'(\infty) = 0. \tag{3.18}$$

The $\mathcal{O}(1)$ problem (3.13) subject to (3.16) is the classical, nonlinear Blasius problem. Its solution can be expressed via a power series expansion around the wall boundary ($\eta \ll 1$, near 0), given by:

$$f_0(\eta) = \sum_{k=0}^{m} \left(-\frac{1}{2}\right)^k \frac{A_k \sigma^{k+1}}{(3k+2)!} \eta^{3k+2}, \tag{3.19}$$

where $A_0 = A_1 = 1$ and A_k is given by the recurrence relation:

$$A_k = \sum_{r=0}^{k-1} \binom{3k-1}{3r} A_r A_{k-r-1} \quad (k \geq 2). \tag{3.20}$$

The parameter $\sigma = f_0''(0) \approx 0.33206$ represents the non-dimensional wall shear stress. Because the $\mathcal{O}(1)$ problem corresponds to the classical, uncoupled hydrodynamic boundary layer, this well-established baseline value, along with the corresponding boundary layer profiles depicted in Figure 3.2, are adopted directly from canonical numerical solutions of the Blasius equation found in literature [166].

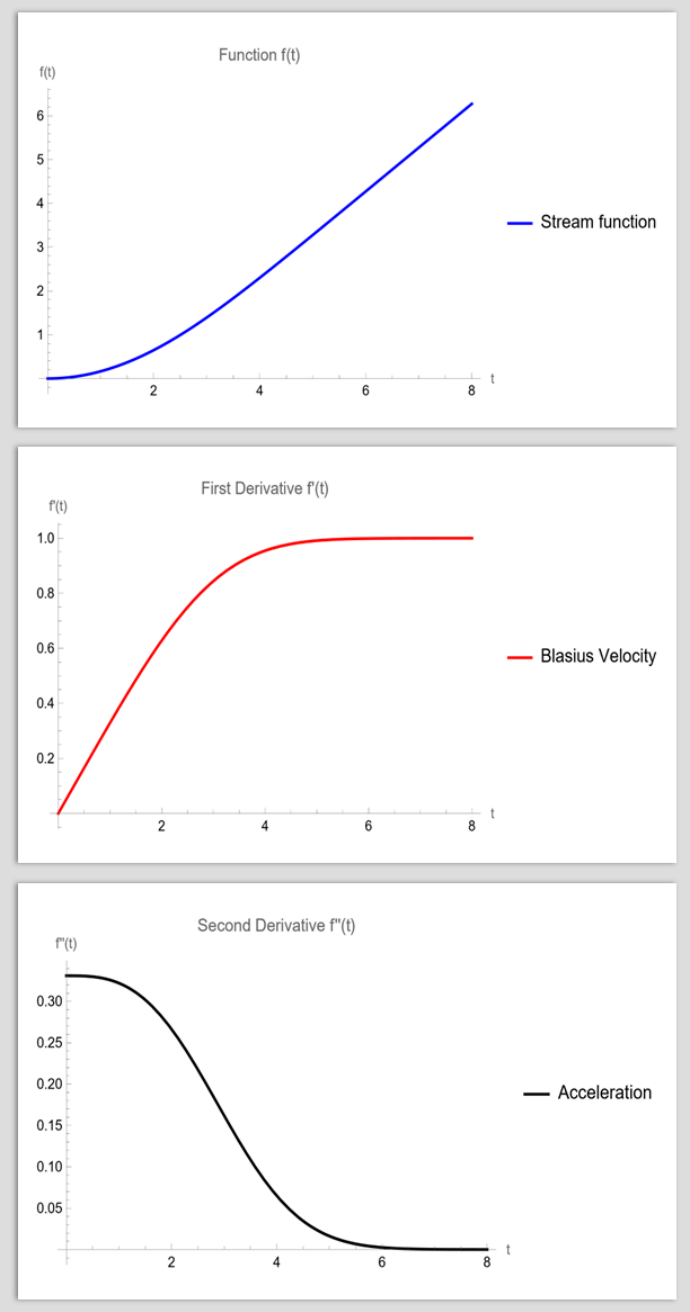

Figure 3.2. Blasius solution. a) Stream function, b) Velocity and c) Acceleration.

The higher-order problems $\mathcal{O}(\varepsilon)$, $\mathcal{O}(\varepsilon^2)$, etc. lead to "linear" ordinary differential equations with variable coefficients that depend on the base state $f_0(\eta)$. The $\mathcal{O}(\varepsilon)$ formulation is modified to include the magnetic Lorentz force term from equation (3.9), allowing for full magnetohydrodynamic flow to be evaluated.

To confirm the convergence of this perturbation series in presence of magnetic field, cumulative velocity profiles at a given streamwise location, $x = 0.05$ were calculated up to second-order from the solution base. The first-order correction shown in Figure 3.3 demonstrates the initial deviation from the base flow, confirming the quantifiable deficit in velocity driven by the consolidated action of the Lorentz force and the negative pressure gradient. While the addition of a second-order term offers only a marginal refinement to this initial profile, a rigorous demonstration of global convergence would require the evaluation of higher-order terms. However, for the purpose of illustrating the primary physical deviations induced by the magnetic field, truncating the expansion at the first order is deemed sufficient for this preliminary analysis.

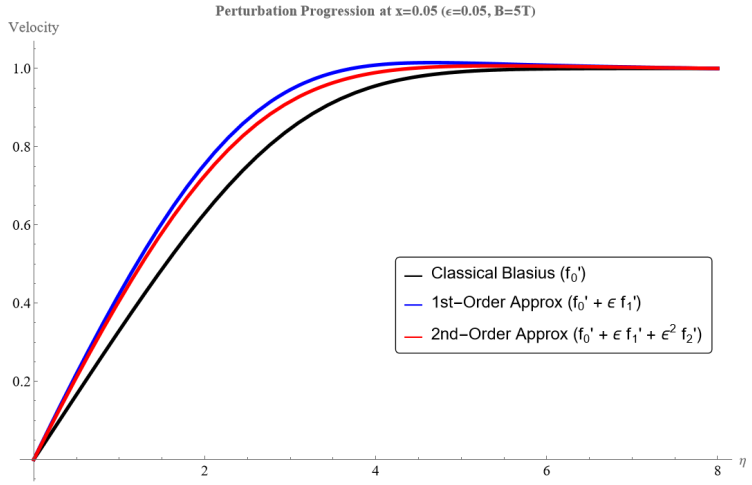

Figure 3.3. Progression of the perturbation series at $x = 0.05$ with $\varepsilon = 0.05$ and $B = 5$ T. The rapid convergence is visually evident as the second-order approximation closely overlays the first-order profile.

With the perturbation model established, we now examine the velocity $f'(x, \eta)$ under varying magnetic field strengths. Figure 3.4 compares the boundary layer development near the leading edge ($x = 0.05$) to a location further downstream ($x = 0.8$) with a fixed perturbation parameter of $\varepsilon = 0.05$.

In both cases, increasing the transverse magnetic field from 0 T to 10 T progressively retards the fluid motion, visibly pushing the velocity profile downward. This

directly illustrates the resistive nature of the Lorentz force. Furthermore, comparing the two locations reveals the effect of the decelerating free-stream velocity. The velocity bounds are significantly lower at $x = 0.8$ due to the macroscopic adverse pressure gradient acting along the plate.

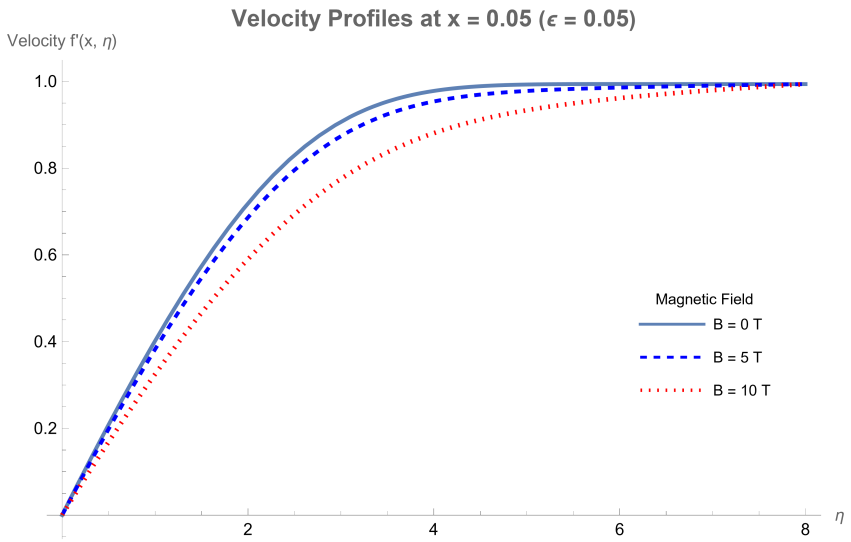

(a) Near the leading edge, $x = 0.05$.

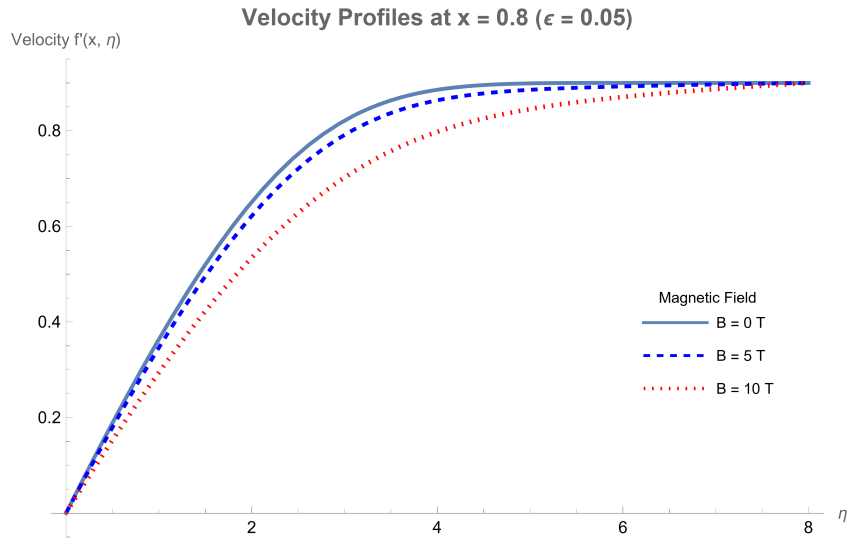

(b) Downstream location, $x = 0.8$.

Figure 3.4. Physical velocity profiles demonstrating the decelerating effect of the applied magnetic field at different streamwise locations.

3.2.3 Homotopy Analysis Method

Now following the theory of homotopy analysis method analysed in the previous chapter we can obtain the non linear operator as:

$$\mathcal{N}[f(\eta)] = f'''[\eta] + af[\eta]f''[\eta] + b\left[1 - \left(f'[\eta]\right)^2\right] + Mf'[\eta], \tag{3.21}$$

while the corresponding linear operator is chosen to be

$$\mathcal{L}[f(\eta)] = f'''[\eta] - \lambda f'[\eta], \tag{3.22}$$

where λ is an auxiliary positive constant that provides flexibility in defining the linear operator.

Accordingly, the 0^{th} order deformation equation is:

$$(1-q)\mathcal{L}[f(\eta;q) - f_0(\eta)] = q\overline{h}\mathcal{N}[f(\eta;q)], \tag{3.23}$$

where q is the embedding parameter and $\overline{h}$ the control parameter. To find the m^{th} order solution it is necessary to first find:

$$f(\eta;q) = f_0(\eta) + \sum_{m=1}^{\infty} f_m(\eta)q^m, \tag{3.24}$$

and if $q = 1$, it converges for

$$f(\eta;1) = f_0(\eta) + \sum_{m=1}^{\infty} f_m(\eta). \tag{3.25}$$

An adequate approximation of $f(\eta)$, is found if we keep M terms of the homotopy series calculated, i.e,

$$f_{ap}(\eta;q) = f_0(\eta) + \sum_{m=1}^{M} f_m(\eta), \tag{3.26}$$

which is called the approximate solution of M-order. The functions $f_m(\eta)$ are the solutions of the so called m^{th} order deformation equations:

$$\mathcal{L}[f_m(\eta) - \chi_m f_{m-1}(\eta)] = \overline{h}R_m(\eta), \tag{3.27}$$

where $\chi_1 = 0$ and $\chi_m = 1$ for $m > 1$. For the present formulation, the auxiliary function is assumed to be unity, $H(\eta) \equiv 1$, and $R_m(\eta)$ is defined as:

$$R_m(\eta) = \frac{1}{(m-1)!}\frac{\partial^{m-1}}{\partial q^{m-1}}\Big[\mathcal{N}\left[f(\eta;q)\right]\Big]\Big|_{q=0}, \tag{3.28}$$

subject to appropriate initial and boundary conditions.

In order to apply HAM in our problem, an appropriate set of base function is required,

$$S = \{e_i(t), i = 0, 1, 2, ...\}\,.$$

This set contains all the solutions that satisfy the initial problem (3.7). An appropriate initial guess for Blasius-type equations like (3.7) satisfying the boundary conditions $f(0) = 0,\ f'(0) = 0,\ f'(\delta) = 1$ is,

$$f_0(\eta) = \eta - \frac{\cosh(\delta)}{\sinh(\delta)} + \frac{1}{2\sinh(\delta)}\left(e^{\delta}e^{-\eta} + e^{-\delta}e^{\eta}\right),$$

where δ in $f_0(x, \eta)$ is obtained from the boundary conditions of ∞. The convergence control parameter $\overline{h}$ is chosen in a way so that the "discrete square residual" error defined by

$$E_M \approx \frac{1}{N+1}\sum_{j=0}^{N}\left[\mathcal{N}\left(\sum_{i=0}^{K} f_i(\eta_j)\right)\right]^2, \tag{3.29}$$

is minimum, where $\eta_j = j\Delta\eta$, $\Delta\eta = 0.16$ and $N = 10$. The non-linear differential equations of the following case with the corresponding boundary conditions are solved using a symbolic package in Computer Algebra System (CAS) Mathematica [92] developed for this study.

No pressure gradient

First, we will test the influence of the magnetic field without a pressure gradient. Thus the equation has the following form,

$$f^{(3)}(\eta) + \frac{1}{2U}(xU' + U)f(\eta)f''(\eta) = -\frac{x}{U}\frac{\sigma B^2}{\rho}f'(\eta). \tag{3.30}$$

The corresponding form for the perturbation method will be,

$$f^{(3)}(\eta) + \frac{1}{2}(\varepsilon + 1)f(\eta)f''(\eta) = -\frac{\varepsilon}{U'}\frac{\sigma B^2}{\rho}f'(\eta). \tag{3.31}$$

For the case where there is no magnetic field the results can be compared also with the numerical solution of the classical Blasius equation ,

$$f^{(3)}(\eta) + \frac{1}{2}f(\eta)f''(\eta) = 0. \tag{3.32}$$

Subsequently, the magnetic field strength will be incrementally increased to demonstrate its effects on the flow dynamics.

No magnetic field, $B = 0T$

Initially, the focus lies on the points close to the leading edge of the surface, where the boundary effects are more dominant. When the magnetic field is absent, $B = 0$, the governing equation reduces to the classical Blasius equation. The Homotopy Analysis Method results indicate that increasing the order of the approximation,N, improves the accuracy of the solution. This is supported by the smooth reduction in convergence error as N increases, as shown in Figure 3.5a. For $N = 10$, the HAM results are in good agreement with the numerical solution, indicating that the selected convergence-control parameters lead to a stable and convergent series. For $B = 0T$, equation (3.30) simplifies to:

$$f^{(3)}(\eta) + \frac{1}{2U}(xU' + U)f(\eta)f''(\eta) = 0, \tag{3.33}$$

which is the same as the Blasius equation when the term $\frac{1}{2U}(xU' + U)$ reduces to $\frac{1}{2}$. This occurs when U is constant. The coefficient $\frac{1}{2U}(xU' + U)$ represents the effect of the streamwise velocity with the boundary layer growth on the nonlinear convective term.

Magnetic field, $B = 5T$**,** $B = 10T$

When a weak magnetic field is introduced, $B = 5T$, the overall behaviour of the solution remains similar to the non-magnetic case. The numerical approximation converges consistently as N increases, accompanied by a steady decrease in the convergence error until it stabilizes Figure 3.6a. However, there is a deviation from the previous case, Figure 3.6b, as now the solution lies under the classic one. This difference reflects the effect of the magnetic field, which acts as a resistive force opposing the flow, leading to a reduction of the velocity.

For stronger magnetic fields $B = 10\,\mathrm{T}$, its influence becomes more intense. The Lorentz suppresses the motion of the fluid, leading to further reduction of the velocity within the boundary layer. Although the homotopy analysis method solution converges, the convergence error exhibits spikes at different N values, Figure 3.7a.

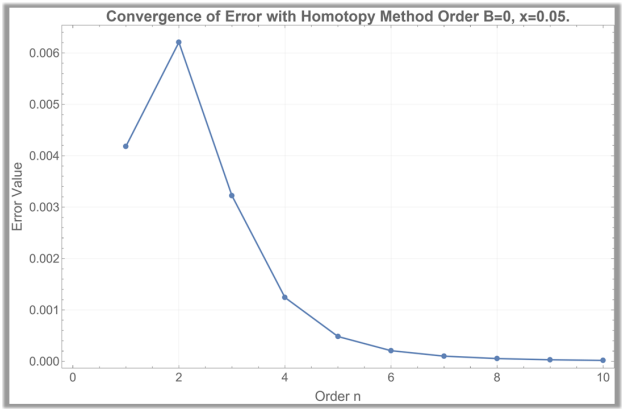

(a)

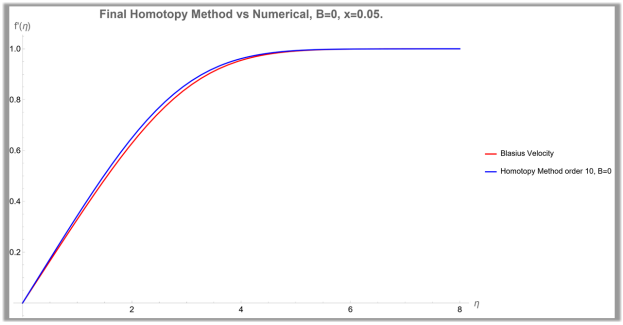

(b)

Figure 3.5. Results without magnetic field, $B = 0\,\mathrm{T}$. (a) The convergence error reduction as the order of HAM increases. (b) Final HAM configuration for 10 terms applied to the Blasius equation.

These fluctuations indicate that the HAM approach is highly sensitive to stronger magnetic fields. Nevertheless, as the order N increases, the solution stabilizes, accurately capturing the dampening effect of the magnetic field on the flow velocity, Figure 3.7b

In summary, the application of a magnetic field introduces an additional resistive force that opposes fluid motion. As the magnetic field intensity increases, this damping effect becomes more prominent, thickening the boundary layer and reducing the overall velocity. A comprehensive comparison of these increasing magnetic field strengths is illustrated in Figure 3.8.

At the end of the surface, $x = 0.8$

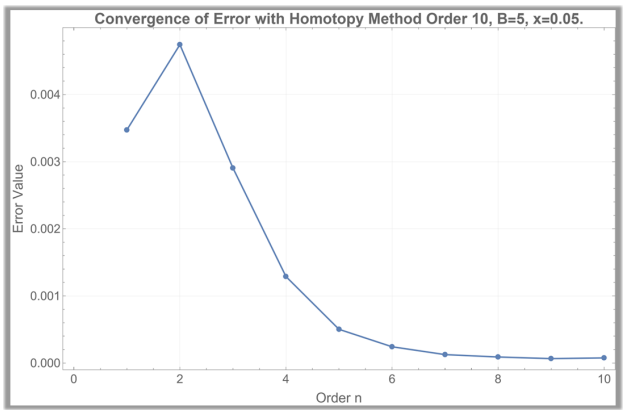

(a)

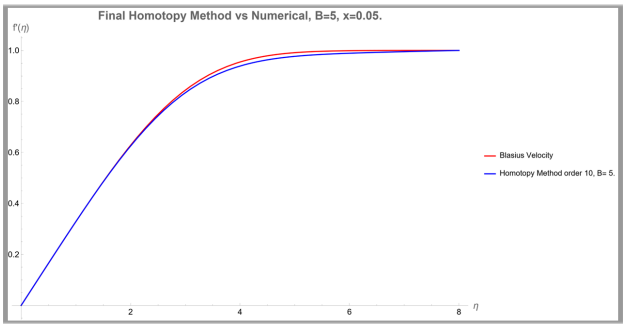

(b)

Figure 3.6. Results for magnetic field $B = 5\,\mathrm{T}$. (a) The convergence error reduction as the order of HAM increases. (b) Final HAM configuration for 10 terms applied to the Blasius equation.

At a downstream location, $x = 0.8$, corresponding close to the end of the surface, the results show a different behaviour. At this point, the boundary layer is developed, and the effects of the viscosity and the magnetic field become more pronounced, affecting the velocity and convergence properties of the solution.

In the absence of a magnetic field, in which the governing equations revert to the Blasius form. Similar to the leading-edge case, the HAM solution converges smoothly to the numerical solution, with the convergence error decreasing steadily as the approximation order N increases.

When the magnetic field is applied and increases gradually, the convergence of the solution is still achieved. However, small oscillations occur in the convergence of

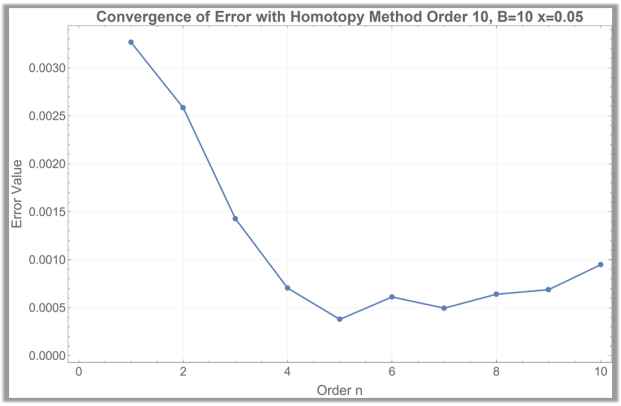

(a)

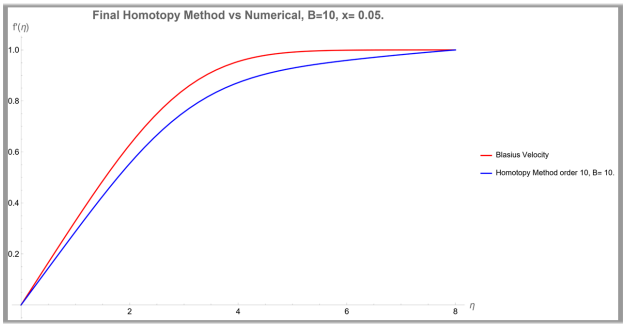

(b)

Figure 3.7. (a) Results for magnetic field $B = 10\,\mathrm{T}$. (a) The convergence error reduction as the order of HAM increases. (b) Final HAM configuration for 10 terms applied to the Blasius equation.

the error as the order increases. The velocity remains lower than the Blasius solution, revealing the effects of the Lorentz force.

As the magnetic field gets more intense the behaviour changes completely. Although convergence is still observed, the convergence of the error leads to alternating spikes as the order increases. Additionally, the velocity profile changes direction compared to the Blasius case. These results indicate strong effects of the magnetic field on the flow in the downstream area.

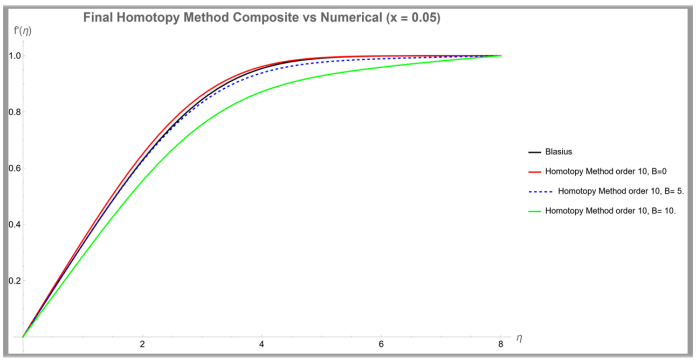

Figure 3.8. Final results with increasing magnetic field.

Adverse Pressure gradient

When an adverse pressure gradient is present, the static pressure of the fluid increases in the direction of the flow ($\frac{dp}{dx} > 0$). In this case, the fluid particles have to face both the viscous friction near the solid boundary and this opposing pressure force. The adverse pressure gradient rapidly decelerates the fluid particles due to the no-slip condition near the wall. The velocity gradient at the wall will eventually decrease to zero, if the opposing pressure forces are sufficiently strong and the fluid near the wall will stop moving downstream. After this point, the flow is reversed, causing the boundary layer to detach from the surface, the known flow separation, leading to highly disturbed patterns. Mathematically, modelling an adverse pressure gradient and the flow separation is highly complex due to the non-linearity of the governing equations near the separation point.

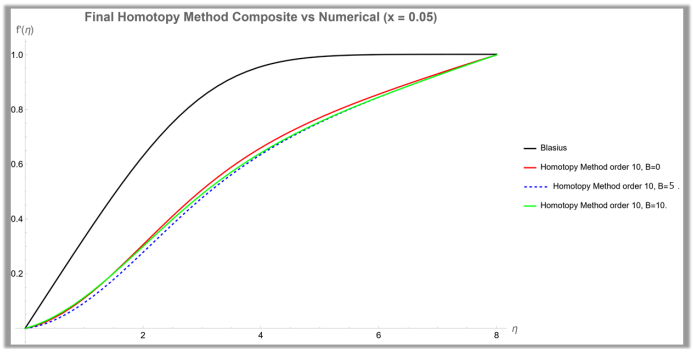

Figure 3.9. Solution of three magnetic fields with adverse pressure gradient at the beginning of the surface.

As observed in Figure 3.9, the combination of a magnetic field and an adverse pressure gradient noticeably affects the flow, even at the very beginning of the surface ($x = 0.05$). In the absence of the magnetic field, $M = 0$, the adverse pressure gradient decelerates the fluid, leading to a deformed velocity profile. As the magnetic parameter increases, the Lorentz force creates additional decrease to the velocity. Consequently, the thickness of the boundary layer decreases as the magnetic field intensity increases, and the fluid requires a shorter distance to achieve free-stream velocity.

3.2.4 Methodological Considerations and Limitations

While the semi-analytical approach presented in this chapter provides valuable cross-validation for the numerical solvers, several methodological limitations must be acknowledged regarding the Homotopy Analysis Method (HAM) and perturbation formulations.

First, in the perturbation expansion (§3.2.2), the perturbation parameter is defined as $\varepsilon = xU'/U$, which is identical to the pressure-gradient parameter b. Consequently, for the limiting case of zero pressure gradient ($b = 0$), the parameter ε becomes identically zero. This degeneracy collapses the perturbation expansion, indicating that the series formulation in Eq. (3.31) is strictly valid only in the presence of an active pressure gradient where $b \neq 0$.

Second, regarding the HAM formulation, the chosen linear operator $\mathcal{L} = f''' - \lambda f'$ possesses characteristic roots of $0, \pm\sqrt{\lambda}$. Because the kernel contains a growing mode ($e^{+\sqrt{\lambda}\eta}$), the initial guess f_0 inherently includes an exponentially growing term. As a result, the boundary conditions can only be strictly satisfied at a finite edge δ (e.g., $f'(\delta) = 1$), rather than at true semi-infinity ($f'(\infty) = 1$). While the truncated domain $\eta \in [0, 1.6]$ was deemed sufficient for evaluating the near-wall behaviour necessary for validating the direct numerical schemes in this thesis, resolving the complete boundary layer out to $\eta \approx 5$ in future work would require adopting the canonical operator $\mathcal{L} = f''' + f''$ alongside decaying base functions $\{\eta^k e^{-n\eta}\}$.

Finally, at ultra-high magnetic fields such as $B \geq 10\,\mathrm{T}$ (Figure 3.7), the velocity profile is observed to change direction. While initially interpreted as severe physical sensitivity to the Lorentz force, this behavior is a known numerical artifact indicating that the HAM series diverges under extreme parameter values. The stability of the semi-analytical solver breaks down at these non-physiological extremes, which is why the primary physiological and numerical validations in the subsequent chapters are restricted to the stable $B \leq 8\,\mathrm{T}$ regime.

3.3 Conclusions

In this chapter, the homotopy analysis method (HAM) was applied to analyze the boundary layer flow of an electrically conducting fluid subject to pressure gradients and an external transverse magnetic field. The governing non-linear partial differential equations were reduced to a dimensionless ordinary differential equation using the Falkner-Skan similarity transformation. The analytical results capture the connection between the pressure gradient and the magnetic parameters. The findings indicate that the presence of the magnetic field decelerates the fluid, an effect that intensifies as the flow progresses toward the end of the surface, making the flow highly susceptible to separation. Furthermore, the introduction of an adverse pressure gradient intensifies the drag forces, leading to a reduction in velocity at a much earlier stage, e.g near the leading edge of the surface. Overall, the semi-analytical approach presented in this chapter provides a robust mathematical framework for understanding the fundamental mechanisms of magnetohydrodynamic (MHD) boundary layer flows.

CHAPTER 4

A two–Dimensional Euler–Lagrange approach with Magnetohydrodynamics

4.1 Introduction

An aneurysm is a bulge in a blood vessel caused by a weakness in the wall of the vessel. The arterial wall can be weakened extensively by elevated blood pressure. There is a variety of arteries that can be affected by an aneurysm leading to pathological blood conditions. The most common locations for an aneurysm to be formed are the arteries supplying the brain and the heart, as well as the aorta. The aneurysm of the descending aorta is called an abdominal aortic aneurysm (AAA). An AAA does not usually threaten health, but there is a risk that a larger aneurysm could burst and rupture. A ruptured aneurysm can be fatal in case of massive internal bleeding. Most unruptured aneurysms are asymptomatic and cannot be detected with the same ease. However, it can impede blood circulation to other tissues and organs. Suspicion of an unrupted aneurysm can be confirmed through diagnostic imaging, such as an Magnetic Resonance Imaging (MRI) or a Computed Tomography (CT) scan [165].

Patients with aneurysms are more probable to be subjected to the effect of a magnetic field through MRI scans to generate images of the organs in the body. Clinical MRI scanners typically operate within the intensity range of $0.5 - 3.0\ \ Tesla\,(T)$, while research MRI scanners can vary in intensity, ranging from $7.0 - 11.7\ Tesla\,(T)$. The static magnetic field in MRI indirectly influences blood flow by affecting the magnetic properties of biomagnetic fluids, such as blood. Hemoglobin, abundant in red blood cells, exhibits diamagnetic properties when oxygenated and paramagnetic properties when deoxygenated. Studies show that under an $8\,T$ magnetic field, human blood flow in a tube is reduced by approximately 30% [188, 83]. In this study, the point of interest is the haemodynamic flow through a pathological vessel under the application of a uniform magnetic field. Thus, the need for more in-depth study

of haemodynamics was created and a new research field of fluid mechanics was developed, biofluid dynamics. Biofluid dynamics (BFD) have contributed to the prediction of blood flow in the human vascular system [118, 119, 207]. In BFD, the velocity and pressure fields of blood flow can be evaluated in pathophysiological arteries of the human body. The development of MRI over recent decades has given rise to the emergence of time-resolved two- or three-dimensional (2D or 3D) Cine Phase Contrast Magnetic Resonance Imaging (PC-MRI) [100, 161]. Haemodynamic patterns through vascular areas of interest may be quantified using PC-MRI. Its availability has expanded to encompass most modern MR systems, making it increasingly preferred for the evaluation of blood flow, cardiac function, and valve performance in both the heart and large vessels. However, the magnetic fields in MRI machines may affect blood flow, causing alterations that are challenging. Computational techniques, nowadays, have been increasingly used by researchers in the prediction of various biological flows. The influence of the magnetic field on blood flow was studied by Tzirtzilakis [188] and Haik et al [82]. In these studies, a mathematical model was developed that treats blood as a Newtonian, homogeneous, incompressible, and electrically conducting fluid with laminar flow. Additionally, more scientists have introduced magnetohydrodynamics (MHD) and ferrohydrodynamics (FHD) terms in blood flow equations for describing the influence of the magnetic field on physiological blood flows in arteries [161].

For flows in body-fit geometries, Shyy et al. have developed the mathematical and numerical Euler–Lagrange framework utilizing the finite volume approach [30, 31, 150, 171, 172, 173, 174, 175]. Recently, a study utilized the Euler-Lagrange equation and the Finite Volume Method to discretize the flow in pathological arteries [204].

In the current study, haemodynamics in a pathological vessel is studied when it is subjected to a static, uniform magnetic field. A nonlinear system of partial differential equations (PDEs) combined with the proper boundary and initial conditions are used to model the physical problem. The problem is addressed by developing a numerical approach based on finite volume analysis and using the aforementioned mathematical model [204]. Generalized curvilinear coordinates (GCCs) are utilized, allowing the numerical evaluation of complicated geometrical structures [108].

4.2 Mathematical Analysis

4.2.1 Dimensionless Equations

Blood flow in a pulsating artery can be described using the fundamental principles of fluid dynamics. Although aneurysms exhibit complex 3D structures, the present study focuses on a simplified, streamlined representation of an abdominal aortic aneurysm (AAA). This intentional focus makes it possible to use a 2D formulation

instead of a 3D one. An axisymmetric flow assumption is introduced, with the angle, ϕ, normal to the flow direction, such that the magnetic field has the maximum impact on the flow. To express the governing equations into a moving body-fitted frame, the Generalized Curvilinear Coordinates (GCC) transformation was employed [186]. The two–dimensional Cartesian form of Newtonian fluid flow equations is expressed as (4.1) – (4.3) [174]. Even though ρ is treated as a constant in the equations, it is retained due to the adoption of specific methodologies that presume highly restricted compressibility in the fluid. This choice enables the integration of volume changes, as defined by the Jacobian of each control volume within this framework. This approach aligns with the work of various researchers [174, 204]

continuity equation

$$\frac{\partial \rho}{\partial \tilde{t}} + \frac{\partial(\rho\tilde{u})}{\partial \tilde{x}} + \frac{\partial(\rho\tilde{v})}{\partial \tilde{y}} = 0, \tag{4.1}$$

x-momentum equation

$$\frac{\partial\left(\rho\tilde{u}\right)}{\partial \tilde{t}} + \frac{\partial\left(\rho\tilde{u}\tilde{u}\right)}{\partial \tilde{x}} + \frac{\partial\left(\rho\tilde{u}\tilde{v}\right)}{\partial \tilde{y}} = -\frac{\partial \tilde{p}}{\partial \tilde{x}} + \left[\frac{\partial}{\partial \tilde{x}}\left(\mu\frac{\partial \tilde{u}}{\partial \tilde{x}}\right) + \frac{\partial}{\partial \tilde{y}}\left(\mu\frac{\partial \tilde{u}}{\partial \tilde{y}}\right)\right] - \overline{F}_L, \tag{4.2}$$

y-momentum equation

$$\frac{\partial\left(\rho\tilde{v}\right)}{\partial \tilde{t}} + \frac{\partial\left(\rho\tilde{u}\tilde{v}\right)}{\partial \tilde{x}} + \frac{\partial\left(\rho\tilde{v}\tilde{v}\right)}{\partial \tilde{y}} = -\frac{\partial \tilde{p}}{\partial \tilde{y}} + \left[\frac{\partial}{\partial \tilde{x}}\left(\mu\frac{\partial \tilde{v}}{\partial \tilde{x}}\right) + \frac{\partial}{\partial \tilde{y}}\left(\mu\frac{\partial \tilde{v}}{\partial \tilde{y}}\right)\right], \tag{4.3}$$

where $\tilde{u}$ and $\tilde{v}$ are the components of the velocity vector, $\bar{q} = (\tilde{u}, \tilde{v})$, $\tilde{p}$ is the pressure, ρ is the density, μ is the dynamic viscosity of the fluid. The term $\overline{F}_L$ yields from the x-component of the Lorentz force $\overline{F}_L = \overline{J} \times \overline{B}$.

In magnetohydrodynamics, the total electromagnetic force acting on a moving, electrically conducting fluid is given by:

$$\overline{F}_L = \rho_e \bar{E} + \bar{J} \times \bar{B}, \tag{4.4}$$

where ρ_e is the electric charge density and $\bar{E}$ is the electric field intensity. The first term represents the electrostatic force, while the second term corresponds to the magnetic force generated by the interaction between the current density $\bar{J}$ and the magnetic field $\bar{B}$. This magnetic component acts on any charged particle or conducting fluid moving under the presence of the magnetic field. According to Ohm's law the total current is given as,

$$\bar{J} = \bar{J}_v + \bar{J}_c, \tag{4.5}$$

where $\bar{J}_v$ is the convection current and it equal to $\bar{J}_v = \rho_e \bar{q}$, where $\bar{q}$ is the velocity field, while $\bar{J}_c$ is the conduction current which is equal to $\bar{J}_c = \sigma(\bar{E} + \bar{q} \times \bar{B})$, where

σ is the electric conductivity of the fluid. Usually, the term $\bar{J}_v$ is negligible and can therefore be omitted from the final equation (4.5). Thus the total current is given by the following formula,

$$\bar{J} = \bar{J}_c = \sigma(\bar{E} + \bar{q} \times \bar{B}). \tag{4.6}$$

If there is no external electric field ($E = 0$), then,

$$\bar{J} = \bar{J}_c = \sigma(\bar{q} \times \bar{B}). \tag{4.7}$$

For the two-dimensional flow case where the velocity field is $\bar{q} = (\tilde{u}, \tilde{v}, 0)$ and the applied magnetic field is transverse to the flow along the y-axis, $\bar{B} = (0, B, 0)$, the induced current density is inherently out-of-plane (in the z-direction) and becomes:

$$\bar{J} = \sigma(0, 0, \tilde{u}B) \tag{4.8}$$

Substituting this into the Lorentz force equation ($\overline{F}_L = \bar{J} \times \bar{B}$), the out-of-plane current interacts with the transverse magnetic field to produce an in-plane resistive force acting strictly on the x-axis, yielding:

$$\overline{F}_L = -\sigma \tilde{u} B^2 \hat{i} \tag{4.9}$$

indicating that the Lorentz force acts opposite to the flow direction. Thus, the magnetic field introduces a resistance term for the flow in the x-direction. Here, σ is the electrical conductivity of the fluid and B is the magnitude of the magnetic field.

In the present study, the magnetic field is applied perpendicular to the flow, and the Lorentz force can be simplified in this formulation [48]. To study the full range of possible MHD interactions, the influence of the magnetic field orientation must be considered. Raptis et al. examined blood flow in an aneurysmal geometry in the presence of a static uniform magnetic field applied from various directions [161]. The assumed conditions included steady, laminar, two-dimensional flow, with blood modelled as a Newtonian, incompressible, and electrically conducting fluid, consistent with the mathematical model employed in [188]. However, in this study, a simplified formulation was implemented due to the exclusive application of a transverse magnetic field. When the magnetic field is applied at an angle smaller than $90°$, the effects decrease.

The system of equations (4.1)–(4.3) can be converted to a dimensionless form of equations (4.11)-(4.13), by introducing the following dimensionless parameters (4.10),

$$x = \frac{\tilde{x}}{R}, \quad y = \frac{\tilde{y}}{R}, \quad t = \frac{\tilde{t}}{R/u_0}, \quad u = \frac{\tilde{u}}{u_0}, \quad v = \frac{\tilde{v}}{u_0}, \quad p = \frac{\tilde{p}}{\rho u_0^2}, \quad c = \frac{\rho}{\rho_0}, \tag{4.10}$$

where u_0 is the characteristic inlet velocity and R is the inlet length of the aneurysmal geometry. ρu_0^2 is the dynamic pressure and c is a compressibility constant. The Reynolds number is introduced to the momentum equations in the dimensionless form, while the continuity equation remains unaltered.

dimensionless continuity equation

$$\frac{\partial c}{\partial t} + \frac{\partial (cu)}{\partial x} + \frac{\partial (cv)}{\partial y} = 0, \tag{4.11}$$

x-dimensionless momentum equation

$$\frac{\partial u}{\partial t} + \frac{\partial \left(uu\right)}{\partial x} + \frac{\partial \left(uv\right)}{\partial y} = -\frac{\partial p}{\partial x} + \frac{\partial}{\partial x}\left(\frac{1}{Re}\frac{\partial u}{\partial x}\right) + \frac{\partial}{\partial y}\left(\frac{1}{Re}\frac{\partial u}{\partial y}\right) - Mu, \tag{4.12}$$

y-dimensionless momentum equation

$$\frac{\partial v}{\partial t} + \frac{\partial \left(uv\right)}{\partial x} + \frac{\partial \left(vv\right)}{\partial y} = -\frac{\partial p}{\partial y} + \frac{\partial}{\partial x}\left(\frac{1}{Re}\frac{\partial v}{\partial x}\right) + \frac{\partial}{\partial y}\left(\frac{1}{Re}\frac{\partial v}{\partial y}\right), \tag{4.13}$$

where u, v are the dimensionless components of the fluid velocity and p the dimensionless fluid pressure. Re is the $Reynolds$ number, M is the magnetic parameter, defined as in equation (4.14), where ν is the kinematic viscosity of the fluid, R is the inlet length of the geometry under consideration, B is the magnetic field, and u_0 is a characteristic velocity of the flow. For this study, u_0 represents the maximum inlet velocity [48, 204].

Additionally, the Womersley number is introduced, a dimensionless expression of the pulsatile flow frequency in relation to the viscous effect, given by the expression,

$$Re = \frac{u_0 R}{\nu}, \quad M = \frac{\sigma R B^2}{\rho u_0}, \quad Wo = R\sqrt{\frac{\omega}{\nu}}, \tag{4.14}$$

where ω is the angular frequency of the pulsations. Applying the generalized curvilinear coordinates (GCCs) transformation, the system of equations (4.11)-(4.13) is transformed in a body–fitted approach.

Using the chain rule for the derivatives, following previous studies [204], and since the fluid is incompressible, ρ = constant, and $c \approx 1$ (almost incompressible) equations (4.11)–(4.13) can be written in curvilinear coordinates, $\xi = \xi(x, y)$, $\eta = \eta(x, y)$, and in dimensionless form as in equations (4.15)–(4.17), [204, 217]. Small compressibility is assumed to incorporate significant parameters affected by the flow, such as the volume alterations of the domain. This formulation yields a set of equations that best describe the flow under consideration.

finite volume continuity equation

$$\frac{\partial J}{\partial t} + \frac{\partial U}{\partial \xi} + \frac{\partial V}{\partial \eta} = 0, \tag{4.15}$$

finite volume x-momentum equation

$$\begin{aligned}\frac{\partial (Ju)}{\partial t} + \frac{\partial (Uu)}{\partial \xi} + \frac{\partial (Vu)}{\partial \eta} = &- \left(y_\eta \frac{\partial p}{\partial \xi} - y_\xi \frac{\partial p}{\partial \eta} \right) \\ &+ \frac{\partial}{\partial \xi} \left[\frac{1}{JRe} \left(q_1 \frac{\partial u}{\partial \xi} - q_2 \frac{\partial u}{\partial \eta} \right) \right] + \frac{\partial}{\partial \eta} \left[\frac{1}{JRe} \left(q_3 \frac{\partial u}{\partial \eta} - q_2 \frac{\partial u}{\partial \xi} \right) \right] - MuJ,\end{aligned} \tag{4.16}$$

finite volume y-momentum equation

$$\begin{aligned}\frac{\partial (Jv)}{\partial t} + \frac{\partial (Uv)}{\partial \xi} + \frac{\partial (Vv)}{\partial \eta} = &- \left(x_\xi \frac{\partial p}{\partial \eta} - x_\eta \frac{\partial p}{\partial \xi} \right) \\ &+ \frac{\partial}{\partial \xi} \left[\frac{1}{JRe} \left(q_1 \frac{\partial v}{\partial \xi} - q_2 \frac{\partial v}{\partial \eta} \right) \right] + \frac{\partial}{\partial \eta} \left[\frac{1}{JRe} \left(q_3 \frac{\partial v}{\partial \eta} - q_2 \frac{\partial v}{\partial \xi} \right) \right],\end{aligned} \tag{4.17}$$

where J denotes the determinant of the inverse Jacobian matrix for the coordinate transformation. Note that this scalar geometric quantity J is completely distinct from the vector current density $\bar{J}$ introduced previously in the Lorentz force formulation.

Based on the Euler–Lagrange approach, the continuity and momentum equations in Cartesian coordinates, equations (4.11)–(4.13), are converted in a body–fitted approach [31, 173].

In equations (4.15)–(4.17), U and V are the transformed, contravariant, velocity components defined in equation (4.18). These velocities take under consideration the arbitrary movement of the domain, where J is the determinant of the inverse Jacobian of the transformation from the initial domain to the normalized one,

$$U = (u - \dot{x})\, y_\eta - (v - \dot{y})\, x_\eta, \quad V = (v - \dot{y})\, x_\xi - (u - \dot{x})\, y_\xi, \tag{4.18}$$

where u, v are the fluid velocities and the arbitrary grid motion velocities respectively, $\dot{x}$, $\dot{y}$ can be given by a first–order backward difference scheme [174]. By defining the motion of the interfaces and the computational domain, an interface tracking technique for moving objects or phase boundaries is provided, using the Euler-Lagrange approach.

Finally, the quantities $q_i, i = 1, 2, 3$ entering in equations (4.15)–(4.17), are defined as follows:

$$q_1 = x_\eta^2 + y_\eta^2, \quad q_2 = x_\xi x_\eta + y_\xi y_\eta, \quad q_3 = x_\xi^2 + y_\xi^2, \tag{4.19}$$

where, x_ξ, x_η, y_ξ, and y_η are the metrics of the transformation that can be computed locally on each cell volume. In this approach, the inverse Jacobian of the transformation, J, is a function of time, and the transformed velocities depend on the physical velocities, u, v, and the velocities of the grid motion, $\dot{x}$, $\dot{y}$ [174].

4.2.2 Boundary and Initial Conditions

This study focuses on a fusiform aneurysm, characterized by a symmetrical dilation across the entire circumference of the aorta. These aneurysms typically involve an elongated section of the aorta, resulting in a tubular or spindle-shaped enlargement. Fusiform aneurysms exhibit a simpler geometry compared to saccular ones, and they are more common in pathology than their saccular counterparts. Additionally this form is less prone to rupture than saccular, due to the even distribution of the stress on the vessel wall [148]. Specialized boundary conditions are necessary for the system of equations that represents blood flow in an aneurysmal geometry when combined with a moving arterial wall. The pulsatility of the aneurysmatic vessel is described by a time–dependent condition for the inlet velocity during the cardiac cycle, which consists of the systolic and diastolic phases. Furthermore, it is assumed that the flow reaches a state of full development at the outflow boundary. This results in a parabolic velocity profile for the fluid and the pressure distribution at the outlet is considered a known parameter. A kinematic boundary condition is imposed at the wall and symmetry boundary condition at the center of the fluid domain, as shown in **Figure 4.1**. The dimensionless boundary conditions of the problem under consideration, following previous studies [204], for the system of equations (4.15)–(4.17), are,

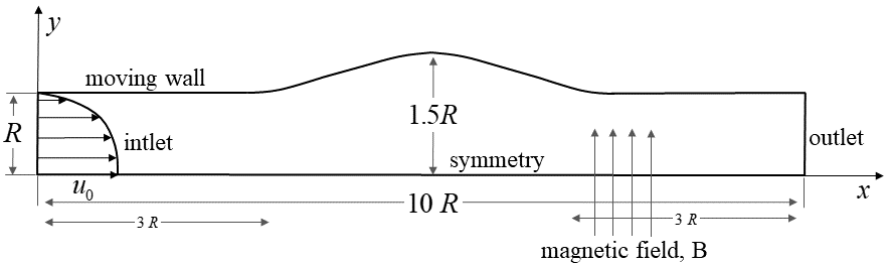

Figure 4.1. An overview of the geometry and boundary conditions of the aneurysm.

- at the inlet, for $t \geq 0$: $u(y,t) = \left[1 - \left(\frac{y}{R}\right)^2\right] \times$ velocity waveform(t), $v = 0, \;\; 0 \leqslant y \leqslant R,$
- at the moving wall : $\;\; u = \dot{x},\; v = \dot{y},\;$ kinematic boundary condition,

- at the symmetry : $\dfrac{\partial u}{\partial y} = 0, \quad \upsilon = 0,$ for $t \geq 0,$
- at the outlet : $p =$ pressure waveform(t), $\dfrac{\partial u}{\partial x} = 0, \quad \dfrac{\partial \upsilon}{\partial x} = 0,$ fully developed flow assumption.

Waveforms of velocity and pressure were extracted from the literature [145] and are fitted with Fourier series [119]. Recent studies employ the most advanced imaging techniques, such as intravascular ultrasonography, magnetic resonance angiography, and computed tomographic angiography (CTA), to precisely quantify the pulsating motion of the aortic wall [10, 193]. In this particular study, the aortic motion pattern utilized represents a condition characterized by low-key pulsatility of the aortic wall.

4.2.3 Geometric Conservation Law

To prevent artificial mass or momentum sources due to the numerical implementation, Thompson and colleagues [174, 186] proposed the equation (4.20). This formulation links the Jacobian temporal variations to the grid velocity components:

$$\frac{\partial J}{\partial t} + \frac{\partial}{\partial \xi}\left(-\dot{x}\frac{\partial y}{\partial \eta} + \dot{y}\frac{\partial x}{\partial \eta}\right) + \frac{\partial}{\partial \eta}\left(-\dot{y}\frac{\partial x}{\partial \xi} + \dot{x}\frac{\partial y}{\partial \xi}\right) = 0. \tag{4.20}$$

Equation (4.21) is the finite–volume, discrete form of equation (4.20) and can be obtained by integrating equation (4.20) employing a first–order fully implicit time integration technique over the same control volume as for mass conservation. For the Jacobian updating formula, this discrete form of the geometric conservation law (GCL) is used, which guarantees the essential requirement for geometric conservation [174].

$$\begin{aligned} \frac{J - J_0}{\Delta t} + \left(-\dot{x}\frac{\partial y}{\partial \eta} + \dot{y}\frac{\partial x}{\partial \eta}\right)_e - \left(-\dot{x}\frac{\partial y}{\partial \eta} + \dot{y}\frac{\partial x}{\partial \eta}\right)_w \\ + \left(-\dot{y}\frac{\partial x}{\partial \xi} + \dot{x}\frac{\partial y}{\partial \xi}\right)_n - \left(-\dot{y}\frac{\partial x}{\partial \xi} + \dot{x}\frac{\partial y}{\partial \xi}\right)_s = 0, \end{aligned} \tag{4.21}$$

where the subscripts $e, w, n,$ and s denote the four faces of each finite volume. In particular, during the solution process in this study, the computational mesh of the fluid domain undergoes deformation, which is more pronounced with increasing wall pulsatility. Despite the low-order method that is utilized for the GCL in equation (4.21), the findings for grid deformations are conservative [174]. Additionally, it is

worth highlighting that high-order GCL schemes have been introduced in other works [129, 130].

4.3 Numerical Solution

To solve the system of equations (4.15)–(4.17) numerically, an Euler–Lagrange technique is devised subject to boundary and initial conditions. The nonlinear set of equations was discretized using the finite volume method on a staggered grid approach. The numerical solution results from a direct numerical approach using MATLAB (MathWorks, Natick, MA, USA). Furthermore, to simplify numerical calculations, the system of equations is expressed in dimensionless form [204].

4.3.1 Finite Volume Discretization Method

The staggered configuration generally outperforms the collocated layout in convective-dominated flows when utilizing the finite volume approach [67, 84]. According to Fletcher [70], this approach is highly stable and provides second-order accuracy for spatial derivatives and first-order accuracy for the temporal derivative. When necessary, the upwind method is incorporated in the discretized equations to assist in solving the problem of high convection terms in the momentum. The final discretized form of equations is similar to the simple case without the magnetic field [204]. The $x-$momentum is implemented as shown below,

$$\begin{aligned}\frac{Ju - J_0u_0}{\Delta t} &+ \left(Uu - \frac{1}{J\,\mathrm{Re}}\left(q_1\frac{\partial u}{\partial \xi} - q_2\frac{\partial u}{\partial \eta}\right) + \frac{\partial y}{\partial \eta}p - MuJ\right)_e \\ &- \left(Uu - \frac{1}{J\,\mathrm{Re}}\left(q_1\frac{\partial u}{\partial \xi} - q_2\frac{\partial u}{\partial \eta}\right) + \frac{\partial y}{\partial \eta}p - MuJ\right)_w \\ &+ \left(Vu - \frac{1}{J\,\mathrm{Re}}\left(-q_2\frac{\partial u}{\partial \xi} + q_3\frac{\partial u}{\partial \eta}\right) - \frac{\partial y}{\partial \xi}p\right)_n \\ &- \left(Vu - \frac{1}{J\,\mathrm{Re}}\left(-q_2\frac{\partial u}{\partial \xi} + q_3\frac{\partial u}{\partial \eta}\right) - \frac{\partial y}{\partial \xi}p\right)_s = 0.\end{aligned} \tag{4.22}$$

where the subscript 0 indicates the previous time level.

A first–order backward difference scheme, such as $\dot{x} = \dfrac{x - x_0}{\Delta t}$, $\dot{y} = \dfrac{y - y_0}{\Delta t}$ is used to estimate the Cartesian components of the mesh velocity vector, $(\dot{x}, \dot{y})$, where x_0 and y_0 are the previous, and x and y the current time step grid positions and Δt is the time step [174].

4.3.2 Grid Independence, CFL Criterion and Speedup Test

Simulations were conducted using a 40×40 grid of finite volume elements over four cardiac cycles. An initial grid and time independence study was undertaken for the hydrodynamic case, as outlined in [204]. In this specific case, a similar study was conducted, although not with the same level of detail as the former. Due to the complexity resulting from the inclusion of the magnetic field term in the system of equations, our focus is primarily on 20×20 and 40×40 grids. Grid independency was validated through the root mean square (RMS) error of the velocity magnitude, as provided in equation (4.23), indicating that the results are grid independent [204],

$$\mathrm{RMS}_{\mathrm{error}} = \sqrt{\frac{\sum_{i=1}^{n} (\tilde{q}_i - q_i)^2}{n}} \tag{4.23}$$

where $\tilde{q}_i$ is the velocity magnitude predicted by the refined 40×40 grid at evaluation point i, q_i is the corresponding velocity magnitude from the 20×20 grid at the exact same spatial coordinate, and n is the total number of evaluation points. The RMS metric is a standard statistical tool used to quantify the aggregate standard deviation of the residuals between two datasets, making it a reliable indicator of spatial convergence. The calculated RMS error between the two grids was found to be sufficiently small, indicating that the 40×40 grid provides grid-independent results.

Stability is limited, due to non-linearities in the Euler–Lagrange Navier–Stokes equations, and even implicit schemes are not unconditionally stable. The Courant–Friedrichs–Lewy (CFL) condition applies, to explicit schemes for hyperbolic and/or parabolic systems of PDEs; it is also a good stability criterion for the problem under consideration.

The addition of the magnetic field retains stable and converged numerical solutions for almost all cases studied following previous results where high pulsatility was present, but with the absence of the magnetic field [204].

The validation of the developed mathematical approach was achieved by using a commercial CFD program, Ansys Fluent (Ansys Inc., Canonsburg, PA). The simulation shows that the two-dimensional Euler–Lagrange model in comparison with a three-dimensional demonstrates that the suggested technique effectively predicts the rigid wall dynamics.[31].

The numerical solution was obtained by developing a direct numerical approach, and a computational program in MATLAB was developed. The simulations were performed for four cardiac cycles on a DellTM PrecisionTM T7500 workstation with two Intel Xeon processors (E5645, 2.40 GHz, 12MB Cache, 5.86GTs-1; Intel QPI).

The developed code was parallelized, distributing the workload to several CPUs, as the number of elements slows down the performance with one core use. The following

Tables 4.1, 4.2 display the time required for the code to be completed using $1 - 20$ cores. As the number of cores is increased, a reduction in completion time is observed. The outcomes for the medium pulsatility case are shown in **Figure 4.2**.

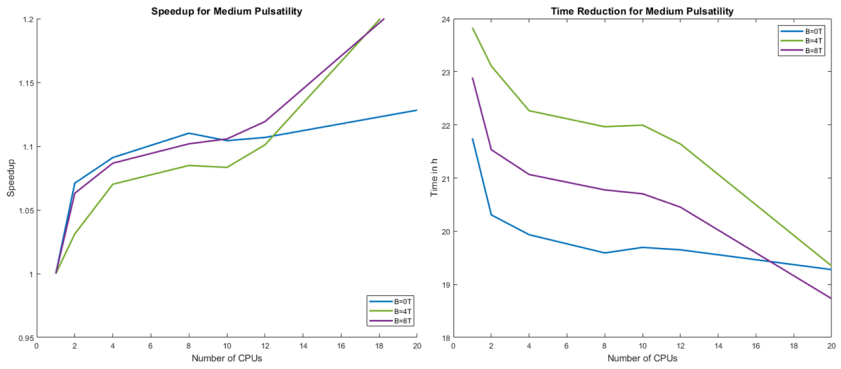

Figure 4.2. Speedup and time reduction for medium pulsatility results and for $1 - 20$ CPUs.

According to the relationship between the serial and parallel time components, T_S/T_P, speed up is shown on the left. The second figure displays how processing time decreases as the number of CPU cores rises. In both figures, it can be seen that for $B = 0T$, the algorithm can be resolved with only 8 CPU cores, since time does not reduce further with the increase of cores. Whereas in the other two cases, the increase of cores speeds up the acquisition time. It is observed that in the case of $B = 0T$, despite the effect of the nonlinearity of the equations, the problem under consideration is solved in less time than the other cases with the magnetic field source terms. On the other side, adding the magnetic field source term causes the problem to be solved requiring more computational time. However, we observe that as we increase the number of CPUs the problem is distributed and thus can be solved in less computational time. The authors hypothesize that the variance in computational time across different magnetic field intensities derives from the interaction of pulsatile flow with the magnetic field. In any case, additional cases need to be performed to extract more results. **Tables 4.1, 4.2** demonstrate the time difference between two distinct grids for medium pulsatility cases. Both cases were performed for a total of 4 cardiac cycles in 20×20 and 40×40 grids. The time reduction is more noticeable in the small grid with a 70% reduction in total, while the same percentage for the larger grids comes up to only 11%. The results

show that speedup performance depends on the nature and complexity of the problem.

In the results section, the results of the fourth cardiac cycle are reported, thus preventing any dynamic disturbances of the numerical solution during the initial cycles.

Speedup Test for Medium Pulsatility									
Magnetic Field	**0 T**			**4 T**			**8 T**		
Cores	**Time (min)**	**Speedup**	**Reduction (%)**	**Time (min)**	**Speedup**	**Reduction (%)**	**Time (min)**	**Speedup**	**Reduction (%)**
1	50.5362			45.6410			46.3027		
2	33.3920	1.5134	33.92	27.9351	1.6338	38.79	28.4874	1.6254	38.48
4	26.3836	1.9154	20.99	20.0137	2.2805	28.36	20.0730	2.3067	29.54
8	22.5523	2.2408	14.52	16.3016	2.7998	18.55	17.3158	2.6740	13.74
10	15.3353	3.2954	32.00	15.2630	2.9903	6.37	15.5216	2.9831	10.36
12	14.8239	3.4091	3.33	15.1308	3.0164	0.87	14.9064	3.1062	3.96

Table 4.1. Parallel performance for medium pulsatility on a 20×20 grid.

Speedup Test for Medium Pulsatility									
Magnetic Field	**0 T**			**4 T**			**8 T**		
Cores	**Time (h)**	**Speedup**	**Reduction (%)**	**Time (h)**	**Speedup**	**Reduction (%)**	**Time (h)**	**Speedup**	**Reduction (%)**
1	21.7483			23.8296			22.8922		
2	20.3063	1.0710	6.63	23.1082	1.0312	3.03	21.5336	1.0630	5.93
4	19.9331	1.0910	1.84	22.2674	1.0701	3.64	21.0667	1.0866	2.17
8	19.5901	1.1101	1.72	21.9654	1.0848	1.36	20.7764	1.1018	1.38
10	19.6939	1.1043	−0.53	21.9963	1.0833	−0.14	20.7039	1.1056	0.35
12	19.6489	1.1068	0.23	21.6423	1.1010	1.61	20.4525	1.1192	1.21
20	19.2763	1.1282	1.90	19.3463	1.2317	12.24	18.7292	1.2222	8.43

Table 4.2. Parallel performance for medium pulsatility on a 40×40 grid.

4.3.3 Direct Solution Approach

The nonlinear algebraic system of equations is solved using a direct solution. This method is distinct from other iterative methodologies that have been introduced. Nonlinear solvers, such as Newton-like approaches, can be used to solve the Euler—Lagrange fluid flow equations.

Both the initial guess values, as well as the actual solution path will affect the path to the solution. In Newton–like methods it is necessary to have a good initial guess and a good estimate of the solution, leading to a reduction of the required time but may suffer from local minima. The nonlinear discretised algebraic system of equations can be solved by employing the Levenberg—Marquardt algorithm (LMA) [177, 217]. The LMA interpolates between the Gauss–Newton algorithm and the method of Gradient Descent. When compared to the standard Gauss-Newton method, the LMA algorithm is considerably more efficient.

4.4 Results and Discussion

A two–dimensional Euler–Lagrange mathematical approach to a viscous fluid flow is presented. Results of blood flow under varying intensities of pulsating arterial wall tissue focusing on velocity and pressure quantities, are also included. Many numerical experiments were performed under the influence of magnetic fields of different intensities. Additionally, recirculation zones during early and late diastole are studied.

4.4.1 Blood Flow in an Aneurysmal Geometry: the Euler–Lagrange Approach

In this study, there are three distinct scenarios, each categorized based on the pulsatility of the aortic wall, specifically classified as low, medium, and high. In this context, low corresponds to a 5.5% change in the initial radius, medium to an 11% change, and high to a 14% change. These categories are based on the level of the walls' pulsatility. The magnetic field strength is then incrementally raised, allowing to observe and analyze the resulting changes. Initially, a brief analysis is conducted on the hydrodynamic case, followed by an increment in the magnetic field to $B = 4T$, and subsequently to $B = 8T$. In all cases, during the end of systole and at the diastolic phase of the cardiac cycle, a recirculation zone develops in the flow field. Specifically, an identifiable vortex near the neck of the aneurysmal geometry influences the inlet jet of blood entering the aneurysm at the onset of diastole. This vortex, positioned above the line of symmetry, persists throughout diastole but progressively diminishes in energy as early systole ensues, coinciding

with the restoration of forward flow. Additionally, it is evident that as the pulsatility increases, the size of the developing vortex becomes smaller. These findings align with previous studies [161, 204]. Moreover, the presence of the magnetic field causes the vortex to relocate toward the neck of the aneurysm. As the strength of the magnetic field increases, the vortex gradually reduces in size until it ultimately vanishes, as depicted in **Figure 4.3**. The presence of pulsatility in conjunction with a magnetic field intensity of $B = 8T$ is sufficient to cause the disappearance of vortices. These findings align with the observations of previous studies employing three-dimensional fluid-structure interaction simulations [205],

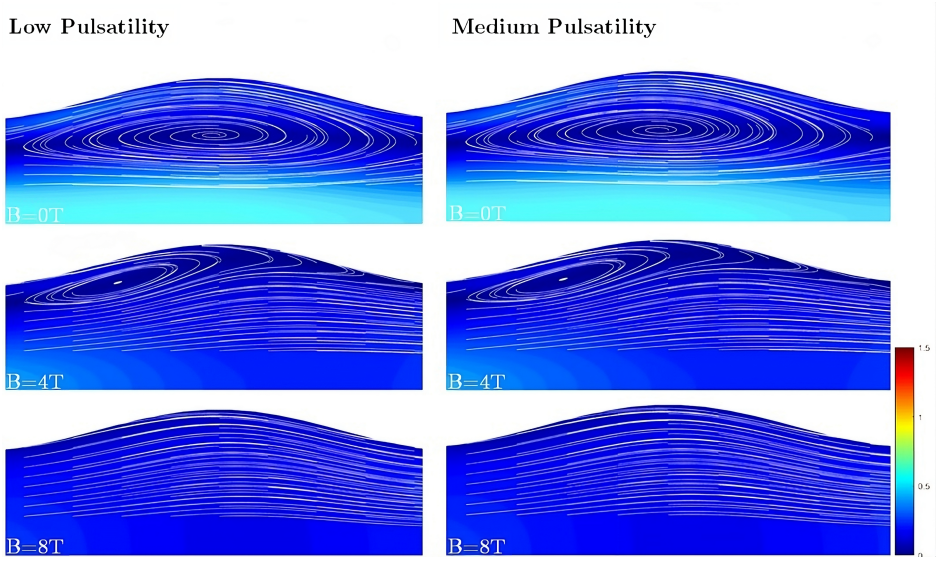

Figure 4.3. Streamlines for low and medium pulsatility in the aneurysmal areas during diastole. Magnetic field intensity 0T, 4T, 8T, bar represents velocity values.

As the pulsatility of the arterial wall increases, Reynolds and Womersley numbers increase for various wall pulsatilities. These phenomena, along with the formation of the aneurysm, could affect cardiovascular risk in individuals with abdominal aortic aneurysms [207, 209].

Variations in both pulsatility and magnetic field strength also impact the velocity and pressure values. Specifically, in the cases of low and medium pulsatility, a decrease in velocity is observed, accompanied by an increase in pressure drop. In the majority of cases, the average velocity experiences a decrease, although it tends to remain relatively stable overall. However, when strong magnetic fields are applied, the results deviate significantly. In particular, while there may be an increase in

velocity when transitioning from a magnetic field strength of $B = 4T$ to $B = 8T$, the general trend still demonstrates a decrease in velocity. The increase of the magnetic field causes the Lorentz force to arise, resulting in a reduction in blood flow velocity. The reduction of blood velocity within aneurysmatic geometries carries significant implications for arterial diseases and their development [169, 170]. Detailed quantitative data for these average and maximum variations are summarized in Table 4.3 and Table 4.4, respectively.

Average Velocity and Pressure Values						
	Systolic Acceleration		**Systolic Deceleration**		**Diastole**	
Velocity	**Vel**	**Decrease (%)**	**Vel**	**Decrease (%)**	**Vel**	**Decrease (%)**
$B = 0\,\mathrm{T}$	0.5720		0.4566		0.4279	
$B = 4\,\mathrm{T}$	0.5659	1.06	0.4511	1.20	0.4211	1.58
$B = 8\,\mathrm{T}$	0.5638	1.43	0.4479	1.90	0.4178	2.36
Pressure	**Pres**	**Increase (%)**	**Pres**	**Increase (%)**	**Pres**	**Increase (%)**
$B = 0\,\mathrm{T}$	1.0951		-1.8691		1.0025	
$B = 4\,\mathrm{T}$	1.3584	24.04	-1.4558	22.11	2.0294	102.43
$B = 8\,\mathrm{T}$	2.0530	87.47	-0.2503	86.60	5.3087	429.54

Table 4.3. Average velocity and pressure variations during the fourth cardiac cycle for medium pulsatility on a 40×40 grid.

The pressure distribution within the AAA lumen, driven by dynamic blood flow patterns throughout the cardiac cycle, constitutes a significant factor in raising wall stresses and exacerbating the risk of rupture. The findings of this study, visually represented in Figure 4.4, highlight that the dimensionless pressure p and the pressure drop, Δp, are at their peak during the systolic phase. The pressure drop, defined as the difference in pressure between the inlet and outlet, remains markedly elevated during systole but experiences a significant decrease in the diastolic phase. Furthermore, the analysis of the pressure field reveals regions with lateral pressure gradients in the aneurysmal region, particularly during the diastolic phase, suggesting a significant disruption in the flow dynamics. Interestingly, for the highest magnetic field intensities simulated, such as $B = 8\,\mathrm{T}$, there is a substantial increase in pressure levels.

Maximum Velocity and Pressure Values						
	Systolic Acceleration		**Systolic Deceleration**		**Diastole**	
Velocity	**Vel**	**Decrease (%)**	**Vel**	**Decrease (%)**	**Vel**	**Decrease (%)**
$B = 0\,\mathrm{T}$	1.9417		1.4572		1.1527	
$B = 4\,\mathrm{T}$	1.9417	0.00	1.4348	1.53	0.9382	18.60
$B = 8\,\mathrm{T}$	1.9417	0.00	1.3884	4.72	0.8928	22.54
Pressure	**Pres**	**Increase (%)**	**Pres**	**Increase (%)**	**Pres**	**Increase (%)**
$B = 0\,\mathrm{T}$	8.5468		0.0870		8.0970	
$B = 4\,\mathrm{T}$	9.1310	6.83	0.6080	598.85	9.5802	18.31
$B = 8\,\mathrm{T}$	10.9472	28.08	2.8338	3157.24	14.6834	81.34

Table 4.4. Maximum velocity and pressure variations during the fourth cardiac cycle for medium pulsatility on a 40×40 grid.

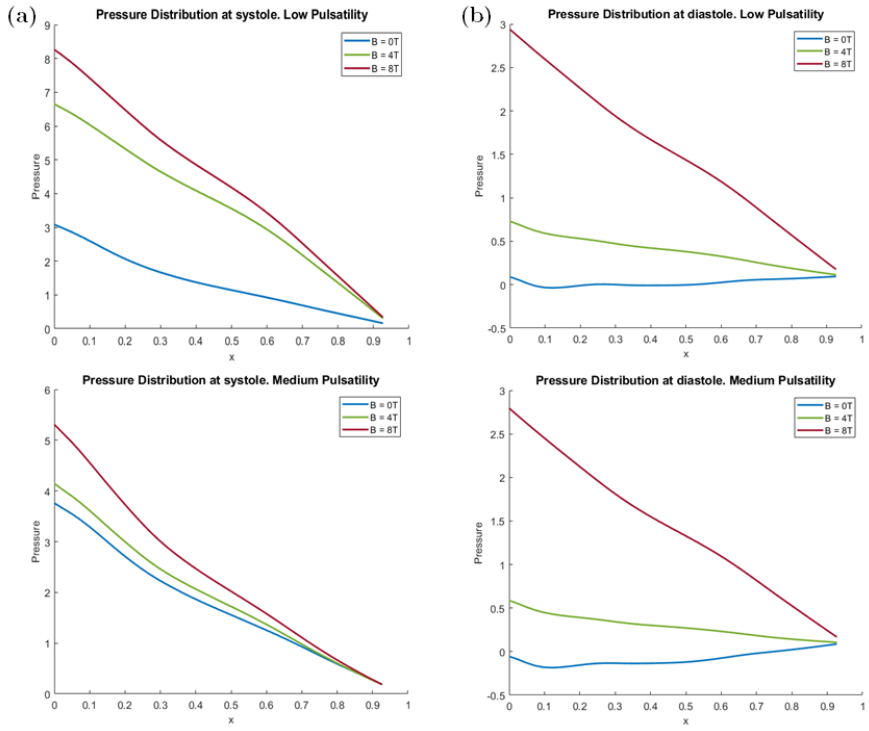

Figure 4.4. Dimensionless Pressure Distribution for low and medium pulsatility at systole (a) and diastole (b).

During the diastolic phase, recirculation zones are clearly observable across all levels of aortic wall pulsatility examined in this study.

These diastolic phase recirculation zones tend to form and extend over a significant portion of the dilated aneurysm body. They cause haemodynamic alterations in the bulging region of the aneurysm, which is clearly captured by the resulting velocity profiles depicted in Figure 4.5.

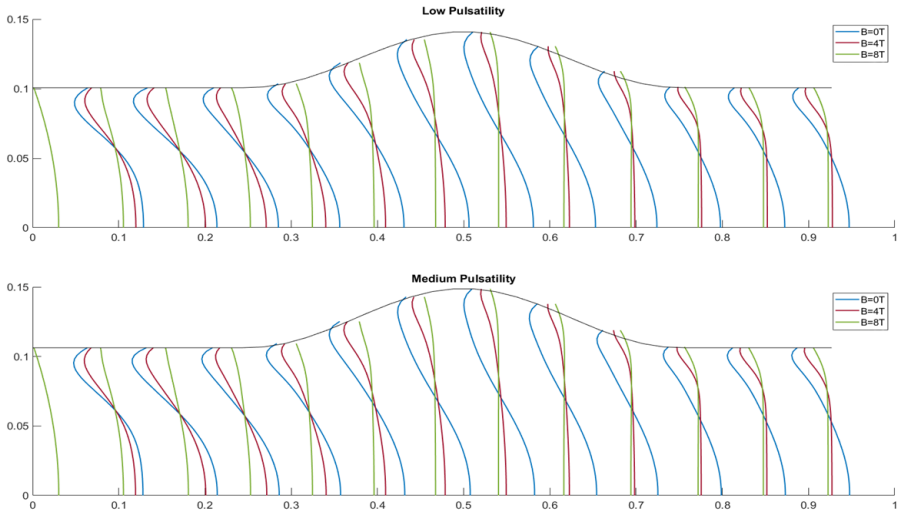

Figure 4.5. Velocity Profile for low and medium pulsatility at diastole.

In addition, the study incorporates an analysis of Wall Shear Stress (WSS) along the dilated portion of the aneurysmal geometry. WSS is an essential metric for quantifying the frictional forces acting on the wall of the abdominal aortic aneurysm (AAA). Its definition involves dimensionless units, as defined by the equation $\tau_{wall} = \frac{\mu R}{u_0}\left(\frac{\partial u}{\partial y} + \frac{\partial v}{\partial x}\right)$, where μ represents the dynamic viscosity of the blood. This methodology offers enhanced accuracy when contrasted with other methods that solely account for the u-velocity gradient. First-order differences are utilized to discretize the velocity gradients.

The results reveal that during the systolic phase, the peak Wall Shear Stress (WSS) on the pulsating wall is higher at the aneurysm's shoulders in comparison to the maximum WSS on the rigid wall. Moreover, across all cases examined, the highest WSS value consistently appears at the distal end of the aneurysm, consistent with prior research outcomes [161].

The study shows that the values of the wall shear stress increase when pulsatility exists, but the presence of the magnetic field decreases this effect. Specifically, in the low pulsatility case, the average WSS experiences a reduction for both the systolic and diastolic phase. At systole, the reduction is approximately 13% for $B = 4T$ and 35%, for $B = 8T$. For diastole the corresponding values are 31%, for $B = 4T$ and 67% for $B = 8T$. Moving to the medium pulsatility case, reductions of 22% and 31% are observed during systole, for $B = 4T$ and $B = 8T$. Meanwhile, during diastole, the reductions are 34% and 74%, for the two magnetic field intensities under consideration. Analytically, the values can be found in **Table 4.5**. For all pulsatilities studied, the WSS reduction is more pronounced at the diastolic phase of the cardiac cycle.

Wall Shear Stress (WSS) Reductions				
	Systolic Phase		**Diastolic Phase**	
Avg WSS (%)	**Low**	**Medium**	**Low**	**Medium**
$B = 4\,\mathrm{T}$	13.19	22.22	31.73	34.39
$B = 8\,\mathrm{T}$	35.16	31.94	67.06	74.52
Max WSS (%)	**Low**	**Medium**	**Low**	**Medium**
$B = 4\,\mathrm{T}$	2.07	5.60	27.79	28.29
$B = 8\,\mathrm{T}$	10.50	5.31	53.57	62.32

Table 4.5. Average and maximum WSS percentage reductions for low and medium pulsatility under magnetic field conditions.

The dynamic WSS profiles observed in this study align with the findings from previous experiments and computational studies [213, 161]. Abnormal WSS levels, whether excessively high or low, and particularly patterns characterized by a sequence of high WSS followed by low WSS, have been identified as significant factors contributing to processes like vasoconstriction, coagulation, platelet aggregation, and deposition. These conditions are likely to facilitate the formation of a thrombus [205, 89].

In the Euler-Lagrange methodology presented here, structured grids are employed for the computational part. An essential step towards the mathematical modeling of pathophysiological conditions of the human cardiovascular system is the development

of such fluid–structure interaction (FSI) techniques. Conditions such as AAA and various other intriguing biomedical problems [118, 182] underscore the necessity for the development of such computational approaches. These approaches have the potential to provide significant information about a patient's condition, offering valuable information that can guide medical professionals in making vital decisions [207].

In earlier investigations, advanced Fluid-Structure Interaction (FSI) simulations were conducted using patient–specific geometries. These simulations modeled the dynamic interaction between haemodynamics within the aneurysmal vessel and wall deformation. The simulations were executed with the assistance of a commercial software program, (ADINA R & D Inc, Watertown, MA) [162, 205, 207, 209].

These FSI studies involved the utilization of patient–specific, three-dimensional geometries reconstructed from CT scans of aortic aneurysms with various configurations, including cases both with and without thrombus formation. These simulations were aimed at predicting potential rupture locations on the surface of the aneurysmal wall [207]. For the fluid dynamics part, the Euler–Lagrange approach was employed to describe the fluid equations [209]. The haemodynamic findings of the present study consistently align with our previous FSI investigations, accurately predicting velocity and pressure distributions, as well as the presence of blood recirculation zones, during the diastolic phase [162, 205]. The WSS distributions obtained in this study correspond with findings from prior experimental and computational studies involving rigid walls [161, 213].

4.4.2 Limitations and Future Work

In the current study, an assumption was made that blood behaves as a Newtonian fluid. While this assumption holds reasonably well for blood flow in larger arteries, it is known to deviate from Newtonian behaviour in smaller vessels [189]. To enhance the accuracy of future simulations non–Newtonian behaviour could be incorporated, especially when smaller blood vessels are involved. Moreover, the motion of the arterial wall was determined based on existing literature data. Future steps should involve the development of a coupled scheme that can accurately capture the hyperelastic and incompressible nature of aortic wall materials [207].

Another potential challenge arises from the outflow boundary condition, which could potentially generate reflecting pressure waves, although this phenomenon was not observed in the current study. To address this concern in future research, a prospective approach could involve coupling the outflow solution with lumped parameters or utilizing one-dimensional models for the downstream domain [71, 196, 209].

A subsequent step would be to create a three-dimensional solver using the finite volume method that could address the fluid-structure interaction (FSI) applications in the biomedical field. However, the complexity of the geometry and the associated

challenges, including non-linearity, coupling, and considerations of time and spatial variables, necessitate comprehensive efforts and an advanced formulation. These FSI issues can currently only be addressed by a very limited number of numerical codes. The development of such FSI approaches that could handle these haemodynamic interactions with the aorta wall, is essential.

4.5 Conclusions

This study introduces a two–dimensional Euler–Lagrange mathematical model that extends the fluid equations into a mixed Euler–Lagrange formulation. This approach is used to investigate blood flow dynamics within an aneurysmal geometry throughout the cardiac cycle. To achieve this, the fluid transport equations of mass and momentum are transformed into a reference frame that moves with the geometry, using generalized curvilinear coordinates (GCC). The resulting system of partial differential equations (PDEs) is discretized using the finite volume method, employing structured grids. Given the strong coupling, the presence of nonlinear terms and the inclusion of intense source terms in these PDEs, a simultaneous solution approach is employed.

The developed model demonstrates its ability to predict the dynamic velocity and pressure profiles of fluid within a pulsating aneurysmal structure. It has been observed that all flow characteristics were significantly influenced by the pulsatile motion of the arterial wall, particularly when subjected to the presence of a magnetic field.

The magnetic field has a significant influence on the flow dynamics within the considered aneurysmal geometry. More specifically, the bulk flow velocity decreases noticeably with increasing magnetic field strength, especially during the diastolic period. Furthermore, the pressure field is impacted by the magnetic field, causing a significant increase in pressure drops during the entire cardiac cycle.

Moreover, the wall shear stress (WSS) near the aneurysmatic wall undergoes alterations, necessitating a deeper investigation into the magnetic field's effects on the pulsating wall. These observed phenomena, in conjunction with the formation of the aneurysm itself, hold the potential to further impact the cardiovascular risk profiles of patients with abdominal aortic aneurysms.

In conclusion, these findings demonstrate the significance of employing Fluid-Structure Interaction (FSI) biomedical modelling approaches and conducting investigations on blood flow under the presence of a magnetic field.

CHAPTER 5

A Three-Dimensional Fluid–Structure Interaction Approach on Aneurysmal Haemodynamics

5.1 Introduction

Prediction of haemodynamic properties, such as flow and/or pressure fields and wall stresses, via biofluid dynamics has a wide range of applications in the human vascular system, from evaluation of cerebral artery pathologies to prediction of abdominal aortic aneurysms (AAAs) [118, 119, 207]. AAAs occur mainly in the infrarenal segment of the abdominal aorta between the renal arteries and the iliac bifurcation and are characterized by dilation of the aorta. As the aneurysm grows, the stresses on the inner wall increase. AAAs are usually asymptomatic, and their growth rates vary among individuals; however, when aortic dilation exceeds tissue strength, rupture can occur, resulting in internal bleeding and a mortality rate of 85–90% [99]. Thus, understanding the haemodynamics of AAAs is essential for prediction and prevention of rupture.

Several research groups have conducted simulations of blood dynamics and interactions with the aortic wall, including computational fluid dynamics (CFD) and fluid–structure interaction (FSI) methodologies [24, 69, 74, 146]. FSI problems involve the interactions between haemodynamics and vessel wall deformation, making them a classic example of multiphysics simulations. Solid mechanics equations are usually formulated and treated with a Lagrangian frame of reference in which the mesh deforms with the material. By contrast, for equations describing fluid flow, an Eulerian frame of reference is adopted, in which fluid particles are allowed to move through an otherwise stationary mesh. In the present study, we use a mixed Euler–Lagrange approach to model blood flow problems with consideration of the motions of blood

vessels.

Many methods have been developed to describe the interactions of fluid and tissue in complicated geometries. For instance, Peskin and collaborators introduced the immersed boundary method to describe the biomechanics of the heart and blood flow [154]. In this method, Navier–Stokes equations are solved on a fixed Eulerian grid, which can be Cartesian or curvilinear [76, 178]. Numerous improvements have been proposed since the introduction of the immersed boundary method [32, 190]. Figueroa et al. introduced the coupled-momentum method, an advanced FSI technique [68] in which three-dimensional (3D) deformable arterial models are described and the deformation equations of the vessel wall are coupled with the fluid domain. Models of flow in compliant vessels in one and three dimensions were introduced by Quarteroni et al. [71], and an Euler–Lagrange numerical framework describing flows in body-fitted geometries, using the finite volume method (FVM), has been developed by Shyy and coworkers [31, 173, 175]. The latter approach ensures consistent treatment of the continuity equation and addresses the skewness of the computational grid on the flow field.

There have been several studies of FSI approaches with applications in the biomedical field, for instance, the use of reconstructed patient-specific geometries from computed tomography scans of the abdominal aorta to determine the risk of rupture, focusing on the effects of the pulsating wall on the aneurysmatic vessel [58, 205, 207, 209]. In these approaches, an arbitrary Lagrangian–Eulerian methodology is used to describe the coupling between blood and the vessel wall, with abnormal values potentially indicating an increased risk of rupture.

However, there is a need for methods more suitable for the study of complex and deformable domains such as those of biological structures. These intricate systems can be mathematically modelled using generalized curvilinear coordinates (GCCs) to convert the system of partial differential equations (PDEs) into a moving body-fitted reference frame. Body-fitted coordinates are a suitable selection for cases with complex geometries or special geometric characteristics (extreme curvature, torsion), as it has been proved that such coordinate systems improve computational efficiency [75].

In the present study, we present a 3D finite volume solver for FSI. This mathematical model describes the interaction between fluid flow and the arterial wall, thereby extending previous modelling work in the two-dimensional (2D) Euler–Lagrange framework [108, 204]. This approach can be applied to many biomedical problems involving a fluid–solid interface. In this study, a simplified idealized geometry (Figure 5.1) is studied with aim of modelling blood flow through this domain. Additionally, according to the literature [165], fusiform aneurysms are characterised by a symmetric dilation along the axial direction, so a direct numerical approach, coupling all equations, is applied in this methodology utilizing trust region methods [106].

5.2 Mathematical Analysis

5.2.1 Dimensionless Equations

A mathematical formulation of the problem under consideration can be given based on the fundamental conservation laws of fluid mechanics, namely the conservation of mass and momentum. These governing equations describe the pulsatile motion of blood within a moving reference frame where flow is assumed laminar and the fluid behaves as Newtonian that is slightly compressible. Such assumptions are commonly adopted in haemodynamic analysis. The system must then be transformed to a generalized coordinate system using GCC. The equations for continuity and momentum in Cartesian coordinates and three dimensions for a Newtonian fluid are as follows [174].

Continuity equation:

$$\frac{\partial \rho}{\partial \tilde{t}} + \frac{\partial(\rho\tilde{u})}{\partial \tilde{x}} + \frac{\partial(\rho\tilde{v})}{\partial \tilde{y}} + \frac{\partial(\rho\tilde{w})}{\partial \tilde{z}} = 0, \tag{5.1}$$

x-momentum equation:

$$\frac{\partial(\rho\tilde{u})}{\partial \tilde{t}} + \frac{\partial(\rho\tilde{u}\tilde{u})}{\partial \tilde{x}} + \frac{\partial(\rho\tilde{u}\tilde{v})}{\partial \tilde{y}} + \frac{\partial(\rho\tilde{u}\tilde{w})}{\partial \tilde{z}} = -\frac{\partial \tilde{p}}{\partial \tilde{x}} + \left[\frac{\partial}{\partial \tilde{x}}\left(\mu\frac{\partial \tilde{u}}{\partial \tilde{x}}\right) + \frac{\partial}{\partial \tilde{y}}\left(\mu\frac{\partial \tilde{u}}{\partial \tilde{y}}\right) + \frac{\partial}{\partial \tilde{z}}\left(\mu\frac{\partial \tilde{u}}{\partial \tilde{z}}\right)\right], \tag{5.2}$$

y-momentum equation:

$$\frac{\partial(\rho\tilde{v})}{\partial \tilde{t}} + \frac{\partial(\rho\tilde{v}\tilde{u})}{\partial \tilde{x}} + \frac{\partial(\rho\tilde{v}\tilde{v})}{\partial \tilde{y}} + \frac{\partial(\rho\tilde{v}\tilde{w})}{\partial \tilde{z}} = -\frac{\partial \tilde{p}}{\partial \tilde{y}} + \left[\frac{\partial}{\partial \tilde{x}}\left(\mu\frac{\partial \tilde{v}}{\partial \tilde{x}}\right) + \frac{\partial}{\partial \tilde{y}}\left(\mu\frac{\partial \tilde{v}}{\partial \tilde{y}}\right) + \frac{\partial}{\partial \tilde{z}}\left(\mu\frac{\partial \tilde{v}}{\partial \tilde{z}}\right)\right], \tag{5.3}$$

z-momentum equation:

$$\frac{\partial(\rho\tilde{w})}{\partial \tilde{t}} + \frac{\partial(\rho\tilde{w}\tilde{u})}{\partial \tilde{x}} + \frac{\partial(\rho\tilde{w}\tilde{v})}{\partial \tilde{y}} + \frac{\partial(\rho\tilde{w}\tilde{w})}{\partial \tilde{z}} = -\frac{\partial \tilde{p}}{\partial \tilde{z}} + \left[\frac{\partial}{\partial \tilde{x}}\left(\mu\frac{\partial \tilde{w}}{\partial \tilde{x}}\right) + \frac{\partial}{\partial \tilde{y}}\left(\mu\frac{\partial \tilde{w}}{\partial \tilde{y}}\right) + \frac{\partial}{\partial \tilde{z}}\left(\mu\frac{\partial \tilde{w}}{\partial \tilde{z}}\right)\right], \tag{5.4}$$

In the equations above $\tilde{u}$, $\tilde{v}$, and $\tilde{w}$ denote the components of velocity vector $\tilde{\bar{q}} = (\tilde{u}, \tilde{v}, \tilde{w})$, while $\tilde{p}$ represents the pressure, ρ the density, and μ the dynamic viscosity of the fluid.

To simplify and generalize the system of equations, we make them non-dimensional by introducing the following dimensionless parameters:

$$x = \frac{\tilde{x}}{R},\ y = \frac{\tilde{y}}{R},\ z = \frac{\tilde{z}}{R},\ t = \frac{\tilde{t}}{R/u_0},\ u = \frac{\tilde{u}}{u_0},\ v = \frac{\tilde{v}}{u_0},\ w = \frac{\tilde{w}}{u_0},\ p = \frac{\tilde{p}}{\rho u_0^2},\ c = \frac{\rho}{\rho_0}, \tag{5.5}$$

where R is the length of the inlet of the aneurysmal structure, u_0 is the characteristic velocity at the inlet, and ρ_0 is a characteristic density.

Moreover, the assumption of *slight compressibility* implies that density variations with pressure are small but not negligible. This process leads to a new form of the equations that includes the Reynolds number, assuming slight compressibility of the fluid.

Dimensionless continuity equation:

$$\frac{\partial c}{\partial t} + \frac{\partial (cu)}{\partial x} + \frac{\partial (cv)}{\partial y} + \frac{\partial (cw)}{\partial z} = 0, \tag{5.6}$$

x-dimensionless momentum equation:

$$\frac{\partial u}{\partial t} + \frac{\partial \left(uu\right)}{\partial x} + \frac{\partial \left(uv\right)}{\partial y} + \frac{\partial \left(uw\right)}{\partial z} = -\frac{\partial p}{\partial x} + \frac{1}{Re}\left[\frac{\partial}{\partial x}\left(\frac{\partial u}{\partial x}\right) + \frac{\partial}{\partial y}\left(\frac{\partial u}{\partial y}\right) + \frac{\partial}{\partial z}\left(\frac{\partial u}{\partial z}\right)\right], \tag{5.7}$$

y-dimensionless momentum equation:

$$\frac{\partial v}{\partial t} + \frac{\partial \left(vu\right)}{\partial x} + \frac{\partial \left(vv\right)}{\partial y} + \frac{\partial \left(vw\right)}{\partial z} = -\frac{\partial p}{\partial y} + \frac{1}{Re}\left[\frac{\partial}{\partial x}\left(\frac{\partial v}{\partial x}\right) + \frac{\partial}{\partial y}\left(\frac{\partial v}{\partial y}\right) + \frac{\partial}{\partial z}\left(\frac{\partial v}{\partial z}\right)\right], \tag{5.8}$$

z-dimensionless momentum equation

$$\frac{\partial w}{\partial t} + \frac{\partial \left(wu\right)}{\partial x} + \frac{\partial \left(wv\right)}{\partial y} + \frac{\partial \left(ww\right)}{\partial z} = -\frac{\partial p}{\partial z} + \frac{1}{Re}\left[\frac{\partial}{\partial x}\left(\frac{\partial w}{\partial x}\right) + \frac{\partial}{\partial y}\left(\frac{\partial w}{\partial y}\right) + \frac{\partial}{\partial z}\left(\frac{\partial w}{\partial z}\right)\right]. \tag{5.9}$$

In these equations, all variables have been replaced by their corresponding dimensionless forms. The parameter $Re = \dfrac{u_0 R}{\nu}$ represents the Reynolds number, and ν is the kinematic viscosity of the fluid.

The next step involves an appropriate selection of a coordinate system that is capable of handling complex and curved geometries such as the aneurysmal geometry. To achieve this, the GCC transformation is employed, ensuring that the effects of the grid motion are incorporated into the numerical approach. This transformation maps the physical domain into a normalized local domain, allowing the equations to be written in a body-fitted form. Applying the chain rule, the first-order derivatives of any quantity ϕ with respect to spatial derivatives can be expressed as:

$$\frac{\partial \phi}{\partial e_i} = \xi_{e_i}\frac{\partial \phi}{\partial \xi} + \eta_{e_i}\frac{\partial \phi}{\partial \eta} + \zeta_{e_i}\frac{\partial \phi}{\partial \zeta}, \tag{5.10}$$

where $\phi = u, v, w, p$ and $e_i = x, y, z$. The coefficients ξ_{e_i}, η_{e_i}, and ζ_{e_i} are the GCC transformation metrics, which can be evaluated in each control volume as follows:

$$\begin{aligned}
\xi_x &= \frac{y_\eta z_\zeta - y_\zeta z_\eta}{|J^{-1}|}, \quad \xi_y = \frac{x_\zeta z_\eta - x_\eta z_\zeta}{|J^{-1}|}, \quad \xi_z = \frac{x_\eta y_\zeta - x_\zeta y_\eta}{|J^{-1}|}, \\
\eta_x &= \frac{y_\zeta z_\xi - y_\xi z_\zeta}{|J^{-1}|}, \quad \eta_y = \frac{x_\xi z_\zeta - x_\zeta z_\xi}{|J^{-1}|}, \quad \eta_z = \frac{x_\zeta y_\xi - x_\xi y_\zeta}{|J^{-1}|}, \\
\zeta_x &= \frac{y_\xi z_\eta - y_\eta z_\xi}{|J^{-1}|}, \quad \zeta_y = \frac{x_\eta z_\xi - x_\xi z_\eta}{|J^{-1}|}, \quad \zeta_z = \frac{x_\xi y_\eta - x_\eta y_\xi}{|J^{-1}|},
\end{aligned} \tag{5.11}$$

where $\left|J^{-1}\right| = \det\left(J^{-1}\right) = x_\xi\left(y_\eta z_\zeta - y_\zeta z_\eta\right) - x_\eta\left(y_\xi z_\zeta - y_\zeta z_\xi\right) + x_\zeta\left(y_\xi z_\eta - y_\eta z_\xi\right)$ is the determinant of the inverse Jacobian.
This method focuses on the motion of the computational grid. To capture the movement of the grid, values $\dot{x} = dx/dt$, $\dot{y} = dy/dt$, and $\dot{z} = dz/dt$ are introduced to describe the grid velocities [68, 17]. When the GCC transformation is applied, the time derivative also changes:

$$\frac{\partial\phi}{\partial t} - \dot{x}\left(\xi_x\frac{\partial\phi}{\partial\xi} + \eta_x\frac{\partial\phi}{\partial\eta} + \zeta_x\frac{\partial\phi}{\partial\zeta}\right) - \dot{y}\left(\xi_y\frac{\partial\phi}{\partial\xi} + \eta_y\frac{\partial\phi}{\partial\eta} + \zeta_y\frac{\partial\phi}{\partial\zeta}\right) - \dot{z}\left(\xi_z\frac{\partial\phi}{\partial\xi} + \eta_z\frac{\partial\phi}{\partial\eta} + \zeta_z\frac{\partial\phi}{\partial\zeta}\right), \tag{5.12}$$

where ϕ is a scalar function as defined before.
For simplicity, throughout the remainder of this text, J^{-1} will denote $\left|J^{-1}\right|$. We also have the following continuity GCC equation:

$$\frac{\partial J^{-1}}{\partial t} + \frac{\partial U}{\partial\xi} + \frac{\partial V}{\partial\eta} + \frac{\partial W}{\partial\zeta} = 0. \tag{5.13}$$

The quantities U, V, and W introduced here are the transformed velocities, which describe the arbitrary motions of the domain on the basis of the Euler–Lagrange approach:

$$\begin{gathered}
U = c_1(u-\dot{x}) + c_2(v-\dot{y}) + c_3(w-\dot{z}), \quad V = c_4(u-\dot{x}) + c_5(v-\dot{y}) + c_6(w-\dot{z}), \\
W = c_7(u-\dot{x}) + c_8(v-\dot{y}) + c_9(w-\dot{z}),
\end{gathered} \tag{5.14}$$

where $\dot{x}, \dot{y}, \dot{z}$ are the arbitrary grid motion velocities and c_i are defined by:

$$\begin{aligned}
c_1 &= y_\eta z_\zeta - y_\zeta z_\eta, \quad c_2 = x_\zeta z_\eta - x_\eta z_\zeta, \quad c_3 = x_\eta y_\zeta - x_\zeta y_\eta, \\
c_4 &= y_\zeta z_\xi - y_\xi z_\zeta, \quad c_5 = x_\xi z_\zeta - x_\zeta z_\xi, \quad c_6 = x_\zeta y_\xi - x_\xi y_\zeta, \\
c_7 &= y_\xi z_\eta - y_\eta z_\xi, \quad c_8 = x_\eta z_\xi - x_\xi z_\eta, \quad c_9 = x_\xi y_\eta - x_\eta y_\xi.
\end{aligned} \tag{5.15}$$

In addition, we have the following equations:

x-momentum GCC equation:

$$\begin{aligned}\frac{\partial J^{-1}u}{\partial t}+\frac{\partial uU}{\partial \xi}+\frac{\partial uV}{\partial \eta}+\frac{\partial uW}{\partial \zeta}=&-\left(c_1\frac{\partial p}{\partial \xi}+c_4\frac{\partial p}{\partial \eta}+c_7\frac{\partial p}{\partial \zeta}\right)+\\ &\frac{1}{Re}\frac{\partial}{\partial \xi}\left(\frac{1}{J^{-1}}\left(q_1\frac{\partial u}{\partial \xi}+q_2\frac{\partial u}{\partial \eta}+q_3\frac{\partial u}{\partial \zeta}\right)\right)+\\ &\frac{1}{Re}\frac{\partial}{\partial \eta}\left(\frac{1}{J^{-1}}\left(q_2\frac{\partial u}{\partial \xi}+q_4\frac{\partial u}{\partial \eta}+q_5\frac{\partial u}{\partial \zeta}\right)\right)+\\ &\frac{1}{Re}\frac{\partial}{\partial \zeta}\left(\frac{1}{J^{-1}}\left(q_3\frac{\partial u}{\partial \xi}+q_5\frac{\partial u}{\partial \eta}+q_6\frac{\partial u}{\partial \zeta}\right)\right),\end{aligned} \tag{5.16}$$

y-momentum GCC equation:

$$\begin{aligned}\frac{\partial J^{-1}v}{\partial t}+\frac{\partial vU}{\partial \xi}+\frac{\partial vV}{\partial \eta}+\frac{\partial vW}{\partial \zeta}=&-\left(c_2\frac{\partial p}{\partial \xi}+c_5\frac{\partial p}{\partial \eta}+c_8\frac{\partial p}{\partial \zeta}\right)+\\ &\frac{1}{Re}\frac{\partial}{\partial \xi}\left(\frac{1}{J^{-1}}\left(q_1\frac{\partial v}{\partial \xi}+q_2\frac{\partial v}{\partial \eta}+q_3\frac{\partial v}{\partial \zeta}\right)\right)+\\ &\frac{1}{Re}\frac{\partial}{\partial \eta}\left(\frac{1}{J^{-1}}\left(q_2\frac{\partial v}{\partial \xi}+q_4\frac{\partial v}{\partial \eta}+q_5\frac{\partial v}{\partial \zeta}\right)\right)+\\ &\frac{1}{Re}\frac{\partial}{\partial \zeta}\left(\frac{1}{J^{-1}}\left(q_3\frac{\partial v}{\partial \xi}+q_5\frac{\partial v}{\partial \eta}+q_6\frac{\partial v}{\partial \zeta}\right)\right),\end{aligned} \tag{5.17}$$

z-momentum GCC equation:

$$\begin{aligned}\frac{\partial J^{-1}w}{\partial t}+\frac{\partial wU}{\partial \xi}+\frac{\partial wV}{\partial \eta}+\frac{\partial wW}{\partial \zeta}=&-\left(c_3\frac{\partial p}{\partial \xi}+c_6\frac{\partial p}{\partial \eta}+c_9\frac{\partial p}{\partial \zeta}\right)+\\ &\frac{1}{Re}\frac{\partial}{\partial \xi}\left(\frac{1}{J^{-1}}\left(q_1\frac{\partial w}{\partial \xi}+q_2\frac{\partial w}{\partial \eta}+q_3\frac{\partial w}{\partial \zeta}\right)\right)+\\ &\frac{1}{Re}\frac{\partial}{\partial \eta}\left(\frac{1}{J^{-1}}\left(q_2\frac{\partial w}{\partial \xi}+q_4\frac{\partial w}{\partial \eta}+q_5\frac{\partial w}{\partial \zeta}\right)\right)+\\ &\frac{1}{Re}\frac{\partial}{\partial \zeta}\left(\frac{1}{J^{-1}}\left(q_3\frac{\partial w}{\partial \xi}+q_5\frac{\partial w}{\partial \eta}+q_6\frac{\partial w}{\partial \zeta}\right)\right),\end{aligned} \tag{5.18}$$

where q_i are defined as

$$\begin{aligned}q_1=c_1^2+c_2^2+c_3^2,\quad q_2=c_1c_4+c_2c_5+c_3c_6,\quad q_3=c_1c_7+c_2c_8+c_3c_9,\\ q_4=c_4^2+c_5^2+c_6^2,\quad q_5=c_4c_7+c_5c_8+c_6c_9,\quad q_6=c_7^2+c_8^2+c_9^2.\end{aligned} \tag{5.19}$$

5.2.2 Boundary and Initial Conditions

Studying blood flow in an aneurysmal geometry, as formulated by the system of equations described in the previous section, requires appropriate boundary and initial

conditions. These conditions ensure that the numerical solution is well-posed and that the simulations reproduce accurately the behaviour of blood flow within the aneurysmatic domain. At the inlet, a time-dependent velocity profile is imposed to describe the pulsatile nature of blood flow throughout the cardiac cycle. Along the vessel walls, kinematic boundary conditions are applied to capture the motion of the arterial wall due to the pulsatility. The displacement of the wall is described through the velocity components $\dot{x}$, $\dot{y}$, $\dot{z}$. At each time step, the computational grid is updated to follow this motion, ensuring that the deformation is accurately captured.

At the outlet, the velocity field is fully developed, corresponding to a parabolic flow profile, and the pressure is known. Symmetry boundary conditions are applied along the central axis of the domain, exploiting the symmetry of the geometry of fusiform aneurysms, as in Figure 5.1, to reduce computational cost while preserving physical accuracy. The full set of boundary conditions is summarised below:

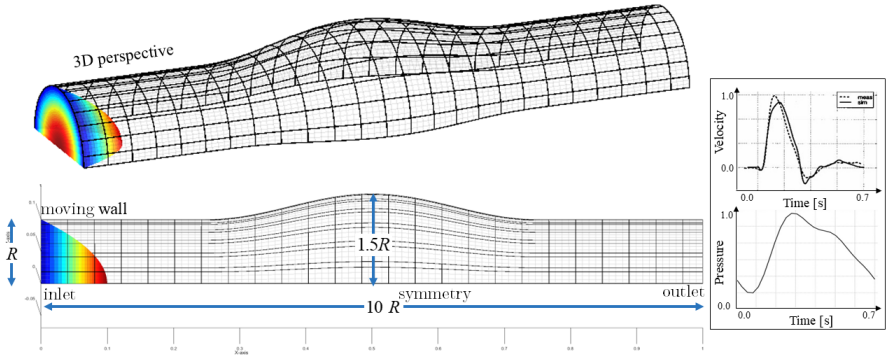

Figure 5.1. The 3D geometry with boundary conditions applied.

- at the inlet, for $t \geq 0$: $u(y,z,t) = \left[1 - \left(\frac{y}{R}\right)^2 - \left(\frac{z}{R}\right)^2\right] \times$ velocity waveform(t),
  $v = 0,\ w = 0,\ -R \leqslant y \leqslant R,\ -R \leqslant z \leqslant R,$
- at the moving wall: $u = \dot{x},\ v = \dot{y},\ w = \dot{z}$ (kinematic boundary condition),
- at the symmetry : $\dfrac{\partial u}{\partial y} = 0,\ \ v = w = 0,$ for $t \geq 0,$
- at the outlet : $p =$ pressure waveform(t), $\dfrac{\partial u}{\partial x} = 0,\ \ \dfrac{\partial v}{\partial x} = 0,\ \ \dfrac{\partial w}{\partial x} = 0$
  (fully developed flow assumption).

where $\dot{x} = \partial x/\partial t, \dot{y} = \partial y/\partial t, \dot{z} = \partial z/\partial t$.

The waveforms describing inlet velocity, outlet pressure, and wall movement were obtained from the literature [145] and fitted using a Fourier series [119]. Experimental and imaging studies, including intravascular ultrasonography, magnetic resonance angiography, and computed tomographic angiography have been used to quantify the pulsatile motion of the aortic wall [10, 193]. The present model treats the wall as a moving boundary, whose movement is described by a time dependent waveform extracted from the literature [145]. The aortic motions specified in this study correspond to low pulsatility (0.73% change in the initial radius) and high pulsatility (4.9% change in the initial radius) of the aortic wall.

5.2.3 Geometric Conservation Law

Artificial sources of mass and momentum may be formed during flow calculations, owing to inconsistent numerical implementation of the PDEs describing the problem under consideration. Studies have shown that correlating the temporal rate of change of the Jacobian (J) with the Cartesian velocity components of the computational grid ($\dot{x}$, $\dot{y}$, $\dot{z}$) to update the Jacobian at the implicit time level can help to eliminate such phenomena [174, 186]. The geometric conservation law ensures that a numerical solution remains accurate when grids are moved or deformed; that is, variations in the volume of the physical domain coincide with the required grid velocities. For this purpose, we introduce the following equation:

$$\frac{\partial J^{-1}}{\partial t} + \frac{\partial}{\partial \xi}\left(\dot{x}\frac{\partial(y,z)}{\partial(\eta,\zeta)} - \dot{y}\frac{\partial(x,z)}{\partial(\eta,\zeta)} + \dot{z}\frac{\partial(x,y)}{\partial(\eta,\zeta)}\right) + \frac{\partial}{\partial \eta}\left(\dot{y}\frac{\partial(x,z)}{\partial(\xi,\zeta)} - \dot{x}\frac{\partial(y,z)}{\partial(\xi,\zeta)} + \dot{z}\frac{\partial(x,y)}{\partial(\xi,\zeta)}\right) + \frac{\partial}{\partial \zeta}\left(\dot{z}\frac{\partial(x,y)}{\partial(\xi,\eta)} - \dot{x}\frac{\partial(y,z)}{\partial(\xi,\eta)} + \dot{y}\frac{\partial(x,z)}{\partial(\xi,\eta)}\right) = 0, \tag{5.20}$$

where $\dfrac{\partial(y,z)}{\partial(\eta,\zeta)}$ is the determinant of the corresponding submatrix of J^{-1}. The FVM is used to integrate equation (5.20), applying a first-order fully implicit time integration scheme over the control volume. High-order geometric conservation law approaches such as this were introduced by Mavriplis [129, 130]. The discretized finite volume form is shown below:

$$\frac{J^{-1}-J_0^{-1}}{\Delta t}+\left(\dot{x}\frac{\partial(y,z)}{\partial(\eta,\zeta)}-\dot{y}\frac{\partial(x,z)}{\partial(\eta,\zeta)}+\dot{z}\frac{\partial(x,y)}{\partial(\eta,\zeta)}\right)_e-\left(\dot{x}\frac{\partial(y,z)}{\partial(\eta,\zeta)}-\dot{y}\frac{\partial(x,z)}{\partial(\eta,\zeta)}+\dot{z}\frac{\partial(x,y)}{\partial(\eta,\zeta)}\right)_w$$
$$+\left(\dot{y}\frac{\partial(x,z)}{\partial(\xi,\zeta)}-\dot{x}\frac{\partial(y,z)}{\partial(\xi,\zeta)}+\dot{z}\frac{\partial(x,y)}{\partial(\xi,\zeta)}\right)_n-\left(\dot{y}\frac{\partial(x,z)}{\partial(\xi,\zeta)}-\dot{x}\frac{\partial(y,z)}{\partial(\xi,\zeta)}+\dot{z}\frac{\partial(x,y)}{\partial(\xi,\zeta)}\right)_s$$
$$+\left(\dot{z}\frac{\partial(x,y)}{\partial(\xi,\eta)}-\dot{x}\frac{\partial(y,z)}{\partial(\xi,\eta)}+\dot{y}\frac{\partial(x,z)}{\partial(\xi,\eta)}\right)_t-\left(\dot{z}\frac{\partial(x,y)}{\partial(\xi,\eta)}-\dot{x}\frac{\partial(y,z)}{\partial(\xi,\eta)}+\dot{y}\frac{\partial(x,z)}{\partial(\xi,\eta)}\right)_b=0. \tag{5.21}$$

5.3 Numerical Solutions

A mixed Euler–Lagrange numerical framework was developed to numerically solve the PDE system subject to the prescribed initial and boundary conditions. The spatial discretization was performed using the FVM on a collocated grid arrangement, while temporal discretization employed the implicit backward Euler scheme. The algorithm was implemented in MATLAB R22a (MathWorks, Natick, MA). To reduce the computational complexity the governing equations were expressed in dimensionless form. Furthermore, parallel programming techniques were applied, to accelerate the computational process. In particular, utilizing 12 CPU cores resulted in an approximately 72% reduction in total computational time [108]. This makes the parallel technique essential for a numerical solution in a reasonable time, especially when larger grid sizes are examined.

5.3.1 Finite Volume Discretization Method

In this study, a collocated arrangement of the grid was adopted, such that only one set of control volumes was required. In this grid, all the variables are stored at the centre of each cell volume, and velocities are interpolated on the n, s, w, e, t, and b surfaces of the control volume [67, 153], as depicted in Figure 5.2.

The suggested method introduces an implicit scheme that is unconditionally stable, resulting in first-order accuracy for time derivatives and second-order accuracy for spatial derivatives [67, 70]. The finite volume discretized form of the continuity and the momentum equations is as follows.

Finite volume discretized continuity equation:

$$\frac{J^{-1}-J_0^{-1}}{\Delta t}+U_e-U_w+V_n-V_s+W_t-W_b=0, \tag{5.22}$$

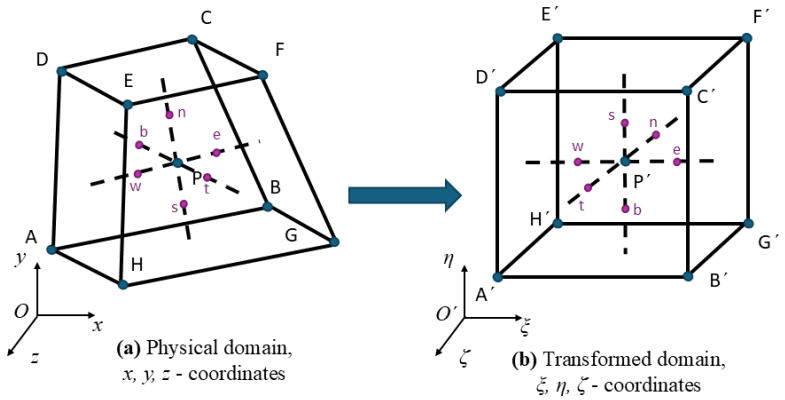

Figure 5.2. Schematics of grid transformation from the physical to the transformed domain.

Finite volume discretized ξ-momentum equation:

$$\begin{aligned}
&\frac{J^{-1}u - J_0^{-1}u_0}{\Delta t} + \\
&+\left[Uu + c_1 p - \frac{1}{J^{-1}}\frac{1}{Re}\left(q_1\frac{\partial u}{\partial \xi} + q_2\frac{\partial u}{\partial \eta} + q_3\frac{\partial u}{\partial \zeta}\right)\right]_e - \left[Uu + c_1 p - \frac{1}{J^{-1}}\frac{1}{Re}\left(q_1\frac{\partial u}{\partial \xi} + q_2\frac{\partial u}{\partial \eta} + q_3\frac{\partial u}{\partial \zeta}\right)\right]_w \\
&+\left[Vu + c_4 p - \frac{1}{J^{-1}}\frac{1}{Re}\left(q_2\frac{\partial u}{\partial \xi} + q_4\frac{\partial u}{\partial \eta} + q_5\frac{\partial u}{\partial \zeta}\right)\right]_n - \left[Vu + c_4 p - \frac{1}{J^{-1}}\frac{1}{Re}\left(q_2\frac{\partial u}{\partial \xi} + q_4\frac{\partial u}{\partial \eta} + q_5\frac{\partial u}{\partial \zeta}\right)\right]_s \\
&+\left[Wu + c_7 p - \frac{1}{J^{-1}}\frac{1}{Re}\left(q_3\frac{\partial u}{\partial \xi} + q_5\frac{\partial u}{\partial \eta} + q_6\frac{\partial u}{\partial \zeta}\right)\right]_t - \left[Wu + c_7 p - \frac{1}{J^{-1}}\frac{1}{Re}\left(q_3\frac{\partial u}{\partial \xi} + q_5\frac{\partial u}{\partial \eta} + q_6\frac{\partial u}{\partial \zeta}\right)\right]_b = 0,
\end{aligned} \tag{5.23}$$

where subscripts e, w, n, s, t, and b refer to the surfaces of each finite volume (Figure 5.2). To estimate the mesh velocity vector $(\dot{x}, \dot{y}, \dot{z})$, the following first-order scheme is used: $\dot{x} = \dfrac{x - x_0}{\Delta t}$, $\dot{y} = \dfrac{y - y_0}{\Delta t}$, $\dot{z} = \dfrac{z - z_0}{\Delta t}$, where x_0, y_0, z_0 are the previous, x, y, z the current time step grid positions, and Δt is the time step [174]. The finite volume forms for the other two momentum equations can be obtained in a similar way.

5.3.2 Grid independence and Courant–Friedrichs–Lewy (CFL) Criterion

This study used a collocated grid, where all the variables are stored in the centre of the volume. This approach is memory-efficient for simulation processes. However, it is essential to investigate the effects of using a finer partition, as increasing the grid density enhances the model's capability to handle discontinuities and discontinuous problematic areas, yielding more accurate results.

To ensure grid-size independent results, a mesh convergence analysis was conducted. The convergence between successive grid configurations was then evaluated over the entire cardiac cycle using the Root Mean Square (RMS) difference of these interpolated velocity magnitudes.

$$RMS = \sqrt{\frac{\sum_{i=1}^{n} (\tilde{q}_i - q_i)^2}{n}} \tag{5.24}$$

where the velocity magnitudes at the same location in the dilation area are represented by $\tilde{q}_i$ and q_i, and n is the total number of elements of the computational grid in the same region.

As expected, increasing the grid size resulted in a reduction in the RMS error, as shown in **Tables 5.1** and **5.2**. In addition, the value of the CFL parameter increased with grid refinement and decreased with smaller time steps (Δt), as depicted in **Tables 5.1** and **5.2**. All tested grid configurations yielded numerically stable and convergent results.

All simulations were performed with a grid size of $40 \times 20 \times 20 = 16\ 000$ finite volume elements. Figure 5.3 shows a computational mesh configuration in the aneurysmal structure from the 2D and 3D perspectives.

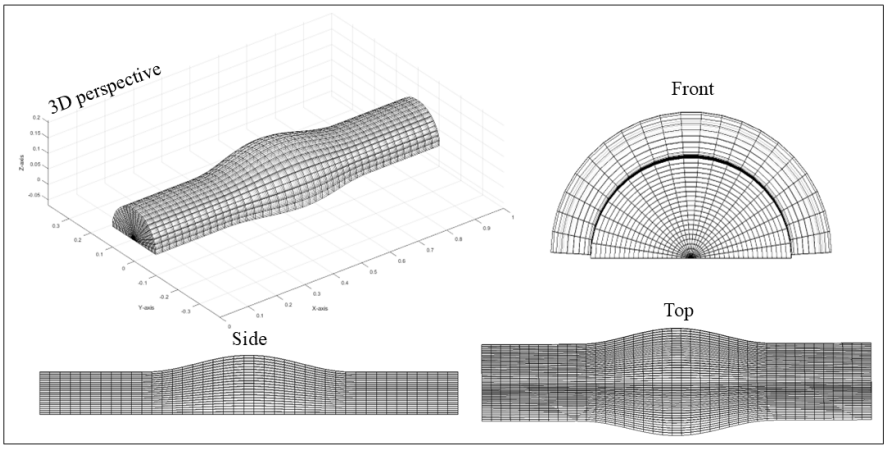

Figure 5.3. The 3D computational grid from various perspectives.

Four cardiac cycles were simulated using a Dell PowerEdge R440 workstation with two Intel Xeon Silver 2 physical processors (4210R, 2.40 GHz, 13.75 MB, 20 cores, 32 GB RAM). When employing numerical methods, it is necessary to ensure that the

solution obtained converges to the solution of the PDE. Intense non-linearities often limit stability in the Euler–Lagrange and Navier–Stokes equations. Thus, the CFL criterion can be used to interpret the ratio of the velocity and local spatial discretization in each direction [54] as follows:

$$CFL = \Delta t \left(\sum_{i=1}^{n} \frac{u_i}{\Delta x_i} \right). \tag{5.25}$$

This CFL condition is applicable to both hyperbolic and parabolic PDEs, including those used in the present study. Tables 5.1, 5.2 show the CFL number for four computational mesh configurations and various time steps and wall pulsatile motions (no wall pulsatility, low wall pulsatility, and high wall pulsatility) at peak systole of the cardiac cycle. The implicit numerical scheme developed here provided convergent and stable numerical solutions for all studied cases. In addition to the CFL and Reynolds numbers, the Womersley number (Wo) is also reported in Tables 5.1, 5.2. It is a dimensionless quantity indicating the unsteady flow frequency in relation to the viscous effect, defined as,

$$Wo = R\sqrt{\frac{\omega}{\nu}}, \tag{5.26}$$

where R is the radius, ν is the kinematic viscosity, and ω is the angular frequency of the pulsations.

Δt	Grid size	*Re*	*Wo*	CFL	RMS	Stability
0.0250	$20 \times 10 \times 10$	199.34	2.60	1.68	0.0046	Yes
0.0125	$20 \times 10 \times 10$	199.34	2.60	1.03	0.0054	Yes
0.0250	$30 \times 15 \times 15$	198.43	2.79	2.91	0.0025	Yes
0.0125	$30 \times 15 \times 15$	198.43	2.79	1.72	0.0027	Yes
0.0250	$40 \times 20 \times 20$	206.11	2.87	3.31	0.0017	Yes
0.0125	$40 \times 20 \times 20$	206.11	2.87	1.97	0.0020	Yes
0.0250	$50 \times 25 \times 25$	202.50	2.93	4.44	–	Yes
0.0125	$50 \times 25 \times 25$	202.50	2.93	2.78	–	Yes

Table 5.1. Grid independence data for the haemodynamic case for various time steps and grid sizes.

Low Pulsatility

Δt	Grid size	*Re*	*Wo*	CFL	RMS	Stability
0.0250	$20 \times 10 \times 10$	199.36	2.60	1.56	0.0048	Yes
0.0125	$20 \times 10 \times 10$	199.63	2.60	0.96	0.0083	Yes
0.0250	$30 \times 15 \times 15$	198.23	2.80	2.77	0.0026	Yes
0.0125	$30 \times 15 \times 15$	198.23	2.79	1.61	0.0042	Yes
0.0250	$40 \times 20 \times 20$	205.91	2.88	4.06	0.0017	Yes
0.0125	$40 \times 20 \times 20$	205.91	2.87	1.78	0.0033	Yes
0.0250	$50 \times 25 \times 25$	202.07	2.94	4.01	–	Yes
0.0125	$50 \times 25 \times 25$	202.07	2.94	2.20	–	Yes

High Pulsatility

Δt	Grid size	*Re*	*Wo*	CFL	RMS	Stability
0.0250	$20 \times 10 \times 10$	200.23	2.63	1.36	0.0097	Yes
0.0125	$20 \times 10 \times 10$	200.23	2.62	0.68	0.0129	Yes
0.0250	$30 \times 15 \times 15$	195.97	2.83	2.23	0.0060	Yes
0.0125	$30 \times 15 \times 15$	195.97	2.81	1.20	0.0082	Yes
0.0250	$40 \times 20 \times 20$	203.61	2.91	2.49	0.0040	Yes
0.0125	$40 \times 20 \times 20$	203.61	2.89	1.33	0.0056	Yes
0.0250	$50 \times 25 \times 25$	198.47	2.97	3.79	–	Yes
0.0125	$50 \times 25 \times 25$	198.47	2.95	2.01	–	Yes

Table 5.2. Grid independence data for the Low and High pulsatility cases.

The following Figure 5.4 summarizes the results presented in the Tables 5.1, 5.2 above,

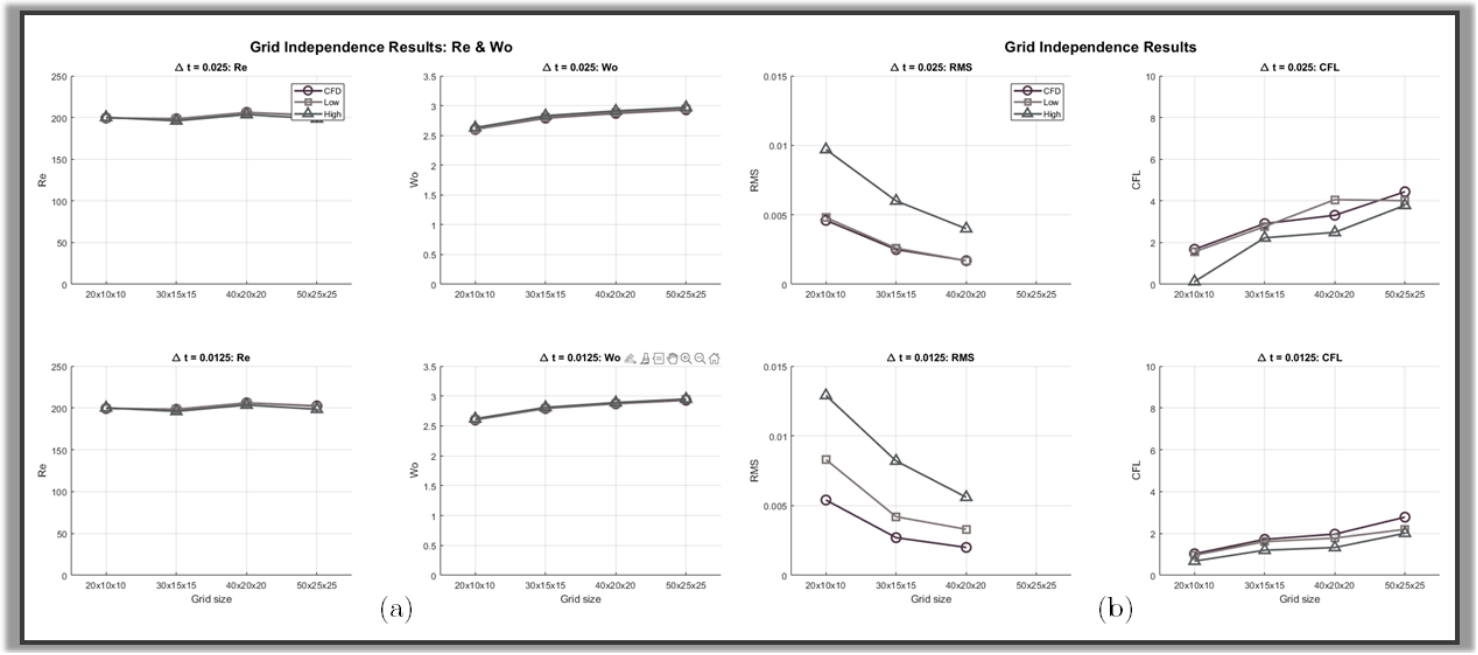

Figure 5.4. Reynolds, Womersley, RMS and CFL grid independence results.

5.3.3 Direct Solution Approach

Various fluid dynamics problems require the solution of a coupled system of PDEs in which the variables of each equation are present in the other equations. In the simultaneous solution approach, all equations are considered to be part of a single large-scale algebraic system, with the discretized equations forming a block structure [67]. Owing to the non-linearity of the system, a non-linear solver is required. A classical approach is to use Newton-like methods; this is the approach we followed in the present study. Other numerical methods have been developed to address similar problems in CFD. For instance, an iterative method based on the SIMPLE algorithm was implemented by Shyy et al. [150, 174]. This approach evaluates unknown variables such as velocity and pressure on the surfaces of the control volume, using an iterative scheme to update the unknown values [31, 174]. Although the SIMPLE algorithm has been implemented in various CFD software programs, the alternation of the governing equations can result in loss of accuracy. However, should convergence be achieved, a very robust numerical solution is obtained without the need to use new equations to correct the unknown variables.

Newton's Method and the Sparse Jacobian Matrix

According to this approach, a direct numerical procedure is implemented. The FVM results in a large non-linear system of algebraic equations, which is easier to solve compared with a non-linear system of PDEs. The numerical solution of the algebraic equation system is obtained using a Newton-like method as follows [28]:

$$\bar{x}^{n+1} = \bar{x}^{n} - \bar{J}^{-1}\left(\bar{x}^{n}\right)\bar{f}\left(\bar{x}^{n}\right), \tag{5.27}$$

where n and $n+1$ indicate the current and next iterations. The solution vector in the current iteration is denoted by $\bar{x}^{n}$, the Jacobian matrix $J\left(\bar{x}^{n}\right)$ is evaluated at $\bar{x}^{n}$, and $\bar{f}\left(\bar{x}^{n}\right)$ are the discretized equations evaluated at $\bar{x}^{n}$. The iteration process ends when the solution vector at the next iteration is close enough to the solution vector at the previous iteration (as determined by the size of ε, a small parameter).

The size of the Jacobian matrix is related to the size of the computational grid under consideration, with a grid of $m \times\ n \times\ k$ resulting in a matrix with $16m^2n^2k^2$ elements for the 3D Navier–Stokes equations. This is due to the total number of equations created by the discretized system, which is, $4 \times m \times n \times k$. Number 4 represents the system of the 3D Navier-Stokes equations along with the Continuity equation. Thus, in large-scale systems, the use of the Jacobian matrix can become challenging owing to memory limitations. However, it has been observed that a large number of elements in the matrix are equal to zero, indicating sparsity. Therefore, the system can be numerically solved by calculating only the non-zero elements. Such

implementations can save substantial amounts of computational resources (both time and space), and improvements in this regard are ongoing [8].

Trust-region Method

Although Newton's method is theoretically easy to implement and straightforward, in practice, its functionality can be limited by local minima or a bad initial guess. To overcome these limitations, Newton's method is often used in combination with trust-region techniques in minimization problems [217]. The goal of such numerical procedures is to find a vector (solution) in which $\bar{f}(\bar{x})$ is as close to zero as possible, or $\bar{f}(\bar{x}) = 0$.

The trust-region method generates a step $\bar{p}$ in which a model function $\bar{m}(\bar{p})$ approximates function $\bar{f}(\bar{x}_k)$, with a trust region defined around the point $\bar{x}_k$. Usually, the model function is quadratic and is generated by expansion of the Taylor series of $\bar{f}$ around point $\bar{x}_k$:

$$\bar{f}(\bar{x}_k + \bar{p}) = \bar{f}(\bar{x}_k) + \bar{\nabla}^T \bar{f}(\bar{x}_k)\,\bar{p} + \frac{1}{2}\bar{p}^T \bar{\nabla}^2 \bar{f}(x_k + tp)\,\bar{p}, \tag{5.28}$$

where $t \in (0, 1)$. In practical applications, an approximation B_k is used instead of the Hessian matrix, which gives the model function, $\bar{m}$. The model function can be written as [138, 144]:

$$\bar{m}_k(\bar{p}) = \bar{f}(\bar{x}_k) + \bar{\nabla}^T \bar{f}(\bar{x}_k)\,\bar{p} + \frac{1}{2}\bar{p}^T B_k \bar{p}. \tag{5.29}$$

The deviation between the model and the objective function is of the order of $\mathcal{O}\left(||\bar{p}||^2\right)$; this has a small value when $\bar{p}$ is relatively small. The step $\bar{p}$ is given by the solution of the following sub-problem:

$$\min_{\bar{p}} m_k(\bar{p}) = \bar{f}(\bar{x}_k) + \bar{\nabla}^T \bar{f}(\bar{x}_k)\,\bar{p} + \frac{1}{2}\bar{p}^T \bar{\nabla}^2 \bar{f}(\bar{x}_k + t\bar{p})\,\bar{p}, \quad \text{so that } ||\bar{p}|| \leq \Delta_k, \tag{5.30}$$

where Δ_k is the trust-region radius at the k-th iteration [214].

A major challenge associated with the trust-region method involves the strategy for choosing a proper radius Δ_k at each iteration. For this purpose, the following ratio is defined [81]:

$$\rho_k = \frac{\bar{f}(\bar{x}_k) - \bar{f}(\bar{x}_k + \bar{p}_k)}{\bar{m}_k(\bar{0}) - \bar{m}_k(\bar{p}_k)}, \tag{5.31}$$

where $\bar{p}_k$ is a given step. In this expression, the numerator is the actual reduction, whereas the denominator is the predicted one. Note that in equation (5.31), $\bar{m}_k(\bar{0})$ is equal to the original function $\bar{f}(\bar{x}_k)$. On the basis of the ratio described in this equation, an algorithm can be constructed as described in [144]. In this study, the

radius Δ_k is a critical factor to be reduced or enlarged as needed so that model function is closely related to the objective function.

5.4 Results and Discussion

We used a 3D Euler–Lagrange mathematical approach to describe a viscous fluid flow coupled with a pulsating arterial wall tissue, focusing primarily on the flow and pressure fields of the fluid. Our approach also takes into consideration the development of recirculation zones , as well as the time-averaged wall shear stress (TAWSS) induced by the fluid on the moving wall during the cardiac cycle. Each cardiac cycle is divided into the following three flow phases.

- *Systolic acceleration*: the initial phase of the cardiac cycle when blood is ejected from the inlet of the vessel.
- *Systolic deceleration*, which occurs as the flow slows after reaching peak velocity. In this phase, the development of vortices is visible at the centre of the aneurysm as the velocity decreases.
- *Diastole*: the last phase of the cycle, in which the blood flow stabilizes. The recirculation zones developed in the previous phase can now shrink in size and lose momentum.

We conducted simulations of four cardiac cycles to obtain a solution independent of the initial dynamics. Blood was considered to be a Newtonian fluid with laminar flow [174]. Two different levels of pulsatilities were studied, low and high. To visualize the results of the velocity and pressure fields, we used a 2D cross-sectional plane to provide a clear representation of flow patterns within the aneurysm. However, for parameters associated with the vessel wall, such as TAWSS and the oscillatory shear index (OSI), we used a 3D view to better capture the variations along the arterial surface.

At the peak of the systolic phase, pressure tended to have higher values near the wall, whereas recirculation zones were observed to develop in the centre of the aneurysm during the diastolic phase, consistent with the findings of previous studies [209].

Biomedical Factors

Wall shear stress (WSS) refers to the force per unit area exerted by the vessel wall on the blood flow [96]. WSS caused by pulsatile flow has been shown to have a

significant impact on the development of atherosclerosis. WSS can be expressed as follows in tensor notation:

$$\tau_{wall} = \mu \left[\nabla \bar{q} + (\nabla \bar{q})^T\right] \cdot \bar{n}, \tag{5.32}$$

where μ is the blood viscosity, $\vec{q}$ is the velocity vector, and $\bar{n}$ is the unit normal vector to the wall. Abnormally low or high WSS could potentially lead to a variety of cardiovascular problems such as thrombus formation. However, high WSS could also cause problems, especially if there are shifts from high to low values of WSS [209, 149] .

TAWSS is the mean value of the WSS over one cardiac cycle and is given by the following formula:

$$TAWSS(s) = \frac{1}{T}\int_0^T |WSS(s,t)|dt. \tag{5.33}$$

OSI quantifies areas of the vessel wall exposed to oscillating WSS throughout the cardiac cycle. Low OSI values reveal minimal flow disruption, whereas higher values identify areas in which instantaneous WSS deviates from the main flow direction for a substantial part of the cardiac cycle. Studies suggest that areas of elevated OSI are prone to atherogenic particle infiltration, and OSI levels above 0.3 are considered to be atherogenic [127, 180]. The formula is as follows:

$$\text{OSI}(s) = 0.5\left[1 - \frac{\frac{1}{T}\left|\int_0^T WSS(s,t)dt\right|}{\frac{1}{T}\int_0^T |WSS(s,t)|dt}\right], \tag{5.34}$$

where t is the time step, T is the time period of the cardiac cycle, and s is the surface of the geometry.

5.4.1 CFD–FSI Comparison

This study is an extension, from 2D to 3D, of our previous work [204]. The new methodology has additional complexity due to the 3D nature of the modelling approach. The algorithms and numerical techniques developed were extended to capture these additional 3D dynamics. Thus, the study brings new scientific insight into aneurysmal geometry, particularly with the formation of complex recirculation zones and secondary flow. Furthermore, the introduction of significant haemodynamic indices provides additional information about the condition of the aneurysmatic structure strengthening this study. Although the computational cost is more demanding, the current results are more realistic, offering detailed information on the pathology.

In the following section, we present results obtained for the CFD and FSI cases. In both cases, the same boundary conditions were applied for the simulations; however, in the FSI case, the movement of the arterial wall was considered. Although the volume flow rate was the same for the two cases, the velocity distribution during the cardiac cycle varied drastically. In the CFD case, there was a strong increase in the velocity of the flow in the acceleration phase during systole, followed by deceleration, whereas in the diastolic phase, the velocity remained relatively low, Figure 5.5 (a). In the FSI case, owing to wall movement, the flow during systole showed a significantly smoother profile compared with that observed in the CFD case, Figure 5.5 (a), and in diastole, the velocity field values were slightly higher than those in the hydrodynamic case, indicating additional flow to the downstream vasculature. This mechanism of retaining blood during systole and providing fluid flow during diastole, when velocities would otherwise be reduced, has been observed in the human arterial system. In addition, recirculation zones were more prominent in the FSI case, owing to the pulsatile movements of the arterial wall due to the kinematic boundary conditions. For the same reasons, the TAWSS values also increased in the FSI case.

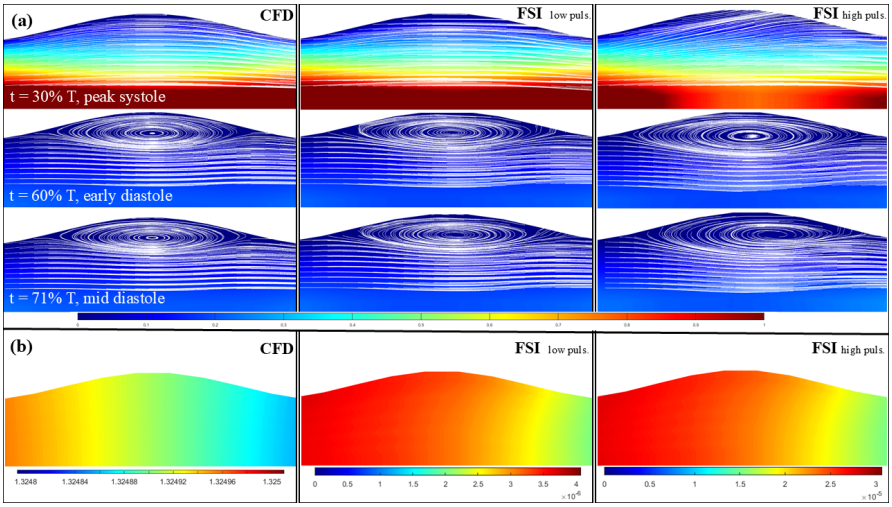

Figure 5.5. (a) Comparison of CFD FSI configurations for the velocity field during the cardiac cycle. (b) Pressure field for the CFD case (left) and pressure differences between the FSI and CFD cases for the two pulsatilities under consideration.

Pressure is a significant factor in the cardiovascular system, and it has an important role in pathophysiological conditions such as AAA. Although the pressure in the FSI case decreased at the peak of systole, it remained at the same level during the

whole systolic phase, as shown in Figure 5.5 (b). Regarding the pressure field, there was a slight reduction during the cardiac cycle in the FSI case compared with the hydrodynamic case, as expected for FSI vessel geometries. Figure 5.5 (b) depicts the pressure field for the CFD case and the absolute pressure difference for the two pulsating cases, showing a small decrease in systolic pressure in the FSI cases compared with the CFD one. These results demonstrate the positive effects of the pulsating arterial wall on flow dynamics, which enable it to compensate for hydrodynamic stresses in the cardiovascular system.

In addition, there were differences in TAWSS and OSI values between cases with and without pulsatility. Specifically, TAWSS increased in the main region of the aneurysm as pulsatility was introduced and further increased with increasing pulsatility see Figure 5.6. Conversely, OSI was reduced near the aneurysm shoulder, indicating reduced flow disruption as pulsatility increased. As previously mentioned, lower OSI values suggest diminished vortex formation, meaning that high pulsatility contributes to stabilization of the flow dynamics. This suggests that increased pulsatility could have beneficial effects in certain cases; these could potentially be realized through specific exercise conditions.

Taken together, these results indicate that FSI simulations offer more accurate representations of flow patterns and WSS compared with the hydrodynamic case [157].

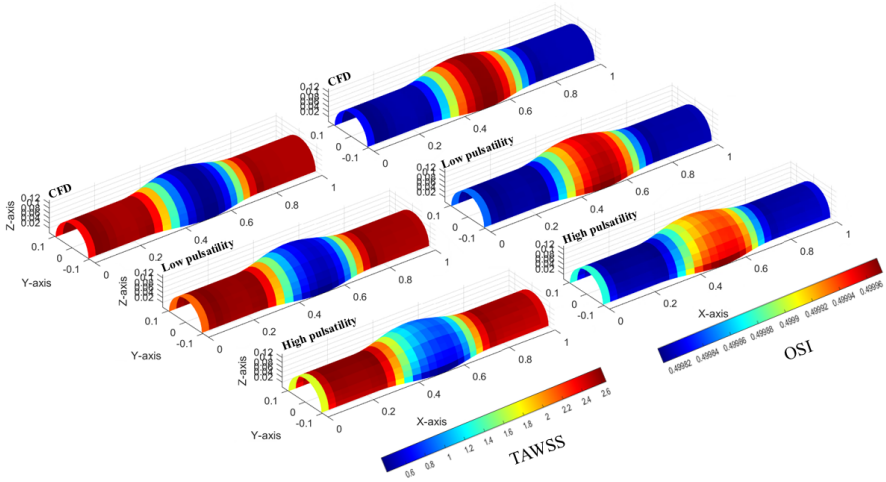

Figure 5.6. Biomedical factors (TAWSS and OSI) for the CFD case and the two pulsatilities under consideration (FSI cases).

5.4.2 Validation

Qualitative comparisons

The study of haemodynamics in aneurysmatic geometries is essential for understanding the conditions that lead to cardiovascular diseases. In both fusiform and saccular cases of aneurysms, blood flow leads to formation of recirculation zones. Studies of the motion of a non-Newtonian fluid consisting of particles have identified similar patterns of flow in aneurysmatic areas [50, 139]. Regions of reduced flow are important, as they may cause alterations in blood flow, leading to other problems such as thrombus creation. Biasetti et al. studied fusiform and saccular AAAs and found that vortices were formed specifically in regions of strong curvature [21]. This implies that geometric properties affect the blood flow through a vessel.

A qualitative comparison of the results of the present study with those of Biasetti [21] showed that our 3D mathematical model predicted all phases of the cardiac cycle very well. During the acceleration of the systolic phase, there was only forward flow; this was then disturbed owing to the deceleration of the flow. At diastole, Biasetti observed several recirculation zones. Similarly, in our study, recirculation started during the deceleration phase and was maintained at diastole, vanishing only when flow acceleration began again in early systole.

Owing to the pulsatile nature of blood flow, the haemodynamic environment within an aneurysm changes during the cardiac cycle, particularly during the systolic deceleration phase, when the flow rate is less strong and the formation of recirculation zones is observed in the pathophysiological case. These vortices remain present for most of the cardiac cycle and maintain their strength [11, 13].

Quantitative comparisons

The numerical results presented in this study were obtained by means of a GCC-based algorithm together with the FVM. Although the results compare qualitatively very well with those of previous studies, further validation is required. The geometry studied here has also been imported to a previously developed CFD software program Fluent 16.1 (Ansys Inc., Canonsburg, PA), with similar fluid properties as well as appropriate initial and boundary conditions. Figure 5.7 (a) shows the numerical results of the custom code used in the present study whereas Figure 5.7 (b) displays the numerical findings obtained using Fluent 16.1. The contours (colour maps) depict the fluid velocity magnitude in both cases, while the streamlines (white colored lines) indicate the vortices created due to the aneurysm. Additionally, the cross-sectional plane assists with the visualization and the figures are focused on the aneurysm area. The results presented correspond to the case of rigid (not moving) walls. The three figures in each case of (a) and (b) represent the fluid flow in specific time steps of the

cardiac cycle and the same behaviour is observed in both cases, validating the results. Specifically, during acceleration in systole, there was a forward flow without any disturbance (see the top two rows of images in Figure 5.7). As the flow decelerated and transitioned to diastole, formation of recirculation zones could be observed in both cases (see the lower two rows of images in Figure 5.7).

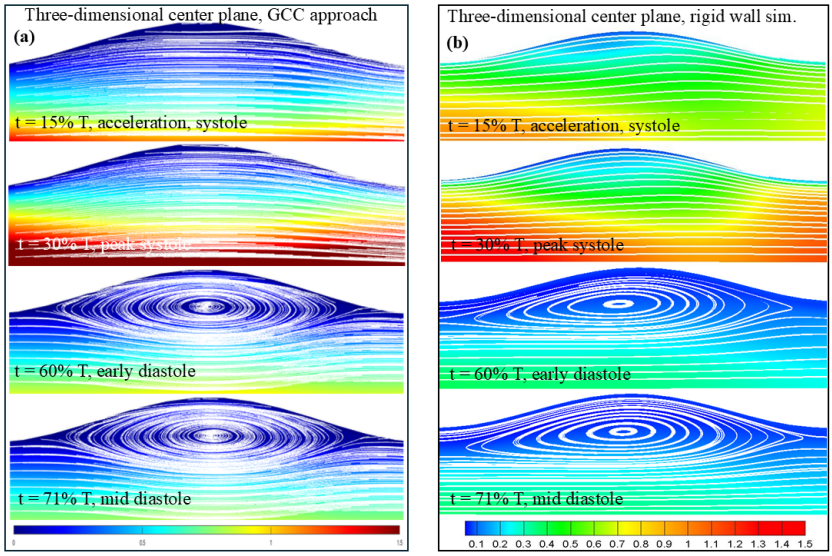

Figure 5.7. (a) Contours of the velocity magnitude and pathlines at different time points of the cardiac cycle, obtained using the 3D CFD model developed in this study. (b) Contours of the velocity magnitude and pathlines obtained using an advanced numerical program. Both parts (a and b) illustrate the cross-sectional plane through the centre (maximum $Re \approx 500$).

5.5 Limitations and Future Work

In this study, we assumed that blood would show Newtonian fluid behaviour. Although this assumption is valid for large arteries, it may not be so for smaller ones. However, as the present study focused on larger arteries, this approach was considered to be appropriate. The grid independence study confirmed the reliability of the numerical solution. Nonetheless, we aim to extend the simulations to finer grids to capture more detailed flow characteristics. Previous studies have shown that vortices can be reduced in the presence of a magnetic field [108, 42]. In future work, we will

develop a 3D model incorporating magnetic field effects.

In addition, future work will aim to examine the behaviour of nanoparticles in terms of their contribution to haemodynamics. These simulations will be conducted using high performance computing, taking advantage of graphics card cores with CUDA programming.

5.6 Conclusions

In this study, we developed a dynamic 3D mathematical model to evaluate blood flow in an aneurysmatic (pathological) structure throughout the cardiac cycle using an Euler–Lagrange mathematical approach to fluid flow equations. The fluid transport PDEs (equations of mass and momentum) were transformed into a body-fitted moving reference frame using the GCC methodology, and the system of PDEs was discretized using the FVM on structured and collocated grids. We simultaneously developed an approach for solution of the strongly coupled and non-linear system of PDEs. The mathematical model accurately predicted the flow and pressure fields of a fluid in a pulsating pathological geometry.

The introduction of the pulsating wall substantially influenced the velocity field, and we observed notable alterations of recirculation zones. With respect to pathological geometry, the pressure field showed areas of lateral gradient. Differentiation of the pressure field was also observed between the FSI cases and the hydrodynamic case; as the pulsatility increased, the Reynolds and Womersley numbers increased compared with those in the hydrodynamic case. The WSS on the pulsating arterial wall provides more information regarding the shear forces acting on the wall than could be obtained using a rigid wall. In addition, important biomedical factors such as TAWSS and OSI may provide information about the pathophysiology of the aneurysm. These factors, as well as the formation of the aneurysm, could influence cardiovascular risk in patients with AAAs. Overall, the findings presented here demonstrate the potential of FSI-based modelling in biomedical applications.

CHAPTER 6

Linking Aneurysmal Geometry and Hemodynamics Using Computational Fluid Dynamics

6.1 Introduction

One of the largest blood vessels of the human body is the aorta, which transfers blood from the heart to the organs and the rest of the body. Abdominal Aortic Aneurysm (AAA) is defined by a localized dilation of the abdominal aorta [165]. This condition is irreversible and is associated with factors such as gender, age, poor lifestyle (smoking), underlying pathologies (hypertension, atherosclerosis), and hereditary predisposition [4, 78, 109, 165, 156]. Additionally, patients with high blood cholesterol are more likely to develop AAAs due to the build-up of lipids and other fatty substances on the artery wall [41].

Two main AAA groups can be categorized based on their morphology: fusiform and saccular aneurysms. The most common are the fusiform, which are characterized by a symmetric dilation across the vessel's length [197]. When inflation is one-sided it belongs to saccular aneurysms and usually looks like a balloon-like aneurysm. It is a natural consequence that the blood flow and the geometry of the aneurysm are closely connected, as disrupted flow alters the nature of the vessel due to the hemodynamic loads on the wall and vice versa. Due to this permanent change of the artery's wall, complex flow patterns occur in the main area of dilation, such as vortices and recirculating regions.

Studying hemodynamics of the cardiovascular system can be achieved with computational methods such as computational fluid dynamics (CFD), which enables the analysis of disturbed blood flow and the calculation of stresses on the arterial wall, thereby providing early diagnostics for doctors.

While the current criterion for endovascular repair is based on the aneurysm's maximum diameter, this has been shown to be insufficient [40, 143, 192]. CFD methods,

on the other hand, make it possible to analyse the velocity, pressure fields within the AAA geometries and calculate the wall shear stresses (WSS) on the vessel's wall. In the literature, more than 47 geometric indices of patient-specific AAA geometries have been identified [192]. The most widely used indices within the academic community are the following: WSS, time-averaged wall shear stress (TAWSS) , oscillatory shear index (OSI) , relative residence time (RRT) and helicity-related indices. Several combinations of the aforementioned indices, such as endothelial cell activation potential (ECAP) are of great interest.

WSS represents the stresses caused by the flowing blood tangentially on the vessel lumen. In regions of low WSS values, flow disturbances and recirculation zones are usually observed. Studies report that the rupture of an AAA is associated with areas of low WSS [72, 110]. However, other studies suggest that the existence of oscillating WSS is associated with the rupture of aneurysms [132]. Considering temporal variations in blood circulation, TAWSS can capture all the changes on the wall during the cardiac cycle. An increase in TAWSS has been observed in cases where the dilation of the aneurysm progresses, likely due to an increase in the localized expansion ratio, leading also to an increase of the blood impingement velocity on the vessel wall. Conversely, areas with low values of TAWSS are often associated with thrombus development and thickening of the vessel's wall [105].

The most common geometric parameters used in the literature refer to the maximum diameter, the curvature, and the tortuosity of the aneurysm [4, 79, 88, 117]. An increase in maximum diameter is linked with reduced WSS, TAWSS and elevated OSI, RRT values, indicating altered hemodynamics and increased rupture risk [4, 85]. More pronounced curvature is associated with higher wall stresses and increased OSI values due to the development of recirculation zones [117]. Greater tortuosity affects the flow patterns inside the aneurysmal sac, resulting in higher OSI and RRT [187].

Geometrical changes affect the flow inside the aneurysm, and the OSI can explain the deviations of WSS vector. Elevated values of OSI highlight areas with recirculation and are associated with high rupture risk. Geometry plays a crucial role in OSI distribution, especially in cases with major alterations in shape or when high tortuosity is present [198].

The combined evaluation of TAWSS and OSI provides insights into the residence time of blood on the aortic wall [87]. Low RRT values correspond to healthy conditions where blood flows smoothly without any disturbances. On the other hand high RRT values are related to pathological cases of increased growth rates of the aneurysm and potential rupture. Increased RRT along the arterial wall could cause absorption of inflammatory cells and biomarkers, contributing to aortic wall degradation that leads to enlargement and rupture [187].

A potential outcome of elevated aortic tortuosity is augmented flow helicity, which

indicates the degree to which blood circulates in a corkscrew-like manner. Helical flow may have a variety of physiological benefits, including improving oxygen transport through the aorta wall, lowering the risk of platelet adhesion, and preventing the accumulation of atherogenic low density lipoproteins on the wall [121, 55].

Several studies have shown that helicity within the arterial flow has a great influence on the stabilization of both laminar and turbulent flows. Under physiological conditions, helical flows are laminar in contrast to turbulent fluctuations, which cause irreversible energy loss and indicate inefficient blood flow. Elevated values of helicity has been associated with the stability of the flow and the reduction of turbulence and wall shear stress oscillations, resulting in the improvement of flow efficiency even in distorted arterial geometries [73, 136].

Intraluminal thrombus (ILT) is a three-dimensional (3D) fibrin structure composed of blood cells, platelets, blood proteins, and cellular debris adhering to the wall of the AAA and is present in approximately 75% of cases [59]. Several studies have revealed that areas with low TAWSS are associated with lumen expansion and ILT development, regardless of the flow near the wall [12, 65, 141].

However, the impact of ILT's in AAA development and rupture is still debated. According to several studies, ILT may operate as a "cushion" absorbing part of the hemodynamic load, thereby reducing peak wall stress and postpone rupture [49]. On the other hand, there has been evidence that ILT may have negative biological effects, including increased proteolytic activity, accelerated inflammatory responses, and hypoxia within the artery wall. These factors might lead to wall thinning, weakening, and rupture [90, 194].

Previous studies on AAAs have investigated multiple factors that may influence the clinical progression of aneurysms, including the growth rate of the maximum diameter, the degree of buckling, and the volume of the stagnation zone [4, 63, 85, 94]. Aneurysm buckling promotes axial growth by creating a curvature that allows its development lengthwise instead of radially. In most cases, this phenomenon postpones rupture; however, in extreme cases, local stress concentrations can accelerate rupture [85].

An increase in the maximum diameter of the aneurysm, combined with thinning of the wall, leads to an increase of the wall stresses values, thus elevating the rupture risk when the diameter grows rapidly [4]. Furthermore, the volume increase of the stagnation zones is linearly linked with the lumen dilation and contributes to both aneurysm growth and rupture [94].

A similar study by Fedotova et al. categorized the data into three types based on the flow patterns obtained from the CFD simulations [65]. In the 1st group, the flow was characterized by a helical main flow channel that affects the wall of the aneurysm, forming vortices in the sac. The 2nd group contains non-helical flows, but with the

presence of a single large vortex. In contrast, in the 3rd group, multiple vortices can be identified, without helical flow. The findings indicate that the 3rd group was associated with lower TAWSS and elevated OSI and RRT values, moderate values for TAWSS, OSI, and RRT for the 1st group, whereas the 2nd group exhibited higher TAWSS, lower OSI and RRT values.

This work aims to provide a comprehensive hemodynamic and morphological analysis of AAAs through CFD simulations applied to a large patient-specific cohort (74 infrarenal AAAs). By integrating a multiscale zero-dimensional to one-dimensional (0D–1D) model with fully 3D simulations, we establish a physiologically representative framework that captures detailed flow behaviour and stress-related indices. This study correlates advanced hemodynamic biomarkers—including TAWSS, OSI, RRT with geometric descriptors such as curvature, torsion, and aneurysm diameter. In doing so, this work contributes to a deeper understanding of AAA pathology and provides a foundation for improved rupture risk assessment beyond conventional diameter-based thresholds. Previous studies linking AAA geometry to hemodynamics are often limited by small cohorts, heterogeneous modelling assumptions, and a focus on a narrow set of geometric descriptors, which can lead to inconsistent findings. Related work in other aortic regions, such as the thoracic aorta and aortic arch, has shown that curvature, dilation, and tortuosity can strongly modulate secondary flows and wall-shear patterns in a region-dependent manner. Compared to these regions, infrarenal AAAs are characterized by pronounced dilation that promotes flow deceleration and recirculation, highlighting that the hemodynamic response to geometric variations depends on both vessel size and anatomical location.

Lastly, regarding the abdominal aorta regional analysis, the aneurysms were divided into the infrarenal segments and the iliac segments and thus, the statistical analysis was conducted separately for each of the aforementioned regions. This approach allowed us to demonstrate that geometry–hemodynamic relationships differ substantially between regions and reveals that the iliac arteries exhibit stronger and previously underappreciated correlations with disturbed hemodynamics. To our knowledge, such a systematic regional comparison has not been comprehensively reported in earlier AAA CFD studies [98].

6.2 Methodology

In this study, we employed a total of 74 3D infrarenal AAA models, 23 obtained from the SAFE-AORTA project, and 51 from the VASCUL-AID project. The SAFE-AORTA models correspond to AAA patients treated at the Department of Vascular Surgery, Attikon University Hospital, Athens, Greece, whereas the VASCUL-AID models are publicly available through an open-access repository

(https://doi.org/10.5281/zenodo.10932957) [3, 164]. The segmentation of the CTA scans and the 3D reconstruction of the AAA models was carried out by a dedicated task force consisting of vascular surgeons and biomedical engineers. The hemodynamic simulations were performed utilizing the specialized biomedical CFD software SimVascular [191]. The simulations were conducted to obtain critical hemodynamic quantities, including pressure, velocity fields and wall shear stress-related quantities.

6.2.1 Governing Equations and Hemodynamic Parameters

Blood was modeled as a Newtonian fluid, which is governed by the incompressible Navier-Stokes and continuity equations expressed as,

$$\bar{\nabla} \cdot \mathbf{u} = 0, \tag{6.1}$$

$$\frac{\partial \mathbf{u}}{\partial t} + \mathbf{u} \cdot \bar{\nabla}\mathbf{u} = -\frac{1}{\rho}\bar{\nabla}p + \nu\Delta\mathbf{u}, \tag{6.2}$$

where Δ is the Laplacian operator, $\mathbf{u}$ is the velocity field, p is the pressure, ν is the kinematic viscosity and ρ is the density of blood.

The use of specialized hemodynamic indices is crucial for the evaluation of the results, as these quantities characterize the flow patterns, quantify the prolonged residence of blood in certain areas, the oscillatory nature of the flow, and consequently contribute to the assessment of potential rupture of the vessel wall. The following parameters, used in this study, are frequently utilized by researchers to evaluate the pathology of each model, as they are strongly related to the occurrence and progression of aneurysms. A crucial parameter for biomedical flows is the WSS, given as the product of dynamic viscosity with the velocity gradient near the wall,

$$\bar{\tau} = \mu \left[\bar{\nabla}\mathbf{u} + (\bar{\nabla}\mathbf{u})^T\right] \cdot \bar{n} \tag{6.3}$$

where $\bar{n}$ is the unit normal vector drawn from the fluid through the wall. TAWSS is defined as the average value of the magnitude of the WSS vector over the cardiac cycle,

$$TAWSS = \frac{1}{T}\int_0^T |WSS| dt, \tag{6.4}$$

where T is the duration of the cardiac cycle and s is the general surface coordinates.

OSI quantifies the directional changes of the WSS vector over the cardiac cycle. Smaller values of OSI, close to zero, indicate unidirectional shear, and higher values indicate purely oscillatory shear.

$$OSI = \frac{1}{2}\left(1 - \frac{\left|\int_0^T WSS dt\right|}{\int_0^T |WSS| dt}\right). \tag{6.5}$$

The RRT index combines the effects of OSI and TAWSS, describing with its magnitude the trapping of blood particles near the wall for the duration of a cardiac cycle. It is defined as the inverse of the product of TAWSS and the directional factor $(1 - 2\,OSI)$,

$$RRT = \frac{1}{(1 - 2\,OSI)\;TAWSS}. \tag{6.6}$$

Additionally, the rotational structures and helicity behaviour are visualized through the local normalized helicity (LNH) parameter ,

$$LNH = \frac{\mathbf{u}(x,t) \cdot \mathbf{w}(x,t)}{|\mathbf{u}(x,t)||\mathbf{w}(x,t)|} = \cos\varphi, \tag{6.7}$$

where φ is the angle between the velocity **u** and the vorticity **w**. This hemodynamic parameter, described as a function of space and time, is an indicator of the helical structures' intensity and rotational direction. When the absolute value of LNH is one, the flow is purely helical. Otherwise, when the value is zero, the flow is symmetric. The sign is of great importance as it dictates the right $(+)$ or left-handed $(-)$ direction of the helical structures. Therefore, the LNH values range between -1 and 1.

6.2.2 Developed Multiscale Model

For the purpose of acquiring a physiological result for the AAA models, we utilized a multiscale, coupled 0D-1D model for the boundary conditions of our simulations. Regarding the equations of the 1D models, they were derived from the incompressible Navier-Stokes equations in cylindrical coordinates, under the conditions of axisymmetry and a parabolic velocity profile. Essentially, they are fluid-structure interaction (FSI) equations, originating from the laws of conservation of mass, momentum, and an equilibrium equation for the arterial wall as presented below,

$$\frac{\partial A}{\partial t} + \frac{\partial q}{\partial x} = 0, \tag{6.8}$$

$$\frac{\partial q}{\partial t} + \frac{1}{A}\frac{\partial}{\partial x}\left(\frac{q^2}{2}\right) + \frac{A}{\rho}\frac{\partial p}{\partial x} = -\frac{8\pi\mu}{\rho}\frac{q}{A}, \tag{6.9}$$

$$p(x,t) - p_0 = E_\theta\left(\frac{A(x,t)}{A_0(x,t)} - 1\right), \tag{6.10}$$

where x is the axial coordinate, $q(x,t)$ is the average blood flow in the cross-sectional area, $A(x,t)$ is the cross-sectional area, $p(x,t)$ is the average blood pressure in the cross-sectional area, μ is the viscosity, and E_θ is Young's modulus.

The above system of equations is a nonlinear, coupled system of PDEs, classified as hyperbolic. As boundary conditions, we used flow and pressure waveforms (inlet conditions), expressed as a Fourier series of 18 harmonic terms each. For spatial discretization of the 1D-0D equations, we used the finite volume method (FVM), which is an integral method adopting a cell-centered grid approach. Therefore, the above system of equations was integrated over a cell volume ΔV and over a period T. For temporal discretization, we used an explicit Euler method and a second-order θ-scheme. For the solution of the non-linear algebraic system occurring from the discretization, we utilized Newton's method.

One of the outcomes of the developed multiscale model is the waveform applied in the infrarenal region, inlet of the in-study models, as depicted for one case in Figure 6.1.

6.2.3 Boundary Conditions

Regarding the inlet conditions in the three-dimensional simulations, we used spatially parabolic waveforms extracted from the multiscale $0D-1D$ models, after smoothing, that were implemented in the Matlab R2024b software program (Natick, Massachusetts, USA). This multiscale modelling ($0D-1D$) approach allowed us to use real values of diameters, areas, etc, for each geometry and extract accurate inlet data.

Regarding the outlet boundary conditions in 3D simulations, we utilized the 3-element Windkessel model (RCR) for the extraction of outlet conditions to acquire a patient-specific approach for each model. For the tuning of the Windkessel parameters, an iterative procedure was adopted to determine the outlet pressures described in [211]. A heuristic approach was followed for the resistances proximal (R_p) and distal (R_d) respectively, suggested in [2, 196] where $R_d \sim 10R_p$. The total peripheral resistance was calculated as,

$$R_{total} = \frac{\text{MAP}}{\bar{Q}_{inlet}}, \tag{6.11}$$

where $\text{MAP} = P_{diast} + (P_{syst} - P_{diast})/3$, is the mean arterial pressure, with P_{syst} and P_{diast} denoting the systolic and diastolic pressures. $\bar{Q}_{inlet}$ represents the mean flow rate at that inlet. The total resistance was distributed,

$$\frac{1}{R_{total}} = \sum_{i=1}^{N} \frac{1}{R_{total,i}} = \sum_{i=1}^{N} \frac{1}{R_{p,i} + R_{d,i}}, \tag{6.12}$$

where N are the total terminal sections of the arterial model, which are the two iliacs in this study.

Figure 6.1. Schematic representation of the waveform, extracted from 0D-1D model, at the inlet and the 3-element Windkessel RCR conditions at the outlet.

Finally, the formula for the calculation of the total aortic vessel compliance is the following [37],

$$C_{total} = \frac{Q_{max} - Q_{min}}{P_{syst} - P_{diast}} \Delta t, \tag{6.13}$$

where Q_{max} and Q_{min} are the maximum and minimum inlet flow rates, respectively, and Δt is the temporal difference between the achieved maximum and minimum flow rates. Therefore, we calculated every parameter of the RCRs for each iliac of each

geometry. Additionally, for the RCR calculation at the iliac region, a workflow is presented in Figure 6.2.

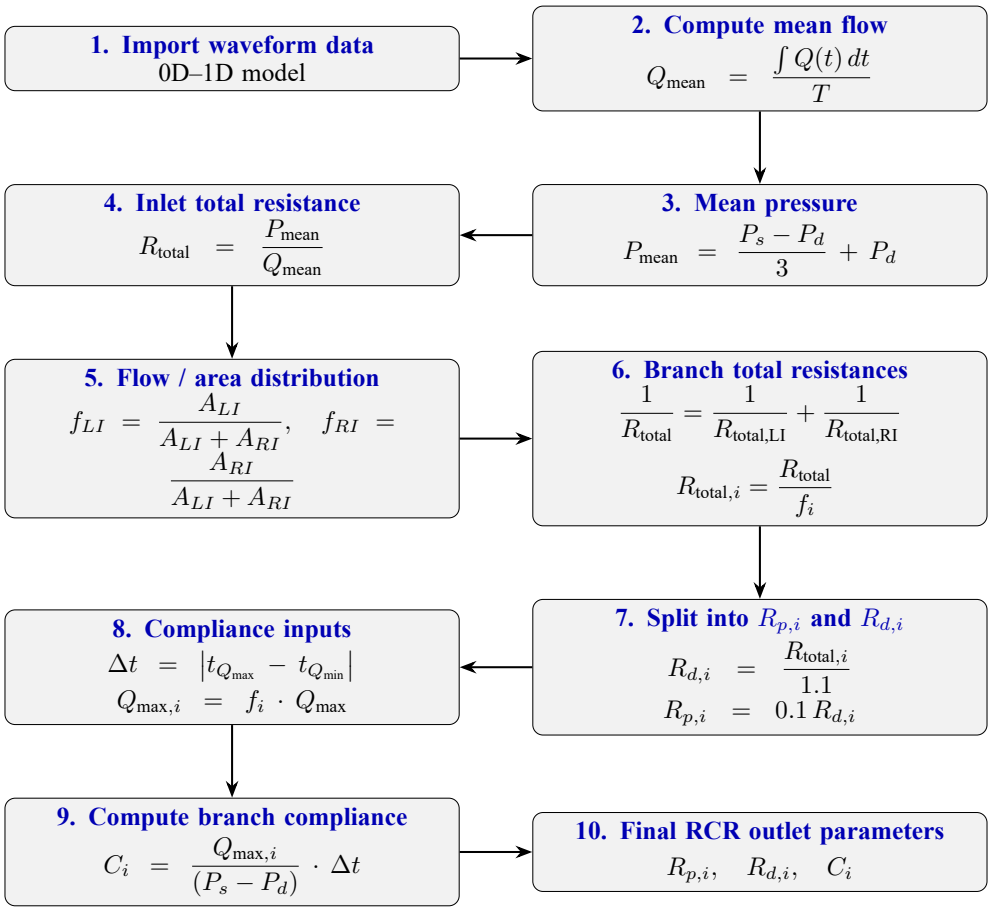

Figure 6.2. Workflow for acquiring iliac RCR outlet parameters from flow waveform and pressure data.

To derive the RCR outlet B.C. we follow a ten-step workflow based on the inlet waveform, derived from multiscale modelling, and the pressure values enforced (80/120 mmHg). Initially, the mean value of the flow waveform and mean arterial pressure (MAP) are calculated. Then the total resistance is calculated, representing the equivalent resistance of the two iliac outlets acting in parallel. Next, the flow is apportioned between the left and right iliac branches according to their anatomical outlet areas, producing fractional flow distribution factors f_{LI} and f_{RI}. These fractions are used to derive each branch's total resistance such that the parallel re-

sistance relationship is preserved. Each branch total resistance is then decomposed into a proximal resistance and a distal resistance using a $90/10$ ratio between the two components. The compliance is calculated according to a known formula. Finally, we conclude to the RCR parameters $(R_{p,i}, C_i, R_{d,i})$ for each iliac outlet ready to be applied to SimVascular.

6.2.4 Computational Hemodynamics

The computational meshes were generated in SimVascular, with a range of $5 \cdot 10^5 - 10^6$ tetrahedral elements, with the open-source software TetGen. This software employs the Delaunay triangulation algorithm. To ensure numerical accuracy and stability, a mesh sensitivity analysis was performed, testing element size from 0.1 to 0.2cm until the differences in maximum velocity between two progressively larger meshes were smaller than 2%. The parameter for the final generation of the grid was set as the size of the maximum edge equal to 0.15cm. Each simulation was performed for 8 cardiac cycles, 8 seconds in total in each simulation, with results extracted from the last cycle to eliminate transient effects from the initial cycles. A time step of $\Delta t = 0.00334$ s was chosen with a total number of 2400 timesteps for the simulation concluding in 300 time steps per cardiac cycle. The results were visualized with Paraview 5.12.0-RC2 (Kitware Inc, Los Alamos National Laboratory).

The numerical solution of the Navier-Stokes equations is achieved by employing the svSolver of SimVascular, which utilizes the streamline-upwind/Petrov-Galerkin (SUPG) method in an arbitrary domain and pressure-stabilizing/Petrov-Galerkin (PSPG) method [201, 191]. This combined approach enables the use of linear tetrahedral elements ($P_1 - P_1$) for velocity and pressure, while maintaining numerical stability for advection-dominated and incompressible flows. The solver also incorporates stabilization terms for both momentum and pressure. The residual value below 10^{-5} was set as the convergence limit of the calculation. Blood is considered an incompressible Newtonian fluid with density $\rho = 1060$ kg/m^3, and viscosity assumed to be $\mu = 0.004$ Pa s. The luminal wall was considered rigid with a no-slip condition. Note that the aortic wall is commonly treated as rigid in elderly AAA patients, as a small change in wall deformation was observed [65].

6.2.5 Statistical Analysis

In this study, 74 AAA cases were simulated and hemodynamic parameters and morphological information such as maximum diameter, torsion and curvature were extracted. To obtain a detailed statistical analysis, Matlab R2024b (Natick, Massachusetts, USA) was utilized. For a more detailed examination, each AAA was divided into two anatomical regions: the infrarenal aorta and the iliac regions. This

separation made it possible to study both the shape and flow characteristics of each part individually, helping to understand better how geometry and blood flow vary across different portions of the aneurysm.

From each region, the morphological descriptors from the centerline were evaluated through the vascular modelling toolkit (VMTK) [7] and the mean and maximum values of the hemodynamic indices of interest (TAWSS-OSI-RRT) via the CFD at the surface. More specifically, the geometric parameters, such as the mean curvature and torsion, were evaluated based on the sum of the corresponding values divided by the number of points in the centerline. Similar procedure was used for the mean values of the hemodynamic parameters on the AAA walls. These indices describe blood flow behaviour and its interaction with vessel walls, identifying regions of disturbed flow. These regions have been linked to aneurysm progression and rupture risk. Therefore, their relation with the morphological aspects of the models are of great interest.

To examine how the geometry of the AAAs relates to their flow characteristics, the Spearman's rank correlation was used to study the relations between morphological and hemodynamic variables. This non-parametric method was chosen because it does not require the data to be normally distributed. The correlations were analyzed separately for both anatomical regions, infrarenal and iliac, allowing us to identify correlations to each region. It should be noted that the present study evaluates multiple, pairwise correlations between geometric and hemodynamic parameters. Considering this, the reported correlations are intended to highlight general patterns and associations rather than definitive effects on the hemodynamic variables.

6.3 Results

6.3.1 Flow Field Characteristics

Figure 6.3 depicts the velocity through axial contours during three selected phases of the cardiac cycle: peak systole, late systole and late diastole. During peak systole, a narrow, jet-like flow was observed entering dynamically following the inner curvature of the aortic lumen. The accelerating flow followed two paths, one towards the proximal neck of the aorta and the other towards the lower part of the aneurysm or the iliac bifurcation, where it reached maximum velocity values. In late systole, an early formation of vortex-like structures was apparent in all models. In AAAs with larger sacs, such as VAID3, VAID7 and VAID53, these structures appeared more intense.

The diastolic phase demonstrated a disturbed yet interesting behaviour. Hemodynamic flow within all aneurysmal geometries exhibited recirculation zones during late diastole, but the location and extent of these zones depend on the geometrical aspects of the aneurysm. Especially, in models VAID7, T1-P8 and T2-P17 a pronounced recirculation was observed locally in the proximal region of the aneurysm. In models

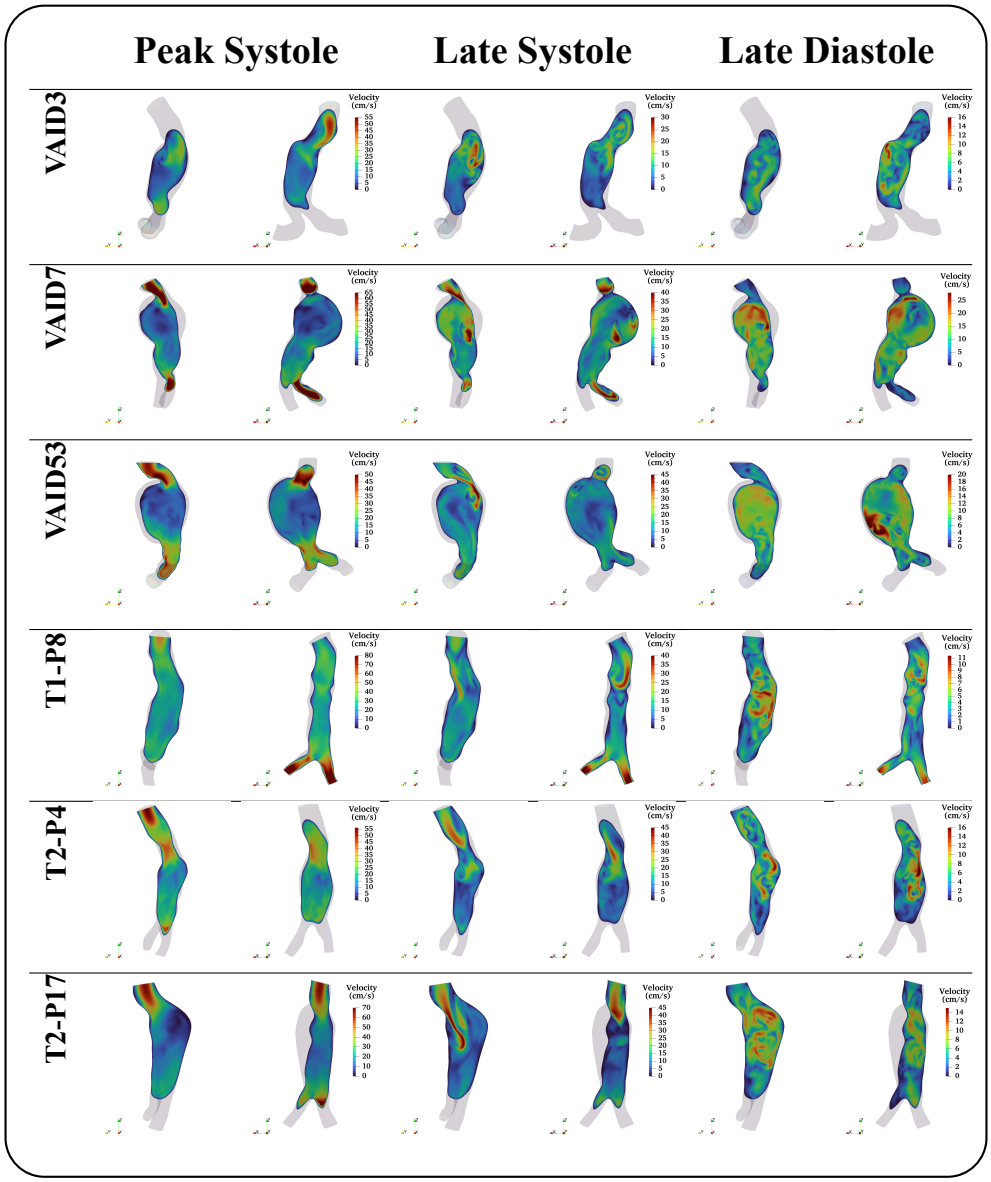

Figure 6.3. Velocity magnitude distributions in the six aortic aneurysm models (VAID3, VAID7, VAID53, T1-P8, T2-P4, and T2-P17) at three cardiac phases: T1: peak systole, T2: late systole, and T3: late diastole. The flow slices demonstrate the hemodynamic changes, highlighting high-velocity inflow jets at peak systole, progressively altering velocity distribution during late systole, and reduced flow behaviour approaching at late diastole.

VAID3, VAID53 and T2-P4 the recirculation regions were located towards the distal side of the aneurysm sac. These differences may be attributed to asymmetries in the sac morphology.

In Figure 6.4, the recirculation zones can be observed in a better manner, especially in models VAID3, VAID7 and VAID53 with vortical cores adjacent to the neck of the aorta. During peak systole, T1-P8, T2-P4 and T2-P17 showed streamlined paths while VAID3, VAID7 and VAID53 showed more disturbed and chaotic paths, especially towards the middle of the aneurysm. Again, a narrow, jet-like flow entered the aneurysmal region, which either moved towards the proximal neck and dissipated or towards the bifurcation region.

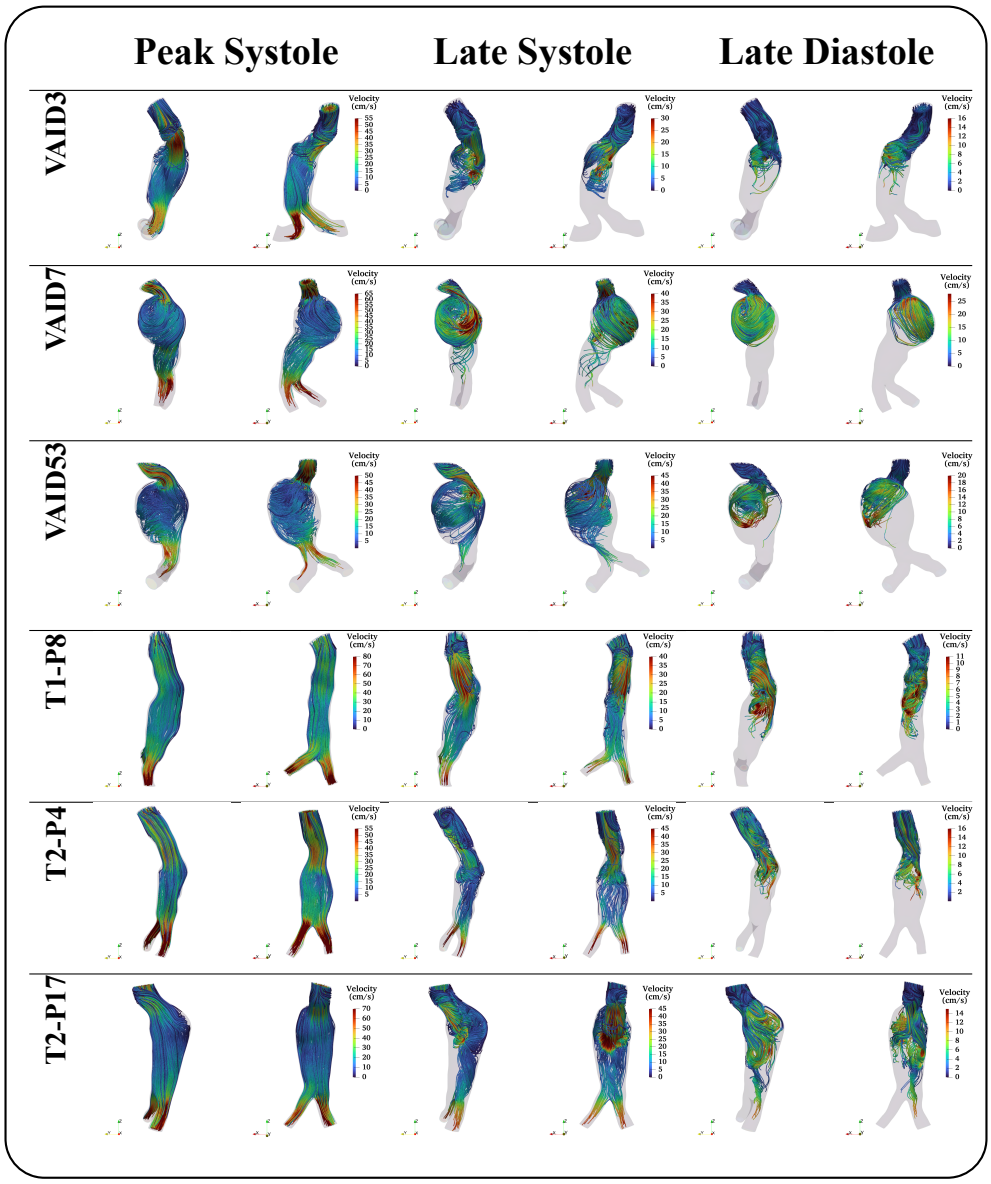

Figure 6.4. Streamlines for the six aortic aneurysm models (VAID3, VAID7, VAID53, T1-P8, T2-P4, and T2-P17) at three cardiac phases: T1: peak systole, T2: late systole, and T3: late diastole. The streamlines demonstrate the hemodynamic changes, highlighting the recirculation regions and the creation of vortices inside the AAAs.

Figure 6.5 presents the velocity magnitude slices of six selected infrarenal

aneurysm models from the entire studied cohort of pathological aortas. They are depicted on three cross-sectional planes $Y1 - Y2 - Y3$ for three different time instances T1: Peak Systole, T2: Late Systole and T3: Late Diastole to visualize the flow behaviour in different time instances and regions of the infrarenal models. The six AAAs presented were selected with diversity criteria in order to discuss aortas with larger cardinality and morphological variety. The velocity fields have units of cm/s, as adopted in this study.

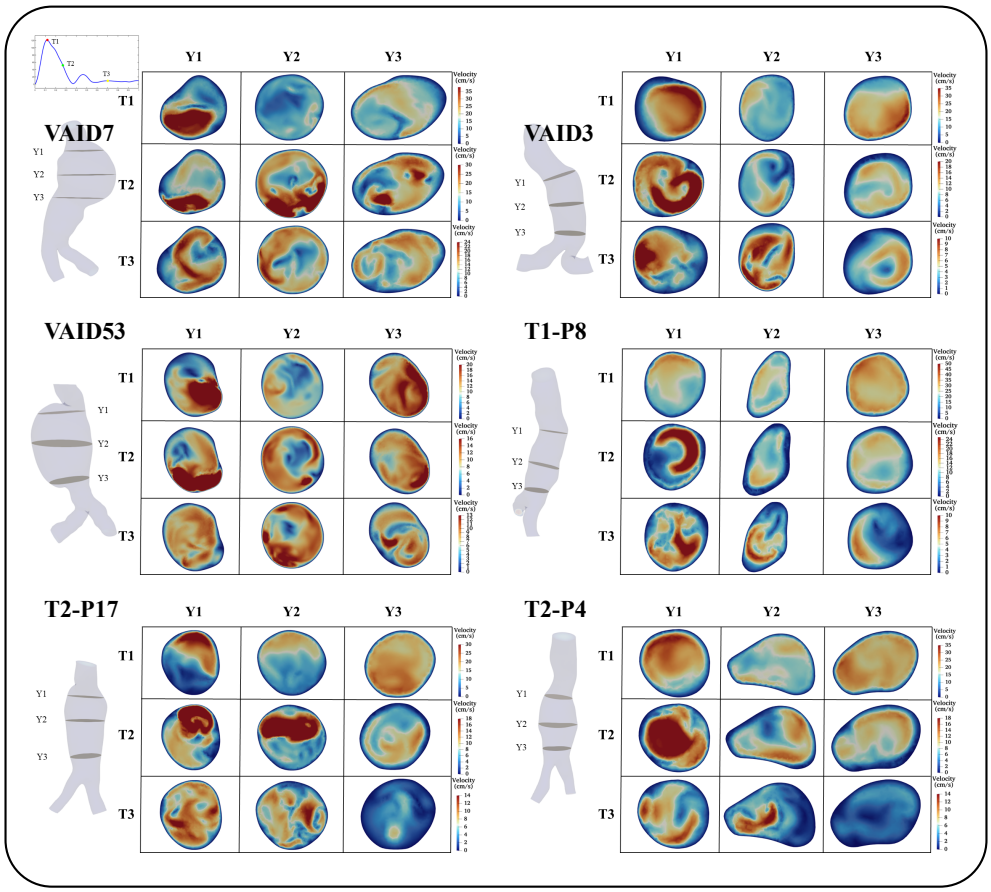

Figure 6.5. Velocity slices for six selected AAA models from the dataset, at three cardiac-cycle times ($T1$: peak systole, $T2$: late systole, $T3$: late diastole). The slices were selected at the proximal neck $Y1$, the aneurysm sac $Y2$ and the distal neck $Y3$. The velocity units are in cm/s.

At peak systole ($T1$), all six models exhibit a high-velocity entry at the proximal aneurysmal sac, $Y1$ position, creating a wall-adjacent flow, revealing a pattern similar to a Dean-type secondary flow. The highest velocity magnitude is observed at this region in most of the studied cases. As flow progresses to the mid-aneurysmal sac, in position $Y2$, the flow reduces its momentum in the aneurysm sac, forming vortices and recirculation regions. Downstream, when the flow reaches the $Y3$ plane, the flow increases its velocity magnitude again due to the contraction of the pathological aorta. In models VAID53, VAID7, and T2-P17, the inflow jet in $Y1$ exhibits asymmetric behaviour due to the curvature of the aortas. In contrast, the other three models exhibit a

more central jet distribution. The distributions at $Y2$ are not uniform, indicating large recirculation regions and the creation of vortices. The $Y3$ section, distal aneurysmal sac, presents a uniform distribution as aorta contraction leads to a more streamlined flow. This behaviour is observed in almost all models, except for VAID7, which presents a recirculating flow due to the large size of the sac and the large curvature of the aorta.

During late systole ($T2$), the jet weakens as the flow decelerates, resulting in complex recirculating areas inside the sac in all six models. In the region $Y1$, the velocity field alters the jet distributions from $T1$, changing in some cases the positioning of the maximum velocity, as can be depicted in the T1-P8 model. This is also highlighted in VAID3, as the maximum velocity moves from the upper side to the bottom, creating two recirculation areas. Additionally, the case T1-P8 exhibits similar behaviour, as the maximum velocity is observed at late systole $T2$ with the creation of a crescent-shaped (horseshoe) of high velocity structure, surrounded by a low velocity area. The other models exhibit a more uniform weakened velocity field.

At late diastole, $T3$, the overall flow velocity decreases significantly, with a lower velocity magnitude compared to $T1$ and $T2$. Multiple vortices and recirculation regions are observed in these distributions as the flow is mixed. The selected AAAs demonstrate a general pattern of fluid flow, with strong peak systolic jets at $T1$, momentum redistribution at $T2$ with a change in the jet flow inside the aorta in several cases, and finally deceleration of the flow with recirculation regions at $T3$.

6.3.2 Wall Shear Stress and Oscillatory Flow Indices

In this section, the WSS-related indices, TAWSS, OSI, and RRT, are discussed due to their importance in the evaluation of the results. In all cases, shown in Figure 6.6, the models exhibit low pathogenic values, especially in the sac, which could lead to ILT formation, endothelium dysfunction, and rupture of the vessel wall. It is highlighted that values less than $4\,dynes/cm^2$ are critical according to the literature [12]. In our models, such regions are demonstrated as a strong indicator of the AAAs pathology. Additionally, in the iliac region there exist areas with high TAWSS, which correspond to areas of high velocity. High values of TAWSS can also have a negative influence on the aorta, as they increase the possibility of the vessel wall weakening and rupture.

The oscillatory flow affects the models as it can contribute to the pathology and progression of the aneurysm. The OSI index is a valuable quantity that provides us with information about the regions that exhibit oscillatory behaviour. Areas exposed to highly oscillating flow are described as pathogenic. Values exceeding the threshold of 0.3, adopted from the literature, are considered pathogenic and can disrupt the flow. In the second column of Figure 6.6, OSI fields are depicted for our in-study models.

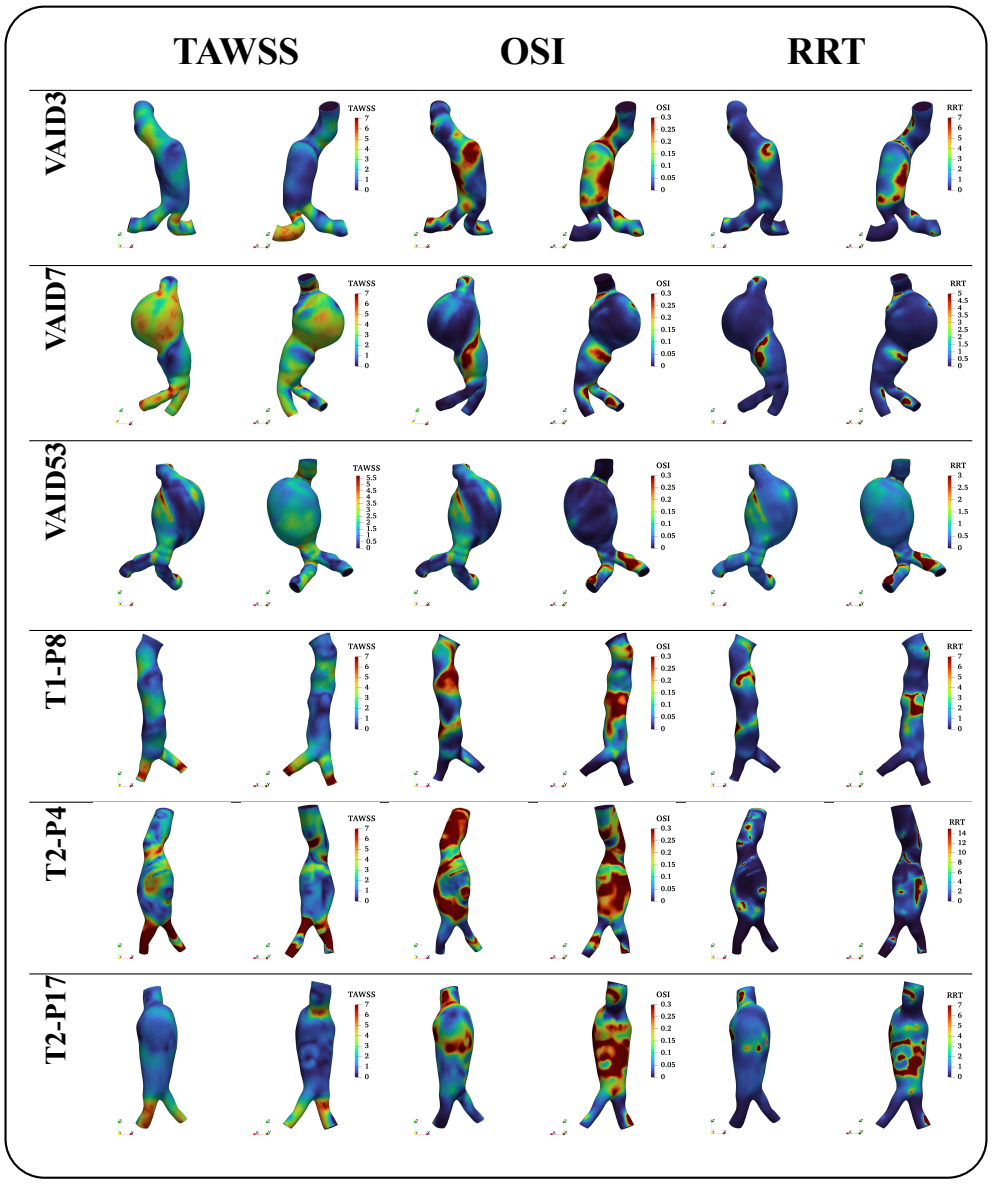

Figure 6.6. Time-averaged wall shear stress (TAWSS) , oscillatory shear index (OSI) , and relative residence time (RRT) for six AAA models. Each case shows anterior (+Y) and posterior (–Y) wall projections. The units of TAWSS are in $dyne/cm^2$, OSI index is dimensionless and RRT has units of $cm^2/dyne$.

Aneurysms with larger sacs, such as VAID7 and VAID53, are exposed to small values of OSI in the sac area, in contrast to the other models, which demonstrate high OSI values in the aneurysmal sac. The aneurysm necks, proximal and distal, are areas of high OSI, a behaviour identical to all six cases presented. A special case is the T1-P8 structure in which the OSI is perturbing in small-high values at the sac due to repetitive dilation and contraction of the sac area. Finally, in almost all cases the iliac region is observed to have areas with large OSI values.

An additional index, RRT, was introduced in the Methodology section, which complements the aforementioned indices. The RRT index provides information about the prolonged residence of blood particles in the lumen of the vessel. Large values of RRT can lead to conditions that are strongly associated with platelet activation, thrombus deposition, and local hypoxia. The combination of low TAWSS and high OSI results in high RRT values, often observed in the aneurysm sacs where stagnant vortices develop. Areas exposed to high RRT are strongly associated with ILT formation and wall weakening, potentially leading to aneurysm growth or rupture. Across the six AAA models in Figure 6.6, large values of RRT are observed in the aneurysm sac, proximal and distal necks, indicating regions of blood stagnation and prolonged residence.

6.3.3 Helical and Vortical Flow Structures

The rotational behaviour of the flow is examined through the interpretation of LNH. A threshold of $|LNH| > 0.3$ was selected according to a previous study [97].

During the peak systolic phase (upper figures) in Figure 6.7, the flow presents a structured helical flow pattern at the proximal neck, leading to a jet-driven acceleration downstream of the aneurysmal sac. This changes gradually as the LNH becomes fragmented in the aneurysm sac. This is clearly observed in the 1st, 5th, and 6th models. In the more expanded and asymmetrical models (2nd, 3rd, and 6th), LNH fields exhibit discontinuous behaviour, indicating a disruption of the helical motion by large recirculating vortices. In contrast, the first and fourth models present a smoother and more continuous LNH field in the systolic phase due to the narrower sac. In the diastolic phase, the LNH field becomes fragmented, indicating discontinuous LNH fields resulting from the increased mix that describes the late diastole phase due to the deceleration of the flow.

The presence of large-scale recirculation and vortex structures within AAA sacs is consistent with prior in-vitro measurements in aneurysm models, which reported similar separated-flow regions under physiologic Reynolds/Womersley conditions. These experimental observations support the physical realism of the qualitative flow structures reported here[25, 29, 212].

To quantitatively support the qualitative flow-pattern interpretation, the observed

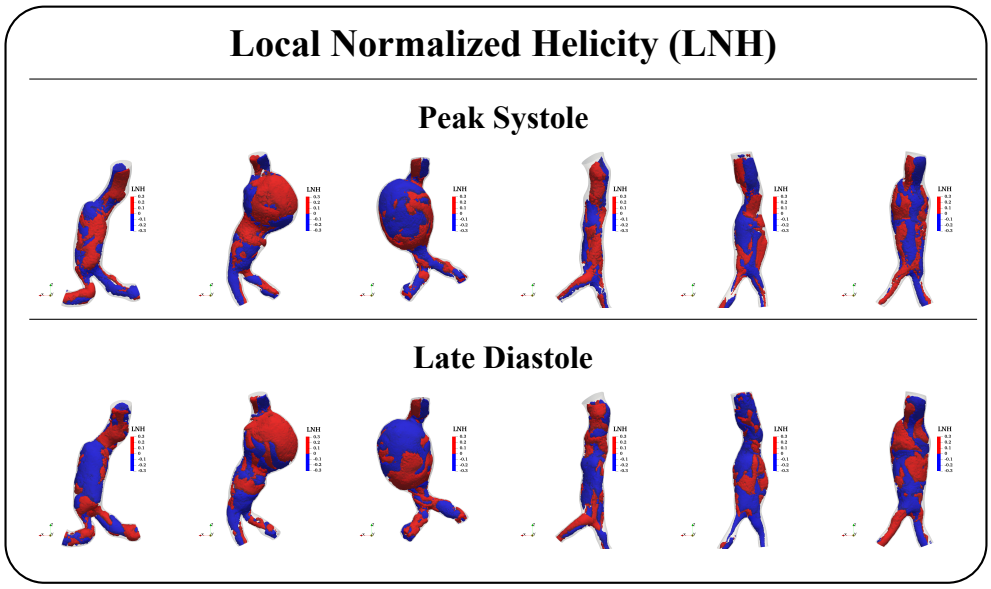

Figure 6.7. Local normalized helicity (LNH) distributions for six AAA models at peak systole and diastole ($|LNH| > 0.3$). In the upper row, there are the six AAAs in peak systole and in the bottom row, at late diastole.

recirculation regions and vortex structures were examined in relation to the extracted hemodynamic descriptors. In particular, areas of persistent low-velocity flow corresponded to reduced TAWSS and elevated RRT values, whereas increased directional variability was reflected by higher OSI. Rotational and helical flow organization was further assessed using the LNH metric. This linkage ensures that the qualitative flow observations are consistently supported by quantitative hemodynamic indicators.

6.3.4 Statistical Analysis

As described in the methodology section, the Spearman correlation was utilized to evaluate the relationships between various hemodynamic parameters obtained through post-processing of the CFD results with geometrical parameters extracted from the centerline of the corresponding AAA using VMTK. The infrarenal part of the AAA exhibited an average diameter of 4.77 cm, an average curvature of 0.33 cm^{-1} and an average torsion of 0.06 cm^{-1}. In comparison, the iliac region displayed an average diameter of 1.75 cm, an average curvature of 0.48 cm^{-1} and an average torsion of 0.06 cm^{-1}. These results provide important insights into how the geometric variability of the aorta influences the blood flow.

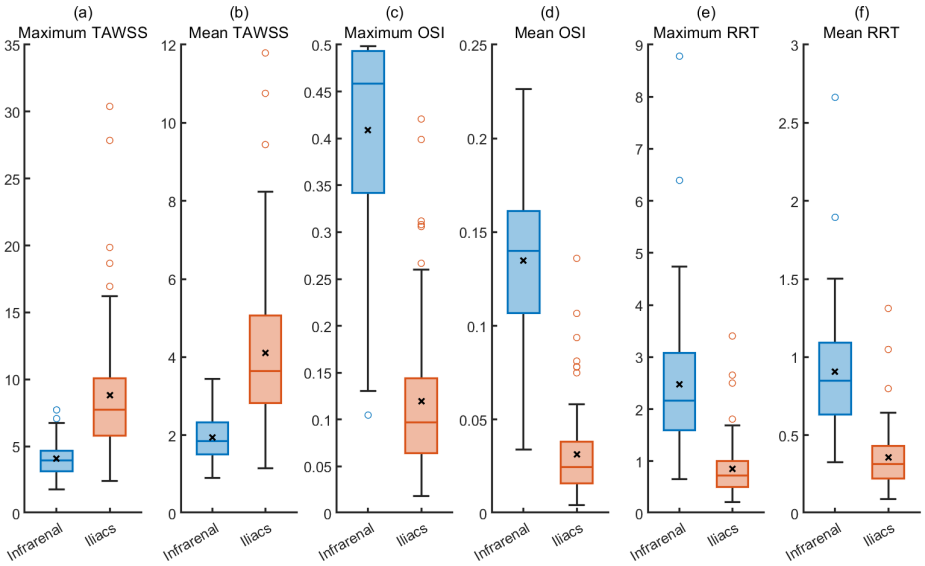

Figure 6.8. Boxplots for the geometric parameters for the infrarenal and iliac parts, respectively. The maximum and mean values of TAWSS are presented in (a) and (b), the maximum and mean values of OSI are presented in (c) and (d) and the maximum and mean values of RRT are presented in (e) and (f), respectively.

In Figure 6.8(a)-(f) the box plots of the hemodynamic parameters are presented along the mean value of each dataset ("x" notation). Infrarenal areas are shown in blue, whereas iliac areas are shown in red and the two groups of the aorta are arranged in the x-axis. The values of the hemodynamic parameters, presented in the y-axis, further highlight the influence of the geometry on blood flow, as each region exhibits substantial differences in its hemodynamic parameters. The most notable comparison arises from the differences in OSI values in the two aorta segments. Similarly, in Figure 6.9(a)-(e), the box plots of the geometric parameters are displayed along with mean values. In this area of the aorta the geometric parameters also present variation in their range of values. The diameter in the infrarenal region show significant difference in comparison to the diameter in the iliac one, a logical result concerning the aneurysm located in the infrarenal parts.

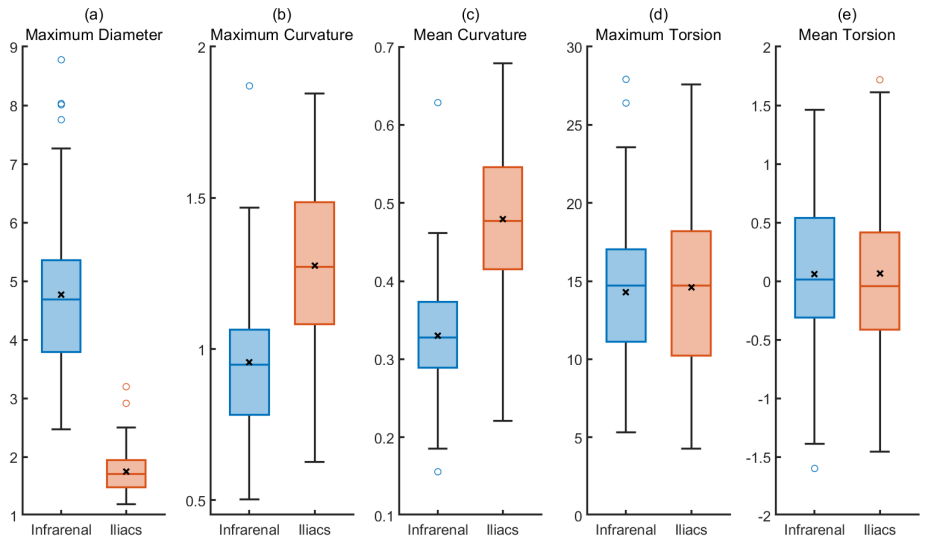

Figure 6.9. Boxplots for the hemodynamic parameters for the infrarenal and iliac parts, respectively. The maximum and mean values of diameter are presented in (a) and (b), the maximum and mean values of curvature are presented in (c) and (d) and the maximum and mean values of torsion are presented in (e) and (f), respectively.

The results of the statistical analysis are displayed in Figure 6.10 where Figure 6.10(a) displays the heatmap for the infrarenal region and Figure 6.10(b) corresponds to the iliac region. In the infrarenal area, the strongest statistical correlation was observed between the maximum diameter with the mean TAWSS with correlation coefficient of $\rho = -0.45$ and a p-value < 0.001 indicating a statistical significance with moderate negative correlation. Similar results were obtained for the maximum diameter and the maximum and mean OSI, with the same p-value ($p< 0.001$) and moderate negative correlation of $\rho = -0.41$ and $\rho = -0.40$, respectively. A further moderate negative correlation was observed between the maximum diameter and the maximum TAWSS with $\rho = -0.38$ and $p< 0.01$. Additionally, weak statistical correlation was found between the maximum diameter and mean RRT ($\rho = 0.25$), the mean curvature and maximum TAWSS ($\rho = 0.25$) as well as the maximum torsion and mean TAWSS ($\rho = 0.23$). In the aforementioned cases their p-value were found to be < 0.05.

In the iliac regions, a different pattern emerged, with the maximum diameter dominating the correlations between the hemodynamic parameters, compared to the other geometric parameters. Strong correlations were found between the maximum diameter and all of the hemodynamic parameters. More specifically, a negative strong

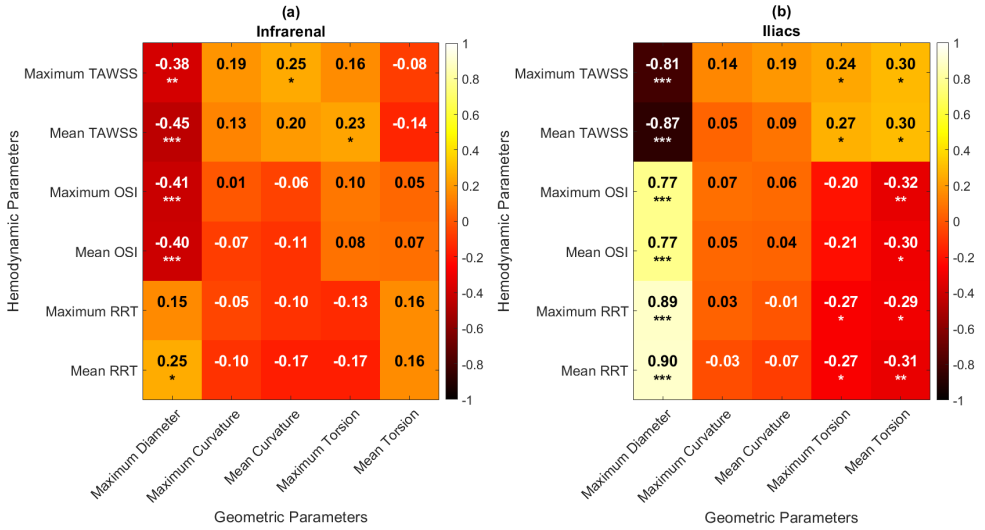

Figure 6.10. Heatmap of the Spearman correlation, for the (a) infrarenal and (b) iliac parts. The colorbar indicates the Spearman correlation coefficient with values in $[-1, 1]$, and statistical significance is represented as * p-value < 0.05, ** p-value < 0.01, *** p-value < 0.001.

correlation between the maximum diameter and the maximum and mean TAWSS was found, whereas a positive one was observed between the maximum and mean OSI and the maximum and mean RRT. In the aforementioned datasets the p-value was < 0.001 [95]. Weak correlations were found between the maximum and mean torsion and all of the hemodynamic parameters, except the maximum torsion and the maximum and mean OSI. The maximum and mean torsion showed a positive correlation with the maximum and mean TAWSS with $\rho \in [0.24, 0.30, 0.27, 0.30]$, while negative correlations were observed between the maximum and mean RRT with $\rho \in [-0.27, -0.29, -0.27, -0.31]$. The mean torsion was negatively correlated with the maximum and mean OSI with $\rho = -0.32$ and $\rho = -0.30$, respectively. In all of the aforementioned cases, the p-values were < 0.05 except the cases of the mean torsion and the maximum OSI and mean RRT where the p-value was < 0.01 in both datasets.

The regression plots between the maximum diameter and hemodynamic parameters are depicted in Figure 6.11(a)-(c) for the infrarenal area, and in Figure 6.11(d)-(f) in the iliac area. In the infrarenal region, the coefficient of determination (R^2) does not have significant values to obtain a reasonable explanation. Specifically, the R^2 for the relationship between the maximum diameter and the mean TAWSS was 0.1584, for the mean OSI 0.2646 and for the mean RRT 0.0244. In contrast, substantially

higher R^2 values were found in the iliac area, indicating a stronger influence on the blood flow. More specifically, for the maximum diameter and the mean TAWSS R^2 was 0.4694, for the mean OSI 0.6505 and for the mean RRT 0.8080. In conclusion, the geometric characteristics of AAAs in the iliac areas have a greater influence on blood flow compared to those in the infrarenal regions.

6.4 Discussion

In this study, we demonstrated that the geometric variations drastically affect blood flow behaviour. The aneurysmal sac size, evaluated with the maximum diameter, plays an important role in the distribution of the velocity field and the path of the streamlines [26, 65, 105, 126, 134]. Larger sacs correspond to lower velocity values, exhibiting substantial recirculation areas. These areas result in the trapping of platelets in a vortex ring that moves in the distal aneurysmal neck. During the vortex break, platelets are released and adhere to regions with low shear stress, contacting the endothelium, thus initiating the formation of a thrombus [26]. In addition, the proximal neck angle affects the flow. Models with larger angles result in more complex and disturbed flows inside the aneurysmal sac with the creation of an intense vortex action that potentially promotes pro-thrombotic conditions in specific wall regions [216]. In contrast, AAAs with more streamlined geometrical aspects showed organized streamlines and velocity fields at the peak systole [198]. At late systole and diastole, the higher diameter models presented trapped streamlines into the sac with larger recirculation regions. As concluded in a previous study, the areas that exhibit flow stagnation during systole and prominent recirculatory flow during diastole are areas where the rupture occurred [134]. The larger proximal angle patients presented separation regions that potentially could lead to pathogenic conditions, endothelium dysfunction and low shear stress values [105, 134]. Finally, flow separation that occurs during late systolic results in vortices forming in the distal end of the aneurysm, which can cause thrombosis formation leading to rupture [105].

Regarding the velocity distribution slices, as depicted in Figure 6.5, they are generally in agreement with previous studies [39, 105]. At peak systole, a jet-like flow is observed at the proximal neck and distal neck (contraction regions) with a favorable side position depending on the angle of the proximal and distal neck. More precisely, the flow at the distal aneurysmal neck is more uniform than that of the proximal aneurysmal neck due to the smaller angles in this area. The late systole and late diastole phases present a disturbed velocity distribution, as expected due to the high mixing of the flow in combination with the irregular shape of the aorta in the aneurysm sac [65, 105]. The recirculation areas created may contribute to the rupture of the vessel wall as described by low WSS, in which the wall could be particularly

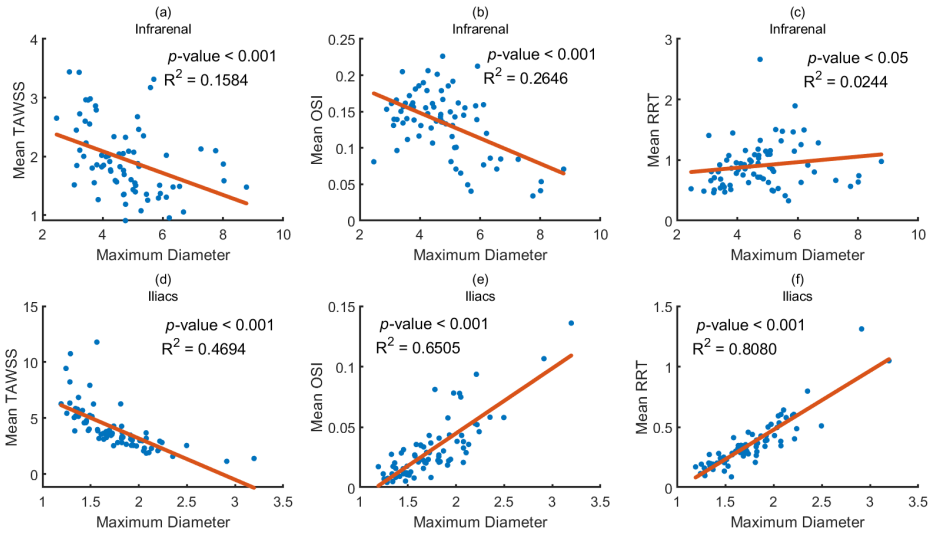

Figure 6.11. Regression analysis between maximum diameter and mean hemodynamic indices. (a–c) Infrarenal region: (a) mean TAWSS versus maximum diameter, (b) mean OSI versus maximum diameter, and (c) mean RRT versus maximum diameter. (d–f) Iliac region: (d) mean TAWSS versus maximum diameter, (e) mean OSI versus maximum diameter, and (f) mean RRT versus maximum diameter. Linear regression lines and coefficients of determination (R^2) are shown, highlighting weaker correlations in the infrarenal aorta and stronger geometry–hemodynamics relationships in the iliac arteries.

weak [26].

Our findings on stress-related indices validate the established perception that the combination of low TAWSS, high OSI, and high RRT is a strong indicator of pathology, as we observed areas with this combination [26, 39, 105, 126, 134, 198]. Low values of TAWSS are related to the formation of thrombus. Biochemically, low values of WSS are related to a decline in the protective nature of the arterial wall against pro-thrombotic activities [215, 216]. The in-study models exhibited areas of low TAWSS, especially in the aneurysmal sacs, high OSI and RRT, in the proximal and distal aneurysmal necks. In Figure 6.6, regions of TAWSS lower than $4\ dyne/cm^2$ are observed, especially in the aneurysm sacs with high diameter, regions of high OSI, values above 0.3 and high RRT values. The discussed regimes have been adopted from the literature [12, 126, 198]. This indicates pathogenic conditions, as high values of OSI, which reveal a highly disturbed flow near the wall, were related to the accumulation of thrombus and the degradation of the vessel wall. This further leads to an acceleration of the development of AAA and atherogenesis [102, 134]. Increased RRT values are associated with increased probability of rupture and their combination with high RRT has been associated with AAA rupture regions [39, 57]. The study of these quantities is fundamental as the identification of these areas is a strong predictor of aneurysm growth and rupture of the vessel wall, as shown in previous studies [12, 126, 134, 198]. We conclude that AAA pathology results in abnormal hemodynamic stresses not only in the infrarenal abdominal aorta, but in the entire aorta, as can be shown in Figure 6.6, where the iliac region and the proximal neck are affected, aligning with the literature [187]. The model T1-P8 was a special case, observing repeated dilation-contraction regions. This abnormal geometric feature resulted in repeated areas of high-low TAWSS, OSI and RRT. The LNH study on AAAs is among the few known to exist, to the best of the authors' knowledge. The structures exhibited fragmented behaviour of the left-handed and right-handed helical structures, especially during the late diastolic phase.

It should be noted that OSI behaviour is not governed by aneurysm sac size alone but primarily reflects the stability of near-wall flow direction over the cardiac cycle. While large aneurysmal sacs often promote flow separation and recirculation, elevated OSI arises mainly when these flow structures are unstable or undergo frequent directional changes. In contrast, large sacs that support relatively coherent and persistent vortical structures with a stable rotational direction may exhibit moderate or even low OSI values despite their size. Therefore, differences in flow directionality and vortex stability can explain the coexistence of both high and low OSI values in aneurysms of similar dimensions.

The stronger geometry–hemodynamics correlations observed in the iliac arteries may be related to their smaller diameter, where geometric variations induce propor-

tionally larger changes in flow acceleration and near-wall shear. In contrast, the enlarged infrarenal aneurysm sac exhibits more diffuse recirculation and competing flow effects, which reduce the sensitivity of hemodynamic indices to individual geometric parameters. Differences in wall compliance between the iliac arteries and the often stiffer aneurysm sac may influence OSI and RRT by modifying local pressure flow phase relationships and near-wall oscillations. Although FSI effects are not included, these compliance-related differences should be considered when interpreting the results.

As presented in Figure 6.10(a), the statistical analysis showed that the maximum diameter, in the infrarenal region, has the biggest influence on the hemodynamic parameters and thus the blood flow behaviour. More specifically, the most correlated parameters were found to be the maximum diameter and the mean TAWSS with $\rho = -0.45$ and p-value < 0.001, indicating a moderate negative correlation. This negative correlation is consistent with flow deceleration and reduced near-wall velocity gradients in dilated areas of the geometry [60]. Statistical significance was also found between the maximum diameter and the maximum TAWSS, maximum and mean OSI as well as the mean RRT. An increase in diameter further enhances the recirculation zones and local varying flow behaviour and thus increases OSI and RRT values. The observed correlations suggest that the maximum diameter is a major component in shaping the hemodynamic behaviour without dominating other geometric parameters [187]. No statistical correlation was found between the maximum curvature and the hemodynamic parameters, whereas the mean curvature was weakly correlated only to the maximum TAWSS. Similarly, only the maximum torsion was found to be weakly statistically correlated with the mean TAWSS, while there was no correlation between the mean torsion and the hemodynamic parameters. The lack of or weakly statistical correlation between hemodynamic parameters and geometric curvature and torsion highlights their secondary role in influencing hemodynamics. While diameter varies due to the aneurysmatic geometric, the curvature and torsion exhibit limited variability, at least in the infrarenal region of the aorta [20].

The results change in the iliac region as depicted in Figure 6.10(b). The strongest statistical correlation was between the maximum diameter and the mean RRT with $\rho = 0.9$, while strong correlations were also found for the rest of the hemodynamic parameters with the maximum diameter. In the iliac area, vessel diameter is smaller compared to the infrarenal region while the geometry presents sharper geometric transitions. Additional flow disturbances originating from the bifurcation area increase the influence on the hemodynamic parameters through near-wall velocity gradient as well as the flow direction and residence time near the walls [29]. Similarly to the infrarenal part, no correlation was found between the maximum curvature and the hemodynamic parameters. In contrast to the infrarenal region, the iliac part of the

aorta did not exhibit correlation between the mean curvature and the hemodynamic parameters. The maximum and mean torsion presented weak statistical correlations, except the maximum torsion and the OSI. The evaluated correlations again suggest that the maximum diameter is the primary key factor for the influence of the hemodynamic parameters.

The most significant observation is that the maximum diameter, in the infrarenal part, showcased negative correlations between the TAWSS and OSI and positive one with the RRT. This differs in the iliac region, where not only the statistical correlation coefficient became greater for all of the hemodynamic parameters, but in the case of OSI, the correlations became positive [65]. This contrast reflects region-specific hemodynamics, where infrarenal dilation promotes shear reduction and localized oscillations, while in the iliac area, variations in diameter within a smaller, more geometrically constrained lumen amplify flow asymmetry and oscillatory behaviour due to stronger secondary flows and geometric confinement [20, 29]. In conclusion, the iliac region of the aorta, was found to be more influential than the infrarenal part of it, while the maximum diameter appears to be the geometric driver. This shows that multiple geometric variables can influence hemodynamic ones [216].

The regression plots between the maximum diameter and the mean hemodynamic parameters, for the infrarenal part, are depicted in Figure 6.11(a)-(c) [198]. Since the correlation between them is, at most, moderate, the coefficient of determination has relatively small values, especially compared to the iliacs, as it can be observed in Figure 6.11(d)-(f). The coefficient of determination, in the iliac region, has clearly higher values, further validating the significant correlation in the iliac area of the aorta. Comparing Figure 6.11(b) with Figure 6.11(e) the correlation sign between the maximum diameter and the mean OSI can be depicted with more clarity, since the slope of the trend line in Figure 6.11(b) is negative while in Figure 6.11(e) the trend line is positive.

6.5 Limitations

The limitations of this study lie in the rigid wall assumption as well as the Newtonian nature of blood, which potentially affects oscillatory shear indices and helicity, particularly in highly dilated aneurysms. While the rigid-wall assumption utilized in this chapter provides valuable insights, there is still a limitation on the pulsating wall stresses. Fully coupled fluid-structure interaction modelling offers a more comprehensive study on capturing how the interplay between blood flow and the arterial wall affects the risk of AAA rupture. The non-Newtonian blood behaviour is most pronounced at low shear rates. Using a Newtonian model may underestimate viscosity in these regions. In the present study, the Newtonian assumption may lead to a

slight underestimation of viscosity within low-velocity recirculation zones inside the aneurysm sac. Consequently, local TAWSS values in these regions may be slightly underestimated or spatially redistributed. However, the overall comparative trends between geometric configurations are expected to remain qualitatively consistent. The dataset of 74 AAA models is moderate and could be extended with the aim of better generalizing the results of the statistical analysis. In future work, we plan to follow a moving wall methodology fluid-structure interactions (FSI), to compare the rigid wall results with the FSI approach on a targeted high-risk subset, acting as a natural extension of Chapters 4 and 5. Additionally, due to the lack of ILT data for all of the 74 models, we did not include a statistical analysis of its correlation as a morphological aspect. Mean curvature and mean torsion are global centerline-averaged metrics that smooth local geometric distortions. Regions of flow stagnation, large recirculation zones, and the values of the biomedical factors (TAWSS, OSI, RRT) are highly associated with the ILT formation. This is clinically critical because while ILT may cushion the wall mechanically, it biologically degrades the underlying tissue, ultimately accelerating wall weakening and elevating rupture risk. As a result, pronounced local bending or twisting may not be fully captured by these measures, potentially under-representing localized flow disturbances and contributing to moderate geometry–haemodynamics correlations. Patient-specific in vivo flow or pressure measurements were not available to validate the inlet waveforms derived from the 0D–1D model. The inlet conditions were therefore generated using a multiscale circulation model calibrated to physiological pressure ranges. While variations in inlet waveforms may affect absolute haemodynamic values, prior studies suggest that relative spatial patterns and correlation trends are less sensitive to moderate boundary condition variations. Finally, 4D MRI data could validate our results and help to enhance our methodology to achieve more accurate results.

6.6 Conclusion

Using multiscale 0D–1D–3D simulations of 74 patient-specific abdominal aortas, we quantified how aneurysmal geometry changes flow patterns and WSS-related biomechanical indices. Several robust conclusions emerge:

- The proximal aneurysmal neck and the size of the aneurysm sac have a decisive influence on haemodynamic behaviour, promoting disturbed flow patterns such as flow separation, recirculation zones, and regions of blood stagnation. These features closely coincide with areas exhibiting low wall shear stress (WSS)
- Pathogenic values of low TAWSS ($< 4\,dyne/cm^2$), altered OSI (> 0.3), and increased RRT were consistently observed in the mid aneurysmal sac and near

the proximal and distal aneurysmal necks. These adverse conditions can lead to the formation of thrombus, endothelial dysfunction, and wall weakening.

- LNH analysis revealed fragmented helical flow structures, particularly during diastole, indicating disrupted and energetically inefficient flow patterns within AAAs.
- The iliac vessels play a crucial and underrecognized role. The strongest correlations between geometry and haemodynamics arise in the iliac arteries, indicating that aneurysm-induced flow disturbances propagate downstream more prominently than assumed in traditional infrarenal-focused analyses.
- Statistical analysis demonstrated meaningful correlations between geometric and haemodynamic parameters. When the aneurysms were evaluated in two anatomical regions—the infrarenal aorta and the iliac segments the infrarenal portion showed moderate correlations, whereas the iliac arteries exhibited stronger associations. In both regions, maximum diameter emerged as the geometric factor most significantly correlated with the haemodynamic indices.

CHAPTER 7

Aortic Valve Replacements

7.1 Introduction

One of the most critical cardiovascular diseases is the aortic valve disease with high rates of morbidity and mortality. Aortic valve disease is a type of heart valve disease related to the narrowing of the valve, flow regurgitation (leaky valve) and other geometrical and pathophysiological aspects (CAVD etc). In the past, Surgical Aortic Valve Replacement (SAVR) was the only solution for treating this disease, however duringthe last years this has completely changed as Transcatheter Aortic Valve Replacement (TAVR) was introduced. Nowadays, hundreds of thousands of TAVR procedures are performed globally each year [163]. Although initially reserved exclusively for elderly or high-surgical-risk patients, the overwhelming clinical success of TAVR has led to its rapid expansion into younger, lower-risk patient populations.

This demographic shift makes the long-term durability and haemodynamic performance of these transcatheter devices more critical than ever. Despite the success of TAVR, a fundamental material dilemma persists. Currently, valve replacements rely primarily on biological (homograft/tissue) or mechanical options, each with significant drawbacks. Biological valves offer excellent, natural haemodynamics but are prone to structural deterioration, typically degrading within 10 to 20 years and often necessitating a high-risk second replacement surgery. Conversely, mechanical valves—historically evolving from caged-ball designs to modern bileaflet configurations—can last a patient's entire lifetime. However, their unnatural flow patterns require patients to adhere to strict, lifelong anticoagulant (blood-thinning) therapy to prevent severe complications like thrombosis and stroke.

Through the years, there were many designs for the mechanical valves that has changed a lot from the caged ball valve (Starr-Edwards) and the monoleaflet valves to the Bileaflet mechanical valve and the self-expandable percutaneous bioprosthesis nowadays.

Transcatheter aortic valves (TAVs) were introduced as a minimally invasive procedure for the aortic valve replacement. Usually, patients had to do a thoracotomy which was very dangerous. In the case of percutaneous heart valves, there are col-

lapsible so they can fit in small catheters (typically from 5 to 8 mm diameter) and delivered through the endovascular system [120]. Over the course of time and ageing a natural consequence is for the aorta to become less flexible, with a thickness increase at the leaflets usually yielding from calcium deposits. This calcification severely restricts the valve's opening and closing capabilities, a biomechanical disruption that is visually compared to a healthy state in Figure 7.1.

Recent studies contributed to the development of a new-generation of polymeric devices, such as the CARD20, which are designed to improve durability and manufacturability replacing the conventional tissue-based valves [176]. The development of such devices is essentially significant for patients with Bicuspid Aortic Valve (BAV), one of the most common congenital heart abnormalities leading to severe aortic stenosis at an earlier age compared to individuals with a standard tricuspid valve [15]. Most transcatheter valve replacements are designed primarily for symmetric tricuspid anatomies, thus using them in patients with asymmetric BAV results in ill fitting and complications. Consequently, patient-based designs and modelling of TAVR devices is crucial [6, 15].

To model valve movement and its interaction with blood flow, fluid structure interaction approaches are required, such as those we analysed in the previous chapters. The valve compartments are moving creating a displacement which alters significantly the domain and the haemodynamics in the area.

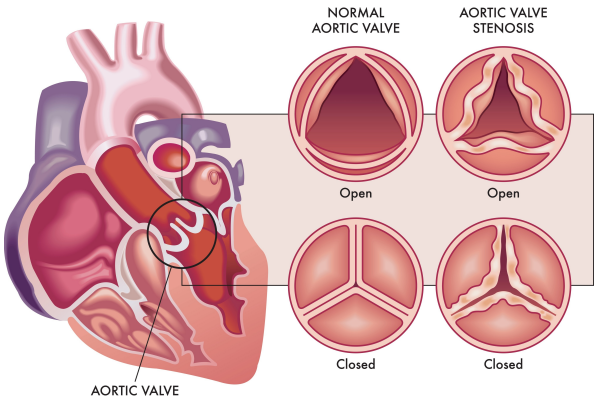

Figure 7.1. Cross-sectional heart model comparing normal and pathological aortic valve function. The restricted opening and closing in the diseased state highlights the biomechanical disruption that necessitates surgical or transcatheter valve replacement.

7.2 Pathologies and Valve Diseases

7.2.1 Calcific Aortic Valve Disease

The condition mentioned above is called calcific aortic valve disease (CAVD) and is characterized by calcification accumulation and thickening of the aortic valve cusps, leading to stenosis and then possible heart failure. Calcific aortic stenosis (CAS) due to calcific aortic valve disease (CAVD) has been a burden leading to high mortality in the Western world during the last 30 years. Calcification usually occurs on the aortic side of the valve and it is similar to bone formation. The anatomical overview of this region and the primary haemodynamic pathway affected by CAVD are illustrated in Figure 7.2.

Although valve replacement can improve patients' lives, constant monitoring is necessary accompanied with regular blood thinning medication.

The calcification of leaflets can alter blood flow through the valve rapidly.

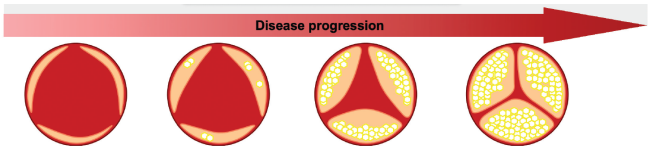

Figure 7.2. Anatomical overview of the heart chambers and the primary haemodynamic pathway.

7.2.2 Clinical Implications: Flow-Induced Thrombogenic Risk

The abnormal flow conditions generated by prosthetic or diseased aortic valves, characterized by areas of elevated shear stress flow stagnation, and recirculation, are the main factors for shear-induced platelet activation (SIPA) [16, 77]. Even brief exposure to high shear stresses during the cardiac cycle can drive platelets over their activation threshold, initiating the coagulation cascade in the absence of chemical agonists [77, 206].

To evaluate the thrombogenic potential, Fluid-Structure Interaction (FSI) modelling is the most efficient approach [16]. FSI approaches enable capturing the dynamic kinematics of leaflets, allowing for precise resolution of transient turbulent stresses, regurgitant jets, and shed vortices in the valve's wake [16, 206]. These dynamic features are critical, as they can trap platelets, increasing their residence time in "hot-spot" flow regions and facilitating aggregation [206].

To quantify thrombogenic risk, virtual platelets are injected into the FSI flow field and utilizing a Lagrangian particle tracking approach to compute their stress loading

histories [16, 77]. The cumulative stress on platelets is calculated as Stress Accumulation (SA) [77]. Furthermore, recent advancements in platelet activation models demonstrate that the dynamic shear loading rates, specifically the rapid acceleration and deceleration of flow characteristic of heart valves, have a significant impact on platelet sensitization and activation [168].

To comprehensively evaluate a valve's performance, the Device Thrombogenicity Emulation (DTE) methodology collapses the stress accumulation of thousands of platelet trajectories into a Probability Density Function [44, 77]. This PDF serves as a "thrombogenic footprint," providing a global metric of a device's potential for platelet activation [44, 43]. Utilizing such FSI-based thrombogenic risk assessments allows for unparalleled optimization of valve design, identifying parameters like leaflet curvature and clearance gaps that can be modified to reduce peak stresses and mitigate the need for long-term anticoagulation therapy [16, 43].

7.3 Anatomy and Pathophysiology of Aortic Valve

Heart is divided in many areas, the aorta and the left ventricle are connected by the aortic valve which enables the transportation of the oxygen rich blood to the rest of the body through the aorta and also prevents backward flow of blood. The specific heart components and the directional movement of blood through the aortic valve are shown in Figure 7.3.

The movement of the valve is caused due to the pressure gradient between the left ventricle and the aorta leading also to extensive exposure of the leaflets to hydrodynamic forces (compression, stretching, and bending). Blood flow here can be complex especially with the development of patterns such as vortices, jet flow and recirculation

Transcatheter aortic valve (TAV) devices consist of three leaflets and are self-expanding or mechanically expanded [199]. The stent is divided into the inflow and outflow tracts. In the inflow tract area are located the three leaflets and the skirt.

All valve prototypes need to satisfy the ISO 5840 standard to verify safety. The development of a suitable valve replacement needs to consider some basic characteristics on the haemodynamic, structural and biological areas etc to verify its durability and functionality. More specifically the characteristics are presented below as they have been identified on previous studies [35, 163]. These primary design requirements, categorized by their respective functional domains, are summarized in Table 7.1

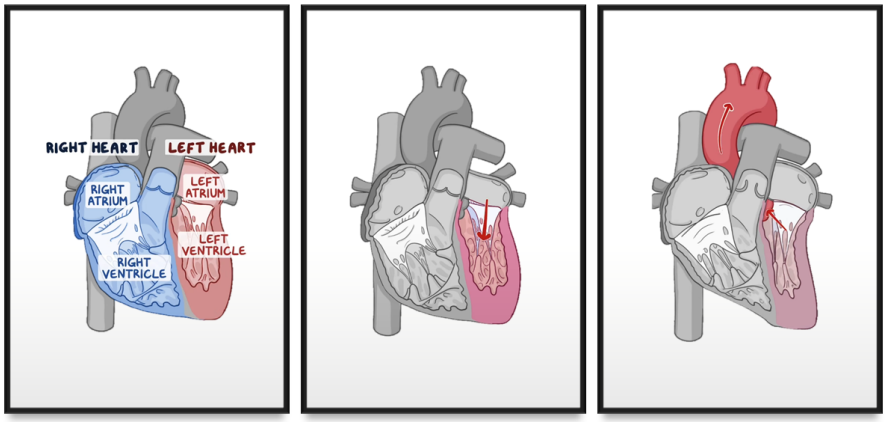

Figure 7.3. Heart components and movement of blood through the aortic valve.

Valve requirements [35]

Category	Requirements
Haemodynamic	• Minimum mean systolic trans-valvular pressure drop • Minimum regurgitation • Large effective orifice area • Minimum loss of ventricular energy • Minimum damage to blood cells and low thrombogenicity
Structural	• No dehiscence • Long durability (FDA: $\geq$ 5 years biological, $\geq$ 15 years mechanical) • Stable physical and geometric features
Biological	• Chemically inert, not damaging blood elements • Minimal tendency to calcify • Integration with host tissues • Good anatomical matching

Surgical	• Easy to implant • Allow alternative surgical approaches • Easy to replace • Wide range of sizes
Manufacture	• Easy to manufacture • Consistent procedure • Suitable for quality control • Easy to sterilize, store, and transport

Table 7.1. Primary design requirements for prosthetic heart valves categorized by functional domains.

Numerous studies have shown that patient-specific design of medical devices and replacements can reduce mortality and morbidity [46, 62, 124]. Meeting all these requirements simultaneously is a very challenging task in engineering. Modern design pipelines for prosthetic heart valves require extensive *in silico* modelling and optimization due to the multifactorial complexity.

7.4 Mathematical Modelling

7.4.1 Geometric Characteristics

The key features for the leaflets geometry are the belly curvature, referring to the angle of the surface of the leaflet, and the attachment curvature, which is the attachment region to the stent. The three-dimensional representation of these features, along with the varying grid densities utilized for each leaflet to ensure numerical accuracy, is illustrated in Figure 7.4. It has been shown that the optimization of these devices, based on the geometric characteristics, accompanied with the patient specific modelling can offer improved performance and minimize thrombogenicity due to the prosthetic valve [16].

7.4.2 Fluid Flow

Blood flow through the valve replacement can be described using the Navier Stokes Equations as we have already established in the previous chapters. The dimensionless

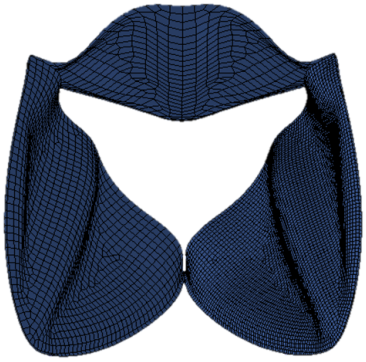

Figure 7.4. Valve Geometry with different grid realization for each leaflet - refining grid.

form of equations is utilized as shown below:

$$\nabla \cdot \bar{q} = 0 \tag{7.1}$$

$$\frac{\partial \bar{q}}{\partial t} + (\bar{q} \cdot \nabla)\bar{q} = -\nabla p + \frac{1}{Re}\nabla^2 \bar{q} \tag{7.2}$$

where $\bar{q} = (u, v, w)$ is the velocity, p the pressure, and $Re = \frac{u_0 R}{\nu}$ the Reynolds number, and ν the kinematic viscosity. Reynolds number in this location can reach $4000 - 6000$ during peak systole, meaning the flow can be transitional or turbulent.

Flow fields produced by different valve opening are characterized in terms of viscous shear, vorticity and Reynolds shear stress [43, 206].

7.4.3 Aortic Valves Mathematical Formulation

Heart valves undergo severe deformations due to the haemodynamic load and they need to remain durable. Valve leaflets are soft and almost incompressible tissues composed of collagen and elastin. Their mechanical behaviour consists of large deformations, pronounced strain-stiffening, and anisotropy. These features make the material suitable for description by hyperelastic models. There is a need to model mathematically the material of the valve to simulate the stresses, strains and predict the performance of the valve. There is a variety of groups of valve replacement with different materials, thus for biological valves meaning natural tissue an anisotropic

material is used, while for polymeric valves isotropic elastomers (rubber-like) are utilized.
Usually, linear models are suitable for cases with linear stress-strain relation and minor displacements gradients [27, 122]. Hyperelastic models are commonly used to describe the mechanical response of many soft biological tissues [181]. Most commonly, the hyperelastic models of Mooney-Rivlin and Ogden are employed.

Incompressible Hyperelastic Materials

The mechanical response of hyperelastic materials is derived from the strain-energy function W, which depends on the tensor of the deformation. For isotropic material W can be expressed as

$$W = W(I_1, I_2, I_3),$$

where $I_1 = tr(C)$, $I_2 = \frac{1}{2}\left[I_1^2 - tr(C^2)\right]$ and $I_3 = det(C)$ where $C = F^T F$ is the right Cauchy-Green deformation tensor.

Mooney-Rivlin Mathematical Model

In non-linear models lower compressive and higher tensile stresses tend to occur on the leaflets, and the deformation was more complex during the movement of the valve [151]. This model for incompressible biological tissues is defined by the following two-parameters strain energy model:

$$W_M = C_1(\bar{I}_1 - 3) + C_2(\bar{I}_2 - 3) + D_1(J-1)^2, \tag{7.3}$$

where W_M is the strain energy density of the current model, C_i, D_1 are the coefficients that define the material and I_1 is the first invariant of the Cauchy-Green deformation tensor.
The Mooney-Rivlin model is commonly used in cardiovascular applications, as it is a simple but stable approach with only two parameters. However, this model refers to isotropic materials, which means a limitation in capturing the directional stiffness induced by collagen fibres. Additionally, the two-term polynomial form of the model may not be able to describe the steep strain-stiffening behaviour of the leaflets.

Ogden Mathematical Model

The Ogden model, introduced in 1972, is a hyperelastic model used for the prediction of nonlinear stress-strain behaviour of rubber or polymers and the strain energy density function is defined as

$$W = \sum_{i=1}^{N} \frac{\mu_i}{\alpha_i} \left(\lambda_1^{\alpha_i} + \lambda_2^{\alpha_i} + \lambda_3^{\alpha_i} - 3\right), \tag{7.4}$$

where $\lambda_j,\ j = 1, 2, 3$ is the principal stretch ratio, and μ_i, α_i are the constants determining the material.
The Ogden model has been employed extensively in biomedical applications, such as the ones we are interested in. Its main advantage is that it provides better approximation of the large-deformations compared to the polynomial models. In both models the reliability depends on the accurate identification of the parameters and validation.

7.4.4 Particles & Smooth–Particle Hydrodynamics

Here blood is also considered as particles and another approach is used to describe the fluid flow problem. Blood consists of four main components: plasma, red and white blood cells, and platelets which all have different phases and material properties. Therefore the assumption of a viscous Newtonian fluid can be valid for all the components, except from the platelets. Platelets are smaller than the other constituents and can be seen as small reactive bodies. Smoothed particle hydrodynamics (SPH) is a numerical method that approximates the solution of equations, especially in fluid mechanics, by replacing the fluid with a set of particles instead of utilizing meshes [133]. In this approach instead of discretizing the domain like most methods, SPH represents fluid with a set of particles that retain their physical properties (mass, velocity, pressure, etc.) but can change drastically, for example during blood coagulation. Even instantaneous changes of the physical properties can significantly affect the behaviour of the flow. This gives a big advantage in cases where there are more than one material. The problems are described by the Lagrangian form of the Navier-Stokes equations as shown below:

$$\rho_i = \sum_j m_j W(\mathbf{r}_i - \mathbf{r}_j, h), \tag{7.5}$$

$$\frac{d\mathbf{v}_i}{dt} = -\sum_j m_j \left(\frac{p_i}{\rho_i^2} + \frac{p_j}{\rho_j^2} + \Pi_{ij}\right) \nabla W(\mathbf{r}_i - \mathbf{r}_j, h) + \mathbf{g} \tag{7.6}$$

The particle approximation of a function is

$$\Pi^h f(x) = \int f(y) W(x - y, h) dy, \tag{7.7}$$

where W is the kernel function defined as

$$W(\mathbf{x}, h) = \frac{1}{h(\mathbf{x})^d}\theta(\mathbf{x}), \tag{7.8}$$

where d is the dimension and $h$the smoothing length (changes in time and space).
For the θ function, it is necessary to be centrally peaked, therefore the most common kernel to use is a cubic B-spline defined as:

$$\theta(u) = C \times \begin{cases} 1 - \frac{3}{2}u^2 + \frac{3}{4}u^3, & for \ \ |u| \leq 1 \\ \frac{1}{4}(2-u)^3, & for \ \ 1 \leq |u| \leq 2 \\ 0 & for \ \ 2 < |u| \end{cases} \tag{7.9}$$

where C is a normalisation constant depending on the dimensions of the space.
The effective orifice area (EOA) is the smallest cross-sectional area of the blood flow jet that passes through the aortic valve, representing the effective opening for flow, not the physical size of the valve itself. It is a critical parameter for assessing the severity of aortic stenosis (a narrowing of the valve) and is typically calculated using the following formula

$$EOA = \frac{Q_{RMS}}{51.6 \times \sqrt{\frac{\Delta p}{\rho}}}, \tag{7.10}$$

the EOA is calculated in cm^2, Q_{RMS} is the root mean square of forward flow (mL/s) during the positive differential pressure period ($\Delta p > 0$), Δp ($mmHg$) is the mean pressure difference, and ρ (g/cm^3) is the density of the fluid [80, 199].
Furthermore, the SPH approach tracks the cumulative stress histories of individual platelets along their specific flow trajectories, providing useful information to evaluate the thrombogenic footprint of the prosthetic device [43, 206].

7.5 Preliminary Results

An FSI framework was implemented via the incompressible computational fluid dynamics multi-physics solver of the ANSYS LS-DYNA software. The leaflets-solid domain - and the fluid domain-particles were modeled to describe the leaflet motion and the interaction with the blood particles, such as red blood cells (RBCs). The specific modelling approach and the corresponding computational meshes for both the leaflets and the fluid particles are illustrated in Figure 7.5 To accurately simulate the dynamic cardiac cycle, time-varying pressure waveforms were applied as boundary conditions at the ventricular inlet and aortic outlet of the fluid domain to simulate the opening and closing kinematics of the leaflets and capturing the fluid-structure interaction during the cardiac cycle.

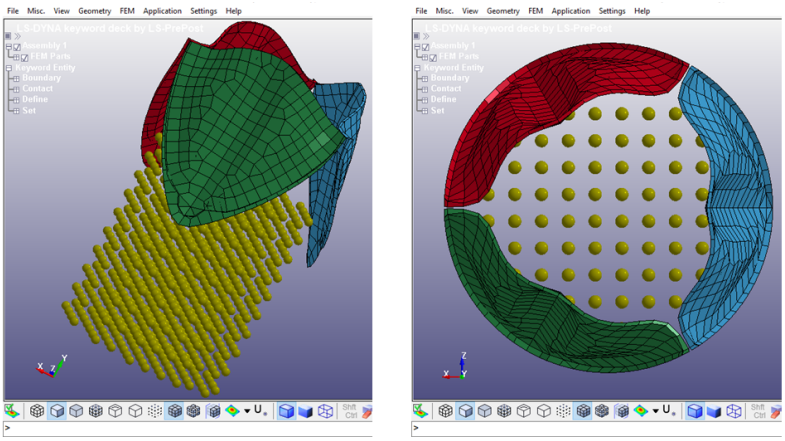

Figure 7.5. Modelling approach and computational meshes for the leaflets and the particles.

The leaflets are described by a hyperelastic material as described in the previous section. The particles could represent the red blood cells or the platelets passing through the valve. Figure 7.6 presents the transient kinematic response of the valve at different time steps, highlighting the complex interaction between the moving solid boundaries and the fluid particles. Initially, the fluid particles move towards the valve, while when reaching the solid part the deformation of the fluid starts and higher values of stresses occur. In the second step the fluid passes through the valve opening and the particles exhibit higher values of stress as they are forced into a smaller cross-sectional area. As the fluid particles exit the valve stress values decrease, but simultaneously a "chaotic" pattern starts to form as the fluid expands back to the vessel boundaries.

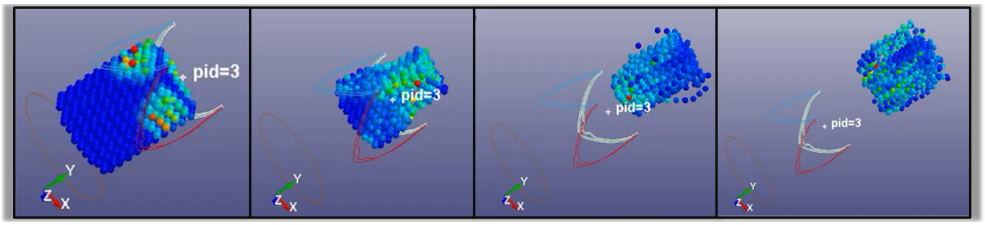

Figure 7.6. Transient kinematic response of the prosthetic valve and corresponding fluid particle trajectories over the cardiac cycle. The fluid particles are color-coded to indicate the instantaneous stress exposure (in dynes/cm^2) induced by the fluid-structure interaction.

The quantification of these dynamics is further explored in Figure 7.7, which relates

individual particle stress accumulation to the overall statistical risk of thrombus formation. Specifically, the "loading history" of blood elements, while the probability density function, Figure 7.7b) provides a global view of the shear stress distribution.

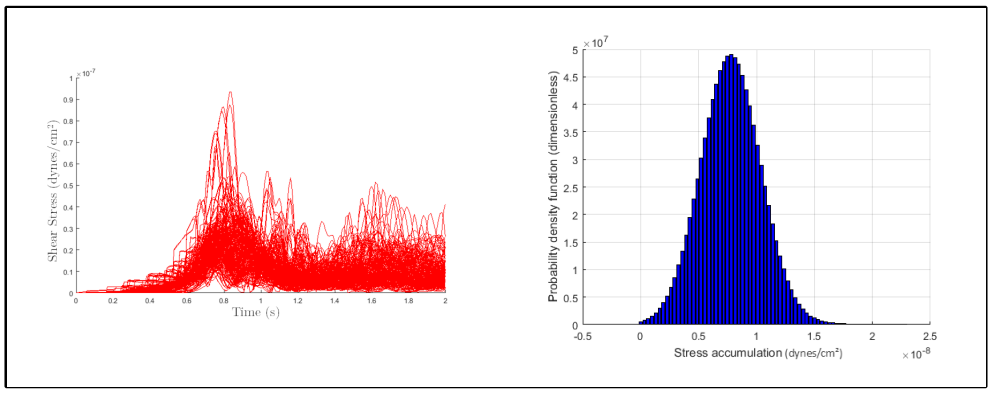

Figure 7.7. Quantification of fluid stress dynamics during valve operation. a) Transient stress accumulation profiles for individual blood particles as they traverse the expanding leaflet orifice. b) A probability density function illustrating the statistical distribution of particle stresses, serving as a critical indicator of flow-induced thrombogenic risk.

The comparison between experimental data, the FSI approach introduced by Piatti et al. [155], and the results obtained from our current SPH-based model is depicted in Figure 7.8. The comparison reveals a strong agreement across the entire cardiac cycle, particularly in capturing the peak flow rate and the duration of the systolic phase.
The validation of this FSI approach is ensured through both its internal consistency and a direct comparison with the numerical results of Piatti et al. [155].
Figure 7.8 presents the comparison among the experimental and numerical results and the results of this study. Following this framework, the results of this study are divided into four stages.
In the Von Mises stress contours, the deformation of the leaflets during the cardiac cycle follows a specific path. In the opening stages (I-II), the model presents the transition to a triangular orifice, essential for minimizing energy loss. In this study, the maximum Von Mises Stress was 0.692 MPa, which closely matches the results of [155] where the peak value reached 0.70 MPa. The highest stress concentrations are observed at the attachment basis of the valve, where the maximum curvature change occurs during the opening phase.
The accurate prediction of leaflet stresses is essential for structural durability analysis. FSI methodologies allow the evaluation of the flow fields surrounding the leaflets,

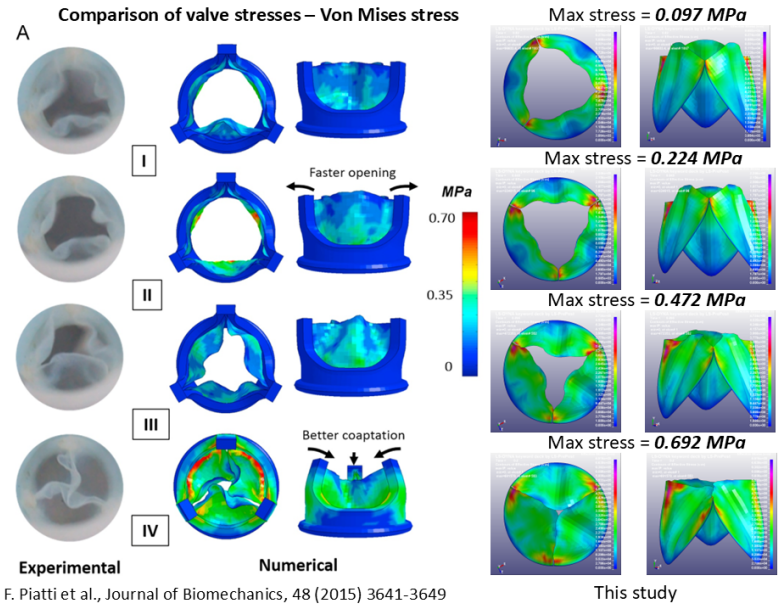

Figure 7.8. Comparison of the experimental data, computational approach introduced by Piatti et.al [155] and the data obtained from this approach during the cardiac cycle.

leading to comprehensive thrombogenic risk assessments of TAVR devices, while optimizing designs to minimize non-physiological flow patterns before clinical implementation [16, 43].

7.6 Limitations

Although, the development of heart valve replacements has improved over the years several complications still exist that need to be addressed especially with the expansion of these replacements to younger patients. Paravalvular leak (PVL), structural valve deterioration (SVD), permanent pacemaker implantation (PPI), valve thrombosis and strokes are the most common complications [51]. Furthermore, studies have revealed that polymeric valves tend to have problems with flow owing to calcification, thrombogenicity, high tensile stresses borne by the material, and biodegradation, which manifests as an overall lack of durability [103, 163].
This chapter introduces a mathematical approach for modelling the interaction of the valve leaflets with the blood cells. These modelling approaches are significant because they can introduce in-silico solutions of a very difficult problem such as the heart valve dynamics. A primary limitation of the current framework is that it does

not account for the immense variability in surgical deployment. Recent computational studies have shown that the orientation and positioning of the transcatheter device within the heart drastically impact postoperative outcomes, particularly in complex BAV patients. Variations in deployment orientation can dictate the severity of Paravalvular Leak (PVL) and the risk of coronary obstruction [5, 86].

7.7 Conclusions

The expansion of transcatheter aortic valve replacement, to younger populations and with lower risk, has increased the need for prosthetic valves. The selection of these valves needs to be carefully done considering all the required features. In this chapter, a fluid-structure interaction approach is presented to describe the complex motion of fluid and its interaction with the valve leaflets. Additionally, the smoothed particle method is analyzed for blood flow and hyperelastic models are presented for the solid mechanics, in this case the valves. The results validate this approach and align with the corresponding experimental results.
While prosthetic heart valves present many limitations, future steps require the integration of patient-specific studies. This step could provide advanced patient-specific modelling and the development of new, safe, durable, and optimized aortic valve replacements.

Bibliography

[1] Abi-Abdallah, D., Drochon, A., Robin, V., and Fokapu, O. Pulsed magnetohydrodynamic blood flow in a rigid vessel under physiological pressure gradient. *Computer Methods in Biomechanics and Biomedical Engineering 12*, 4 (2009), 445–458.

[2] Alastruey, J., Passerini, T., Formaggia, L., and Peiró, J. Physical determining factors of the arterial pulse waveform: theoretical analysis and calculation using the 1-D formulation. *Journal of Engineering Mathematics 77.1* (2012), 19–37.

[3] Alblas, D., Suk, J., Brune, C., Yeung, K. K., and Wolterink, J. M. Sire: Scale-invariant, rotation-equivariant estimation of artery orientations using graph neural networks. *Medical Image Analysis* (2025), 103467.

[4] Anagnostakos, J., and Lal, B. K. Abdominal aortic aneurysms. *Progress in Cardiovascular Diseases 65* (2021), 34–43.

[5] Anam, S., Kovarovic, B., Parikh, P., Slepian, M., Hamdan, A., Haj-Ali, R., and Bluestein, D. Impact of device type and orientation on post-transcatheter aortic valve replacement complications in bicuspid aortic valve patients: A computational study. *ASAIO Journal 72*, 1 (2026), 20–31.

[6] Anam, S. B., Kovarovic, B. J., Ghosh, R. P., Bianchi, M., Hamdan, A., Haj-Ali, R., and Bluestein, D. Assessment of paravalvular leak severity and thrombogenic potential in transcatheter bicuspid aortic valve replacements using patient-specific computational modeling. *Journal of Cardiovascular Translational Research 15*, 4 (2022), 834–844.

[7] Antiga, L., Piccinelli, M., Botti, L., Ene-Iordache, B., Remuzzi, A., and Steinman, D. A. An image-based modeling framework for patient-specific

computational hemodynamics. *Medical & Biological Engineering & Computing 46*, 11 (2008), 1097–1112.

[8] Anzt, H., Boman, E., Falgout, R., Ghysels, P., Heroux, M., Li, X., Curfman McInnes, L., Tran Mills, R., Rajamanickam, S., Rupp, K., Smith, B., Yamazaki, I., and Meier Yang, U. Preparing sparse solvers for exascale computing. *Philosophical Transactions of the Royal Society A 378*, 2166 (2020), 20190053.

[9] Argyris, J. H., and Kelsey, S. *Energy Theorems and Structural Analysis*, vol. 960. Springer, 1960.

[10] Arko, F. R., Murphy, E. H., Davis III, C. M., Johnson, E. D., Smith, S. T., and Zarins, C. K. Dynamic geometry and wall thickness of the aortic neck of abdominal aortic aneurysms with intravascular ultrasonography. *Journal of Vascular Surgery 46*, 5 (2007), 891–897.

[11] Arzani, A. Accounting for residence-time in blood rheology models: Do we really need non-newtonian blood flow modelling in large arteries? *Journal of The Royal Society Interface 15*, 146 (2018), 20180486.

[12] Bappoo, N., Syed, M. B. J., Khinsoe, G., Kelsey, L. J., Forsythe, R. O., Powell, J. T., Hoskins, P. R., McBride, O. M. B., Norman, P. E., Jansen, S., Newby, D. E., and Doyle, B. J. Low shear stress at baseline predicts expansion and aneurysm-related events in patients with abdominal aortic aneurysm. *Circulation: Cardiovascular Imaging 14*, 12 (2021), 1112–1121.

[13] Basciano, C., Kleinstreuer, C., Hyun, S., and Finol, E. A relation between near-wall particle-hemodynamics and onset of thrombus formation in abdominal aortic aneurysms. *Annals of Biomedical Engineering 39* (2011), 2010–2026.

[14] Batchelor, G. K. *An Introduction to Fluid Dynamics*. Cambridge University Press, 2000.

[15] Baylous, K., Helbock, R., Kovarovic, B., Slepian, M. J., and Bluestein, D. Development of a polymeric tavr device tailored to bicuspid aortic valve patients using in silico design optimization and evaluation. *Annals of Biomedical Engineering* (2025), 1–16.

[16] Baylous, K., Kovarovic, B., Paz, R. R., Anam, S., Helbock, R., Horner, M., Slepian, M., and Bluestein, D. Thrombogenic risk assessment of transcatheter prosthetic heart valves using a fluid-structure interaction approach. *Computer Methods and Programs in Biomedicine 257* (2024), 108469.

[17] Bazilevs, Y., Takizawa, K., and Tezduyar, T. E. *Computational Fluid–Structure Interaction: Methods and Applications*. John Wiley & Sons, 2013.

[18] Bender, C. M., and Orszag, S. A. *Advanced Mathematical Methods for Scientists and Engineers I: Asymptotic Methods and Perturbation Theory*. Springer Science & Business Media, 2013.

[19] Bercovier, M., and Pironneau, O. Error estimates for finite element method solution of the Stokes problem in the primitive variables. *Numerische Mathematik 33*, 2 (1979), 211–224.

[20] Biasetti, J., Gasser, T. C., Auer, M., Hedin, U., and Labruto, F. Hemodynamics of the normal aorta compared to fusiform and saccular abdominal aortic aneurysms with emphasis on a potential thrombus formation mechanism. *Annals of Biomedical Engineering 38*, 2 (2010), 380–390.

[21] Biasetti, J., Hussain, F., and Gasser, T. C. Blood flow and coherent vortices in the normal and aneurysmatic aortas: a fluid dynamical approach to intraluminal thrombus formation. *Journal of The Royal Society Interface 8*, 63 (2011), 1449–1461.

[22] Biraki, K. N., Kyriakoudi, K. C., Felias, A. C., and Xenos, M. A. The finite element method with applications to fluid mechanics. *Mathematical Analysis, Differential Equations and Applications* (2024), 139–174.

[23] Blazek, J. *Computational Fluid Dynamics: Principles and Applications*. Butterworth-Heinemann, 2015.

[24] Bluestein, D., Dumont, K., De Beule, M., Ricotta, J., Impellizzeri, P., Verhegghe, B., and Verdonck, P. Intraluminal thrombus and risk of rupture in patient specific abdominal aortic aneurysm–fsi modelling. *Computer Methods in Biomechanics and Biomedical Engineering 12*, 1 (2009), 73–81.

[25] Bluestein, D., Niu, L., Schoephoerster, R. T., and Dewanjee, M. K. Steady flow in an aneurysm model: Correlation between fluid dynamics and blood platelet deposition. *Journal of Biomechanical Engineering 118*, 3 (1996), 280–286.

[26] Boniforti, M. A., Di Bella, L., and Magini, R. On the role of hemodynamics in predicting rupture of the abdominal aortic aneurysm. *Journal of Zhejiang University - Science A 22*, 12 (2021), 957–978.

[27] Borowski, F., Sämann, M., Pfensig, S., Wüstenhagen, C., Ott, R., Kaule, S., Siewert, S., Grabow, N., Schmitz, K.-P., and Stiehm, M. Fluid-structure interaction of heart valve dynamics in comparison to finite-element analysis. *Current Directions in Biomedical Engineering 4*, 1 (2018), 259–262.

[28] Bose, S. *Numerical Methods of Mathematics Implemented in Fortran*. Forum for Interdisciplinary Mathematics. Springer Nature Singapore, 2019.

[29] Boutsianis, E., Guala, M., Olgac, U., Wildermuth, S., Hoyer, K., Ventikos, Y., and Poulikakos, D. Cfd and ptv steady flow investigation in an anatomically accurate abdominal aortic aneurysm. *Journal of Biomechanical Engineering 131* (2009).

[30] Braaten, M. E., and Shyy, W. Comparison of iterative and direct solution methods for viscous flow calculations in body-fitted co-ordinates. *International Journal for Numerical Methods in Fluids 6*, 6 (1986), 325–349.

[31] Braaten, M. E., and Shyy, W. Motion of a spherical and direct solution methods for viscous flow calculations in body-fitted co-ordinates. *International Journal for Numerical Methods in Fluids 6*, 6 (1986), 325–349.

[32] Brackbill, J. U., Kothe, D. B., and Zemach, C. A continuum method for modeling surface tension. *Journal of Computational Physics 100*, 2 (1992), 335–354.

[33] Brenner, S. C., Scott, L. R., and Scott, L. R. *The Mathematical Theory of Finite Element Methods*, vol. 3. Springer, 2008.

[34] Brezzi, F., and Fortin, M. *Mixed and Hybrid Finite Element Methods*, vol. 15. Springer Science & Business Media, 2012.

[35] Burriesci, G., Marincola, F. C., and Zervides, C. Design of a novel polymeric heart valve. *Journal of Medical Engineering & Technology 34*, 1 (2010), 7–22.

[36] Cebeci, T., and Bradshaw, P. *Physical and Computational Aspects of Convective Heat Transfer*. Springer Science & Business Media, 2013.

[37] Cebull, H. L., Aremu, O. O., Kulkarni, R. S., Zhang, S. X., Samuels, P., Jermy, S., Ntusi, N. A. B., and Goergen, C. J. Simulating subject-specific aortic hemodynamic effects of valvular lesions in rheumatic heart disease. *Journal of Biomechanical Engineering 145*, 11 (2023), 111003.

[38] Chapra, S. C., and Canale, R. P. *Numerical Methods for Engineers*, vol. 1221. McGraw-Hill New York, 2011.

[39] Che, Y., Cao, X., Cao, Z., Zhang, Y., Zhu, J., Shu, C., Luo, M., and Zhang, X. Rupture prediction of medium to large-sized abdominal aortic aneurysm combining wall shear stress-related parameters and anatomical characteristics: A computational, experimental, and statistical analysis. *Physics of Fluids 37* (01 2025), 011908.

[40] Choke, E., Cockerill, G., Wilson, W., Sayed, S., Dawson, J., Loftus, I., and Thompson, M. A review of biological factors implicated in abdominal aortic aneurysm rupture. *European Journal of Vascular and Endovascular Surgery 30*, 3 (2005), 227–244.

[41] Choudhury, S., Anupindi, K., and Patnaik, B. Influence of wall shear stress and geometry on the lumen surface concentration of low density lipoprotein in a model abdominal aortic aneurysm. *Physics of Fluids 31*, 1 (2019).

[42] Chrimatopoulos, G., Tzirtzilakis, E. E., and Xenos, M. A. Magnetohydrodynamic and ferrohydrodynamic fluid flow using the finite volume method. *Fluids 9*, 1 (2023), 5.

[43] Claiborne, T. E., Xenos, M., Sheriff, J., Chiu, W.-C., Soares, J., Alemu, Y., Gupta, S., Judex, S., Slepian, M. J., and Bluestein, D. Toward optimization of a novel trileaflet polymeric prosthetic heart valve via device thrombogenicity emulation. *ASAIO Journal 59*, 3 (2013), 275–283.

[44] Claiborne, T. E., Xenos, M., Sheriff, J., Peter, D., Alemu, Y., Kato, Y., Pinchuk, L., Einav, S., Jesty, J., and Bluestein, D. Development and optimization of a novel polymeric prosthetic heart valve using the device thrombogenicity emulation (dte) methodology. In *Summer Bioengineering Conference* (2012), vol. 44809, American Society of Mechanical Engineers, pp. 465–466.

[45] Conejo, A. J., and Baringo, L. *Power System Operations*, vol. 11. Springer, 2018.

[46] Conti, C. A., Votta, E., Della Corte, A., Del Viscovo, L., Bancone, C., Cotrufo, M., and Redaelli, A. Dynamic finite element analysis of the aortic root from MRI-derived parameters. *Medical Engineering & Physics 32*, 2 (2010), 212–221.

[47] Courant, R., Friedrichs, K., and Lewy, H. On the partial difference equations of mathematical physics. *IBM Journal of Research and Development 11*, 2 (1967), 215–234.

[48] Cramer, K. R., and Pai, S.-I. *Magnetofluid Dynamics for Engineers and Applied Physicists*. McGraw-Hill, New York, 1973.

[49] Cyron, C. J., Wilson, J. S., and Humphrey, J. D. Mechanobiological stability: a new paradigm to understand the enlargement of aneurysms? *Journal of the Royal Society Interface 11*, 100 (2014), 20140680.

[50] Czaja, B., Závodszky, G., Azizi Tarksalooyeh, V., and Hoekstra, A. Cell-resolved blood flow simulations of saccular aneurysms: Effects of pulsatility and aspect ratio. *Journal of The Royal Society Interface 15*, 146 (2018), 20180485.

[51] Dasi, L. P., Hatoum, H., Kheradvar, A., Zareian, R., Alavi, S. H., Sun, W., Martin, C., Pham, T., Wang, Q., Midha, P. A., et al. On the mechanics of transcatheter aortic valve replacement. *Annals of Biomedical Engineering 45*, 2 (2017), 310–331.

[52] Davidson, P. A. *Introduction to Magnetohydrodynamics*. Cambridge University Press, 2017.

[53] Davies, M. Aortic aneurysm formation. *Circulation 98* (1998), 193–195.

[54] De Moura, C. A., and Kubrusly, C. S. The Courant–Friedrichs–Lewy (CFL) condition. *AMC 10*, 12 (2013), 45–90.

[55] De Nisco, G., Kok, A. M., Chiastra, C., Gallo, D., Hoogendoorn, A., Migliavacca, F., Wentzel, J. J., and Morbiducci, U. The atheroprotective nature of helical flow in coronary arteries. *Annals of Biomedical Engineering 47*, 2 (2019), 425–438.

[56] Deville, M. O., Fischer, P. F., Mund, E., et al. *High-Order Methods for Incompressible Fluid Flow*, vol. 9. Cambridge University Press, 2002.

[57] Di Achille, P., Tellides, G., Figueroa, C. A., and Humphrey, J. D. A haemodynamic predictor of intraluminal thrombus formation in abdominal aortic aneurysms. *Proceedings of the Royal Society A: Mathematical, Physical and Engineering Sciences 470*, 2172 (2014), 20140163.

[58] Di Martino, E. S., Guadagni, G., Fumero, A., Ballerini, G., Spirito, R., Biglioli, P., and Redaelli, A. Fluid–structure interaction within realistic three-dimensional models of the aneurysmatic aorta as a guidance to assess the risk of rupture of the aneurysm. *Medical Engineering & Physics 23*, 9 (2001), 647–655.

[59] Doyle, B. J., McGloughlin, T. M., Kavanagh, E. G., and Hoskins, P. R. From detection to rupture: A serial computational fluid dynamics case study of a rapidly expanding, patient-specific, ruptured abdominal aortic aneurysm. In *Computational Biomechanics for Medicine* (2014), B. Doyle, K. Miller, A. Wittek, and P. M. F. Nielsen, Eds., pp. 53–68.

[60] Dua, M. M., and Dalman, R. L. Hemodynamic influences on abdominal aortic aneurysm disease: Application of biomechanics to aneurysm pathophysiology. *Vascular Pharmacology 53*, 1 (2010), 11–21.

[61] Falkner, V., and Skan, S. LXXXV. Solutions of the boundary-layer equations. *The London, Edinburgh, and Dublin Philosophical Magazine and Journal of Science 12*, 80 (1931), 865–896.

[62] Fan, R., and Sacks, M. S. Simulation of planar soft tissues using a structural constitutive model: Finite element implementation and validation. *Journal of Biomechanics 47*, 9 (2014), 2043–2054.

[63] Fan, T., Wang, J., Wang, X., Chen, X., Zhao, D., Xie, F., and Chen, G. Integrated multidisciplinary approach to aneurysm hemodynamic analysis: Numerical simulation, in vitro experiment, and deep learning. *Frontiers in Bioengineering and Biotechnology 13* (2025), 1602190.

[64] Farooq, U., Hayat, T., Alsaedi, A., and Liao, S. Series solutions of non-similarity boundary layer flows of nano-fluids over stretching surfaces. *Numerical Algorithms 70*, 1 (2015), 43–59.

[65] Fedotova, Y., Kalachev, I., Epifanov, R., Totmina, E., Borisova, K., Lysikov, D., Karpenko, A., and Mullyadzhanov, R. Association of hemodynamics and morphology with local surface growth of abdominal aortic aneurysm using spatial pattern analysis. *Physics of Fluids 37*, 2 (2025), 021919.

[66] Fefferman, C. L. Existence and smoothness of the Navier-Stokes equation. *The Millennium Prize Problems 57*, 67 (2006), 22.

[67] Ferziger, J. H., Perić, M., and Street, R. L. *Computational Methods for Fluid Dynamics*. Springer, 2019.

[68] Figueroa, C. A., Vignon-Clementel, I. E., Jansen, K. E., Hughes, T. J., and Taylor, C. A. A coupled momentum method for modeling blood flow in three-dimensional deformable arteries. *Computer Methods in Applied Mechanics and Engineering 195*, 41-43 (2006), 5685–5706.

[69] Fillinger, M. F., Marra, S. P., Raghavan, M. L., and Kennedy, F. E. Prediction of rupture risk in abdominal aortic aneurysm during observation: wall stress versus diameter. *Journal of Vascular Surgery 37*, 4 (2003), 724–732.

[70] Fletcher, C. A. *Computational Techniques for Fluid Dynamics. Volume 1-Fundamental and General Techniques. Volume 2-Specific Techniques for Different Flow Categories*, vol. 1. 1988.

[71] Formaggia, L., Gerbeau, J.-F., Nobile, F., and Quarteroni, A. On the coupling of 3d and 1d navier–stokes equations for flow problems in compliant vessels. *Computer Methods in Applied Mechanics and Engineering 191*, 6-7 (2001), 561–582.

[72] Forneris, A., Marotti, F. B., Satriano, A., Moore, R. D., and Di Martino, E. S. A novel combined fluid dynamic and strain analysis approach identified abdominal aortic aneurysm rupture. *Journal of Vascular Surgery Cases and Innovative Techniques 6*, 2 (2020), 172.

[73] Gallo, D., Steinman, D. A., Bijari, P. B., and Morbiducci, U. Helical flow in carotid bifurcation as surrogate marker of exposure to disturbed shear. *Journal of Biomechanics 45*, 14 (2012), 2398–2404.

[74] Ghaffari, M., Alaraj, A., Du, X., Zhou, X. J., Charbel, F. T., and Linninger, A. A. Quantification of near-wall hemodynamic risk factors in large-scale cerebral arterial trees. *International Journal for Numerical Methods in Biomedical Engineering 34*, 7 (2018), e2987.

[75] Ghaffari, M., Tangen, K., Alaraj, A., Du, X., Charbel, F. T., and Linninger, A. A. Large-scale subject-specific cerebral arterial tree modeling using automated parametric mesh generation for blood flow simulation. *Computers in Biology and Medicine 91* (2017), 353–365.

[76] Gilmanov, A., and Sotiropoulos, F. A hybrid cartesian/immersed boundary method for simulating flows with 3d, geometrically complex, moving bodies. *Journal of Computational Physics 207*, 2 (2005), 457–492.

[77] Girdhar, G., Xenos, M., Alemu, Y., Chiu, W.-C., Lynch, B. E., Jesty, J., Einav, S., Slepian, M. J., and Bluestein, D. Device thrombogenicity emulation: a novel method for optimizing mechanical circulatory support device thromboresistance. *PLoS One 7*, 3 (2012), e32463.

[78] Golledge, J. Abdominal aortic aneurysm: Update on pathogenesis and medical treatments. *Nature Reviews Cardiology 16*, 4 (2019), 225–242.

[79] Golledge, J., Norman, P. E., Murphy, M. P., and Dalman, R. L. Challenges and opportunities in limiting abdominal aortic aneurysm growth. *Journal of Vascular Surgery 65*, 1 (2017), 225–233.

[80] Gorlin, R., and Gorlin, S. Hydraulic formula for calculation of the area of the stenotic mitral valve, other cardiac valves, and central circulatory shunts. i. *American Heart Journal 41*, 1 (1951), 1–29.

[81] Grippo, L., and Sciandrone, M. *Introduction to Methods for Nonlinear Optimization*, vol. 152. Springer Nature, 2023.

[82] Haik, Y., Pai, V., and Chen, C.-J. Development of magnetic device for cell separation. *Journal of Magnetism and Magnetic Materials 194*, 1-3 (1999), 254–261.

[83] Haik, Y., Pai, V., and Chen, C.-J. Apparent viscosity of human blood in a high static magnetic field. *Journal of Magnetism and Magnetic Materials 225*, 1-2 (2001), 180–186.

[84] Harlow, F. H., and Welch, J. E. Numerical calculation of time-dependent viscous incompressible flow of fluid with free surface. *Physics of Fluids 8*, 12 (1965), 2182–2189.

[85] Hejazi, M., and Phani, A. S. On growth, buckling, and rupture of aneurysms: Cylindrical tube analogy. *Journal of Biomechanics 144* (2022), 111313.

[86] Helbock, R. T., Anam, S. B., Kovarovic, B. J., Slepian, M. J., Hamdan, A., Haj-Ali, R., and Bluestein, D. Designing a novel asymmetric transcatheter aortic valve for stenotic bicuspid aortic valves using patient-specific computational modeling. *Annals of Biomedical Engineering 51*, 1 (2023), 58–70.

[87] Himburg, H. A., Grzybowski, D. M., Hazel, A. L., LaMack, J. A., Li, X.-M., and Friedman, M. H. Spatial comparison between wall shear stress measures and porcine arterial endothelial permeability. *American Journal of Physiology-Heart and Circulatory Physiology 286*, 5 (2004), H1916–H1922.

[88] Hirschhorn, M., Tchantchaleishvili, V., Stevens, R., Rossano, J., and Throckmorton, A. Fluid–structure interaction modeling in cardiovascular medicine–a systematic review 2017–2019. *Medical Engineering & Physics 78* (2020), 1–13.

[89] Hoque, K., Ferdows, M., Sawall, S., Tzirtzilakis, E., and Xenos, M. The impact of hemodynamic factors in a coronary main artery to detect the

atherosclerotic severity: Single and multiple sequential stenosis cases. *Physics of Fluids 33*, 3 (2021), 031903.

[90] Houard, X., Rouzet, F., Touat, Z., Philippe, M., Dominguez, M., Fontaine, V., Sarda-Mantel, L., Meulemans, A., Le Guludec, D., Meilhac, O., et al. Topology of the fibrinolytic system within the mural thrombus of human abdominal aortic aneurysms. *The Journal of Pathology: A Journal of the Pathological Society of Great Britain and Ireland 212*, 1 (2007), 20–28.

[91] Husain, I., Labropulu, F., Langdon, C., and Schwark, J. A comparison of Newtonian and non-Newtonian models for pulsatile blood flow simulations. *Journal of the Mechanical Behavior of Materials 21* (2013), 147–153.

[92] Inc., W. R. Mathematica, Version 14.3. Champaign, IL, 2025.

[93] Johnston, B. M., Johnston, P. R., Corney, S., and Kilpatrick, D. Non-newtonian blood flow in human right coronary arteries: steady state simulations. *Journal of Biomechanics 37*, 5 (2004), 709–720.

[94] Joly, F., Soulez, G., Garcia, D., Lessard, S., and Kauffmann, C. Flow stagnation volume and abdominal aortic aneurysm growth: Insights from patient-specific computational flow dynamics of lagrangian-coherent structures. *Computers in Biology and Medicine 92* (2018), 98–109.

[95] Joly, F., Soulez, G., Lessard, S., Kauffmann, C., and Vignon-Clementel, I. A cohort longitudinal study identifies morphology and hemodynamics predictors of abdominal aortic aneurysm growth. *Annals of Biomedical Engineering 48*, 2 (2020), 606–623.

[96] Katritsis, D., Kaiktsis, L., Chaniotis, A., Pantos, J., Efstathopoulos, E. P., and Marmarelis, V. Wall shear stress: theoretical considerations and methods of measurement. *Progress in Cardiovascular Diseases 49*, 5 (2007), 307–329.

[97] Katsoudas, S., Malatos, S., Raptis, A., Matsagkas, M., Giannoukas, A., and Xenos, M. Blood flow simulation in bifurcating arteries: A multiscale approach after fenestrated and branched endovascular aneurysm repair. *Mathematics 13*, 9 (2025).

[98] Katsoudas, S. C., Kyriakoudi, K. C., Chrimatopoulos, G. T., Linardopoulos, P. D., Chrimatopoulos, C. T., Raptis, A. A., Moulakakis, K. G., Kakisis, J. D., Manopoulos, C. G., Xenos, M. A., et al. Linking aneurysmal geometry and hemodynamics using computational fluid dynamics. *Physics of Fluids 38*, 3 (2026).

[99] Kent, K. C. Abdominal aortic aneurysms. *New England Journal of Medicine 371*, 22 (2014), 2101–2108.

[100] Kilner, P. J., Gatehouse, P. D., and Firmin, D. N. Flow measurement by magnetic resonance: a unique asset worth optimising. *Journal of Cardiovascular Magnetic Resonance 9*, 4 (2007), 723–728.

[101] Klabunde, R. *Cardiovascular Physiology Concepts*. Lippincott Williams & Wilkins, 2011.

[102] Klaus, V., Tanios-Schmies, F., Reeps, C., Trenner, M., Matevossian, E., Eckstein, H.-H., and Pelisek, J. Association of matrix metalloproteinase levels with collagen degradation in the context of abdominal aortic aneurysm. *European Journal of Vascular and Endovascular Surgery 53*, 4 (2017), 549–558.

[103] Kovarovic, B., Helbock, R., Baylous, K., Rotman, O. M., Slepian, M. J., and Bluestein, D. Visions of TAVR future: Development and optimization of a second generation novel polymeric tavr. *Journal of Biomechanical Engineering 144*, 6 (2022), 061008.

[104] Ku, D. N. Blood flow in arteries. *Annual Review of Fluid Mechanics 29*, 1 (1997), 399–434.

[105] Kumar, S., Kumar, B., and Rai, S. Influence of abdominal aortic aneurysm shape on hemodynamics in human aortofemoral arteries: A transient open-loop study. *Physics of Fluids 35*, 4 (2023).

[106] Kyriakoudi, K. C., Chrimatopoulos, G. T., Tzirtzilakis, E. E., and Xenos, M. A. Aneurysmal haemodynamics: a three-dimensional fluid–structure interaction approach. *Royal Society Open Science 13*, 1 (2026).

[107] Kyriakoudi, K. C., and Xenos, M. A. Finite element methods with higher order polynomials. *Exploring Mathematical Analysis, Approximation Theory, and Optimization: 270 Years Since A.-M. Legendre's Birth* (2023), 161–176.

[108] Kyriakoudi, K. C., and Xenos, M. A. Magnetohydrodynamic effects on a pathological vessel: an Euler–Lagrange approach. *Physics of Fluids 35*, 12 (2023), 121912.

[109] Lederle, F. A., Johnson, G. R., Wilson, S. E., Chute, E. P., Hye, R. J., Makaroun, M. S., Barone, G. W., Bandyk, D., Moneta, G. L., Makhoul, R. G., et al. The aneurysm detection and management study screening program: Validation cohort and final results. *Archives of Internal Medicine 160*, 10 (2000), 1425–1430.

[110] Lee, U. Y., Jung, J., Kwak, H. S., Lee, D. H., Chung, G. H., Park, J. S., and Koh, E. J. Wall shear stress and flow patterns in unruptured and ruptured anterior communicating artery aneurysms using computational fluid dynamics. *Journal of Korean Neurosurgical Society 61*, 6 (2018), 689–699.

[111] Levenberg, K. A method for the solution of certain non-linear problems in least squares. *Quarterly of Applied Mathematics 2*, 2 (1944), 164–168.

[112] Liao, S. *Beyond Perturbation: Introduction to the Homotopy Analysis Method*. Chapman and Hall/CRC, 2003.

[113] Liao, S. Notes on the homotopy analysis method: Some definitions and theorems. *Communications in Nonlinear Science and Numerical Simulation 14*, 4 (2009), 983–997.

[114] Liao, S. *Homotopy Analysis Method in Nonlinear Differential Equations*, vol. 153. Springer, 2012.

[115] Liao, S.-J. *The Proposed Homotopy Analysis Technique for the Solution of Nonlinear Problems*. PhD thesis, Ph. D. Thesis, Shanghai Jiao Tong University Shanghai, 1992.

[116] Liao, S.-J. An explicit, totally analytic approximate solution for Blasius' viscous flow problems. *International Journal of Non-Linear Mechanics 34*, 4 (1999), 759–778.

[117] Lindquist Liljeqvist, M., Bogdanovic, M., Siika, A., Gasser, T. C., Hultgren, R., and Roy, J. Geometric and biomechanical modeling aided by machine learning improves the prediction of growth and rupture of small abdominal aortic aneurysms. *Scientific Reports 11*, 1 (2021), 18040.

[118] Linninger, A. A., Xenos, M., Sweetman, B., Ponkshe, S., Guo, X., and Penn, R. A mathematical model of blood, cerebrospinal fluid and brain dynamics. *Journal of Mathematical Biology 59*, 6 (2009), 729–759.

[119] Linninger, A. A., Xenos, M., Zhu, D. C., Somayaji, M. R., Kondapalli, S., and Penn, R. D. Cerebrospinal fluid flow in the normal and hydrocephalic human brain. *IEEE Transactions on Biomedical Engineering 54*, 2 (2007), 291–302.

[120] Liu, X., Lee, A., Wang, Y., Hoang, T. P., Yee, K. S., Mosse, L., Karajan, N., Winlaw, D. S., Naficy, S., and Fletcher, D. F. Fluid-structure interaction analysis of bioinspired polymeric heart valves with experimental validation. *Computer Methods and Programs in Biomedicine* (2025), 108839.

[121] Liu, X., Sun, A., Fan, Y., and Deng, X. Physiological significance of helical flow in the arterial system and its potential clinical applications. *Annals of Biomedical Engineering 43*, 1 (2015), 3–15.

[122] Liu, X., Zhang, W., Ye, P., Luo, Q., and Chang, Z. Fluid-structure interaction analysis on the influence of the aortic valve stent leaflet structure in hemodynamics. *Frontiers in Physiology 13* (2022), 904453.

[123] Logan, J. D. *Applied Mathematics*. John Wiley & Sons, 2013.

[124] Long, C., Marsden, A., and Bazilevs, Y. Shape optimization of pulsatile ventricular assist devices using FSI to minimize thrombotic risk. *Computational Mechanics 54*, 4 (2014), 921–932.

[125] Lu, H., and Daugherty, A. Aortic aneurysms. *Arteriosclerosis, Thrombosis, and Vascular Biology 37* (2017), e59–e65.

[126] Lu, T., Cha, Y., Hu, W., Lu, L., Xia, Z., and Xiong, J. Hemodynamic characteristic analysis of ruptured abdominal aortic aneurysms based on computational fluid dynamics. *Physics of Fluids 37*, 8 (08 2025), 081906.

[127] Malatos, S., Fazzini, L., Raptis, A., Nana, P., Kouvelos, G., Tasso, P., Gallo, D., Morbiducci, U., Xenos, M. A., Giannoukas, A., and Matsagkas, M. Evaluation of hemodynamic properties after chimney and fenestrated endovascular aneurysm repair. *Annals of Vascular Surgery 104* (2024), 237–247.

[128] Marquardt, D. An algorithm for least-squares estimation of nonlinear parameters. *Journal of the Society for Industrial and Applied Mathematics 11*, 2 (1963), 431–441.

[129] Mavriplis, D. J., and Nastase, C. R. On the geometric conservation law for high-order discontinuous Galerkin discretizations on dynamically deforming meshes. *Journal of Computational Physics 230*, 11 (2011), 4285–4300.

[130] Mavriplis, D. J., and Yang, Z. Construction of the discrete geometric conservation law for high-order time-accurate simulations on dynamic meshes. *Journal of Computational Physics 213*, 2 (2006), 557–573.

[131] Meier, H., Alves, J., and Mori, M. Comparison between staggered and collocated grids in the finite-volume method performance for single and multi-phase flows. *Computers & Chemical Engineering 23*, 3 (1999), 247–262.

[132] Meng, H., Tutino, V. M., Xiang, J., and Siddiqui, A. H. High WSS or low WSS? Complex interactions of hemodynamics with intracranial aneurysm initiation, growth, and rupture: Toward a unifying hypothesis. *AJNR: American Journal of Neuroradiology 35*, 7 (2014), 1254–1262.

[133] Monaghan, J. J. Smoothed particle hydrodynamics. *Reports on Progress in Physics 68*, 8 (2005), 1703.

[134] Moon, K., Lee, Y., Lee, J., Son, Y., Woo, Y., Jang, E., Yun, S., Park, S., and Kim, J. Hemodynamic predictors of rupture in abdominal aortic aneurysms: a case series using computational fluid dynamics. *Frontiers in Cardiovascular Medicine 12* (2025).

[135] Morales, H. G., Larrabide, I., Geers, A. J., Aguilar, M. L., and Frangi, A. F. Newtonian and non-Newtonian blood flow in coiled cerebral aneurysms. *Journal of Biomechanics 46*, 13 (2013), 2158–2164.

[136] Morbiducci, U., Ponzini, R., Rizzo, G., Cadioli, M., Esposito, A., Montevecchi, F. M., and Redaelli, A. Mechanistic insight into the physiological relevance of helical blood flow in the human aorta: An in vivo study. *Biomechanics and Modeling in Mechanobiology 10*, 3 (2011), 339–355.

[137] Moré, J. J. The Levenberg-Marquardt Algorithm: Implementation and Theory. *Numerical Analysis* (1978), 105–116.

[138] Moré, J. J., and Sorensen, D. C. Computing a trust region step. *SIAM Journal on Scientific and Statistical Computing 4*, 3 (1983), 553–572.

[139] Mountrakis, L., Lorenz, E., and Hoekstra, A. Where do the platelets go? A simulation study of fully resolved blood flow through aneurysmal vessels. *Interface Focus 3*, 2 (2013), 20120089.

[140] Mustapha, N., Amin, N., Chakravarty, S., and Mandal, P. K. Unsteady magnetohydrodynamic blood flow through irregular multi-stenosed arteries. *Computers in Biology and Medicine 39*, 10 (2009), 896–906.

[141] Mutlu, O., Salman, H. E., Al-Thani, H., El-Menyar, A., Qidwai, U. A., and Yalcin, H. C. How does hemodynamics affect rupture tissue mechanics in abdominal aortic aneurysm: Focus on wall shear stress derived parameters, time-averaged wall shear stress, oscillatory shear index, endothelial cell activation potential, and relative residence time. *Computers in Biology and Medicine 154* (2023), 106609.

[142] Nayfeh, A. H. *Perturbation Methods*. John Wiley & Sons, 2024.

[143] Nicholls, S. C., Gardner, J. B., Meissner, M. H., and Johansen, K. H. Rupture in small abdominal aortic aneurysms. *Journal of Vascular Surgery 28*, 5 (1998), 884–888.

[144] Nocedal, J., and Wright, S. *Numerical Optimization*. Springer Series in Operations Research and Financial Engineering. Springer New York, 2006.

[145] Olufsen, M. S., Peskin, C. S., Kim, W. Y., Pedersen, E. M., Nadim, A., and Larsen, J. Numerical simulation and experimental validation of blood flow in arteries with structured-tree outflow conditions. *Annals of Biomedical Engineering 28*, 11 (2000), 1281–1299.

[146] Papaharilaou, Y., Ekaterinaris, J. A., Manousaki, E., and Katsamouris, A. N. A decoupled fluid structure approach for estimating wall stress in abdominal aortic aneurysms. *Journal of Biomechanics 40*, 2 (2007), 367–377.

[147] Park, H. D., Paul, M., Hammond, G. E., and Valocchi, A. J. Newton trust-region methods with primary variable switching for simulating high temperature multiphase porous media flow. *Advances in Water Resources 168* (2022), 104285.

[148] Park, S.-H., Yim, M.-B., Lee, C.-Y., Kim, E., and Son, E.-I. Intracranial fusiform aneurysms: it's pathogenesis, clinical characteristics and managements. *Journal of Korean Neurosurgical Society 44*, 3 (2008), 116.

[149] Paszkowiak, J. J., and Dardik, A. Arterial wall shear stress: observations from the bench to the bedside. *Vascular and Endovascular Surgery 37*, 1 (2003), 47–57.

[150] Patankar, S. *Numerical Heat Transfer and Fluid Flow*. CRC Press, 2018.

[151] Patterson, E., Howard, I., and Thornton, M. A comparative study of linear and nonlinear simulations of the leaflets in a bioprosthetic heart valve during the cardiac cycle. *Journal of Medical Engineering & Technology 20*, 3 (1996), 95–108.

[152] Pedley, T. J. *The Fluid Mechanics of Large Blood Vessels*. University Press, 1980.

[153] Perić, M., Kessler, R., and Scheuerer, G. Comparison of finite-volume numerical methods with staggered and colocated grids. *Computers & Fluids 16*, 4 (1988), 389–403.

[154] Peskin, C. S. The immersed boundary method. *Acta Numerica 11* (2002), 479–517.

[155] Piatti, F., Sturla, F., Marom, G., Sheriff, J., Claiborne, T. E., Slepian, M. J., Redaelli, A., and Bluestein, D. Hemodynamic and thrombogenic analysis of a trileaflet polymeric valve using a fluid–structure interaction approach. *Journal of Biomechanics 48*, 13 (2015), 3641–3649.

[156] Polzer, S., Gasser, T. C., Vlachovskỳ, R., Kubíček, L., Lambert, L., Man, V., Novák, K., Slažanskỳ, M., Burša, J., and Staffa, R. Biomechanical indices are more sensitive than diameter in predicting rupture of asymptomatic abdominal aortic aneurysms. *Journal of Vascular Surgery 71*, 2 (2020), 617–626.

[157] Pons, R., Guala, A., Rodríguez-Palomares, J. F., Cajas, J., Dux-Santoy, L., Teixidó-Tura, G., Molins, J. J., Vázquez, M., Evangelista, A., and Martorell, J. Fluid–structure interaction simulations outperform computational fluid dynamics in the description of thoracic aorta haemodynamics and in the differentiation of progressive dilation in marfan syndrome patients. *Royal Society Open Science 7*, 2 (2020), 191752.

[158] Ramamurthy, G., and Shanker, B. Magnetohydrodynamic effects on blood flow through a porous channel. *Medical and Biological Engineering and Computing 32*, 6 (1994), 655–659.

[159] Raptis, A., Kyriakoudi, K., and Xenos, M. A. Finite Element Analysis in Fluid Mechanics. *Mathematical Analysis and Applications* (2019), 481–510.

[160] Raptis, A., Xenos, M., Georgakarakos, E., Kouvelos, G., Giannoukas, A., Labropoulos, N., and Matsagkas, M. Comparison of physiological and post-endovascular aneurysm repair infrarenal blood flow. *Computer Methods in Biomechanics and Biomedical Engineering 20*, 3 (2017), 242–249.

[161] Raptis, A., Xenos, M., Tzirtzilakis, E., and Matsagkas, M. Finite element analysis of magnetohydrodynamic effects on blood flow in an aneurysmal geometry. *Physics of Fluids 26*, 10 (2014), 101901.

[162] Ricotta, J. J., Pagan, J., Xenos, M., Alemu, Y., Einav, S., and Bluestein, D. Cardiovascular disease management: the need for better diagnostics. *Medical & Biological Engineering & Computing 46*, 11 (2008), 1059–1068.

[163] Rotman, O. M., Bianchi, M., Ghosh, R. P., Kovarovic, B., and Bluestein, D. Principles of TAVR valve design, modelling, and testing. *Expert Review of Medical Devices 15*, 11 (2018), 771–791.

[164] Rygiel, P., Alblas, D., Brune, C., Yeung, K. K., and Wolterink, J. M. Global control for local so(3)-equivariant scale-invariant vessel segmentation. *arXiv:2403.15314* (2024).

[165] Sakalihasan, N., Limet, R., and Defawe, O. D. Abdominal aortic aneurysm. *The Lancet 365*, 9470 (2005), 1577–1589.

[166] Schlichting, H., and Gersten, K. *Boundary-Layer Theory*. Springer, 2016.

[167] Shang, J. Three decades of accomplishments in computational fluid dynamics. *Progress in Aerospace Sciences 40*, 3 (2004), 173–197.

[168] Sheriff, J., Soares, J. S., Xenos, M., Jesty, J., and Bluestein, D. Evaluation of shear-induced platelet activation models under constant and dynamic shear stress loading conditions relevant to devices. *Annals of Biomedical Engineering 41*, 6 (2013), 1279–1296.

[169] Shit, G., and Majee, S. Magnetic field interaction with blood flow and heat transfer through diseased artery having abdominal aortic aneurysm. *European Journal of Mechanics-B/Fluids 71* (2018), 1–14.

[170] Shit, G. C. Computational modelling of blood flow development and its characteristics in magnetic environment. *Modelling and Simulation in Engineering 2013* (2013), 16–16.

[171] Shyy, W. *Computational Modeling for Fluid Flow and Interfacial Transport*. Courier Corporation, 2014.

[172] Shyy, W., Kang, C.-k., Chirarattananon, P., Ravi, S., and Liu, H. Aerodynamics, sensing and control of insect-scale flapping-wing flight. *Proceedings of the Royal Society A: Mathematical, Physical and Engineering Sciences 472*, 2186 (2016), 20150712.

[173] Shyy, W., Tong, S. S., and Correa, S. M. Numerical recirculating flow calculation using a body-fitted coordinate system. *Numerical Heat Transfer 8*, 1 (1985), 99–113.

[174] Shyy, W., Udaykumar, H., Rao, M. M., and Smith, R. W. *Computational Fluid Dynamics with Moving Boundaries*. Courier Corporation, 2012.

[175] Shyy, W., and Vu, T. C. On the adoption of velocity variable and grid system for fluid flow computation in curvilinear coordinates. *Journal of Computational Physics 92*, 1 (1991), 82–105.

[176] Slepian, M. J., Kovarovic, B., Rotman, O. M., Helbock, R., Baylous, K., and Bluestein, D. CARD20: A novel polymeric transcatheter aortic valve as alternative to tissue-based valves. *ASAIO Journal 68*, Supplement 2 (2022), 54–55.

[177] Somayaji, M. R., Xenos, M., Zhang, L., Mekarski, M., and Linninger, A. A. Systematic design of drug delivery therapies. *Computers & Chemical Engineering 32*, 1-2 (2008), 89–98.

[178] Sotiropoulos, F., and Yang, X. Immersed boundary methods for simulating fluid–structure interaction. *Progress in Aerospace Sciences 65* (2014), 1–21.

[179] Sprague, M., and Geers, T. Legendre spectral finite elements for structural dynamics analysis. *Communications in Numerical Methods in Engineering 24*, 12 (2008), 1953–1965.

[180] Suess, T., Anderson, J., Danielson, L., Pohlson, K., Remund, T., Blears, E., Gent, S., and Kelly, P. Examination of near-wall hemodynamic parameters in the renal bridging stent of various stent graft configurations for repairing visceral branched aortic aneurysms. *Journal of Vascular Surgery 64*, 3 (2016), 788–796.

[181] Sun, W., Abad, A., and Sacks, M. S. Simulated bioprosthetic heart valve deformation under quasi-static loading. 905–914.

[182] Sweetman, B., Xenos, M., Zitella, L., and Linninger, A. A. Three-dimensional computational prediction of cerebrospinal fluid flow in the human brain. *Computers in Biology and Medicine 41*, 2 (2011), 67–75.

[183] Tenek, L. T., and Argyris, J. *Finite Element Analysis for Composite Structures*, vol. 59. Springer Science & Business Media, 2013.

[184] Tezduyar, T. E., Mittal, S., Ray, S., and Shih, R. Incompressible flow computations with stabilized bilinear and linear equal-order-interpolation velocity-pressure elements. *Computer Methods in Applied Mechanics and Engineering 95*, 2 (1992), 221–242.

[185] Thiriet, M., Delfour, M., and Garon, A. Vascular stenosis: An Introduction. *PanVascular Medicine* (2015), 781–868.

[186] Thompson, J. F., Warsi, Z. U., and Mastin, C. W. *Numerical Grid Generation: Foundations and Applications*. Elsevier North-Holland, Inc., 1985.

[187] Trenti, C., Ziegler, M., Bjarnegård, N., Ebbers, T., Lindenberger, M., and Dyverfeldt, P. Wall shear stress and relative residence time as potential risk factors for abdominal aortic aneurysms in males: A 4D flow cardiovascular magnetic resonance case–control study. *Journal of Cardiovascular Magnetic Resonance 24*, 1 (2022), 18.

[188] Tzirtzilakis, E. A mathematical model for blood flow in magnetic field. *Physics of Fluids 17*, 7 (2005).

[189] Tzirtzilakis, E., Xenos, M., Loukopoulos, V., and Kafoussias, N. Turbulent biomagnetic fluid flow in a rectangular channel under the action of a localized magnetic field. *International Journal of Engineering Science 44*, 18-19 (2006), 1205–1224.

[190] Unverdi, S. O., and Tryggvason, G. A front-tracking method for viscous, incompressible, multi-fluid flows. *Journal of Computational Physics 100*, 1 (1992), 25–37.

[191] Updegrove, A., Wilson, N. M., Merkow, J., Lan, H., Marsden, A. L., and Shadden, S. C. Simvascular: An open source pipeline for cardiovascular simulation. *Annals of Biomedical Engineering 45*, 3 (2017), 525–541.

[192] Urrutia, J., Roy, A., Raut, S. S., Antón, R., Muluk, S. C., and Finol, E. A. Geometric surrogates of abdominal aortic aneurysm wall mechanics. *Medical Engineering & Physics 59* (2018), 43–49.

[193] Van Keulen, J., Van Prehn, J., Prokop, M., Moll, F., and Van Herwaarden, J. Dynamics of the aorta before and after endovascular aneurysm repair: a systematic review. *European Journal of Vascular and Endovascular Surgery 38*, 5 (2009), 586–596.

[194] Vande Geest, J. P., Wang, D. H. J., Wisniewski, S. R., Makaroun, M. S., and Vorp, D. A. Towards a noninvasive method for determination of patient-specific wall strength distribution in abdominal aortic aneurysms. *Annals of Biomedical Engineering 34*, 7 (2006), 1098–1106.

[195] Versteeg, H., and Malalasekera, W. Computational Fluid Dynamics: The Tinite Volume Method. *Harlow, England: Longman Scientific & Technical* (1995).

[196] Vignon-Clementel, I. E., Figueroa, C. A., Jansen, K. E., and Taylor, C. A. Outflow boundary conditions for three-dimensional finite element modeling of blood flow and pressure in arteries. *Computer Methods in Applied Mechanics and Engineering 195*, 29-32 (2006), 3776–3796.

[197] Wang, X., Carpenter, H. J., Ghayesh, M. H., Kotousov, A., Zander, A. C., Amabili, M., and Psaltis, P. J. A review on the biomechanical behaviour of the aorta. *Journal of the Mechanical Behavior of Biomedical Materials 144* (2023), 105922.

[198] Wang, X., Ghayesh, M. H., Li, J., Kotousov, A., Zander, A. C., Dawson, J. A., and Psaltis, P. J. Impact of Geometric Attributes on Abdominal Aortic Aneurysm Rupture Risk: An In Vivo FSI-Based Study. *International Journal for Numerical Methods in Biomedical Engineering 40*, 12 (2024), e3884.

[199] Wei, Z. A., Sonntag, S. J., Toma, M., Singh-Gryzbon, S., and Sun, W. Computational fluid dynamics assessment associated with transcatheter heart valve prostheses: A position paper of the ISO working group. *Cardiovascular Engineering and Technology 9*, 3 (2018), 289–299.

[200] White, F. M., and Majdalani, J. *Viscous Fluid Flow*, vol. 3. McGraw-Hill New York, 2006.

[201] Whiting, C. H., and Jansen, K. E. A stabilized finite element method for the incompressible Navier–Stokes equations using a hierarchical basis. *International Journal for Numerical Methods in Fluids 35*, 1 (2001), 93–116.

[202] Womersley, J. R. Method for the calculation of velocity, rate of flow and viscous drag in arteries when the pressure gradient is known. *The Journal of Physiology 127*, 3 (1955), 553–563.

[203] Womersley, J. R. Xxiv. Oscillatory motion of a viscous liquid in a thin-walled elastic tube—I: The linear approximation for long waves. *The London, Edinburgh, and Dublin Philosophical Magazine and Journal of Science 46*, 373 (1955), 199–221.

[204] Xenos, M. An Euler–Lagrange approach for studying blood flow in an aneurysmal geometry. *Proceedings of the Royal Society A: Mathematical, Physical and Engineering Sciences 473*, 2199 (2017), 20160774.

[205] Xenos, M., Alemu, Y., Zamfir, D., Einav, S., Ricotta, J. J., Labropoulos, N., Tassiopoulos, A., and Bluestein, D. The effect of angulation in abdominal aortic aneurysms: fluid–structure interaction simulations of idealized geometries. *Medical & Biological Engineering & Computing 48*, 12 (2010), 1175–1190.

[206] Xenos, M., Girdhar, G., Alemu, Y., Jesty, J., Slepian, M., Einav, S., and Bluestein, D. Device thrombogenicity emulator (DTE)- Design optimization

methodology for cardiovascular devices: A study in two bileaflet MHV designs. *Journal of Biomechanics 43*, 12 (2010), 2400–2409.

[207] Xenos, M., Labropoulos, N., Rambhia, S., Alemu, Y., Einav, S., Tassiopoulos, A., Sakalihasan, N., and Bluestein, D. Progression of abdominal aortic aneurysm towards rupture: refining clinical risk assessment using a fully coupled fluid–structure interaction method. *Annals of Biomedical Engineering 43*, 1 (2015), 139–153.

[208] Xenos, M., Labropoulos, N., Rambhia, S., Alemu, Y., Einav, S., Tassiopoulos, A., Sakalihasan, N., and Bluestein, D. Progression of abdominal aortic aneurysm towards rupture: refining clinical risk assessment using a fully coupled fluid-structure interaction method. *Annals of Biomedical Engineering 43* (01 2015), 139–153.

[209] Xenos, M., Rambhia, S. H., Alemu, Y., Einav, S., Labropoulos, N., Tassiopoulos, A., Ricotta, J. J., and Bluestein, D. Patient-based abdominal aortic aneurysm rupture risk prediction with fluid structure interaction modeling. *Annals of Biomedical Engineering 38*, 11 (2010), 3323–3337.

[210] Xenos, M., and Raptis, A. Magnetohydrodynamic effects on the granular temperature of red blood cells in microvasculature. *Journal of Mechanics in Medicine and Biology 17*, 01 (2017), 1750003.

[211] Xiao, N., Alastruey, J., and Alberto Figueroa, C.

[212] Yu, S. Steady and pulsatile flow studies in abdominal aortic aneurysm models using particle image velocimetry. *International Journal of Heat and Fluid Flow 21*, 1 (2000), 74–83.

[213] Yu, S., Chan, W., Ng, B., and Chua, L. A numerical investigation on the steady and pulsatile flow characteristics in axi-symmetric abdominal aortic aneurysm models with some experimental evaluation. *Journal of Medical Engineering & Technology 23*, 6 (1999), 228–239.

[214] Yuan, Y.-x. Recent advances in trust region algorithms. *Mathematical Programming 151* (2015), 249–281.

[215] Zambrano, B., Gharahi, H., Lim, C., Jaberi, F., Choi, J., Lee, W., and Baek, S. Association of intraluminal thrombus, hemodynamic forces, and abdominal aortic aneurysm expansion using longitudinal CT images. *Annals of Biomedical Engineering 44*, 5 (2015), 1502–1514.

[216] Zambrano, B. A., Gharahi, H., Lim, C. Y., Lee, W., and Baek, S. Association of vortical structures and hemodynamic parameters for regional thrombus accumulation in abdominal aortic aneurysms. *International Journal for Numerical Methods in Biomedical Engineering 38*, 2 (2022), e3555.

[217] Zhang, L., Kulkarni, K., Somayaji, M. R., Xenos, M., and Linninger, A. A. Discovery of transport and reaction properties in distributed systems. *AIChE Journal 53*, 2 (2007), 381–396.

[218] Zhao, Y., Zhang, X., Ho, S. L., and Fu, W. An Adaptive Mesh Method in Transient Finite Element Analysis of Magnetic Field using a Novel Error Estimator. *IEEE Transactions on Magnetics 48*, 11 (2012), 4160–4163.

[219] Zhu, J., and Zienkiewicz, O. Adaptive Techniques in The Finite Element Method. *Communications in Applied Numerical Methods 4*, 2 (1988), 197–204.

APPENDIX A

APPENDIX A

Miscellaneous Mathematical Concepts

Banach Space A normed linear space $(V, \|\cdot\|)$ which is complete with respect to the metric induced by the norm.

Bilinear Form A bilinear form $b(\cdot, \cdot)$ on a linear space V is a mapping

$$b : V \times V \to \mathbb{R}$$

such that each of the maps $v \mapsto b(v, w)$ and $w \mapsto b(v, w)$ is linear.

Symmetric The bilinear form is symmetric if

$$b(v, w) = b(w, v), \qquad \forall v, w \in V.$$

Boundary Conditions Constraints necessary for the solution of a differential equation (or system of equations) in a domain.

Dirichlet Specifies the value that the unknown function takes on the boundary.

Neumann Specifies the value of the derivative of the solution on the boundary.

Hilbert Space A complete inner product space; in Chapter 2, this is identified as the H^1 Sobolev space where first derivatives are square-integrable.

Coercivity A property of a bilinear form $a(\cdot, \cdot)$ such that there exists a constant $\delta > 0$ where

$$a(v, v) \geq \delta \|v\|_H^2$$

for all $v \in V$.

Condition

No-Slip The physical boundary condition applies only to real fluids and is a consequence of the non-slipping of fluid particles that are in contact with a solid boundary. Consequently, the tangential component of the fluid velocity at a stationary boundary is zero. This property of real fluids is the cause behind the formation of the boundary layer.

Kinematic This condition applies both to the contact surface between a solid and a fluid, and to the interface between two immiscible fluids. Under this condition, the velocity components normal to the surface of the two media are equal. In the case of a stationary solid boundary, the normal velocity component is zero. This is a general condition that applies to both ideal and real fluids.

Lax-Milgram Theorem A theorem ensuring the existence and uniqueness of a solution for a variational problem given a continuous, coercive bilinear form in a Hilbert space.

Riesz Representation Theorem States that every continuous linear functional on a Hilbert space can be represented by an inner product with a unique element of that space.

Contraction Mapping Principle Ensures that a mapping T has a unique fixed point if it satisfies the contraction inequality

$$\|Tu_1 - Tu_2\| \leq M\|u_1 - u_2\|$$

with $0 < M < 1$.

Inf-Sup (LBB) Condition A stability requirement for saddle-point problems (like the Stokes equations) ensuring that the choice of velocity and pressure spaces does not lead to spurious oscillations.

Jacobian Matrix A matrix of all first-order partial derivatives of a vector-valued function, used in Newton's method to solve non-linear algebraic systems.

Homotopy A continuous variation or deformation used in the Homotopy Analysis Method to continuously deform an initial guess into the exact solution.

Geometric Conservation Law (GCL) A principle ensuring that the temporal rate of change of the control volume Jacobian is consistently correlated with the Cartesian velocity components of the moving computational grid, preventing artificial mass or momentum sources.

Taylor-Hood Elements Mixed finite elements containing the (P_k, P_{k-1}) pair of polynomials (with $k \geq 2$) typically used for solving the Stokes and Navier-Stokes equations to satisfy the Inf-Sup (LBB) condition.

Trust Region Method An iterative optimization method that generates a step by minimizing a quadratic model function within a restricted region (the trust region) around the current iteration point, ensuring global convergence even when the initial guess is far from the solution.

Gauss-Newton Method An iterative algorithm used to solve non-linear least squares problems by approximating the Hessian matrix, forming the basis for the more robust Levenberg-Marquardt algorithm.

Falkner-Skan Transformation A similarity transformation used in boundary layer theory to simplify the governing non-linear partial differential equations by reducing them to a dimensionless form dependent on a single similarity variable.

Collocated Grid A mesh arrangement in the Finite Volume Method where all flow variables (pressure, velocity components, scalars) are stored at the same location, typically the cell centers.

Staggered Grid A mesh arrangement where physical parameters of the flow are stored in different locations within the control volume (e.g., velocity components at cell faces, pressure at cell centers) to naturally prevent spurious checkerboard pressure oscillations.

Theorem A.0.1. ***(Lax-Milgram)*** *Given a Hilbert space $(V, (\cdot, \cdot))$, a continuous, coercive bilinear form $a(\cdot, \cdot)$ and a continuous linear functional $F \in V'$, there exists a unique solution $u \in V$, such that,*

$$a(u, v) = F(v), \quad \forall\, v \in V. \tag{A.1}$$

Before proving the theorem it is necessary to mention the following Lemma and Theorem.

Lemma A.0.2. ***(Contraction Mapping Principle)*** *Given a Banach space V and a mapping $T : V \to V$ satisfying*

$$\|Tu_1 - Tu_2\| \leq M \|u_1 - u_2\| \tag{A.2}$$

for all $u_1, u_2 \in V$ and fixed $0 \leq M < 1$, there exists a unique $u \in V$ such that

$$u = Tu. \tag{A.3}$$

Thus the contraction mapping T has a unique fixed point u.

Theorem A.0.3. ***(Riesz Representation Theorem)*** *Any continuous linear functional L on a Hilbert space H can be represented uniquely as*

$$L(v) = (u, v) \tag{A.4}$$

for some $u \in H$. Furthermore, we have

$$\|L\|_{H'} = \|u\|_H \tag{A.5}$$

Remark. According to the Riesz Representation Theorem, there is a natural isomorphism between H and H' ($u \in H \longleftrightarrow L_u \in H'$). For this reason, H and H' are often identified. For example, we can write $W_2^m(\Omega) \cong W_2^{-m}(\Omega)$(although they are completely different Hilbert spaces). We will use τ to represent the isomorphism from H' onto H.

Proof. For any $u \in V$, define a functional, Au, by $Au(v) = a(u, v)$, $\forall v \in V$. Au, is linear since

$$\begin{aligned} Au(\gamma v_1 + \delta v_2) &= a(u, \gamma v_1 + \delta v_2) \\ &= \gamma a(u, v_1) + \delta a(u, v_2) \\ &= \gamma Au(v_1) + \delta Au(v_2), \ \ \forall v_1, v_2 \in V, \gamma, \delta \in \mathbb{R}. \end{aligned}$$

Au, is also continuous since, for all $v \in V$,

$$|Au(v)| = |a(u, v)| \leq C \|u\| \|v\|,$$

where C is the constant from the definition of continuity for $a(\cdot, \cdot)$. Therefore,

$$\|Au\|_{V'} = \sup_{v \neq 0} \frac{|Au(v)|}{\|v\|} \leq C \|u\| < \infty.$$

Thus, $Au \in V'$. Similarly, one can show that the mapping $u \to Au$, is a linear map from $V$to V' which is continuous with $\|A\|_{L(V,V')} \leq C$. Now, by the Riesz Representation Theorem, for any $\phi \in V'$ there exists a unique $\tau\phi \in V$ such that $\phi(v) = (\tau\phi, v)$, for any $v \in V$. We must find a unique u, such that

$$Au(v) = F(v) \ \ \forall v \in V$$

In other words, we want to find a unique u such that

$$Au = F \ \ (\in V')$$

or

$$\tau Au = \tau F \ \ (\in V)$$

since $\tau : V' \longrightarrow V$ is a one-to-one mapping. Based on the Contraction Mapping Principle we solve this last equation. We want to find $\rho \neq 0$, such that the mapping $T : V \longrightarrow V$ is a contraction mapping where T is defined by

$$Tv := v - \rho\left(\tau Av - \tau F\right) \forall v \in V. \tag{A.6}$$

If T is a contraction mapping then there exists a unique $u \in V$, such that

$$Tu = u - \rho\left(\tau Au - \tau F\right) = u, \tag{A.7}$$

that is $\rho\left(\tau Au - \tau F\right) = 0$, or $\tau Au = \tau F$. It remains to show that such a $\rho \neq 0$ exists. For any $v_1, v_2 \in V$, let $v = v_1 - v_2$. Then,

$$\begin{aligned}
\|Tv_1 - Tv_2\|^2 &= \|v_1 - v_2 - \rho\left(\tau Av_1 - \tau Av_2\right)\|^2 \\
&= \|v - \rho(\tau Av)\|^2 \\
&= \|v\|^2 - 2\rho(\tau Av, v) + \rho^2 \|\tau Av\|^2 \\
&= \|v\|^2 - 2\rho Av(v) + \rho^2 Av(\tau Av) \\
&= \|v\|^2 - 2\rho a(v, v) + \rho^2 a(v, \tau Av) \\
&\leq \|v\|^2 - 2\rho\gamma \|v\|^2 + \rho^2 C \|v\| \|\tau Av\| \\
&\leq (1 - 2\rho\gamma + \rho^2 C^2) \|v\|^2 \\
&= (1 - 2\rho\gamma + \rho^2 C^2) \|v_1 - v_2\|^2 \\
&= M^2 \|v_1 - v_2\|^2
\end{aligned}$$

Here, γ is the constant in the definition of coercivity of $a(\cdot, \cdot)$. Note that $\|\tau\| \, Av = \|A\| \, v \leq C \|v\|$ was used in the last inequality. We thus need

$$1 - 2\rho\gamma + \rho^2 C^2 < 1$$

for some ρ, i.e, $\rho(\rho C^2 - 2\gamma) < 0$. If we choose $\rho \in \left(0, 2\gamma/C^2\right)$ then $M < 1$ and the proof is complete. □

Definition A.0.1 (The MINI Element)**.** The MINI element is a stable mixed finite element pair used for the numerical approximation of the Stokes and Navier-Stokes equations, originally introduced by Arnold, Brezzi, and Fortin. It enriches the standard continuous piecewise linear velocity space with internal "bubble" functions to satisfy the Ladyzhenskaya-Babuška-Brezzi (inf-sup) condition, while utilizing standard continuous piecewise linear functions for the pressure.
Let $\mathcal{T}_h$ be a regular triangulation of the domain $\Omega \subset \mathbb{R}^n$ (typically $n = 2$ or 3) consisting of simplices (triangles or tetrahedra) denoted by K.
The pressure approximation space Q_h is defined as the standard space of continuous, piecewise linear functions:

$$Q_h = \{q_h \in C^0(\overline{\Omega}) : q_h|_K \in P_1(K) \quad \forall K \in \mathcal{T}_h\}$$

To define the velocity space, a bubble function b_K must first be constructed on each element K. Let $\lambda_1, \ldots, \lambda_{n+1}$ represent the barycentric coordinates of the element K. The bubble function is defined as their product:

$$b_K = \prod_{i=1}^{n+1} \lambda_i$$

In two dimensions, this forms a cubic polynomial (P_3) that vanishes entirely on the boundary of the element (∂K). The global space of these bubble functions, B_h, is defined as:

$$B_h = \{v_h \in C^0(\overline{\Omega}) : v_h|_K \in \text{span}\{b_K\} \quad \forall K \in \mathcal{T}_h\}$$

The velocity approximation space V_h is then defined as the standard continuous piecewise linear space enriched by the bubble space:

$$V_h = \{v_h \in [C^0(\overline{\Omega})]^n : v_h|_K \in [P_1(K) \oplus \text{span}\{b_K\}]^n \quad \forall K \in \mathcal{T}_h\}$$

This finite element pair (V_h, Q_h) is often denoted as the $P_1^+ - P_1$ or $P_1\text{b} - P_1$ element. By enriching the velocity space with these bubble nodes, the MINI element successfully circumvents the instability issues (spurious pressure oscillations) inherent in standard $P_1 - P_1$ approximations.

APPENDIX B

Appendix B

Acronyms

AAA	Abdominal Aortic Aneurysm
ALE	Arbitrary Lagrangian–Eulerian
AMR	Adaptive Mesh Refinement
AS	Aortic Stenosis
BC	Boundary Condition
BVP	Boundary Value Problem
CFD	Computational Fluid Dynamics
CFL	Courant–Friedrichs–Lewy number
CTA	Computed Tomography Angiography
CV	Control Volume
DICOM	Digital Imaging and Communications in Medicine
DG	Discontinuous Galerkin
EOA	Effective Orifice Area
FEA	Finite Element Analysis
FEM	Finite Element Method
FHD	Ferrohydrodynamics
FSI	Fluid–Structure Interaction

FVM	Finite Volume Method
GCC	Generalized Curvilinear Coordinates
GCL	Geometric Conservation Law
GSM	Gradient Smoothed Method
HAM	Homotopy Analysis Method
ILT	Intraluminal Thrombus
LBB	Ladyzhenskaya–Babuška–Brezzi condition
LM	Levenberg–Marquardt algorithm
LNH	Local Normalized Helicity
LV	Left Ventricle
MAP	Mean Arterial Pressure
MHD	Magnetohydrodynamics
MRI	Magnetic Resonance Imaging
ODE	Ordinary Differential Equation
OSI	Oscillatory Shear Index
PDE	Partial Differential Equation
PC-MRI	Phase Contrast Magnetic Resonance Imaging
PSPG	Pressure-Stabilizing/Petrov-Galerkin
RCR	Windkessel 3-element model: R: Resistance, C: Capacitor
Re	Reynolds Number
RRT	Relative Residence Time
SPH	Smoothed Particle Hydrodynamics
SUPG	Streamline-Upwind/Petrov-Galerkin
TAWSS	Time-Averaged Wall Shear Stress

TAVR	Transcatheter Aortic Valve Replacement
Wo	Womersley Number
WRM	Weighted Residual Method
WSS	Wall Shear Stress

Index

Author's Publications

Publications

Kyriakoudi, Konstantina C., Grigorios T. Chrimatopoulos, Efstratios E. Tzirtzilakis, Michail A. Xenos, "Aneurysmal haemodynamics: a three-dimensional fluid–structure interaction approach," *R Soc Open Sci*, 13(1):251928, 2026. DOI: 10.1098rsos.251928

Katsoudas, S. C., **Kyriakoudi, K. C.**, Grigorios T. Chrimatopoulos, P. D. Linardopoulos, C. T. Chrimatopoulos, A. A. Raptis, and E. E. Tzirtzilakis, "Linking Aneurysmal Geometry and Hemodynamics Using Computational Fluid Dynamics," *Physics of Fluids, 38 (3): 031910*, 2025. DOI: 10.10635.0315857

Kyriakoudi, K. C., G. T. Chrimatopoulos, A. C. Felias, P. D. Linardopoulos, E. E. Tzirtzilakis, and M. A. Xenos, "Fluid-Structure Interaction in Arterial Hemodynamics: A Mathematical Approach," *Mathematical Analysis, Optimization and Data Science*, World Scientific Publishing Company, (to be published).

Felias, A. C., **Kyriakoudi, K. C.**, M. T. Rassias, and M. A. Xenos, "Fluid–Structure Interaction (FSI) Methods in Biofluid Mechanics," *Trends in Applied Mathematical Analysis*, Springer, (to be published).

Biraki, K. N., **Kyriakoudi, K. C.**, A. C. Felias, and M. A. Xenos, "The Finite Element Method with Applications to Fluid Mechanics," *Mathematical Analysis, Differential Equations and Applications*, World Scientific, 2024, pp. 139–174. DOI: 10.1142/9789811264429_0006

Kyriakoudi, K. C., and M. A. Xenos, "Magnetohydrodynamic effects on a patho-

logical vessel: An Euler–Lagrange approach," *Physics of Fluids*, 35(12), 2023. DOI: 10.10635.0177036

Kyriakoudi, K. C., and M. A. Xenos, "Finite Element Methods with Higher Order Polynomials," *Exploring Mathematical Analysis, Approximation Theory, and Optimization: 270 Years Since A.-M. Legendre's Birth*, Springer, 2023, pp. 161–176. DOI: 10.1007978-3-031-46487-4_10

Felias, A. C., **Kyriakoudi, K. C.**, K. N. Mpiraki, and M. A. Xenos, "Analytic and Numerical Solutions to Nonlinear Partial Differential Equations in Biomechanics," *Analysis, Geometry, Nonlinear Optimization and Applications*, World Scientific, 2023, pp. 331–403. DOI: 10.11429789811261572_0012

Raptis, A., **Kyriakoudi, K.**, and M. A. Xenos, "Finite Element Analysis in Fluid Mechanics," *Mathematical Analysis and Applications*, Springer, Cham, 2019, pp. 481–510. DOI: 10.1007978-3-030-31339-5_18

Conferences

20th European Mechanics of Materials Conference - EMMC20, Florence, Italy, 2026. Presentation "Mechanics of Aneurysmal Blood Flow: A Three-Dimensional Fluid–Structure Interaction Study".

4th Young Researchers Conference in areas of Mathematical Sciences, Ioannina, Greece, 2026. Presentation: "Three-Dimensional Computational Modelling of Fluid-Structure Interaction in Abdominal Aortic Aneurysms".

19th Panhellenic Conference of Mathematical Analysis, Athens, Greece, 2025. Presentation: "Mathematical Modelling of Blood Flow in Aneurysms".

1st HICOMP, Hellenic-Italian Conference on Computational Mechanics, Biomechanics and Mechanics of Materials, Rhodes, Greece, 2025. Presentation: "Simulation of Blood Flow in Pathological Vessels: A Finite Volume Approach".

13th Panhellenic Conference of Biomaterials, Ioannina, Greece, 2025. Presentation: "Hemodynamics in Aneurysmal Geometries Using the Finite Volume Method".

30th Summer School-Conference, "Dynamical Systems and Complexity", Poseidi, Greece, 2024. Presentation: "Fluid Dynamics in Aneurysmal Blood Vessels under Magnetic Influence".

11th IC-SCCE, Loutraki, Greece, 2024. Presentation: "Magnetohydrodynamic flow on a pathological vessel, introducing an Euler-Lagrange approach".

2nd Workshop GWM, Athens, Greece, 2024. Presentation: "Magnetic Field Effects on Hemodynamics".

3rd Young Researchers Conference in areas of Mathematical Sciences, Ioannina, Greece, 2024. Presentation: "Magnetohydrodynamic effects on blood flow in pathological vessels".

FLOW 2024, Thessaloniki, Greece, 2024. Presentation: "Magnetohydrodynamic effects on a pathological vessel: An Euler-Lagrange approach".

DIONI, Ioannina, Greece, 2023. Presentation: "Magnetic fields and blood flow: A comprehensive study on hemodynamics".

29th Summer School-Conference, "Dynamical Systems and Complexity", Athens, Greece, 2023. Presentation: "Magnetic field effects on hemodynamics: Investigating blood flow alterations".

28th Summer School-Conference, "Dynamical Systems and Complexity", Chania, Crete, 2022. Presentation: "Navier-Stokes Magnetohydrodynamics".

26th Summer School-Conference, "Non-Linear Dynamical Systems and Complexity", Athens, Greece, 2019. Poster: "Navier-Stokes in the biomedical field".

Short CV

Konstantina Kyriakoudi is a PhD candidate in Applied and Computational Mathematics at the Department of Mathematics, University of Ioannina, Greece, under the supervision of Prof. Michail Xenos. Her research focuses on biofluid mechanics, including numerical and analytical modelling of arterial and venous blood flow, fluid–structure interaction, and aneurysmal hemodynamics. She holds an MSc in Applied Mathematics and Computer Science and a BSc in Mathematics from the University of Ioannina. Her research has been supported by national and international funding programs, including the Dioni computing infrastructure project and the Safe Aorta clinical decision support project. She has contributed to multiple publications in peer-reviewed journals and conferences, covering topics such as finite element methods, magnetohydrodynamics, and numerical solutions of non-linear partial differential equations in biomechanics. In addition to her research, she has teaching experience in programming, numerical analysis, and fluid mechanics courses, and has participated in international research placements and summer schools in high-performance computing and applied mathematics. Her work combines computational modelling, interdisciplinary collaboration, and advanced numerical techniques to address challenges in cardiovascular fluid mechanics.